

Multiscale modeling of the methanol synthesis: from surface reaction kinetics to techno-economic analysis

Zur Erlangung des akademischen Grades eines

DOKTORS DER INGENIEURWISSENSCHAFTEN
(Dr.-Ing.)

von der KIT-Fakultät für
Chemieingenieurwesen und Verfahrenstechnik
des Karlsruher Instituts für Technologie (KIT)

genehmigte
DISSERTATION

von
M. Sc. Bruno Lacerda de Oliveira Campos
aus
Lagoa da Prata (MG), Brasilien

Tag der mündlichen Prüfung: 24.04.2023
Erstgutachter: Prof. Dr. -Ing. Jörg Sauer
Zweitgutachter: Prof. Dr. -Ing. Bastian J. M. Etzold

Declaration

I, Bruno Lacerda de Oliveira Campos, declare that this thesis represents my own work and that I have written it independently by myself, without the use of other documents or sources beyond those stated in the references.

Bruno Lacerda de Oliveira Campos

Acknowledgements

Here, I'd like to properly thank everybody that contributed to this PhD work, as their support was essential and highly appreciated.

First of all, I thank God for giving me this opportunity, for guiding me throughout the process, for answering my prayers, and for being there for me. Without His help and blessing, it would have been impossible for me to get the positive response from Karla (who neither knew me before nor got recommendations from friends), and the full PhD scholarship, and have success in performing the research. To Him and to His Son Jesus Christ be all the glory!

I'd like to thank my dear wife and fellow PhD student, Mariana Myriam Campos Fraga, who was always there for me, gave me good advices, brought me new motivation, persistently prayed together with me, commemorated each victory with me, and cheered me up each time something went wrong or when I was stuck in some task. Life is definitely sweeter and more amazing with you at my side!

I'd like to thank my parents, Camilo and Ângela Campos, who were patient with me, and gave me support and motivation in my education from the very beginning! Thank you inspiring me never to give up and to always trust in God!

I'd also like to thank my other relatives and friends, especially my sister, Juliana Campos, and my neighbors Florian, Helen, Harald and Christine Martini, and Klaus P. Hasselbach. Thank you for the moral support and motivation, for being there for me, and commemorating each victory with me!

I'd like to thank Prof. Jörg Sauer for the opportunity to be in his group and for supervising the work. Thank you, Prof. Sauer, for your availability for meetings despite your overloaded schedule. Thanks for the very interesting discussions and clarifying teachings, and for sharing knowledge from your experience in the industry. Each time I was in your office, I could learn something new. Thanks also for giving me the opportunity to help within the subject *Prozessentwicklung und Scale-up* (English: Process Development and Scale-up), where I could have contact with the students and practice teaching. This was an enriching, fun and necessary experience for me, who intends to pursue an academic career.

I'd like to thank Dr. Karla Herrera Delgado for being my direct supervisor. Thanks for writing the project with me, for your availability, for always giving good ideas and good advices, for your patience, for your dedication in reviewing so many abstracts, presentations, manuscripts... Thanks for your great help in the lab and in modeling, for being open to new/parallel projects, and for your support and advices regarding my future in the academia.

I'd like to thank Dr. Stephan Pitter for his general support during the PhD thesis. Thank you for your good advices, for your detailed manuscript corrections, and for bringing your chemistry and catalyst design background to the scientific discussions, which was much

needed for me and taught me a lot. Thanks also for being open and supportive to the parallel projects I was involved.

I'd like to thank Prof. Dr. Felix Studt for his cooperation within the microkinetic modeling of the methanol synthesis. Thank you for your availability for meetings, for the enlightening discussions and key explanations regarding the surface reaction mechanism and the density functional theory.

I'd like to thank my fellow PhD student Stefan Wild for his great support in the lab. Thanks a lot for your availability and patience to teach me how to use the lab plant and how to solve issues. Thanks for your friendship, for the interesting discussions, and for the great work we could develop in cooperation.

I'd like to thank Kelechi John for his support in the plant simulation and economic evaluation of the methanol synthesis. Thanks for your work, your help, and for the great explanations and good advice regarding the Aspen Plus simulations and the cost estimation, which really contributed to the work and to improved my knowledge in this field.

I'd like to thank Prof. Dr. Nicolaus Dahmen for his support in the plant simulation and economic evaluation of the methanol synthesis, and also for valuable teachings regarding scientific writing.

I'd like to thank Philipp Beeskow, who helped me as a research assistant. Thank you for great support in the simulation of heat transfer inside the methanol reactor, which involved understanding tricky equations, gathering the necessary data, and implementing everything in Matlab. Thanks also for your support in the cost estimation.

I'd like to thank Julian Schunk, whom I could supervise during his bachelor work (title: Implementation and modification of the state-of-the-art formal kinetic model of the methanol synthesis). Thanks for your dedicated work, with gave good information and pointed out many important details that were relevant for the development of the formal kinetic models (Chapter 3).

I'd like to thank Julia Arnold, whom I could supervise during her bachelor work (title: Economic optimization of the dimethyl ether synthesis from carbon dioxide and hydrogen). Thanks for your hard work, and for your persistence and patience in spite of me frequently changing the process flow diagram. I could learn a lot from your work, which had the answers to some questions that appeared later when I worked on the process and economic analysis of the methanol synthesis from H_2/CO_2 (Chapter 4).

I'd like to thank Dr. Steffen Tischer for valuable explanations regarding the equations of the microkinetic model and the thermodynamic consistency method.

I'd like to thank Dr. Thomas Zevaco for the scientific discussions that came up during the group meetings, for his availability and support in the lab.

I'd like to thank the colleagues Egbert Kehrwecker (mechanical workshop), Volker Meinzer (e-workshop), Holger Kahrau (e-workshop), Siegbert Johnsen, and Ricki Drexler for their availability and great support in the lab, either fixing something, building something new, or finding solutions for issues.

I'd like to thank Birgit Rolli for her support and patience with the Gas Chromatograph. Although in the end I didn't use this equipment in my thesis, I could learn a lot with her about the equipment, the technique, the software, and how to search and solve problems in the field of gas chromatography.

I'd like to thank Roland Fritz for his IT support. Thank you for your availability and patience, and for your fast response in problem solving.

I'd like to thank the colleagues, who friendly gave me support in administrative matters. Many thanks to Michaela Schmidt, Kerstin Barnack, Katharina Verdion, Martin Bergermann, Bernard Hemmer, and Monika Zimmer.

Finally, I'd like to thank the whole staff of the *Institut für Katalyseforschung und -technologie* (IKFT) for the interesting and joyful conversations, the commemorative meetings, the coffee cups drank together, the seminars, the friendship, and the welcoming atmosphere. IKFT is a great place to work, and I'm glad and thankful that I had this privilege.

Last but not least, I'd like to acknowledge Coordenação de Aperfeiçoamento de Pessoal de Nível Superior (CAPES), a Brazilian public foundation, for financing my PhD scholarship (Process Number: 88881.174609/2018-01). I also thank the Helmholtz Research Program "Materials and Technologies for the Energy Transition (MTET), Topic 3: Chemical Energy Carriers" for financial support related to the laboratory experiments. Finally, I acknowledge the financial support from the KIT-Publication Fund of the Karlsruhe Institute of Technology, enabling two of the publications to be open access.

*“It is the glory of God to conceal things, but
the glory of kings is to search things out”.*

Proverbs 25:2, The Holy Bible (ESV)

Preamble

This is a paper-based thesis, and, therefore, part of the content presented here has been previously published. Hence, parts of the text are identical to published articles, with minor modifications, such as formatting, citation style or even modification of the figures, tables, and layout.

In order to avoid the repetition of introductory text in each chapter, a detailed introduction of the methanol synthesis is provided in Chapter 1, which is named “An introduction to the methanol synthesis”.

In the publication entitled “Surface reaction kinetics of the methanol synthesis and the water gas shift reaction on Cu/ZnO/Al₂O₃”, an error in the calculations was found after publishing the paper. Therefore, simulations have been remade, and the respective correction file was sent to the journal and published. In Chapter 2 of this thesis, a modified version of the original manuscript is provided, containing only simulations after the correction procedure.

Abstract

One of the most challenging aspects of the future energy system is the efficient and decentralized production of chemical energy carriers with low CO₂ footprint. In this sense, the conversion of renewable H₂/CO/CO₂ to methanol could be a key intermediate step, as methanol is an adequate energy storage medium and a feedstock for a variety of added-value chemicals and liquid fuels.

An accurate mathematical description of the reaction kinetics is the foundation for process optimization and new equipment design, also contributing to the development of more active catalytic systems. Thereby, the main goal of this thesis was to improve the mechanistic understanding of the methanol synthesis on Cu/Zn-based catalysts, in the light of the interplay between the catalyst and applied process parameters. In order to address this target, three objectives were proposed and fulfilled.

The first objective was the development and experimental validation of a detailed microkinetic model of the methanol synthesis on Cu/Zn-based catalysts based on *ab initio* density functional theory (DFT) calculations from literature. Here, CO hydrogenation, CO₂ hydrogenation and the water-gas shift were considered, and the copper/zinc synergy in the catalyst matrix was taken into account. With the validated model (with own experiments and literature data), key insights were obtained regarding the preferential reaction pathways (via reaction flow analysis) and the rate-determining steps (via sensitivity analysis).

The second objective was the development and experimental validation of a formal kinetic model derived from the microkinetic model, in order to significantly reduce computational costs to perform simulations. Different approaches led to three kinetic models, with the most successful being Model-6p (6p → 6 fitted parameters). In Model-6p, key insights obtained with the microkinetic model were considered, such as the preferential reaction pathways, the rate-determining steps (RDS), and the predominant adsorbed intermediates. Direct CO hydrogenation was neglected, and six lumped parameters were fitted to the experiments. The resulting Model-6p is adequate for model-based applications, including process scale-up, process optimization, and detailed reactor simulation with computational fluid dynamics.

Finally, the third objective was the application of the proposed formal kinetic model in a detailed simulation of a methanol production plant from renewable H₂/CO₂, including heat integration and optimization of process parameters to minimize reactant consumption. The potential of including intermediate condensation steps to improve the overall process was investigated and compared to a conventional approach via process and techno-economic analyses.

In this thesis, a step-by-step process from detailed surface kinetics to applied reaction engineering is presented, linking theory and application in a systematic way. Therefore, aside from contributing to the understanding of the kinetics of the methanol synthesis, this work provides comprehensive support to analogous future projects (e.g. higher hydrocarbon production).

Zusammenfassung

Eine der größten Herausforderungen des zukünftigen Energiesystems ist die effiziente und dezentrale Produktion von chemischen Energieträgern mit geringem CO₂-Fußabdruck. In diesem Sinne könnte die Umwandlung von erneuerbarem H₂/CO/CO₂ in Methanol ein wichtiger Zwischenschritt sein, da Methanol ein geeignetes Energiespeichermedium und ein Edukt für eine Vielzahl von Mehrwertchemikalien und flüssigen Kraftstoffen ist.

Eine genaue mathematische Beschreibung der Reaktionskinetik ist die Grundlage für die Prozessoptimierung und den Entwurf neuer Anlagen und trägt zusätzlich zur Entwicklung aktiverer katalytischer Systeme bei. Das Hauptziel dieser Arbeit war es daher, das mechanistische Verständnis der Methanolsynthese an Katalysatoren auf Cu/Zn-Basis unter Berücksichtigung des Zusammenspiels zwischen dem Katalysator und den verwendeten Prozessparametern zu verbessern. Um dies zu erreichen, wurden drei Zwischenziele vorgeschlagen und umgesetzt.

Das erste Zwischenziel war die Entwicklung und experimentelle Validierung eines detaillierten mikrokinetischen Modells der Methanolsynthese an Cu/Zn-basierten Katalysatoren auf der Grundlage von ab initio Dichtefunktionaltheorie (DFT) Berechnungen aus der Literatur. Dabei wurden die CO-Hydrierung, die CO₂-Hydrierung und die Wassergas-Shift-Reaktion berücksichtigt. Auch die Cu/Zn-Synergie in der Katalysatormatrix wird in Betracht gezogen. Mit dem validierten Modell (mit eigenen Experimenten und Literaturdaten) wurden Erkenntnisse über die bevorzugten Reaktionswege (mittels Reaktionsflussanalyse) und die geschwindigkeitsbestimmenden Schritte (mittels Sensitivitätsanalyse) gewonnen.

Das zweite Zwischenziel war die Entwicklung und experimentelle Validierung eines formalen kinetischen Modells, das aus dem mikrokinetischen Modell abgeleitet wurde, um den Rechenaufwand für die Durchführung von Simulationen erheblich zu verringern. Verschiedene Ansätze führten zu drei kinetischen Modellen, von denen das Modell-6p das beste war (6p → 6 angepasste Parameter). Bei diesem Ansatz wurden wichtige Erkenntnisse aus dem mikrokinetischen Modell verwendet, wie der bevorzugte Reaktionsmechanismus, die geschwindigkeitsbestimmenden Schritte und die vorherrschenden adsorbierten Zwischenprodukte. Die direkte CO-Hydrierung wird vernachlässigt und sechs zusammengefasste Parameter wurden an die experimentellen Daten angepasst. Das daraus resultierende Modell-6p eignet sich für modellbasierte Anwendungen, einschließlich Scale-up von Prozessen, Prozessoptimierung und detaillierte Reaktorsimulationen mit Computational Fluid Dynamics (CFD).

Das dritte Zwischenziel war die Anwendung des vorgeschlagenen formalen kinetischen Modells in einer detaillierten Simulation einer Methanolanlage aus erneuerbarem H₂/CO₂, einschließlich Wärmeintegration und Optimierung der Prozessparameter zur Minimierung des Reaktantenverbrauchs. Das Potenzial der Einbeziehung von Zwischenkondensationsschritten zur Verbesserung des Gesamtprozesses wurde untersucht und mittels Prozess- und techno-ökonomischer Analysen mit einem konventionellen Ansatz verglichen.

In dieser Arbeit wird ein schrittweiser Prozess von der detaillierten Oberflächenkinetik bis zur angewandten Reaktionstechnik vorgestellt, der Theorie und Anwendung auf systematische Weise miteinander verbindet. Daher trägt diese Arbeit nicht nur zum Verständnis der Kinetik der Methanolsynthese bei, sondern bietet auch umfassende Unterstützung für analoge künftige Projekte (z. B. die Produktion höherer Kohlenwasserstoffe).

Content

Declaration	I
Acknowledgements	II
Preamble	VI
Abstract	VII
Zusammenfassung	VIII
Content	X
Chapter 1. An introduction to the methanol synthesis	1
1.1 Methanol in the current global scenario	2
1.2 History	3
1.3 Catalysts	4
1.4 Kinetic modeling	5
1.5 Process Technology	10
1.6 Objectives and outline of the thesis	12
Chapter 2. Surface reaction kinetics of the methanol synthesis and the water gas shift reaction on Cu/ZnO/Al₂O₃	14
Abstract Chapter 2	15
2.1 Introduction	16
2.2 Experimental setup	16
2.3 Kinetic model development and numerical simulation	17
2.3.1 Three-site surface reaction mechanism	17
2.3.2 Kinetic equations	18
2.3.3 Thermodynamic consistency	21
2.3.4 Estimation of the active site distribution	24
2.3.4.1 Theoretical approach – Kuld et al.	24
2.3.4.2 Simplified approach	26
2.3.5 Estimation of the active catalytic area	27
2.3.6 Reactor equations	28
2.3.6.1 Fixed-bed tube reactor	28
2.3.6.2 Continuous stirred tank reactor	29
2.3.7 Sensitivity analysis	29
2.4 Results and discussion	30
2.4.1 Model validation	30
2.4.2 Reaction flow and sensitivity analysis	34

2.5 Summary and conclusions	41
Chapter 3. Development of consistent kinetic models derived from a microkinetic model of the methanol synthesis	43
Abstract Chapter 3	44
3.1 Introduction	45
3.2 Development of the kinetic models	45
3.2.1 Model-1p: direct reduction of the microkinetic model	45
3.2.2 Model-9p: fitting the lumped parameters	48
3.2.3 Model-6p: CO hydrogenation not considered	49
3.2.4 Reactor modeling and parameter estimation	50
3.3 Results and discussion	52
3.3.1 Models considering the whole operating region	53
3.3.2 Models considering operation with CO ₂ in feed	57
3.3.3 Summary of the models	61
3.4 Conclusions	63
Chapter 4. A detailed process and techno-economic analysis of the methanol synthesis from H₂ and CO₂ with intermediate condensation steps	65
Abstract Chapter 4	66
4.1 Introduction	67
4.2 Methodology	67
4.2.1 Process Overview	67
4.2.1.1 One-step approach – Process description	68
4.2.1.2 Three-step approach – Process description	69
4.2.2 Process simulation in Matlab	70
4.2.3 Process analysis and optimization	72
4.2.4 Detailed plant simulation in Aspen Plus	73
4.2.5 Efficiency Evaluation	74
4.2.6 Techno-economic evaluation	74
4.3 Results and discussion	77
4.3.1 One-step process	77
4.3.1.1 Selecting key parameters	77
4.3.1.2 Detailed plant simulation and process analysis	78
4.3.2 Three-step process	80
4.3.2.1 Selecting key parameters	80
4.3.2.2 Detailed plant simulation and process analysis	82
4.3.3 Techno-economic analysis	85
4.4 Conclusions	86

Chapter 5. Summary, Conclusions and Outlook	89
5.1 Summary and Conclusions	90
5.2 Outlook	92
References	94
Supplementary Material	99
S1. Supplementary Material – Chapter 2	100
S1.1 Experimental setup	100
S1.2 Thermodynamic Consistency	108
S1.3 Surface coverage – Initial guess	109
S1.4 Reactor simulation – Solving the differential equations of the PFR	110
S1.5 Reactor simulation – Solving the differential equations of the CSTR	111
S1.6 Reaction flow analysis	112
S1.7 Degree of rate control	114
S2. Supplementary Material – Chapter 3	116
S2.1 Mathematical derivation of the kinetic equations	116
S2.2 Parameter re-estimation of the model from Slotboom et al.	121
S2.3 Parameter re-estimation of the model from Seidel et al.	124
S3. Supplementary Material – Chapter 4	126
S3.1. Mathematical derivation of the reactor equations	126
S3.2. Calculation of the heat transfer coefficient in the reactor	128
S3.3. Flash drums and distillation column – Assumptions for the Matlab simulations	130
S3.4. Kinetic model implementation in Aspen Plus	131
S3.5. One-step process – Simulation in Aspen Plus and stream properties	134
S3.6. Three-step process – Simulation in Aspen Plus and stream properties	139
S3.7. Equipment dimensioning	146
S.3.7.1 Flash drum	146
S3.7.2 Distillation column	147
S3.7.3 Heat exchanger	147
S3.8 Techno-economic analysis	149
Nomenclature	154
List of Abbreviations	158
List of Figures	160
List of Tables	163

List of Publications

166

Chapter 1. An introduction to the methanol synthesis

This chapter contains content of the following publication:

Lacerda de Oliveira Campos, B.; Herrera Delgado, K.; Wild, S.; Studt, F.; Pitter, S.; Sauer, J. Surface reaction kinetics of the methanol synthesis and the water gas shift reaction on Cu/ZnO/Al₂O₃. *React. Chem. Eng.*, 2021, **6**, 868-887. DOI: 10.1039/d1re00040c

1.1 Methanol in the current global scenario

Due to the economic and population growth, the global energy demand has been continuously increasing, reaching almost 600 EJ or 14,300 MTOE (million tons of oil equivalent) in 2021.¹ As a consequence, CO₂ yearly emissions have been steadily rising (33.8 Gt in 2021),¹ causing serious concerns regarding climate change. In an effort to reduce fossil fuel dependency and CO₂ emissions, significant investments have been made in renewable energy in the last decades, with its share in global primary energy demand increasing from 7.0% (2000) to 13.5% (2021).¹ These efforts are commendable, but a much higher pace is required to meet the main goal of the Paris Agreement: holding the global average temperature increase below 2 °C (or preferably 1.5 °C) in relation to pre-industrial levels.²

Within this scenario of implementing and expanding a sustainable energy system, much has been debated on efficient strategies to store, transport, and use energy. Hydrogen plays an important role in this system as a main product of a primary conversion of biomass (e.g. via gasification) or renewable electricity (e.g. via water electrolysis). There are several possible end-uses for hydrogen, such as in the heat provision section, in power generation, in grid balancing, and in the transportation section.³ However, the volumetric energy density of H₂ is low even at extreme conditions (gas H₂ at 200 bar: 1.3 MJ·L⁻¹, gas H₂ at 690 bar: 4.5 MJ·L⁻¹, liquid H₂: 8.5 MJ·L⁻¹), much inferior than of conventional fuels (e.g.: gasoline: 34 MJ·L⁻¹, diesel: 38.6 MJ·L⁻¹). This limits H₂ utilization in the transportation section to large vehicles,³ and contributes to higher costs of H₂ storage in comparison with other fuels. Besides, while H₂ can be blended into the existing natural gas pipeline structure to kick-start a so-called "hydrogen economy", a dedicated infrastructure is essential in a subsequent stage, which is yet to be constructed.³ Therefore, instead of concentrating efforts to achieve a hydrogen economy, an efficient conversion of hydrogen into secondary carbon-based energy carriers should be a better approach to implement a sustainable energy system: first because existing infrastructures of present fossil energy carriers could be used, and second because the storage issue associated with the low density of hydrogen would be solved.^{4,5}

Methanol is a suitable candidate as energy storage medium, which can be directly produced from syngas (H₂/CO/CO₂). The methanol synthesis is a mature process with a sizable global production capacity (164 Mton in 2021),⁶ and an annual capacity increase of ca. 10% projected for the next decade.⁶ Methanol can be converted to a variety of chemicals (e.g. formaldehyde, acetic acid, olefins) and fuels (e.g. gasoline, diesel, jet fuel, methyl-tert-butyl-ether, oxymethylene ethers, dimethyl ether). It is also a suitable fuel itself, with a relevant market size in China (5.7 Mton in 2019) for thermal applications (boilers, kilns, and cooking stoves) and in the transportation section.⁷ Additionally, methanol can also be used in fuel cells, both directly (direct methanol fuel cells, DMFC) or indirectly as a hydrogen carrier. In Fig. 1.1, the pathways to methanol production and utilization are illustrated.

Regarding the properties of methanol, it is the simplest alcohol (CH_3OH), liquid at ambient conditions (boiling temperature: $64\text{ }^\circ\text{C}$), easily transportable, and with a considerable energy density ($15.6\text{ MJ}\cdot\text{L}^{-1}$). Methanol is safer to transport than gasoline or diesel, due to its higher auto-ignition temperature.⁸ Although its toxicity is comparable to gasoline,⁸ if an accident occurs where methanol is spilled into the environment, the impact is less serious compared to hydrocarbons, because it is easily bio- and photodegradable (half-life of 18 days) and completely miscible with water, which would dilute methanol to safer concentrations in the case of a ship accident.^{8,9}

Thereby, the so-called “methanol economy” has significantly advantages in comparison with the hydrogen economy, and is expected to play an important role in the development of a sustainable energy system.⁵

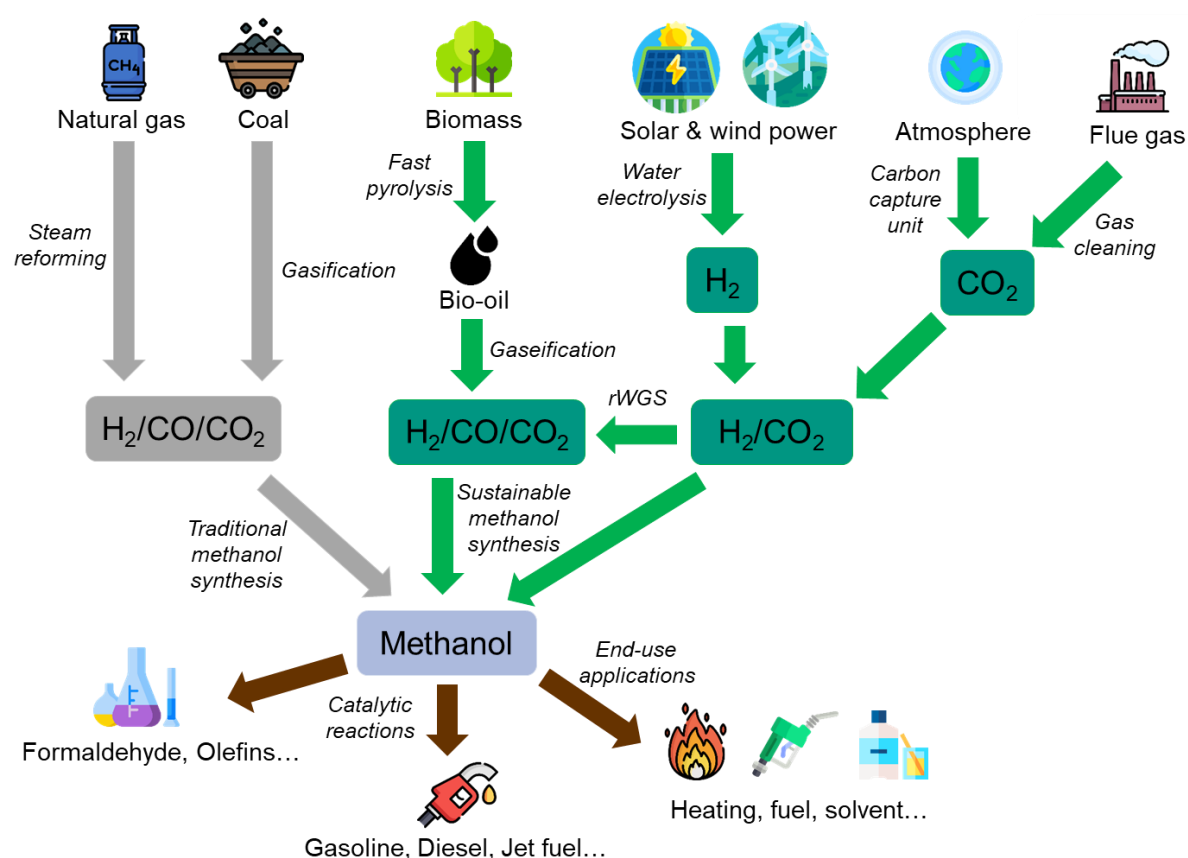


Fig. 1.1 From syngas sources to higher added-value chemicals and fuels via methanol synthesis. Icons: Freepik, Flaticon.¹⁰ Reproduced with permission from Campos et al.¹¹ Copyright 2022, MDPI.

1.2 History

In 1661, Sir Robert Boyle obtained methanol for the first time via rectification of crude wood vinegar over milk of limewater. In the 19th and the beginning of the 20th century, methanol was mainly obtained by dry distillation of wood, and was called “wood alcohol”. In 1923, the first large-scale production of methanol began in BASF Leuna Works. The syngas

used in the methanol synthesis was produced via coal gasification, containing some contaminants, such as sulfur. The methanol synthesis occurred on a sulfur-resistant ZnO/Cr₂O₃ catalyst, which was developed by Alwin Mittasch and was only active at high temperatures (320-450 °C) and high pressures (250-350 bar).^{12, 13}

In 1947, Eugeniusz Blasiak discovered that Cu/ZnO/Al₂O₃ (CZA) was highly active to the methanol synthesis, although not being resistant to sulfur.¹⁴ In 1966, with the development of methane steam reforming, which produced a much cleaner syngas, it was possible for ICI to implement a methanol synthesis route using a Cu/Zn-based catalyst, which occurred at relatively milder conditions (200-300 °C, 50-100 bar) and a much higher methanol selectivity (> 99.5%).¹³

Currently, industrial methanol production still relies on Cu/Zn-based catalysts at mild conditions and syngas with low CO₂-content, which is mainly produced via steam reforming of methane or via coal gasification. Nonetheless, e-methanol and e-gasoline large-scale production plants powered by water electrolysis from renewable electricity and captured carbon are planned to start production in 2024/2025.^{15, 16}

1.3 Catalysts

The previously mentioned Cu/ZnO/Al₂O₃ (CZA) is the most used catalyst in industrial methanol synthesis to this day. Its main qualities are: relatively high activity, extremely high selectivity to methanol (> 99.5%), long lifetime at full load (> 3 years), and relatively low costs.¹³

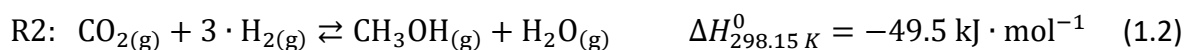
Although there is still discussion in literature regarding the role of zinc in the CZA catalyst, many researchers agree that the high activity of this catalyst comes from a Cu/Zn synergy, with zinc enhancing the stabilization of oxygen-bound species.¹⁷⁻²⁰ The major contributions of the alumina support are to increase copper dispersion and improve the mechanical stability of the catalyst.^{17, 21, 22}

CZA composition varies from one manufacturer to the other, with normally a high Cu content (20-76% m/m), a moderate Zn content (10-50% m/m), and a low Al₂O₃ content (3-30% m/m).^{13, 23} Other metals have been tested as additional promoters, such as magnesium, zirconium and rare earth oxides, in order to improve activity and stability. The substitution of Al₂O₃ for ZrO₂ has received particular attention in research, with the Cu/ZnO/ZrO₂ (CZZ) showing considerably higher activity than the commercial CZA for a syngas rich in CO₂.²⁴

Alternatives to Cu-based catalysts have been investigated, such as Pd alloys,^{25, 26} Pt alloys,²⁷ In₂O₃,^{28, 29} as well as metal-organic frameworks (MOFs).³⁰ At CO₂-rich conditions, these alternative catalysts presented higher resistance to sintering and lowered CO production via rWGS (a side reaction in the methanol synthesis from H₂/CO₂). However, disadvantages of these catalysts in relation to Cu/Zn-based catalysts are often lower activities and higher catalysts costs.

1.4 Kinetic modeling

The methanol synthesis consists in three main reactions: CO hydrogenation to methanol (Eq. 1.1), CO₂ hydrogenation to methanol (Eq. 1.2), and the water-gas shift reaction (WGSR) (1.3).



Since any of these three reactions can be described as a linear combination of the other two, there has been an historical discussion about the preferred carbon source for methanol production (CO or CO₂). This lack of consensus is seen in the different formal kinetic models that have been developed to simulate the methanol synthesis on CZA. They can be organized in four groups, according to the considered reactions:

- a. All three reactions are considered (R1, R2, R3) ³¹⁻³⁴
- b. Methanol is formed from both CO and CO₂, and the WGSR is neglected (R1, R2) ^{35, 36}
- c. Methanol is formed only from CO and the WGSR is present (R1, R3) ³⁷
- d. Methanol is only formed from CO₂ and the WGSR is present (R2, R3) ³⁸⁻⁴¹

Regarding the number of different active sites, there are models considering a single site,³⁵⁻⁴¹ two sites,³¹ and three sites.³²⁻³⁴ The models of Klier et al.³⁵ and Seidel et al.³⁴ also accounts for dynamic structural changes on the catalyst surface, which modifies the quantity of active sites. This phenomenon has been experimentally observed, and is caused by zinc mobility at typical methanol synthesis conditions on Cu/Zn-based catalysts, causing rapid alterations in the catalyst structure if the operating conditions (especially feed composition) are changed, which can affect catalyst activity.⁴²⁻⁴⁵

In Table 1.1, a summary of formal kinetic models for the methanol synthesis on Cu/Zn-based catalysts is presented. It should be mentioned that these models were written considering the reverse water-gas shift reaction (rWGSR) as the forward direction of reaction R3.

Table 1.1 Summary of different formal kinetic models reported in literature until 2020.

Authors (Year)	Reactions	Types of active sites and predominant adsorbed gases	Number of parameters	Operating conditions	Reaction rates	Equation Number
Klier et al. ³⁵ (1982)	R1: CO Hyd.	A: for H ₂ , CO, and CO ₂	12	75 bar 225-250 °C	$\dot{r}_{CO} = k_{CO} \cdot \left(1 + \frac{p_{CO}}{K_{redox} \cdot p_{CO_2}}\right)^{-3} \cdot \frac{K_{CO} \cdot K_{H_2}^2 \cdot (p_{CO} \cdot p_{H_2}^2 - p_{CH_3OH} \cdot K_{P,CO\ hyd.}^0)^{-1}}{(1 + K_{CO} \cdot p_{CO} + K_{CO_2} \cdot p_{CO_2} + K_{H_2} \cdot p_{H_2})}$	(1.4)
	R2: CO ₂ Hyd.				$\dot{r}_{CO_2} = k_{CO_2} \cdot \left(p_{CO_2} - \frac{p_{CH_3OH} \cdot p_{H_2O}}{K_{P,CO_2\ hyd.}^0 \cdot p_{H_2}^3}\right)$	(1.5)
Villa et al. ³⁷ (1985)	R1: CO Hyd.	A: for H ₂ , CO, and CO ₂	10	30–95 bar 215-245 °C	$\dot{r}_{CO} = \frac{f_{CO} \cdot f_{H_2}^2 - f_{CH_3OH} \cdot K_{P,CO\ hyd.}^0}{(A_1 + A_2 \cdot p_{CO} + A_3 \cdot p_{H_2} + A_4 \cdot p_{CO_2})}$	(1.6)
	R3: rWGSR				$\dot{r}_{rWGSR} = \frac{f_{CO_2} \cdot f_{H_2} - f_{CO} \cdot f_{H_2O} \cdot K_{P,rWGSR}^0}{A_6}$	(1.7)
Graaf et al. ³¹ (1988)	R1: CO Hyd.	A: for CO and CO ₂ B: for H ₂ and H ₂ O	12	15–50 bar 210-245 °C	$\dot{r}_{CO} = \frac{k_{CO} \cdot K_{CO} \cdot (f_{CO} \cdot f_{H_2}^{1.5} - f_{CH_3OH} \cdot f_{H_2}^{-0.5} \cdot K_{P,CO\ hyd.}^0)}{(1 + K_{CO} \cdot f_{CO} + K_{CO_2} \cdot f_{CO_2}) \cdot [f_{H_2}^{0.5} + (K_{H_2O} \cdot k_{H_2}^{-0.5}) \cdot f_{H_2O}]}$	(1.8)
	R2: CO ₂ Hyd.				$\dot{r}_{CO_2} = \frac{k_{CO_2} \cdot K_{CO_2} \cdot (f_{CO_2} \cdot f_{H_2}^{1.5} - f_{CH_3OH} \cdot f_{H_2O} \cdot f_{H_2}^{-1.5} \cdot K_{P,CO_2\ hyd.}^0)}{(1 + K_{CO} \cdot f_{CO} + K_{CO_2} \cdot f_{CO_2}) \cdot [f_{H_2}^{0.5} + (K_{H_2O} \cdot k_{H_2}^{-0.5}) \cdot f_{H_2O}]}$	(1.9)
	R3: rWGSR				$\dot{r}_{rWGSR} = \frac{k_{rWGSR} \cdot K_{CO_2} \cdot (f_{CO_2} \cdot f_{H_2} - f_{H_2O} \cdot f_{CO} \cdot K_{P,rWGSR}^0)}{(1 + K_{CO} \cdot f_{CO} + K_{CO_2} \cdot f_{CO_2}) \cdot [f_{H_2}^{0.5} + (K_{H_2O} \cdot k_{H_2}^{-0.5}) \cdot f_{H_2O}]}$	(1.10)
Skrzypek et al. ³⁸ (1991)	R2: CO ₂ Hyd.	A: for H ₂ , CO, CO ₂ , CH ₃ OH, and H ₂ O	14	30–90 bar 187-277 °C	$\dot{r}_{CO_2} = \frac{k_1 \cdot K_{H_2}^2 \cdot K_{CO_2} \cdot [p_{CO_2} \cdot p_{H_2}^2 - p_{CH_3OH} \cdot p_{H_2O} \cdot (p_{H_2} \cdot K_{P,CO_2\ hyd.}^0)^{-1}]}{(1 + K_{H_2} \cdot p_{H_2} + K_{CO_2} \cdot p_{CO_2} + K_{CH_3OH} \cdot p_{CH_3OH} + K_{H_2O} \cdot p_{H_2O} + K_{CO} \cdot p_{CO})^3}$	(1.11)
	R3: rWGSR				$\dot{r}_{rWGSR} = \frac{k_2 \cdot K_{H_2} \cdot K_{CO_2} \cdot [p_{CO_2} \cdot p_{H_2} - p_{CO} \cdot p_{H_2O} \cdot (K_{P,rWGSR}^0)^{-1}]}{(1 + K_{H_2} \cdot p_{H_2} + K_{CO_2} \cdot p_{CO_2} + K_{CH_3OH} \cdot p_{CH_3OH} + K_{H_2O} \cdot p_{H_2O} + K_{CO} \cdot p_{CO})^2}$	(1.12)

Table 1.1 (Continuation)

Authors (Year)	Reactions	Types of active sites and predominant adsorbed gases	Number of parameters	Operating conditions	Reaction rates	Equation Number
Vanden Bussche and Froment ³⁹ (1996)	R2: CO ₂ Hyd.	A: for H ₂ and H ₂ O	10	15–51 bar	$\dot{r}_{CO_2} = \frac{k_{CO_2} \cdot [p_{CO_2} \cdot p_{H_2} - p_{CH_3OH} \cdot p_{H_2O} \cdot p_{H_2}^{-2} \cdot K_{P,CO_2 hyd.}^{-1}]}{(1 + K_{H_2O} \cdot p_{H_2O} \cdot (K_8 \cdot K_9 \cdot K_{H_2} \cdot p_{H_2})^{-1} + (K_{H_2} \cdot p_{H_2})^{0.5} + K_{H_2O} \cdot p_{H_2O})^3}$	(1.13)
	R3: rWGSR			180-280 °C	$\dot{r}_{rWGSR} = \frac{k_{rWGSR} \cdot [p_{CO_2} - p_{CO} \cdot p_{H_2O} \cdot (K_{P,rWGSR} \cdot p_{H_2})^{-1}]}{(1 + K_{H_2O} \cdot p_{H_2O} \cdot (K_8 \cdot K_9 \cdot K_{H_2} \cdot p_{H_2})^{-1} + (K_{H_2} \cdot p_{H_2})^{0.5} + K_{H_2O} \cdot p_{H_2O})}$	(1.14)
Kubota et al. ⁴⁰ (2001)	R2: CO ₂ Hyd.	A: for CO ₂ and H ₂ O	11	49 bar	$\dot{r}_{CO_2} = \frac{k_{CO_2} \cdot [p_{CO_2} \cdot p_{H_2} - p_{CH_3OH} \cdot p_{H_2O} \cdot p_{H_2}^{-2} \cdot K_{P,CO_2 hyd.}^{-1}]}{(1 + K_{CO_2} \cdot p_{CO_2} + K_{H_2O} \cdot p_{H_2O})^2}$	(1.15)
	R3: rWGSR			200-275 °C	$\dot{r}_{rWGSR} = \frac{k_{rWGSR} \cdot [p_{CO_2} - p_{CO} \cdot p_{H_2O} \cdot p_{H_2}^{-1} \cdot K_{P,rWGSR}^{-1}]}{1 + K_{CO_2} \cdot p_{CO_2} + K_{H_2O} \cdot p_{H_2O}}$	(1.16)
Lim et al. ³² (2009)	R1: CO Hyd.	A: for CO	14*	50 bar	$\dot{r}_{CO} = \frac{k_{CO} \cdot K_{CO} \cdot K_{H_2}^2 \cdot K_{CH,CO} \cdot (p_{CO} \cdot p_{H_2}^2 - p_{CH_3OH} \cdot K_{P,CO hyd.}^{-1})}{(1 + K_{CO} \cdot f_{CO}) \cdot (1 + K_{H_2}^{0.5} \cdot p_{H_2}^{0.5} + K_{H_2O} \cdot p_{H_2O})}$	(1.17)
	R2: CO ₂ Hyd.	B: for CO ₂		250-280 °C	$\dot{r}_{CO_2} = \frac{k_{CO_2} \cdot K_{CO_2} \cdot K_{H_2} \cdot K_{CH,CO_2} \cdot (p_{CO_2} \cdot p_{H_2} - p_{CH_3OH} \cdot p_{H_2O} \cdot p_{H_2}^{-2} \cdot K_{P,CO_2 hyd.}^{-1})}{(1 + K_{CO_2} \cdot p_{CO_2}) \cdot (1 + K_{H_2}^{0.5} \cdot p_{H_2}^{0.5} + K_{H_2O} \cdot p_{H_2O})}$	(1.18)
	R3: rWGSR	C: for H ₂ and H ₂ O		$\dot{r}_{rWGSR} = \frac{k_{rWGSR} \cdot K_{CO_2} \cdot K_{H_2}^{0.5} \cdot (p_{CO_2} \cdot p_{H_2}^{0.5} - p_{H_2O} \cdot p_{CO} \cdot p_{H_2}^{-0.5} \cdot K_{P,rWGSR}^{-1})}{(1 + K_{CO_2} \cdot p_{CO_2}) \cdot (1 + K_{H_2}^{0.5} \cdot p_{H_2}^{0.5} + K_{H_2O} \cdot p_{H_2O})}$	(1.19)	
Ma et al. ³⁶ (2009)	R1: CO Hyd.	A: for H ₂ , CO, and CO ₂	10	80 bar	$\dot{r}_{CO} = \frac{k_{CO} \cdot (f_{CO} \cdot f_{H_2}^2 - p_{CH_3OH} \cdot K_{P,CO hyd.}^{-1})}{(1 + K_{CO} \cdot f_{CO} + K_{CO_2} \cdot f_{CO_2} + K_{H_2} \cdot f_{H_2})}$	(1.20)
	R2: CO ₂ Hyd.			200-262 °C	$\dot{r}_{CO_2} = \frac{k_{CO} \cdot (f_{CO_2} \cdot f_{H_2}^3 - f_{CH_3OH} \cdot f_{H_2O} \cdot K_{P,CO_2 hyd.}^{-1})}{(1 + K_{CO} \cdot f_{CO} + K_{CO_2} \cdot f_{CO_2} + K_{H_2} \cdot f_{H_2})}$	(1.21)

* Without counting the parameters for DME formation as a side reaction, proposed by the authors (6 extra parameters).

Table 1.1 (Continuation)

Authors (Year)	Reactions	Types of active sites and predominant adsorbed gases	Number of parameters	Operating conditions	Reaction rates	Equation Number
Park et al. ³³ (2014)	R1: CO Hyd.	A: for CO	12*	50–90 bar 230–340 °C	$\dot{r}_{CO} = \frac{k_{CO} \cdot K_{CO} \cdot (f_{CO} \cdot f_{H_2}^{1.5} - f_{CH_3OH} \cdot f_{H_2}^{-0.5} \cdot K_{P,CO}^0 \cdot K_{hyd}^{-1})}{(1 + K_{CO} \cdot f_{CO}) \cdot (1 + K_{H_2}^{0.5} \cdot f_{H_2}^{0.5} + K_{H_2O} \cdot f_{H_2O})}$	(1.22)
	R2: CO ₂ Hyd.	B: for CO ₂			$\dot{r}_{CO_2} = \frac{k_{CO_2} \cdot K_{CO_2} \cdot (f_{CO_2} \cdot f_{H_2}^{1.5} - f_{CH_3OH} \cdot f_{H_2O} \cdot f_{H_2}^{-1.5} \cdot K_{P,CO_2}^0 \cdot K_{hyd}^{-1})}{(1 + K_{CO_2} \cdot f_{CO_2}) \cdot (1 + K_{H_2}^{0.5} \cdot f_{H_2}^{0.5} + K_{H_2O} \cdot f_{H_2O})}$	(1.23)
	R3: rWGS	C: for H ₂ and H ₂ O			$\dot{r}_{rWGS} = \frac{k_{rWGS} \cdot K_{CO_2} \cdot (f_{CO_2} \cdot f_{H_2} - f_{H_2O} \cdot f_{CO} \cdot K_{P,rWGS}^0)^{-1}}{(1 + K_{CO_2} \cdot f_{CO_2}) \cdot (1 + K_{H_2}^{0.5} \cdot f_{H_2}^{0.5} + K_{H_2O} \cdot f_{H_2O})}$	(1.24)
Seidel et al. ³⁴ (2018)	R1: CO Hyd.	A: for CO	12	30–70 bar 230–260 °C	$\dot{r}_{CO} = \frac{(1 - \phi_{Zn})k_{CO} \cdot (f_{CO} \cdot f_{H_2}^2 - f_{CH_3OH} \cdot K_{P,CO}^0 \cdot K_{hyd}^{-1})}{(1 + K_{CO} \cdot f_{CO}) \cdot (1 + K_{H_2}^{0.5} \cdot f_{H_2}^{0.5})^4}$	(1.25)
	R2: CO ₂ Hyd.	B: for H ₂ , CO ₂ , and H ₂ O			$\dot{r}_{CO_2} = \frac{\phi_{Zn}^2 \cdot k_{CO_2} \cdot (f_{CO_2} \cdot f_{H_2}^2 - f_{CH_3OH} \cdot f_{H_2O} \cdot f_{H_2}^{-1} \cdot K_{P,CO_2}^0 \cdot K_{hyd}^{-1})}{[1 + (K_{H_2O} \cdot K_O \cdot K_{H_2}^{-1}) \cdot f_{H_2O} \cdot f_{H_2}^{-1} + K_{CO_2} \cdot f_{CO_2} + K_{H_2O} \cdot f_{H_2O}]^2 \cdot (1 + K_{H_2}^{0.5} \cdot f_{H_2}^{0.5})^4}$	(1.26)
	R3: rWGS	C: for H ₂			$\dot{r}_{rWGS} = \frac{\phi_{Zn} \cdot (1 - \phi_{Zn})^{-1} \cdot k_{rWGS} \cdot (f_{CO_2} - f_{H_2O} \cdot f_{CO} \cdot f_{H_2}^{-1} \cdot K_{P,rWGS}^0)^{-1}}{[1 + (K_{H_2O} \cdot K_O \cdot K_{H_2}^{-1}) \cdot f_{H_2O} \cdot f_{H_2}^{-1} + K_{CO_2} \cdot f_{CO_2} + K_{H_2O} \cdot f_{H_2O}] \cdot (1 + K_{CO} \cdot f_{CO})}$	(1.27)
					$\phi = 0.5 \cdot \left[1 - \frac{1 - \sqrt{K_1 \cdot K_2 \cdot p_{H_2} \cdot p_{CO} \cdot p_{H_2O}^{-1} \cdot p_{CO_2}^{-1}}}{1 + \sqrt{K_1 \cdot K_2 \cdot p_{H_2} \cdot p_{CO} \cdot p_{H_2O}^{-1} \cdot p_{CO_2}^{-1}}} \right]$	(1.28)
Slotboom et al. ⁴¹ (2020)	R2: CO ₂ Hyd.	A: for H ₂ , H ₂ O, and CH ₃ OH	6	20–70 bar 210–260 °C	$\dot{r}_{CO_2} = \frac{k_{CO_2} \cdot (f_{CO_2} \cdot f_{H_2}^2 - f_{CH_3OH} \cdot f_{H_2O} \cdot f_{H_2}^{-1} \cdot K_{P,CO_2}^0 \cdot K_{hyd}^{-1})}{[k_{H_2} \cdot f_{H_2}^{0.5} + k_{H_2O/9} \cdot f_{H_2O} + f_{CH_3OH}]^2}$	(1.29)
	R3: rWGS				$\dot{r}_{rWGS} = \frac{k_{rWGS} \cdot (f_{CO_2} \cdot f_{H_2}^{0.5} - f_{H_2O} \cdot f_{CO} \cdot f_{H_2}^{-0.5} \cdot K_{P,rWGS}^0)^{-1}}{[k_{H_2} \cdot f_{H_2}^{0.5} + k_{H_2O/9} \cdot f_{H_2O} + f_{CH_3OH}]}$	(1.30)

* Without counting the parameters for DME formation as a side reaction, proposed by the authors (6 extra parameters).

In formal kinetic models of the Langmuir-Hinshelwood type, each reaction rate is obtained first by considering a dominant reaction mechanism, and then by assuming a rate-determining step (RDS). Although several models are supported by some degree of theory to choose the reaction mechanisms or the RDSs, a common practice is to test different RDS assumptions, fit the parameters to experimental data, and choose the combination of RDSs with the lowest sum of squared errors.^{31, 41} While the models might adequately simulate the laboratory experiments in a certain operating window, these assumptions and the parameter lumping may merge different effects with kinetics and cause the models to diverge outside the training region, which is often narrow.⁴⁶

A more detailed approach to chemical reactions is microkinetic modeling. This type of model takes into account the chemistry behind the process,⁴⁶ being useful for better understanding of the system, for process optimization and for catalyst development. Based on data derived from first principles density functional theory (DFT), detailed microkinetic models have been proposed for methanol synthesis,⁴⁷⁻⁵² in which different surface reaction paths are considered and all reactions are potentially rate limiting. Grabow and Mavrikakis⁴⁷ proposed a mechanism for CO/CO₂ hydrogenation and the WGS on Cu (111). In the adsorption steps, sticking coefficients equal to one were considered. The authors concluded that a more open surface (e.g. Cu (110), Cu (100), Cu (211)) could better represent the catalyst active area, and that the synergic effect of ZnO has to be taken into account, both conclusions being later confirmed by Behrens et al.¹⁷ Van Rensburg et al.⁴⁸ used previously reported DFT data^{17, 53} to test microkinetic mechanisms for CO and CO₂ hydrogenation on different facets, i.e., Cu (111), Cu (211), and Cu/Zn (211), without including a mechanism for the WGS. Liu et al.⁴⁹ compared the mechanisms on Cu₂O (111) and on Cu (111), and concluded that CO hydrogenation is faster on Cu₂O, whereas CO₂ hydrogenation is the dominating path on Cu (111). Park et al.⁵⁰ proposed a mechanism on Cu (211), in which adsorption and activation energies were taken from DFT derived data, and pre-exponential factors were fitted to experimental data. Xu et al.⁵¹ proposed a mechanism on Cu (211) and compared three situations: clean surface, preadsorbed O*, and preadsorbed OH*. The conclusion was that the preadsorbed species create faster reaction paths for the hydrogenation of formate. Huš et al.⁵² developed a mechanism on Cu (111) for different metal oxides (Zn₃O₃, Cr₃O₃, Fe₃O₃, Mg₃O₃) combined with copper, and concluded that the Zn₃O₃/Cu system has a superior performance.

In the aforementioned DFT-based models, single active sites were considered, and no structural changes in the catalyst were mentioned. To the best of our knowledge, only Huš et al.⁵² validated their model with own experimental data. The other models cited above were either validated with experiments reported in literature,³¹ or there was no validation at all. Finally, only Van Rensburg et al.⁴⁸ considered the steeped facets of both Cu (211) and Cu/Zn (211), which are the most active ones according to Behrens et al.¹⁷ and Studt et al.^{18, 54} Still, Van Rensburg et al.⁴⁸ did not include the WGS.

Therefore, the development of a full microkinetic model which takes these important features into account is not available in literature, to the best of our knowledge. Such a model is of high interest to better understand the reaction mechanism of the methanol synthesis, and might help in the design of new catalysts and in process optimization.

1.5 Process technology

Since the methanol formation reactions are exothermic and the mole quantity is reduced, increased pressure and reduced temperature are favored thermodynamically (see Fig. 1.2). However, the activity of Cu/Zn-based catalysts drops substantially below 200-220 °C. Therefore, the typical conditions mentioned in Section 1.2 (200-300 °C and 50-100 bar) are applied industrially.

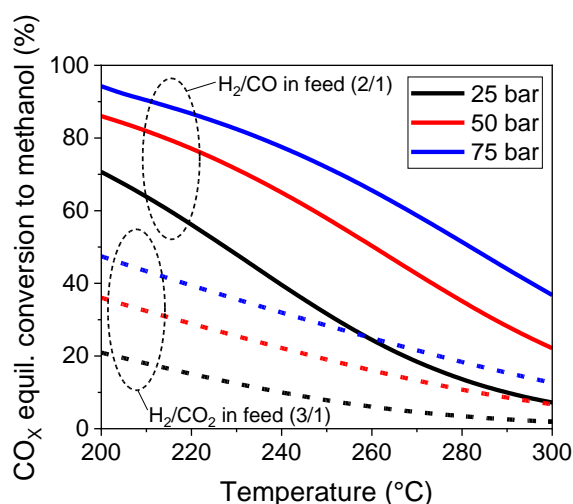


Fig. 1.2 CO_x equilibrium conversion to methanol at different temperatures and pressures, with stoichiometric feed gas composition. Solid lines: H₂:CO feed ratio of 2:1. Dashed lines: H₂:CO₂ feed ratio of 3:1. Data generated with Aspen Plus (property method: Peng-Robinson).

Due to the exothermic nature of the reactions, cooling is required to control temperature, allowing higher CO_x conversion and protecting the catalyst against strong deactivation caused by high temperatures. Different strategies were developed, and the reactor types can be divided in adiabatic reactors with intermediate cooling (direct or indirect) and polytrophic reactors. In Fig. 1.3, schemes of the basic reactor types are provided.

In adiabatic reactors with direct intermediate cooling (Fig. 1.3a), also called quench reactors, pre-heated syngas enters one side of the reactor, which has several catalyst beds. Between each catalyst bed, cold syngas is distributed to cool the system back to lower temperatures (200-230 °C) while also recovering heat. In the ICI (now Johnson Matthey) & Casale process, syngas flows in the axial direction, while radial flow is proposed in the Halder Topsoe process, reducing pressure loss.¹³ This is the simplest process with the lowest investment costs, but flow distribution may be irregular, which could create cold and hot

zones. While cold zones reduce catalyst activity, hot zones accelerate catalyst deactivation and enhance by-product formation.¹³

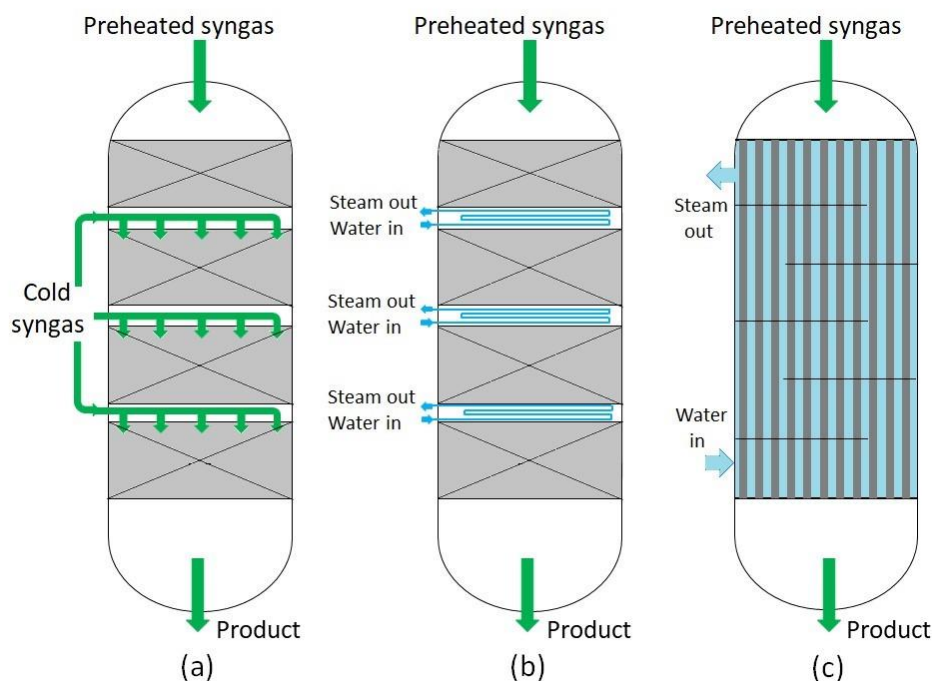


Fig. 1.3 Basic types of methanol reactor. (a) Adiabatic reactor with direct intermediate cooling. (b) Adiabatic reactor with indirect intermediate cooling. (c) Polytrophic reactor. Reproduced with permission from Perret et al.⁵⁷. Copyright 2022, Wiley.

In adiabatic reactors with indirect intermediate cooling (Fig. 1.3b), there are also several catalyst beds disposed in series. The feed gas enters one side of the reactor, and is cooled after each reaction step with water at its boiling point, which vaporizes. The produced steam can be applied to other processes or used to generate electricity. Modifications of this process include a cascade of spherical reactors (Kellogg process),¹³ and a cylindrical reactor with radial flow (Toyo Engineering process).⁵⁵

Polytrophic reactors (Fig. 1.3c) are sometimes called isothermal reactors (although a ΔT as high as 60 K can be reached along the reactor), and have some similarities to heat exchangers of the tube-and-shell type. The catalyst fills the inner tubes, while the cooling fluid (normally water at its boiling point) flows on the shell side. In this configuration, the reacting medium is continuously cooled, resulting in better temperature control. Consequently, the catalyst life and the methanol selectivity are enhanced. In the Linde Engineering process, helically inner tubes are used to avoid tension problems.⁵⁶ In the Lurgi combined methanol converter, two reactors are displaced in series. The first one is operated at high temperatures, with the catalyst bed placed in the tube side, and cooling performed by water at its boiling point. The second one is operated at lower temperatures, the catalyst bed placed in the shell side, and cooling performed by the inlet feed gas, which is pre-heated in the process.¹³

It is important to mention that the processes just described were developed for CO-rich feed gases with low CO₂ content, produced via steam reforming or coal gasification. If a H₂/CO₂ feed (e.g. from a green process) is used instead, the maximum possible CO₂ conversion in a single-pass is significantly lower (see Fig. 1.2), which would then require higher recycle and purge streams, increasing production costs. Besides, without CO to consume water through the WGS, water accumulates in the system, which may slow down the methanol synthesis by blocking active sites (see the different proposed reaction rates in Table 1.2).

In this situation, a possible strategy would be to remove the products (i.e., methanol and water) from the reacting system, in order to shift the thermodynamic equilibrium towards higher methanol yield. This approach has been studied using alternative reactor designs with in situ condensation,^{58, 59} or membrane reactors,⁶⁰ but these technologies have not been applied industrially yet. A feasible approach using commercially proven technology is the implementation of intermediate condensation steps between reactor units displaced in series. In the Davy series loop methanol process, two reactors with an intermediate condensation unit are proposed for large scale methanol production from CO-rich syngas.^{12, 61} Although the implementation of intermediate condensation steps is a promising strategy to increase methanol yield from H₂/CO₂ syngas, such approach has still not received particular attention, and plant simulations with heat integration and techno-economic analyses are not available in literature yet, to the best of our knowledge.

1.6 Objectives and outline of the thesis

The main goal of this work was to improve the mechanistic understanding of the methanol synthesis on Cu/Zn-based catalysts, in the light of the interplay between the catalyst and applied process parameters. As an outcome of these investigations, a quantitative description of these effects by purpose-developed kinetic and surface activity modeling was to be achieved, which was then applied for process development and evaluation. This main goal is then divided into three objectives:

1. Development of a microkinetic model

The first objective of this work was to enhance microkinetic modeling of the methanol synthesis on Cu/Zn-based catalysts (Chapter 2), using input from ab initio Density Functional Theory (DFT) calculations, and validating the model with experiments at different operating conditions. The simulations of the detailed model shall address the following questions:

- Which is the main reaction pathway of the methanol synthesis, and how is the contribution of alternative (secondary) pathways?
- Which steps of the reaction mechanism are rate-determining?
- Can mathematical descriptions of catalyst structural changes improve the kinetic modeling?

2. Development of a formal kinetic model derived from the microkinetic model

The second goal of this work was to use the developed microkinetic model and the insights gained from its simulations to derive a formal kinetic model (Chapter 3). Formal kinetic models are easier to implement and require less computational costs in their simulations, thereby being more adequate for practical applications, such as scale-up, reactor optimization, simulations with computational fluid dynamics (CFD), and simulations of the whole plant, including integration with other processes.

3. Process evaluation in industrial scale

The third objective of this work was to apply the developed formal kinetic model to evaluate the economic viability of the methanol synthesis from sustainable H₂ and CO₂ (Chapter 4). It is intended to address the following questions:

- How expensive is the methanol production from sustainable H₂ and CO₂?
- How does an addition of intermediate condensation steps improve this system? Has this changed process configuration an economical advantage compared to the conventional approach?
- How does the rWGS affect CO content in the plant? Which level of CO concentration will be reached inside the reactor?

In Fig. 1.4, the outline of the thesis is graphically illustrated.

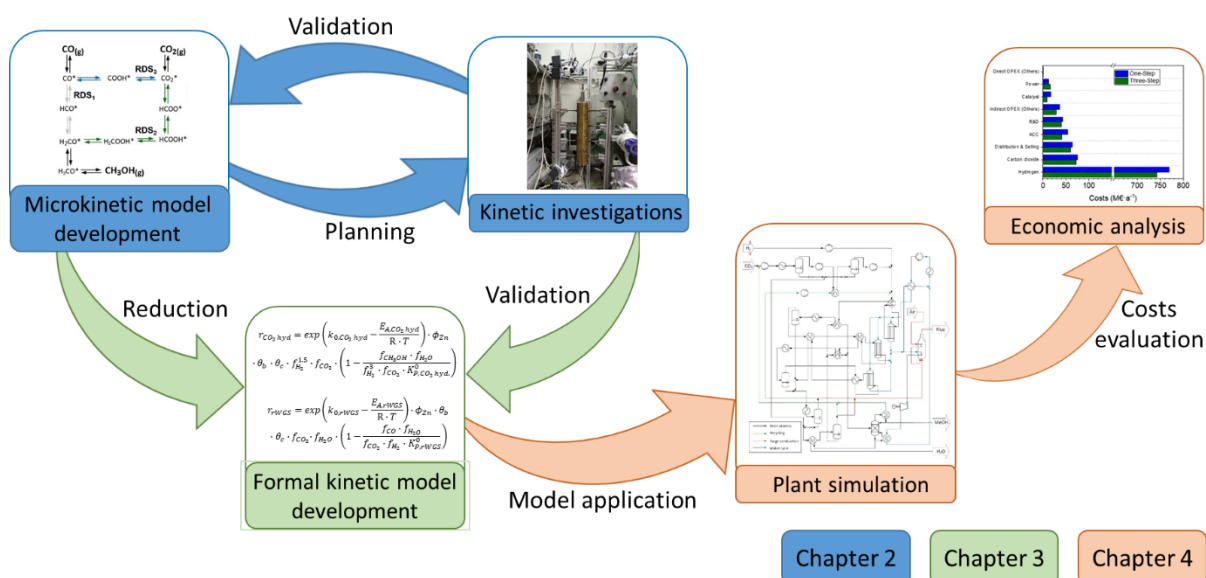


Fig. 1.4 Outline of the PhD thesis.

Chapter 2. Surface reaction kinetics of the methanol synthesis and the water gas shift reaction on Cu/ZnO/Al₂O₃

Declaration of contributions:

Bruno Lacerda de Oliveira Campos performed the experiments, processed and organized the data, developed and validated the microkinetic model, analyzed the results, and wrote the manuscript.

Karla Herrera Delgado conceptualized the work, gave support to the realization of the experiments and the development of the model, supervised the work, contributed to the discussion, and reviewed the manuscript.

Stefan Wild gave support to the realization of the experiments, contributed to the discussion, and reviewed the manuscript.

Felix Studt gave support to the development of the microkinetic model, contributed to the discussion, and reviewed the manuscript.

Stephan Pitter supervised the work, contributed to the discussion, and reviewed the manuscript.

Jörg Sauer supervised the work, contributed to the discussion, and reviewed the manuscript.

Chapter redrafted after:

Main publication:

Lacerda de Oliveira Campos, B.; Herrera Delgado, K.; Wild, S.; Studt, F.; Pitter, S.; Sauer, J. Surface reaction kinetics of the methanol synthesis and the water gas shift reaction on Cu/ZnO/Al₂O₃. *React. Chem. Eng.*, 2021, **6**, 868-887. DOI: 10.1039/d1re00040c

Corrigendum:

Lacerda de Oliveira Campos, B.; Herrera Delgado, K.; Wild, S.; Studt, F.; Pitter, S.; Sauer, J. Correction: Surface reaction kinetics of the methanol synthesis and the water gas shift reaction on Cu/ZnO/Al₂O₃. *React. Chem. Eng.*, 2021, **6**, 1483-1486. DOI: 10.1039/d1re90031e

Abstract Chapter 2

A three-site mean-field extended microkinetic model was developed based on ab initio DFT calculations from the literature, in order to simulate the conversion of syngas ($\text{H}_2/\text{CO}/\text{CO}_2$) to methanol on Cu (211) and Cu/Zn (211). The reaction network consists of 25 reversible reactions, including CO and CO_2 hydrogenation to methanol and the water-gas shift reaction. Catalyst structural changes were also considered in the model. Experiments were performed in a plug flow reactor on Cu/ZnO/ Al_2O_3 at various gas hourly space velocities (24–40 $\text{L}\cdot\text{h}^{-1}\cdot\text{g}_{\text{cat}}^{-1}$), temperatures (210–260 °C), pressures (40–60 bar), hydrogen feed concentrations (35–60% v/v), CO feed concentrations (3–30% v/v), and CO_2 feed concentrations (0–20% v/v). These experiments, together with experimental data from the literature, were used for a broad validation of the model (a total of 690 points), which adequately reproduced the measurements. A degree of rate control analysis showed that the hydrogenation of formic acid is the major rate controlling step, and formate is the most sensitive surface species. The developed model contributes to the understanding of the reaction kinetics, and should be applicable for industrial processes (e.g. scale-up and optimization).

2.1 Introduction

As mentioned in the first chapter, to the best of our knowledge, there is no published kinetic model containing all these key features in methanol synthesis on Cu/ZnO/Al₂O₃, which are:

- The global mechanism considers all three global reactions (Eq. 1.1–1.3).
- All surface reactions are potentially rate limiting (detailed microkinetic approach).
- The facet of Cu (211), a more open and active surface of the catalyst, is considered.
- Three-site approach: besides the Cu (211) active site (site a), the synergy of zinc is taken into account with the assumption of a Cu/Zn or Cu/Zn^{δ+} (211) active center (site b), and a separate site is considered for the adsorption of H₂ and H₂O (site c).
 - The structural changes of the catalyst, which are dependent on temperature and gas phase composition variations, are quantitatively taken into account.
 - An extensive experimental validation is made covering the most important parameters in methanol synthesis: pressure, temperature, gas hourly space velocity (GHSV), and feed composition (H₂, CO and CO₂).

In this work, a multiscale kinetic model for the methanol synthesis and the WGS is presented, in which all these aspects are considered. Experiments were performed in a plug flow reactor (PFR), and the database was expanded with literature experiments, allowing a model validation at a wide range of operating conditions.

2.2 Experimental setup

A total of 359 experiments were conducted in a single fixed-bed plug flow reactor (PFR). The operating conditions were varied in terms of temperature (210–260 °C), pressure (40–60 bar), gas hourly space velocity (GHSV) (24–40 L h⁻¹ g_{cat.}⁻¹), hydrogen feed concentration (35–60% v/v), CO feed concentration (3–30% v/v), and CO₂ feed concentration (0–20% v/v). Full experimental data is provided in the Supplementary Material (SM) (Section S1.1, Table S1.1).

The PFR set-up consisted of a stainless steel tube with 460 mm length, an inner diameter of 12 mm, and an inner concentric tube (2 mm) for temperature measurements in the axial direction. The feed gases were hydrogen (99.999% v/v), carbon monoxide (99.97% v/v), nitrogen (99.9999% v/v), and a mixture of carbon dioxide and nitrogen (50:50 ± 1.0% v/v) (Air Liquide Germany GmbH). The reactant gases supply was regulated via mass flow controllers (MFCs, Bronkhorst High Tech), by using proportional-integral-derivative (PID) control. The MFCs were calibrated with a flowmeter (Defender 530+, Mesalabs, standard error: 1.0% v/v). Both reactants (via bypass) and products were analyzed with a Fourier transform infrared

spectrometer (FTIR, Gaset CX4000). A flow diagram of the experimental setup is shown in the SM (Section S1.1, Fig. S1.1).

The reactor was filled with a commercial CuO/ZnO/Al₂O₃ catalyst provided by an industrial partner. The catalyst was crushed and sieved to a particle size range between 250 and 500 μm. As the methanol synthesis is exothermic, and in order to avoid hot spots and to ensure isothermal operation, five portions of 0.30 g catalyst (in total 1.50 g), were separately mixed, each with 8.18 g of silicon carbide (SiC, Hausen Mineraliengroßhandel GmbH) (in total 40.90 g). Each mixture was then consecutively filled into the reactor, forming a catalytic bed length of 200 mm. Pure SiC completed the upper and lower ends of the bed.

The catalyst was activated as follows: a volume flow of 300 mL_S·min⁻¹ containing 5% v/v of H₂ in N₂ was applied to the reactor, and the system was heated from 100 to 200 °C at a heating rate of 20 °C·h⁻¹. This temperature was hold for one hour, followed by further heating to 240 °C at a heating rate of 12 °C h⁻¹. Finally, the H₂ concentration in the flow was increased to 50% v/v, maintaining the same total flow rate for one more hour.

In order to obtain a stable catalyst in steady-state conditions, the reactor was operated for 320 h at 40 bar, different temperatures (210–260 °C), and different feed gas compositions, before starting the measurements reported here.

The temperature axial profile was measured using a type-K thermocouple (NiCr–Ni) for the two data points with the highest methanol productivity, and thus the highest energy release due to the exothermic reactions. Since the maximum temperature difference was lower than 2 °C, the assumption of isothermal conditions is reasonable. The temperature profiles are presented in the SM (Section S1.1, Fig. S1.2).

2.3 Kinetic model development and numerical simulation

2.3.1 Three-site surface reaction mechanism

The developed kinetic model is based on the DFT calculations of Studt et al.^{18, 54} for CO and CO₂ hydrogenation to methanol, and the WGSR. The adsorption energies of CO₂* and H₂O* were taken from Polierer et al.⁶²

Studt et al.^{18, 54} applied the calculations on two stepped model surfaces: Cu (211), denoted in the presented mechanism as “site (a)”, and a fully Zn-covered Cu (211), denoted “site (b)”. The (211) facets were chosen, as it was found through experiments and theoretical calculations that they are the most active surfaces for the methanol synthesis.^{17, 18, 47, 51, 54} Since surface defects scale linearly with the overall observed activity, the reactivity of other facets (e.g. 111) can be neglected.¹⁷ Besides, from a modeling point of view, the consideration of a most representative (i.e. most active) single facet is desirable, because to consider an additional facet would double the amount of reactions and surface species, which increases model complexity and requires higher computational costs.

In this work, all reaction paths studied by Studt et al.^{18, 54} were originally implemented and tested for different operating conditions. The initial tests confirmed remarks proposed by

Studt et al.,¹⁸ that CO hydrogenation on Cu/Zn (211) and CO₂ hydrogenation on Cu (211) are negligible. Therefore, CO hydrogenation on Cu/Zn (211) was eliminated from the final microkinetic model. The CO₂ hydrogenation on Cu (211), however, was kept in the model, as it describes the accumulation of formate on the Cu (211) surface, which reduces the number of free sites and could therefore slow down other reactions, e.g. CO hydrogenation.

Studt et al.⁵⁴ made DFT calculations for four WGS reaction pathways on both Cu (211) and Cu/Zn (211) surfaces: the redox mechanism, the water-assisted redox mechanism, the carboxyl mechanism, and the water assisted carboxyl mechanism (totalizing eight possible reaction routes). After implementing and testing all these eight possible reaction pathways for different conditions, it was confirmed that the water-assisted carboxyl mechanism is dominant, and it is active on both Cu (211) and Cu/Zn (211). Thus, only this WGS reaction pathway (on both surfaces) is taken into account in the final kinetic model. After all, non-relevant reaction paths will only add complexity and increase the computational costs of the simulations without contributing to the accuracy of the results.

It is known that formate (HCOO*) is able to cover a significant part of the catalyst surface, being an intermediate for CO₂ hydrogenation and inhibiting other reactions, such as CO hydrogenation.¹⁸ It is, however, unlikely that formate inhibits hydrogen adsorption, because there should be still enough small sites available between adsorbed formate. A comparable situation is seen in the ammonia synthesis, in which it was shown that the interaction (or inhibition) of nitrogen with hydrogen is not significant.^{63, 64} Another important feature is that, in the CO₂ hydrogenation, the decomposition of H₂COOH* into H₂CO* and OH* would need an additional free site, and could therefore be inhibited by high formate concentrations. However, this does not seem to be realistic, as H₂COOH* is a large molecule that should not need extra space for its decomposition.¹⁸ Therefore, a third site, either Cu (211) or Cu/Zn (211), is considered in our model, denoted as “site (c)”, which is available for hydrogen and water adsorption. Similar approaches were published by other groups.^{18, 34, 41}

The final kinetic model takes into account 23 surface species, of which ten are related to Cu (211) [CO_(a), HCO_(a), HCOO_(a), HCOOH_(a), H₂COOH_(a), H₂CO_(a), H₃CO_(a), COOH_(a), CO_{2(a)}, free site (a)], nine are related to Cu/Zn (211) [CO_(b), HCOO_(b), HCOOH_(b), H₂COOH_(b), H₂CO_(b), H₃CO_(b), COOH_(b), CO_{2(b)}, free site (b)] and four are related to site (c) [H_(c), OH_(c), H₂O_(c), free site (c)].

The reaction network of the carbon-containing species is shown in Fig. 2.1. It consists of five reaction pathways: CO hydrogenation on Cu (211), CO₂ hydrogenation on Cu (211), WGSR (water-assisted carboxyl mechanism) on Cu (211), CO₂ hydrogenation on Cu/Zn (211), and WGSR (water-assisted carboxyl mechanism) on Cu/Zn (211).

2.3.2 Kinetic equations

The catalyst surface is modeled considering a random distribution of the adsorbed species (mean-field approximation). A surface reaction is expressed as:

$$\sum_{i=1}^{N_g+N_s} (v'_{ik} \cdot \chi_i) \rightarrow \sum_{i=1}^{N_g+N_s} (v''_{ik} \cdot \chi_i) \quad (2.1)$$

$$\text{With } v_{ik} = v''_{ik} - v'_{ik} \quad (2.2)$$

Here, N_g and N_s are the number of gaseous and surface species, respectively, χ_i is the respective species i , v'_{ik} and v''_{ik} are the stoichiometric coefficients of the reactants and the products (species i in reaction k), respectively, and v_{ik} is the stoichiometric gain of species i in reaction k .

As the methanol synthesis is typically operated at elevated pressures (50–100 bar),⁶⁵ the ideal gas consideration may give partial pressures that differ significantly from the actual fugacities of the gases. Slotboom et al.⁴¹ reported deviations up to 10% comparing ideal and real gas approaches. Therefore, the Peng–Robinson equation of state⁶⁶ is used in our model to calculate the fugacities, using binary interaction parameters (k_{ij}) and other necessary data reported in literature,^{67, 68} and including an effective hydrogen acentric factor ($\omega = -0.05$).⁶⁹

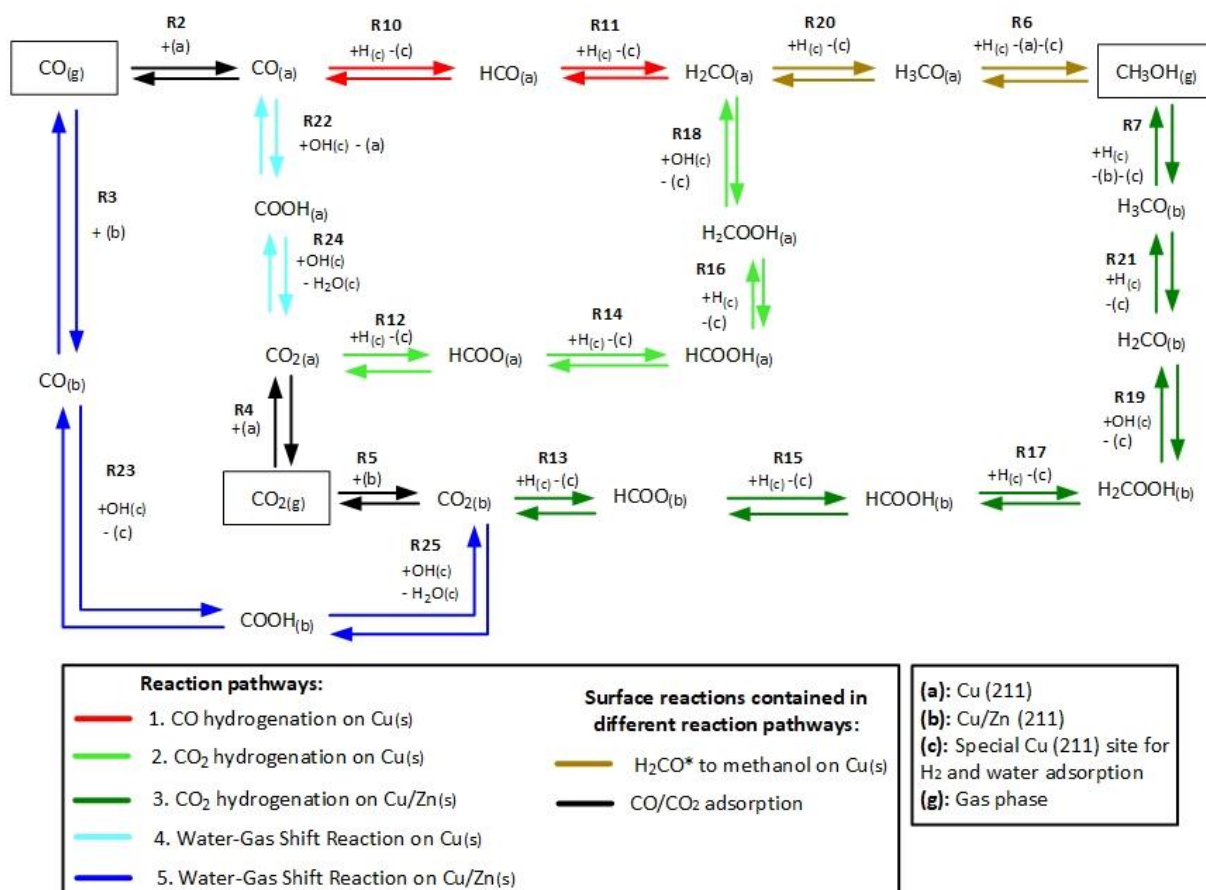


Fig. 2.1 Reaction network of the carbon-containing species in the methanol synthesis and the WGSR. Reproduced with permission from Campos et al.⁷⁰. Copyright 2021, Royal Society of Chemistry.

In the present kinetic model, all surface species are considered to occupy a single site ($\sigma_i = 1$ for all species). The surface coverage of a species i (θ_i) on a specific active site represents the fraction of this site that is occupied by that species. The calculation of the surface coverages is shown in Eq. (2.3), and the sum of all coverages from a specific site must be 1 (Eq. 2.4).

$$\theta_i = \frac{c_i \cdot \sigma_i}{\Gamma} \quad (2.3)$$

$$\sum \theta_{i(a)} = \sum \theta_{i(b)} = \sum \theta_{i(c)} = 1 \quad (2.4)$$

Where c_i is the concentration of surface species i , σ_i is the number of surface sites occupied by species i , and Γ is the surface site density. The turnover rate r (Eq. 8) consists in three multiplying functions: one dependent on temperature (F_T),^{71, 72} one dependent on the gaseous species fugacities (F_G), and one dependent on the surface species coverages (F_S).

$$r = F_T \cdot F_G \cdot F_S \quad (2.5)$$

$$F_T = T^{(1+\beta)} \cdot \frac{k_b}{h} \cdot \exp\left(-\frac{E_A}{R \cdot T} + \frac{\Delta S^\ddagger}{R}\right) \quad (2.6)$$

$$F_G = \prod_{j=1}^{N_g} \left[\left(\frac{f_j}{p_0} \right)^{v'_{j,k}} \right] \quad (2.7)$$

$$F_S = \prod_{i=N_g+1}^{N_g+N_s} [(\phi_i \cdot \theta_i)^{v''_{i,k}}] \quad (2.8)$$

Here, T is the reaction temperature, β is a correction due to the thermodynamic consistency (see section 2.3.3), k_b is the Boltzmann constant, h is the Planck constant, E_A is the reaction activation energy, ΔS^\ddagger is the reaction entropy barrier, f_j is the fugacity of the gas component j , p_0 is the reference pressure (1 bar), R is the universal gas constant, and θ_i is the surface coverage of species i . ϕ_i represents the fraction of the site type of surface species i in relation to the total number of sites for carbon-containing compounds (sites a and b). Substituting Eq. (2.6-2.8) into Eq. (2.5), the turnover rate of a reversible reaction k is:

$$\begin{aligned} r_k = & T^{(1+\beta_k^+)} \cdot \frac{k_b}{h} \cdot \exp\left(-\frac{E_{A,k}^+}{R \cdot T} + \frac{\Delta S_k^{\ddagger,+}}{R}\right) \cdot \prod_{j=1}^{N_g} \left[\left(\frac{f_j}{p_0} \right)^{v'_{j,k}} \right] \cdot \prod_{i=N_g+1}^{N_g+N_s} [(\phi_i \cdot \theta_i)^{v''_{i,k}}] \\ & - T^{(1+\beta_k^-)} \cdot \frac{k_b}{h} \cdot \exp\left(-\frac{E_{A,k}^-}{R \cdot T} + \frac{\Delta S_k^{\ddagger,-}}{R}\right) \cdot \prod_{j=1}^{N_g} \left[\left(\frac{f_j}{p_0} \right)^{v'''_{j,k}} \right] \cdot \prod_{i=N_g+1}^{N_g+N_s} [(\phi_i \cdot \theta_i)^{v''''_{i,k}}] \end{aligned} \quad (2.9)$$

Where the superscripts + and – refer to the forward and the reverse reaction, respectively. The reaction rate is related to the turnover rate by:

$$\dot{s}_k = r_k \cdot \Gamma \quad (2.10)$$

The dependency of (ϕ_i) to the site type is shown in Table 2.1. The estimation of the zinc coverage (ϕ_{Zn}) is discussed in section 2.3.4.

Table 2.1 Values of ϕ_i depending on the site type. Reproduced with permission from Campos et al.⁷⁰. Copyright 2021, Royal Society of Chemistry.

Site type	ϕ_i
Site (a)	$(1 - \phi_{Zn})$
Site (b)	ϕ_{Zn}
Site (c)	1

2.3.3 Thermodynamic consistency

The microkinetic model has to correctly predict the thermodynamic equilibrium. The objective of the thermodynamic consistency corrections is to ensure reversibility of each elementary step according to the properties of the gas-phase species involved, which are known. The method described here is an adapted version of an approach developed in the Deutschmann's group,^{73, 74} considering a temperature operating range between $T_1 = 200$ °C and $T_2 = 300$ °C.

Goos et al.⁷⁵ reported thermodynamic data of gas species involved in the methanol synthesis. The free Gibbs energy function G_j^0 of each gas species j at the reference pressure of 1 bar is:

$$G_j^0(T) = R \cdot \left[a_{6,j} + (a_{1,j} - a_{7,j}) \cdot T - \frac{a_{2,j}}{2} \cdot T^2 - \frac{a_{3,j}}{6} \cdot T^3 - \frac{a_{4,j}}{12} \cdot T^4 - \frac{a_{5,j}}{20} \cdot T^5 - a_{1,j} \cdot T \cdot \ln(T) \right] \quad (2.11)$$

Here, $a_{1-7,j}$ are compound-specific constants.⁷⁵ The free Gibbs energy variation of the three global reactions (Eq. 2.12-2.14) is:

$$\Delta G_{CO_{Hyd.}}^0(T) = G_{CH_3OH}^0(T) - G_{CO}^0(T) - 2 \cdot G_{H_2}^0(T) \quad (2.12)$$

$$\Delta G_{CO_2_{Hyd.}}^0(T) = G_{CH_3OH}^0(T) + G_{H_2O}^0(T) - G_{CO_2}^0(T) - 3 \cdot G_{H_2}^0(T) \quad (2.13)$$

$$\Delta G_{WGSR}^0(T) = G_{CO_2}^0(T) + G_{H_2}^0(T) - G_{CO}^0(T) - G_{H_2O}^0(T) \quad (2.14)$$

The assumption of constant heat capacity (c_p) was made for the global reactions in the temperature range of 200 to 300 °C. With this consideration, the Gibbs function was reduced from seven to three parameters (A_{1-3}) (Eq. 2.15-2.16) with the least square regression method (Eq. 2.17).

$$\Delta G_{m,3p}^0(T) = (\Delta H_{Tr,m}^0 - \Delta c_{p,m} \cdot T_r) + (\Delta c_{p,m} + \Delta c_{p,m} \cdot \ln T_r - \Delta S_{Tr,m}^0) \cdot T + (-\Delta c_{p,m}) \cdot T \cdot \ln T \quad (2.15)$$

$$\Delta G_{m,3p}^0(T) = A_{1,m} + A_{2,m} \cdot T + A_{3,m} \cdot T \cdot \ln T \quad (2.16)$$

$$\min \left[\int_{T_1}^{T_2} (\Delta G_{m,7p}^0(T) - \Delta G_{m,3p}^0(T))^2 dT \right] \quad (2.17)$$

Where $\Delta G_{m,3p}^0$ is the Gibbs energy change of the global reaction m considering three parameters, $\Delta H_{Tr,m}^0$ and $\Delta S_{Tr,m}^0$ are the enthalpy and entropy change of the global reaction m at the standard temperature ($T_r = 298.15$ K), $\Delta c_{p,m}$ is the heat capacity change of the global reaction m , and $A_{1-3,m}$ are the regression parameters 1–3 of the global reaction m .

The estimated regression parameters are summarized in the SM (Section S1.2, Table S1.2). When comparing the three-parameter functions with the seven-parameter ones, the average relative error of $\Delta G_{m,3p}^0$ was below 0.002%, and the maximum relative error was 0.007%. Therefore, a constant heat capacity sufficiently describes the free Gibbs energy change of the reactions involved in the methanol synthesis between 200 and 300 °C.

From DFT calculations, the free Gibbs energy change ($\Delta G_{k,DFT}^0$) of a reversible surface reaction k is given in the form:

$$\Delta G_{k,DFT}^0(T) = (E_{A,k}^+ - E_{A,k}^-) - T \cdot (\Delta S_k^{\neq,+} - \Delta S_k^{\neq,-}) \quad (2.18)$$

The free Gibbs energy change ($\Delta G_{k,DFT}^0$) of a global reaction pathway m (described in Fig. 2.1) is then calculated:

$$\Delta G_{m,DFT}^0(T) = \sum_{k=1}^{N_r} \zeta_{k,m} \cdot \Delta G_k^0(T) \quad (2.19)$$

Here, N_r is the number of reactions, $\zeta_{k,m}$ is the stoichiometric coefficient of a reversible surface reaction k in the global reaction pathway m .

In Eq. (2.18) and Eq. (2.19) there is no term multiplying $T \cdot \ln(T)$ for $\Delta G_{m,DFT}^0$, like there is in Eq. (2.18) and (2.19) for $\Delta G_{m,3p}^0$. Each $\Delta G_{m,DFT}^0$ needs to be modified with the addition of parameter β multiplying $T \cdot \ln(T)$, so that the equations are able to match. The calculation of β can also be seen in other thermodynamic consistency processes of surface kinetic mechanisms reported in literature.^{73, 74} The new free Gibbs energy change ($\Delta G_{m,DFT}^{0,TC}$) is calculated with the corrected terms ($E_{A,k}^{+,TC}$, $E_{A,k}^{-,TC}$, $\Delta S_k^{\neq,+,TC}$, $\Delta S_k^{\neq,-,TC}$, $\beta_k^{+,TC}$, $\beta_k^{-,TC}$), as shown in Eq. (2.20), and these terms are estimated so that Eq. (2.21) holds for all reaction pathways:

$$\Delta G_{m,DFT}^{0,TC}(T) = \sum_{k=1}^{N_r} \zeta_{k,m} \cdot [(E_{A,k}^{+,TC} - E_{A,k}^{-,TC}) - T \cdot (\Delta S_k^{\neq,+,TC} - \Delta S_k^{\neq,-,TC}) - T \cdot \ln(T) \cdot (\beta_k^{+,TC} - \beta_k^{-,TC})] \quad (2.20)$$

$$\Delta G_{m,DFT}^{0,TC}(T) = \Delta G_{m,3p}^0(T) \quad (2.21)$$

In Eq. (2.21), the two functions will only be equal for a range of different temperatures (200–300 °C) if their corresponding terms match, namely the independent terms (Eq. 2.22), the terms accompanying T (Eq. 2.23), and terms accompanying $T \cdot \ln(T)$ (Eq. 2.24).

$$q_{1,m} = A_{1,m} - \sum_{k=1}^{Nr} \zeta_{k,m} \cdot (E_{A,k}^{+,TC} - E_{A,k}^{-,TC}) = 0 \quad (2.22)$$

$$q_{2,m} = A_{2,m} - \sum_{k=1}^{Nr} \zeta_{k,m} \cdot (\Delta S_k^{\neq,+ ,TC} - \Delta S_k^{\neq,- ,TC}) = 0 \quad (2.23)$$

$$q_{3,m} = A_{3,m} - \sum_{k=1}^{Nr} \zeta_{k,m} \cdot (\beta_k^{+,TC} - \beta_k^{-,TC}) = 0 \quad (2.24)$$

Where $q_{1-3,m}$ represent the thermodynamic constraints. As in most microkinetic models, this is an underdetermined algebraic system, because there are 150 variables (6 parameters \times 25 reactions) and only 15 equations (Eq. 2.22–2.24) for the five reaction pathways. Herrera Delgado et al.⁷³ proposed an objective function that minimizes the individual corrections of E_A , the pre-exponential factor (a term which contains ΔS_k^{\neq}), and β . In this work, however, it was preferred to minimize the difference between the corrected Gibbs energy barrier ($\Delta G^{\neq,TC} = E_A^{TC} - T \cdot \Delta S^{\neq,TC} - T \cdot \ln T \cdot \beta^{TC}$) and the original DFT-based one ($G^{\neq,Orig} = E_A^{Orig} - T \cdot \Delta S^{\neq,Orig}$), for both forward and reverse reactions. This approach was chosen, because the model is more sensitive to modifications in the ΔG^{\neq} than in its individual parameters. Besides, the model is also sensitive to ΔG changes of all surface reactions ($\Delta G = \Delta G^{\neq,+} - \Delta G^{\neq,-}$), even of fast steps usually in equilibrium, as changing the ΔG will alter this equilibrium, affecting the whole mechanism. The constrained objective function is shown in Eq. (2.25).

$$f_{obj} = \min \int_{T_1}^{T_2} \left\{ \sum_{k=1}^{Nr} w_k \cdot \left\{ [E_{A,k}^{+,TC} - T \cdot (\Delta S_k^{\neq,+ ,TC} + \ln(T) \cdot \beta_k^{+,TC}) - (E_{A,k}^{+,Orig} - T \cdot \Delta S_k^{\neq,+ ,Orig})]^2 + [E_{A,k}^{-,TC} - T \cdot (\Delta S_k^{\neq,- ,TC} + \ln(T) \cdot \beta_k^{-,TC}) - (E_{A,k}^{-,Orig} - T \cdot \Delta S_k^{\neq,- ,Orig})]^2 \right\} \right\} dT \quad (2.25)$$

$$\text{Subject to: } q_{1,m} = q_{2,m} = q_{3,m} = 0 \quad m = 1:5$$

Here, w_k are selectable weights, which are chosen to protect the most sensitive reactions against changes. In this work, the weights of reactions R1, R2, R14, R16, and R17 were set to 10^5 and the other weights were set to one. This minimization problem can be solved with the method of the Lagrange multipliers (further explanation is given in the SM, Section S1.2).

In Fig. 2.2, the capability of the model to predict the equilibrium is presented. The methanol concentration of the equilibrium for different operating conditions is calculated with Aspen Plus, using the RGibbs approach. Simulations with the same operating conditions are made with the microkinetic model considering a sufficiently long PFR, in order to achieve the equilibrium. When comparing the values, the conclusion is that the equilibrium is accurately predicted by the model, and the slight overestimations are probably due to rounding numbers and small differences in the thermodynamic data.

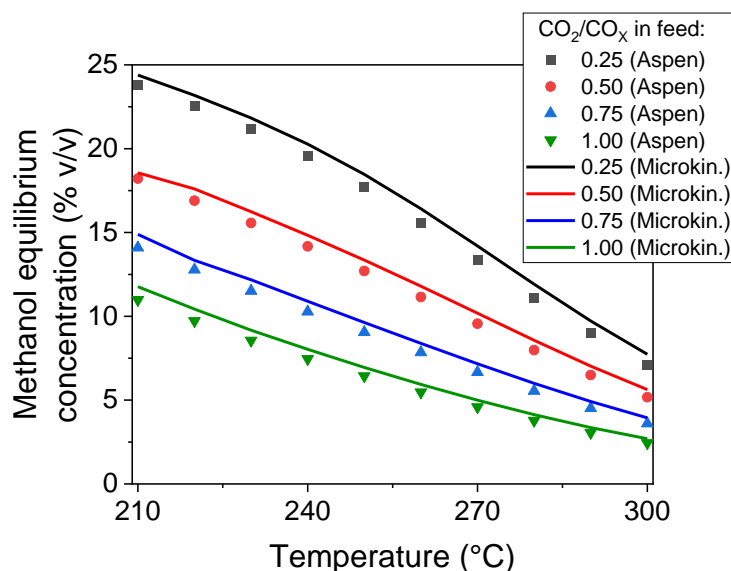


Fig. 2.2 Methanol equilibrium concentration calculated with Aspen Plus and with the microkinetic model. Operating conditions: 60 bar, and a feed concentration of $\text{H}_2/\text{CO}_x = 80/20\%$ v/v. Reproduced with permission from Campos et al.⁷⁰. Copyright 2021, Royal Society of Chemistry.

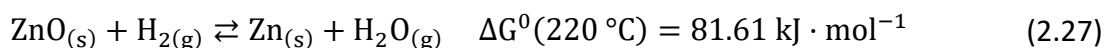
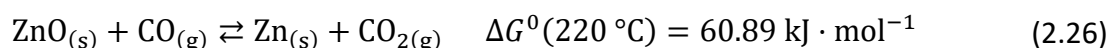
2.3.4 Estimation of the active site distribution

A significant number of experimental observations have shown that the different active sites of the Cu/ZnO-based catalysts are adjusted dynamically to the operating conditions.^{43, 76} It is therefore relevant to correctly model this phenomenon, in order to estimate the fraction of Cu (site a) and Cu/Zn (site b) on the surface for different operating conditions.

In this work, two different methods to estimate the active site distribution are applied: the theoretical approach from Kuld et al.⁴⁵, and a simplified approach, which are explained as follows.

2.3.4.1 Theoretical approach – Kuld et al.

The formation of a Cu–Zn alloy by reduction of zinc oxide and migration to the copper bulk can be described by the following reactions:^{45, 77}



Kuld et al.⁴⁵ proposed a detailed method to estimate the zinc fraction on the surface of the catalyst. First, the solubility of zinc in the Cu-bulk (X_{Zn}) is calculated considering the equilibrium of the zinc reduction via carbon monoxide (Eq. 2.26). The effect of the lower atom coordination in nanoparticles was considered for both zinc oxide and copper.

$$\ln(X_{Zn}) = -\frac{\Delta G_{Zn\ red.}^0(T)}{R \cdot T} - \ln(\gamma_{Zn}) + \ln\left(\frac{a_{CO}}{a_{CO_2}}\right) + 4 \cdot \frac{\bar{\gamma}_{ZnO} \cdot M_{ZnO}}{d_{ZnO} \cdot \rho_{ZnO} \cdot R \cdot T} - 4 \cdot \frac{\bar{\gamma}_{Cu} \cdot M_{Cu}}{d_{Cu} \cdot \rho_{Cu} \cdot R \cdot T} + \ln(a_{ZnO}) \quad (2.28)$$

Where $\Delta G_{Zn\ red.}^0(T)$ is the free Gibbs energy change in the zinc reduction via CO at the reference pressure (1 bar) and the reaction temperature T , γ_{Zn} is the activity coefficient of zinc in Cu, a_{CO_2} and a_{CO} are the activities of CO₂ and CO respectively, $\bar{\gamma}_{ZnO}$ and $\bar{\gamma}_{Cu}$ represent the respective surface energy of zinc oxide and copper, M_{ZnO} and M_{Cu} are the molar masses of zinc oxide and copper, d_{ZnO} and d_{Cu} are the crystallite diameter of zinc oxide and copper, ρ_{ZnO} and ρ_{Cu} are the density of zinc oxide and copper, and a_{ZnO} is the activity of zinc oxide. The values of activity coefficient, surface energies and crystallite diameters were reported by Kuld et al.⁴⁵

The activity of the zinc oxide is assumed to be 1. Although not specifically noted by the authors, this assumption has probably been made considering that the typical quantity of metallic zinc in the copper bulk is not significant compared to the zinc oxide bulk.

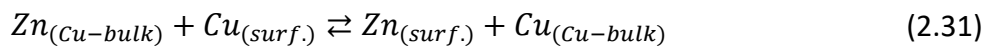
In typical industrial methanol production, the WGS is generally in equilibrium. Therefore, as the free Gibbs energy change of the reduction of zinc via hydrogen (Eq. 2.30) is significantly higher than via carbon monoxide (Eq. 2.26), the most probable way that hydrogen and water affect the reduction of zinc is by changing the a_{CO}/a_{CO_2} ratio through the WGS. Kuld et al.⁴⁵ proposed an effective a_{CO}/a_{CO_2} ratio to be used in Eq. (2.28) to account for the H₂/H₂O effect.

$$\left(\frac{a_{CO}}{a_{CO_2}}\right)_{eff} = \frac{a_{CO} \cdot a_{H_2}}{a_{CO_2} \cdot a_{H_2O}} \cdot \frac{1}{K_{WGS}(T)} \quad (2.29)$$

Here, K_{WGS} is the equilibrium constant of the WGS. The activities of the gases can be represented by their fugacities. That is:

$$\left(\frac{a_{CO}}{a_{CO_2}}\right)_{eff} = \left(\frac{f_{CO}}{f_{CO_2}}\right)_{eff} = \frac{f_{CO} \cdot f_{H_2}}{f_{CO_2} \cdot f_{H_2O}} \cdot \frac{1}{K_{WGS}(T)} \quad (2.30)$$

The segregation of metallic zinc from the Cu-bulk into the catalyst surface is then considered.



Kuld et al.⁴⁵ performed DFT calculations of this segregation on different facets, taking into account Zn–Zn interactions. For the facet Cu (211), the authors reported enthalpy variations (ΔH_{seg}^0) of -27.01 kJ mol⁻¹ for a Zn-free surface, -18.36 kJ mol⁻¹ for a 0.333 Zn monolayer (ML), and -8.71 kJ·mol⁻¹ for a 0.667 Zn monolayer (ML). The ΔH_{seg}^0 is then calculated (in kJ·mol⁻¹) as a function of the zinc coverage on the surface (ϕ_{Zn}):

$$\Delta H_{seg}^0 = -27.01 \cdot (1 - \phi_{Zn}) \quad (2.32)$$

The entropy change (ΔS_{seg}^0) of the segregation process on a Cu (211) facet was estimated to be $7.1 \text{ J} \cdot \text{mol}^{-1} \cdot \text{K}^{-1}$, and effects of Zn–Zn interactions in the entropy were neglected.⁴⁵ The zinc coverage on the surface (ϕ_{Zn}) is calculated by solving Eq. (2.33), in which it is considered that the segregation of zinc to the surface is in equilibrium.

$$K_{seg} = \frac{\phi_{Zn} \cdot (1 - X_{Zn})}{X_{Zn} \cdot (1 - \phi_{Zn})} = \exp \left[\frac{-(\Delta H_{seg}^0 - T \cdot \Delta S_{seg}^0)}{R \cdot T} \right] \quad (2.33)$$

In Fig. 2.3, estimated values of zinc solubility in copper (X_{Zn}) and the zinc coverage (ϕ_{Zn}) are illustrated as a function of the Gas Reducing Power (GRP) and temperature.

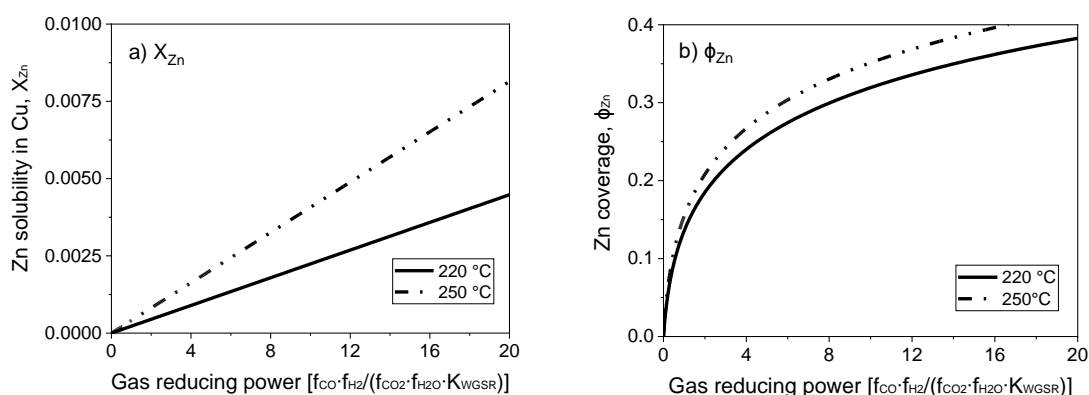


Fig. 2.3 Solubility of zinc in the Cu-bulk (a) and zinc coverage (b) as functions of the gas reducing power. Reproduced with permission from Campos et al.⁷⁰. Copyright 2021, Royal Society of Chemistry.

For the simulation of experiments without CO_2 in feed, the zinc coverage is maximized, as GRP tends to infinite. In this extreme case, it was considered a constant value of $\phi_{Zn} = 0.90$. For the experiments from Seidel et al.³⁴ with H_2/CO in feed, our model was initially overestimating methanol formation. As the catalyst used is not exactly the same, we believe that in the experiments of Seidel et al.³⁴ zinc could be covering more surface, leaving less Cu sites for the CO hydrogenation. Therefore, in the simulation of Seidel's experiments, it is assumed that $\phi_{Zn} = 0.95$.

2.3.4.2 Simplified approach

As already mentioned, the zinc coverage on the catalyst is reduced by an increase in the CO_2/CO_x ratio ($\bar{y}_{\text{CO}_2,0}$). In this simplified approach, a constant value for the zinc coverage is assumed according to the $\bar{y}_{\text{CO}_2,0}$ in feed, divided in three parts: the 1st with very low CO_2 content ($\bar{y}_{\text{CO}_2,0} < 0.001$), the 2nd with very high CO_2 content ($\bar{y}_{\text{CO}_2,0} > 0.90$), and the 3rd being an intermediate region ($0.001 \leq \bar{y}_{\text{CO}_2,0} \leq 0.90$). In Table 2.2, each condition and the corresponding zinc value is summarized.

Table 2.2 Zinc coverage value depending on the CO₂ to CO_x ratio in feed. Reproduced with permission from Campos et al.⁷⁸. Copyright 2021, Royal Society of Chemistry.

Condition	Zn Value
CO ₂ /CO _x ratio < 0.001	0.90 (for Campos' data) 0.95 (for Seidel's data)
0.001 ≤ CO ₂ /CO _x ratio ≤ 0.90	0.50
CO ₂ /CO _x ratio > 0.90	0.10

2.3.5 Estimation of the active catalytic area

Because of the dynamic behavior of the Cu/ZnO/Al₂O₃ and the three-site approach, characterization tests (e.g. N₂O chemisorption) can just estimate an initial active catalytic area, since it changes depending on the experimental conditions. Still, these estimations serve as a reference in comparing different catalysts. The determination of the surface site density is a challenge for the same reason. Therefore, it was chosen to use experimental data to fit the specific catalyst site quantity ($n_{M,Cat}$) in terms of mol of active sites per catalyst mass unit Eq. (2.38). The total active surface area (A_{Cat}) is then calculated by Eq. (2.39).

$$n_{M,Cat} = \frac{\text{Number of active sites (mol)}}{\text{Catalyst mass (kg)}} \quad (2.34)$$

$$A_{Cat} = \frac{n_{M,Cat} \cdot m_{Cat}}{\Gamma} \quad (2.35)$$

Here, m_{Cat} is the mass of the catalyst inside the reactor. By estimating the $n_{M,Cat}$, the need to quantify the surface site density (Γ) is avoided, as shown in the next section.

The $n_{M,Cat}$ is estimated by minimizing the prediction errors of the methanol output with the experimental data. When the experimental data has values that differ significantly (e.g. 0.08% v/v and 12.00% v/v), a better distribution of each point's importance can be made with introducing weights. Common approaches are the inverse of squared experimental value,^{79, 80} the inverse of the squared simulated value,⁸¹ or the inverse of experimental multiplied by simulated value.⁸² Here, the inverse of the squared experimental value was used as weights. The function `fminsearch` from Matlab was used, and the objective function is shown as follows.

$$f_{obj} = \sum_{n=1}^{N_p} \left(\frac{y_{CH_3OH,out}^n - \hat{y}_{CH_3OH,out}^n}{y_{CH_3OH,out}^n} \right)^2 \quad (2.36)$$

Here, $y_{CH_3OH,out}^n$ and $\hat{y}_{CH_3OH,out}^n$ are the experimental and simulated value of point n , respectively.

2.3.6 Reactor equations

In this work, the microkinetic model is applied to simulate steady-state operation of two types of reactor: a fixed-bed tube reactor (own experiments and literature data)^{33, 41} and a CSTR (literature data)³⁴. Isothermal operation was considered in both cases.

2.3.6.1 Fixed-bed tube reactor

In the tube reactor model, only variations along the reactor length are assumed, given the ratio between the diameter of the reactor and the particle size ($24 \leq d_R/d_p \leq 48$). The influence of back-mixing is neglected (plug flow reactor assumption, PFR). A total molar balance along the catalyst bed length (L) is calculated:

$$\frac{d\dot{n}}{dz} = \frac{A_{cat}}{L} \cdot \sum_{j=1}^{N_g} \sum_{k=1}^{N_r} (v_{jk} \cdot \dot{s}_k) \quad (2.37)$$

Where \dot{n} is the total gas mole flow, z is the axial direction, N_r is the number of reactions. Substituting Eq. (2.10) and Eq. (2.35) in Eq. (2.37):

$$\frac{d\dot{n}}{dz} = \frac{n_{M,Cat} \cdot m_{cat}}{\Gamma \cdot L} \cdot \sum_{j=1}^{N_g} \sum_{k=1}^{N_r} (v_{jk} \cdot r_k \cdot \Gamma) \quad (2.38)$$

$$\frac{d\dot{n}}{dz} = \frac{n_{M,Cat} \cdot m_{cat}}{L} \cdot \sum_{j=1}^{N_g} \sum_{k=1}^{N_r} (v_{jk} \cdot r_k \cdot \Gamma) \quad (2.39)$$

The axial reactor profile of the molar fraction of each gaseous species j (y_j) is calculated via a component balance of the gas phase.

$$\frac{dy_j}{dz} = \frac{1}{\dot{n}} \cdot \left\{ \frac{n_{M,Cat} \cdot m_{cat}}{L} \cdot \sum_{k=1}^{N_r} (v_{jk} \cdot r_k) - y_j \cdot \frac{d\dot{n}}{dz} \right\} \quad (2.40)$$

The coverage θ_i of each surface species i at a certain point in time is calculated via a component balance of the surface.

$$\frac{d\theta_i}{dt} = \sum_{k=1}^{N_r} (v_{jk} \cdot r_k) \quad (2.41)$$

Comments on solving this system of differential equations are given in the SM (Section S1.3 and S1.4).

2.3.6.2 Continuous stirred tank reactor

In the CSTR model, a total molar balance in the reactor is calculated:

$$\frac{dn}{dt} = \dot{n}_{in} - \dot{n}_{out} + n_{M,Cat} \cdot m_{Cat} \cdot \sum_{j=1}^{N_g} \sum_{k=1}^{N_r} (v_{jk} \cdot r_k) \quad (2.42)$$

Where dn/dt is the total mole accumulation in time, \dot{n}_{in} is the mole flow entering the reactor, and \dot{n}_{out} is the mole flow leaving the reactor. Assuming no gas accumulation in the reactor:

$$\dot{n}_{out} = \dot{n}_{in} + n_{M,Cat} \cdot m_{Cat} \cdot \sum_{j=1}^{N_g} \sum_{k=1}^{N_r} (v_{jk} \cdot r_k) \quad (2.43)$$

The component mole balance in the reactor is calculated:

$$\frac{dy_j}{dt} = \frac{1}{n} \cdot \left\{ \dot{n}_{in} \cdot y_{j,in} - \dot{n}_{out} \cdot y_j + n_{M,Cat} \cdot m_{Cat} \cdot \sum_{j=1}^{N_g} \sum_{k=1}^{N_r} (v_{jk} \cdot r_k) \right\} \quad (2.44)$$

Where dy_j/dt is the change in time of the mole fraction of component j , n is the total mole quantity in the gas phase, $y_{j,in}$ is the mole fraction of component j entering the reactor, and y_j is the mole fraction of component j in the reactor. The mole quantity in the gas phase can be calculated with the Peng–Robinson equation of state.⁶⁶ Like in the PFR, the coverages of the surface species are calculated by:

$$\frac{d\theta_i}{dt} = \sum_{k=1}^{N_r} (v_{jk} \cdot r_k) \quad (2.45)$$

Comments on solving this system of differential equations are given in the SM (Section S1.5).

2.3.7 Sensitivity analysis

In order to evaluate the most sensitive reaction rate parameters in the kinetic model, the Campbell degree of rate control (DRC) method was applied.^{83, 84} This method consists in slightly changing the Gibbs energy (G_i) of a surface intermediate or a transition state, while keeping the Gibbs energy of the other species $G_{w \neq i}$ constant, and it has the advantage of maintaining the thermodynamic consistency of the model. For a set of reversible reactions, the degree of rate control of surface species or a transition state i (DRC_i) is defined as:

$$DRC_i = \left[\frac{\partial \ln(r_{CH_3OH,prod.})}{\partial \ln(k_i)} \right]_{G_{w \neq i}^0} = \left[-\frac{R \cdot T}{r_6 + r_7} \cdot \frac{\partial (r_5 + r_6)}{\partial (G_i^0)} \right]_{G_{w \neq i}^0} \quad (2.46)$$

Here, $(r_6 + r_7)$ is the methanol production rate, and G_i^0 is the free Gibbs energy of species i at the reference pressure (1 bar). The method of finite differences is used as an approximation to solve Eq. (2.46), and a step $\delta = 0.01 \text{ kJ} \cdot \text{mol}^{-1}$ was chosen. Eq. (2.47) is used to calculate the

sensitivity of methanol generation, and Eq. (2.48) is used for sensitivity of CO generation, which makes sense at high CO₂ content.

$$DRC_i \approx \frac{-R \cdot T}{\delta \cdot (r_6 + r_7)} \cdot \{[r_6(G_i^0 + \delta) + r_7(G_i^0 + \delta)] - [r_6(G_i^0) + r_7(G_i^0)]\} \quad (2.47)$$

$$DRC_i \approx \frac{-R \cdot T}{\delta \cdot (-r_2 - r_3)} \cdot \{[-r_2(G_i^0 + \delta) - r_3(G_i^0 + \delta)] - [-r_2(G_i^0) - r_3(G_i^0)]\} \quad (2.48)$$

2.4 Results and discussion

2.4.1 Model validation

A microkinetic model for syngas (H₂/CO/CO₂) conversion to methanol including a three-site approach and structural changes was successfully developed. The complete set of 25 reversible reactions and their respective parameters to calculate the turnover rates are summarized in Table 2.3. The thermodynamic consistency of the model was ensured (see section 2.3.3). The estimated value of the catalytic site quantity ($n_{M,Cat}$) was 2.00 mol·kg_{cat}⁻¹.

The validation of the model was done using own experiments and data from literature.^{33, 34, 41} The operating conditions in the respective setups are significantly different from ours, which contributes to a broader validation range. In Table 2.4, the operating conditions of each setup is summarized.

In Fig. 2.4, the normalized residues of CO output concentration of the original model is shown for each carbon-containing species. By comparing simulations with experimental data, it was found that the WGSR is adequately predicted. However, if the operating conditions favor rWGSR, generally for feed ratios of CO₂/CO_x ($\bar{y}_{CO_2,0}$) higher than 0.65 (CO_x = CO + CO₂), the simulation of CO production through the rWGSR was significantly higher than the experimental values, as shown in Fig. 2.4 especially for Slotboom's experiments (in which $\bar{y}_{CO_2,0} = 1$). This overestimation is seen by using both the Kuld's approach and the simplified approach for the zinc coverage.

This suggests that the Gibbs energy barrier ($\Delta G^\ddagger = E_A - T \cdot \Delta S^\ddagger$) is influenced by higher concentrations of CO₂ and H₂O or by surface intermediates derived from them, namely HCOO* and OH*, respectively. Different approaches were tested to improve the simulations in this region, including the addition of coverage dependency terms. The solution found was to add 15.44 kJ·mol⁻¹ to the activated complex energies of the most sensitive reactions of the rWGSR (R24 and R25) if the feed ratio of CO₂/CO_x is higher than 0.65 (see Table 2.3). With this procedure, the model remains thermodynamically consistent.

With the two-case approach, the experiments are simulated with the microkinetic model, first calculating the zinc coverage with Kuld's method (Fig. 2.5a-c), and then using the simplified method (Fig. 2.5d-f). In Fig. 2.5, the normalized residues for both cases are shown for each carbon-containing species, with the model quantitatively simulating the experiments. The simplified approach gave better results than the theoretical approach, as is clearly seen

when comparing the methanol simulation error (Fig. 2.5c and Fig.2.5f). Our hypothesis is that Kuld's method could be underestimating the zinc coverage, especially at high CO_2/CO_x , conditions which may give ϕ_{Zn} as low as 0.02.

Table 2.3 Three-site field extended reaction mechanism for the methanol synthesis and the water-gas shift reaction over Cu (211) and Cu/Zn (211), thermodynamically consistent. (a): Cu (211), (b): Cu/Zn (211), (c): special Cu (211) site for hydrogen and water adsorption. Reproduced with permission from Campos et al.⁷⁰. Copyright 2021, Royal Society of Chemistry.

No.	Reaction	Forward reaction			Reverse reaction		
		$\Delta S_f^\ddagger \cdot 10^3$ [kJ·(mol·K) ⁻¹]	$E_{A,f}$ [kJ·mol ⁻¹]	β [-]	$\Delta S_r^\ddagger \cdot 10^3$ [kJ·(mol·K) ⁻¹]	$E_{A,r}$ [kJ·mol ⁻¹]	β [-]
R1	$\text{H}_{2(g)} + 2 \cdot (c) \rightleftharpoons 2 \cdot \text{H}_{(c)}$	-119.24	69.57	0.000	1.72	93.01	0.000
R2	$\text{CO}_{(g)} + (a) \rightleftharpoons \text{CO}_{(a)}$	-158.23	0.00	0.000	0.00	58.37	0.000
R3	$\text{CO}_{(g)} + (b) \rightleftharpoons \text{CO}_{(b)}$	-151.60	8.90	-0.119	-6.64	0.00	0.119
R4	$\text{CO}_{2(g)} + (a) \rightleftharpoons \text{CO}_{2(a)}$	-144.74	0.00	-0.129	-7.22	52.29	0.129
R5	$\text{CO}_{2(g)} + (b) \rightleftharpoons \text{CO}_{2(b)}$	-138.11	0.00	-0.249	-13.86	51.59	0.249
R6	$\text{H}_3\text{CO}_{(a)} + \text{H}_{(c)} \rightleftharpoons \text{CH}_3\text{OH}_{(g)} + (a) + (c)$	56.99	81.22	-0.547	-181.26	32.93	0.547
R7	$\text{H}_3\text{CO}_{(b)} + \text{H}_{(c)} \rightleftharpoons \text{CH}_3\text{OH}_{(g)} + (b) + (c)$	47.03	92.56	-0.368	-171.30	23.61	0.368
R8	$\text{H}_2\text{O}_{(g)} + (c) \rightleftharpoons \text{H}_2\text{O}_{(c)}$	-177.19	0.00	0.378	21.08	31.21	-0.378
R9	$\text{H}_2\text{O}_{(c)} + (c) \rightleftharpoons \text{OH}_{(c)} + \text{H}_{(c)}$	5.99	79.84	0.140	21.60	105.17	-0.140
R10	$\text{CO}_{(a)} + \text{H}_{(c)} \rightleftharpoons \text{HCO}_{(a)} + (c)$	25.38	84.62	-0.299	-21.90	20.55	0.299
R11	$\text{HCO}_{(a)} + \text{H}_{(c)} \rightleftharpoons \text{H}_2\text{CO}_{(a)} + (c)$	15.73	56.26	-0.299	-8.10	92.81	0.299
R12	$\text{CO}_{2(a)} + \text{H}_{(c)} \rightleftharpoons \text{HCOO}_{(a)} + (c)$	36.44	77.74	-0.249	8.72	109.64	0.249
R13	$\text{CO}_{2(b)} + \text{H}_{(c)} \rightleftharpoons \text{HCOO}_{(b)} + (c)$	43.07	60.24	-0.368	2.08	105.43	0.368
R14	$\text{HCOO}_{(a)} + \text{H}_{(c)} \rightleftharpoons \text{HCOOH}_{(a)} + (c)$	10.42	128.23	0.000	-153.70	29.81	0.000
R15	$\text{HCOO}_{(b)} + \text{H}_{(c)} \rightleftharpoons \text{HCOOH}_{(b)} + (c)$	10.42	136.53	0.000	-153.70	7.72	0.000
R16	$\text{HCOOH}_{(a)} + \text{H}_{(c)} \rightleftharpoons \text{H}_2\text{COOH}_{(a)} + (c)$	-150.42	46.89	0.000	-25.96	62.43	0.000
R17	$\text{HCOOH}_{(b)} + \text{H}_{(c)} \rightleftharpoons \text{H}_2\text{COOH}_{(b)} + (c)$	-150.42	1.54	0.000	-25.96	48.92	0.000
R18	$\text{H}_2\text{COOH}_{(a)} + (c) \rightleftharpoons \text{H}_2\text{CO}_{(a)} + \text{OH}_{(c)}$	-20.59	20.52	-0.249	-15.21	38.77	0.249
R19	$\text{H}_2\text{COOH}_{(b)} + (c) \rightleftharpoons \text{H}_2\text{CO}_{(b)} + \text{OH}_{(c)}$	-13.95	11.22	-0.368	-21.85	9.96	0.368
R20	$\text{H}_2\text{CO}_{(a)} + \text{H}_{(c)} \rightleftharpoons \text{H}_3\text{CO}_{(a)} + (c)$	42.42	52.66	-0.547	-13.47	107.12	0.547
R21	$\text{H}_2\text{CO}_{(b)} + \text{H}_{(c)} \rightleftharpoons \text{H}_3\text{CO}_{(b)} + (c)$	32.46	51.46	-0.368	-3.51	132.06	0.368
R22	$\text{CO}_{(a)} + \text{OH}_{(c)} \rightleftharpoons \text{COOH}_{(a)} + (c)$	-11.31	79.90	-0.119	-3.74	16.05	0.119
R23	$\text{CO}_{(b)} + \text{OH}_{(c)} \rightleftharpoons \text{COOH}_{(b)} + (c)$	-11.31	13.33	-0.119	-3.74	16.05	0.119
R24	$\text{COOH}_{(a)} + \text{OH}_{(c)} \rightleftharpoons \text{CO}_{2(a)} + \text{H}_2\text{O}_{(c)}$	9.92	17.09	-0.119	-22.36	60.82	0.119
R25	$\text{COOH}_{(b)} + \text{OH}_{(c)} \rightleftharpoons \text{CO}_{2(b)} + \text{H}_2\text{O}_{(c)}$	9.92	17.09	-0.119	-22.37	60.82	0.119
If the CO_2/CO_x ratio in feed is higher than 0.65, the activation energies of reactions 24 and 25 are adjusted:							
R24	$\text{COOH}_{(a)} + \text{OH}_{(c)} \rightleftharpoons \text{CO}_{2(a)} + \text{H}_2\text{O}_{(c)}$	9.92	32.53	-0.119	-22.36	76.22	0.119
R25	$\text{COOH}_{(b)} + \text{OH}_{(c)} \rightleftharpoons \text{CO}_{2(b)} + \text{H}_2\text{O}_{(c)}$	9.92	32.53	-0.119	-22.37	76.22	0.119

Table 2.4 Operating conditions of the considered database, which consists of different setups. Reproduced with permission from Campos et al.⁷⁰. Copyright 2021, Royal Society of Chemistry.

Database	This work	Seidel	Park*	Slotboom
N° of points	359	139	98	94
Reactor	PFR	CSTR	PFR	PFR
Pressure (bar)	40 – 60	30 – 70	50 – 90	20 – 50
Temperature (°C)	210 – 260	230 – 260	230 – 340	178 – 260
GHSV (L h ⁻¹ g _{cat.} ⁻¹)	24 – 40	3.6	8 – 40	1.3 – 6.5
H ₂ feed (% v/v)	35 – 60	60 – 76	50 – 83	66 – 80
CO feed (% v/v)	3 – 30	0 – 21	7 – 29	0
CO ₂ feed (% v/v)	0 – 20	0 – 13	2 – 16	12 – 25
Inert feed (% v/v)	20 – 50	15 – 16	0 – 28	0 - 11
CO _x Conversion (%)	0.9 – 30.9	2.9 – 52.8	5.1 – 56.0	0.4 – 9.6

*Only the experiments containing both CO and CO₂ in the feed were considered.

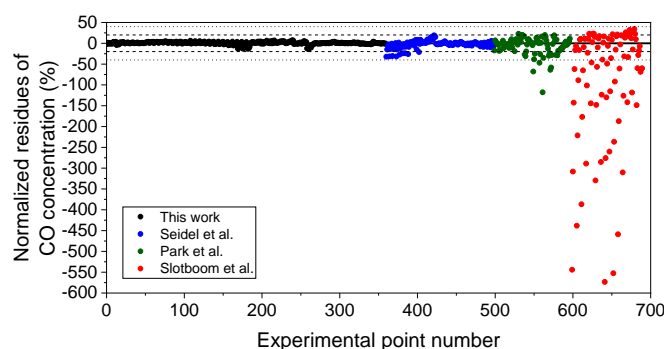


Fig. 2.4 Original model simulation (one-case): normalized residues of CO concentration in the simulation of the experiments from this work (1-359), from Seidel et al.³⁴ (360-498), from Park et al.³³ (499-596), and from Slotboom et al.⁴¹ (597-690). Simulation considering the simplified approach for the zinc coverage. Adapted with permission from Campos et al.⁷⁸. Copyright 2021, Royal Society of Chemistry.

The sum of the relative squared errors (χ^2) was calculated as follows:

$$\chi^2 = \sum_{j=1}^3 \sum_{n=1}^{N_p} \left(\frac{y_{j,out}^n - \hat{y}_{j,out}^n}{y_{j,out}^n} \right)^2 \quad (2.49)$$

The simplified method of zinc coverage estimation gave better results than the theoretical method ($\chi^2 = 74.7$ against $\chi^2 = 120.7$). Therefore, all further simulations and corresponding discussion is made considering the simplified method of zinc coverage estimation.

The mean error (ME_j) and the mean squared error of the predictions are calculated for CO ($j = 1$), CO₂ ($j = 2$), and methanol ($j = 3$), and are shown in Table 2.5.

$$ME_j = \frac{1}{N_p} \cdot \sum_1^{N_p} \left| \frac{y_{j,out}^n - \hat{y}_{j,out}^n}{y_{j,out}^n} \right| \quad (2.50)$$

$$MSE_j = \frac{1}{N_p} \cdot \sum_1^{N_p} \left(\frac{y_{j,out}^n - \hat{y}_{j,out}^n}{y_{j,out}^n} \right)^2 \quad (2.51)$$

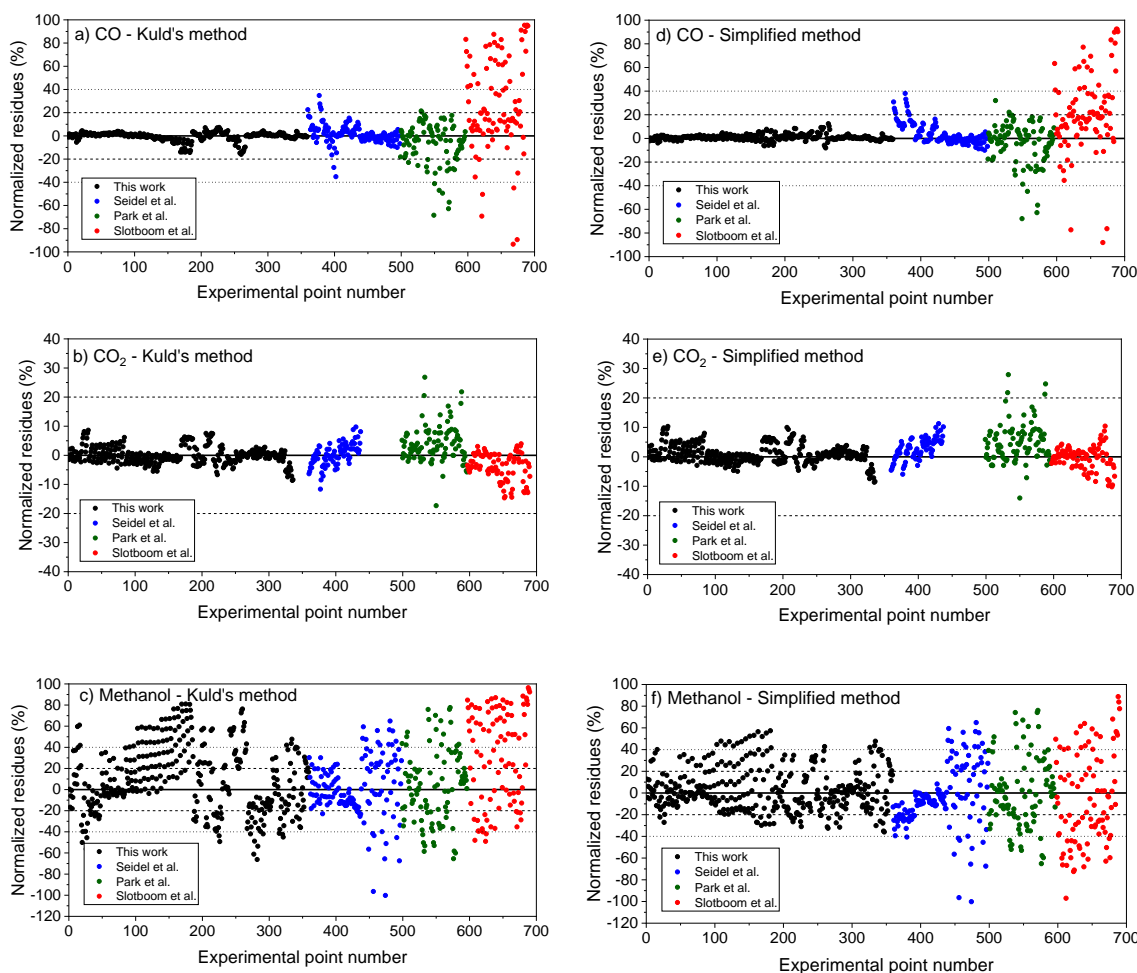


Fig. 2.5 Two-case model simulation: normalized residues of the simulation of the experiments from this work (1-359), from Seidel et al.³⁴ (360-498), from Park et al.³³ (499-596), and from Slotboom et al.⁴¹ (597-690). A) Carbon monoxide. B) Carbon dioxide. C) Methanol. Adapted with permission from Campos et al.⁷⁸. Copyright 2021, Royal Society of Chemistry.

Considering all experiments, the mean error (ME) values of CO, CO₂ and methanol concentration are 8.3, 3.2, and 21.3%, respectively. These values are even lower when looking only to mixed feeds (H₂/CO/CO₂). The mean squared errors (MSE) are also significantly low (see Table 2.5). The majority of the points are between the $\pm 20\%$ lines (89% of CO points, 99% of CO₂ points, 57% of MeOH points), while 84% of the MeOH points are between the $\pm 40\%$ lines.

Table 2.5 Statistical indicators of the model performance in predicting the carbon-containing compounds. Considerations: two-case model, simplified method for zinc coverage estimation. Adapted with permission from Campos et al.⁷⁸. Copyright 2021, Royal Society of Chemistry.

Feed:		H ₂ /CO/CO ₂			H ₂ /CO		H ₂ /CO ₂		All
Data:	This work	Seidel	Park	This work	Seidel	Seidel	Slotboom		
N° of points		324	46	98	35	61	32	94	690
χ^2		13.05	0.55	15.31	2.44	9.29	3.02	32.31	75.97
CO	ME	0.0192	0.0431	0.1371	0.0105	0.0269	0.1751	0.2978	0.0830
	MSE	0.0008	0.0035	0.0444	0.0002	0.0013	0.0342	0.1530	0.0295
CO ₂	ME	0.0227	0.0430	0.0601			0.0301	0.0309	0.0321
	MSE	0.0010	0.0027	0.0067			0.0011	0.0017	0.0022
CH ₃ OH	ME	0.1499	0.0643	0.2559	0.2299	0.3220	0.2275	0.3749	0.2128
	MSE	0.0385	0.0057	0.1051	0.0695	0.1510	0.0535	0.1890	0.0785

In Fig. 2.6, it is shown the experimental and simulated values of methanol output concentration for different conditions and setups. It can be seen that the simulations are significantly close to the experiments and the trends are adequately predicted. In Fig. 2.7, the error of the prediction of the carbon-containing compounds is shown as a function of $\bar{y}_{CO_2,0}$ (x-axis) and temperature (y-axis) for our experiments at the operating conditions of 41 bar, 24 L·h⁻¹·g_{cat}⁻¹ and H₂/CO_x/N₂ ≈ 45.3/14.3/40.4% v/v. The model simulates CO and CO₂ accurately for the entire studied region. The simulation of methanol is also reasonable, with slight overestimations at low temperatures and low $\bar{y}_{CO_2,0}$, and moderate underestimations at low temperatures and high $\bar{y}_{CO_2,0}$. This leads to the conclusion that there is some positive effect on CO₂ hydrogenation at low temperature when the concentration of CO₂ is increased, which is not reflected in this model. This effect is shown in both our own experiments and experiments from literature.⁸⁵

2.4.2 Reaction flow and sensitivity analysis

The validated model was used to simulate the methanol synthesis at an extended range of conditions. In Fig. 2.8, it is shown the turnover frequency of the different reaction paths and the CO_x conversion along the reactor. The operating conditions are 60 bar, 220 °C, 4.8 L_S·h⁻¹·g_{cat}⁻¹, and a feed concentration of H₂/CO_x = 80/20% v/v. Fig. 2.8 is complemented by the coverages of the surface species (Fig. 2.9). In the SM (Section S1.6), analogous diagrams are shown for an operating temperature of 250 °C.

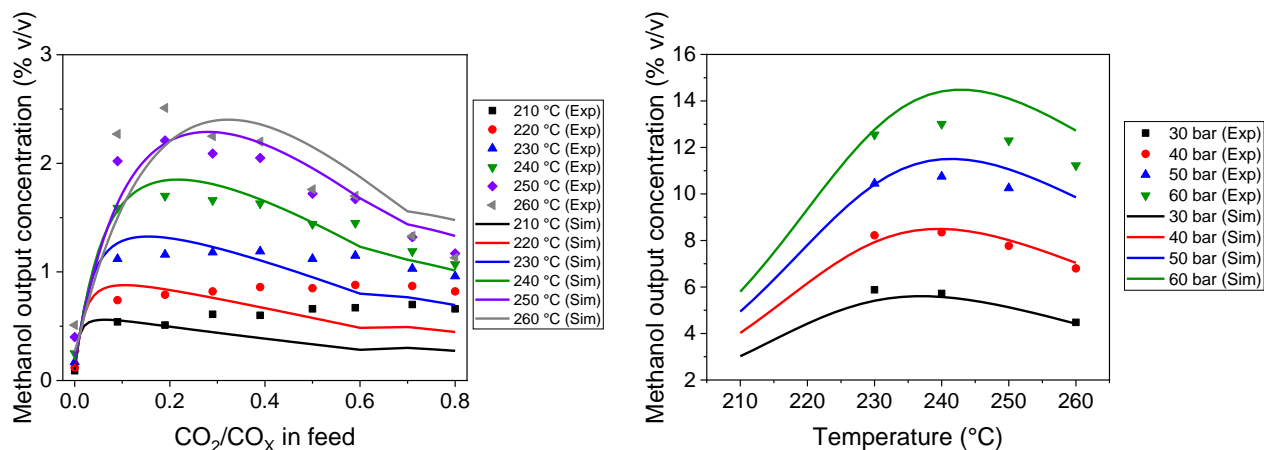


Fig. 2.6 Experimental and simulated values of methanol output concentration at different conditions. Databases: A) This work. B) Seidel et al.³⁴ Adapted with permission from Campos et al.⁷⁸. Copyright 2021, Royal Society of Chemistry.

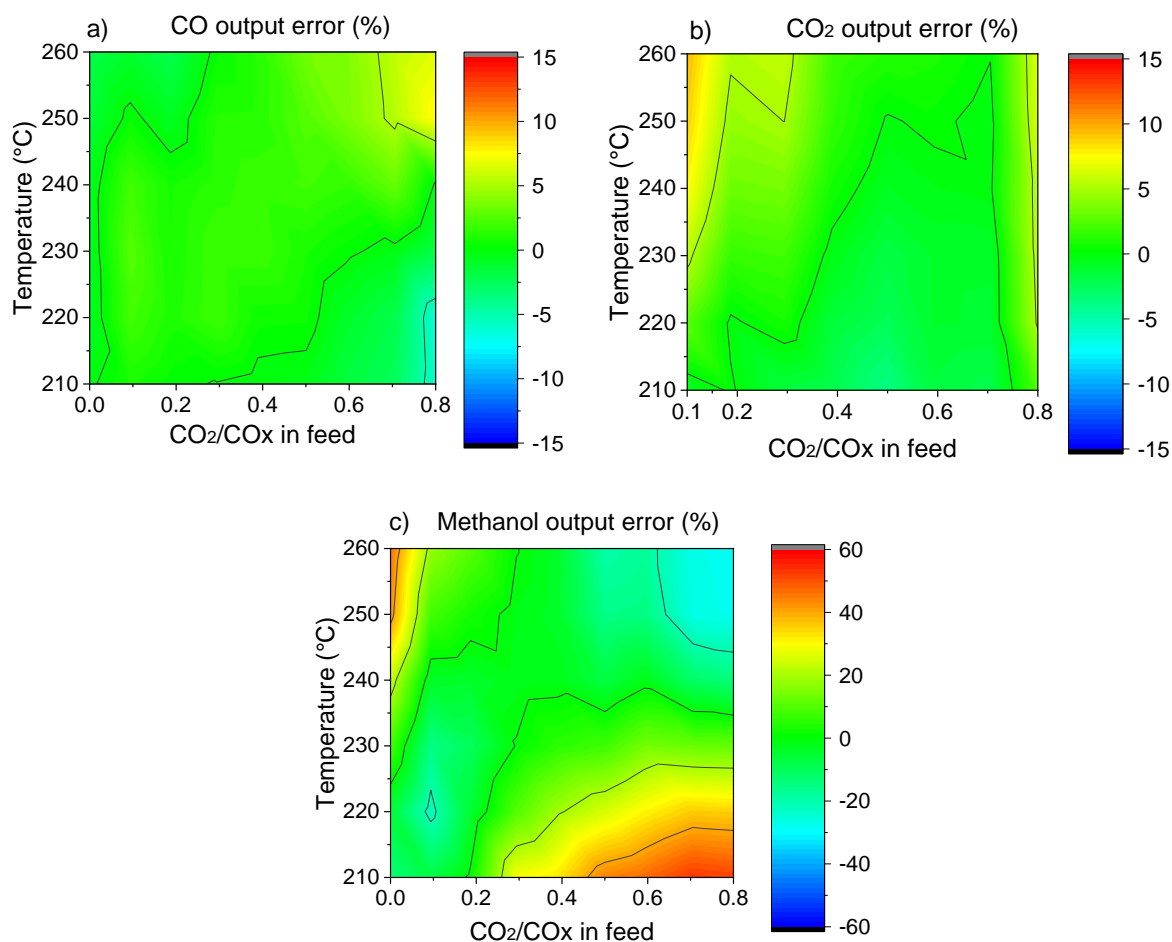


Fig. 2.7 Simulation error (color) as a function of CO₂/CO_x in feed and temperature. Operating conditions: 41 bar, GHSV = 24 L_S·h⁻¹·g_{cat}⁻¹, feed concentration: H₂/CO_x/N₂ = 45.3/14.3/40.4% v/v. a) CO. b) CO₂. c) Methanol. Adapted with permission from Campos et al.⁷⁰. Copyright 2021, Royal Society of Chemistry.

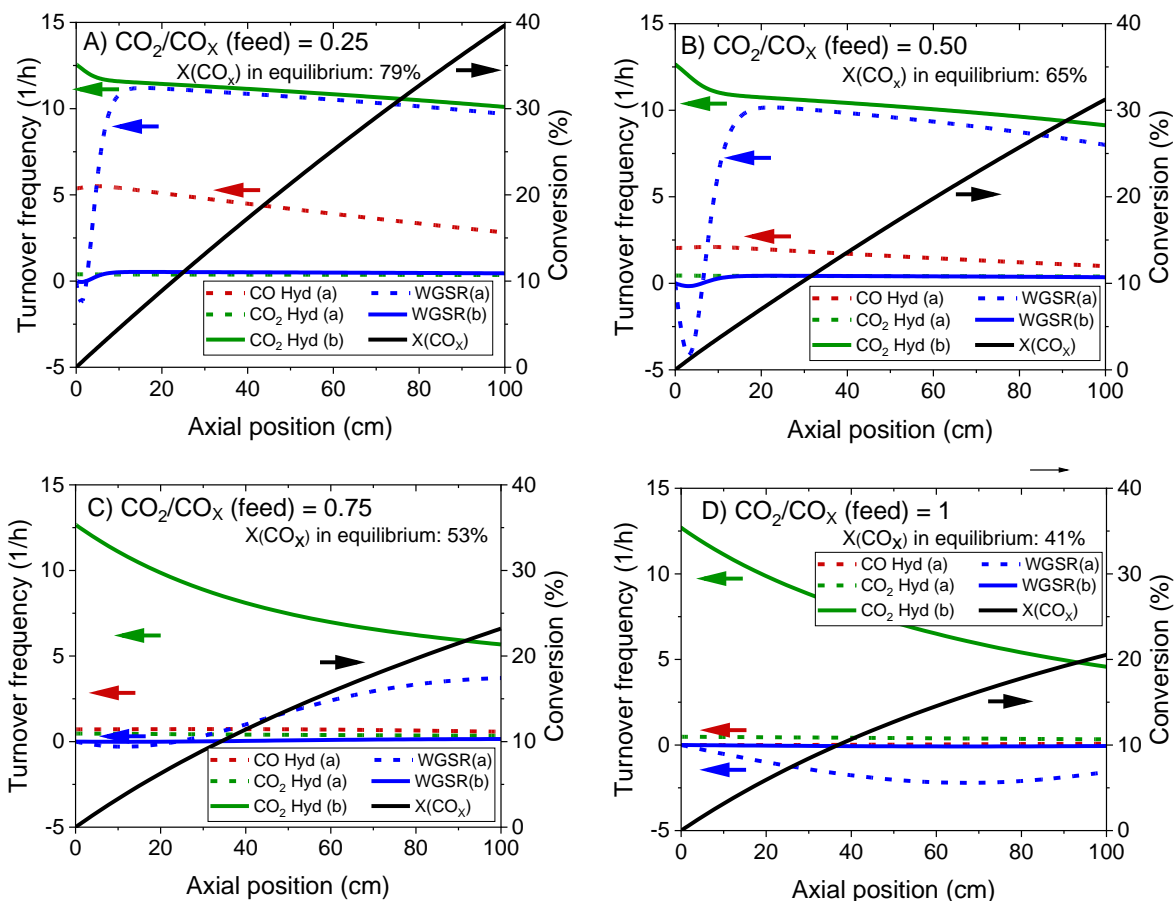


Fig. 2.8 Turnover frequency and conversion of CO_x (X) along a methanol synthesis reactor with a length of 100 cm, simulated with the kinetic model. The arrows show to which y-axis the curves belong. Operating conditions: 220 °C, 60 bar, GHSV = 4.8 $\text{L}_\text{S}\cdot\text{h}^{-1}\cdot\text{g}_{\text{cat}}^{-1}$, feed concentration: $\text{H}_2/\text{CO}_x = 80/20$. A) $\text{CO}_2/\text{CO}_x = 0.25$. B) $\text{CO}_2/\text{CO}_x = 0.50$. C) $\text{CO}_2/\text{CO}_x = 0.75$. D) $\text{CO}_2/\text{CO}_x = 1.00$. Adapted with permission from Campos et al.⁷⁰. Copyright 2021, Royal Society of Chemistry.

According to the simulations, CO hydrogenation on site a (Cu) is only relevant at CO-rich feeds (e.g. ca. 30% of the methanol production at $\bar{y}_{\text{CO}_2,0} = 0.25$), CO_2 hydrogenation on site a (Cu) does not occur significantly at any condition, and CO_2 hydrogenation on site b (Cu/Zn) is the main reaction path for the production of methanol, in agreement with findings from DFT studies.^{17, 18}

At CO-rich conditions (e.g. $\bar{y}_{\text{CO}_2,0} \leq 0.50$), CO_2 conversion and (consequently) water generation are fast within the initial 10 cm of the reactor, mainly due to CO_2 hydrogenation, but probably also due to contributing rWGSR (depending on the CO_2/CO_x ratio and the temperature). Furthermore, the WGSR rate increases rapidly along the reactor, and after a certain amount of water has been produced (it is dependent on the operating conditions), the WGSR rate is approximately equal to the CO_2 hydrogenation rate. From this axial position on (ca. 10 cm, Fig. 2.9A and B), CO_2 concentration remains constant, because it is consumed in the CO_2 hydrogenation but regenerated in the WGSR. Therefore, from this axial position on,

only CO is converted, through the combination of WGSR and CO₂ hydrogenation and through direct CO hydrogenation.

With more CO₂ content in the feed (e.g. $\bar{y}_{CO_2,0} \geq 0.75$), a higher conversion of CO₂ is achieved, which implies that higher amounts of water are generated, and the methanol synthesis is severely slowed down. At CO₂-rich feeds, there is significant CO production via the rWGSR, increasing with temperature (see Section S1.6, in the SM).

At constant temperature and pressure, the decrease of CO₂ hydrogenation rate on Cu/Zn, along the reactor length, has two main causes:

- The decrease of H_(c) coverage, which is caused by H_{2(g)} consumption;
- The product inhibition with the increase of H₃CO_(b) and OH_(b), because of methanol and water accumulation, respectively.

From our simulations, the product inhibition has the highest effect in reducing the reaction rate. This is particularly relevant for CO₂-rich feeds, in which a significant water accumulation takes place and, thus, OH_(c) reduces the amount of free sites (c), as shown in Fig. 2.9C and D.

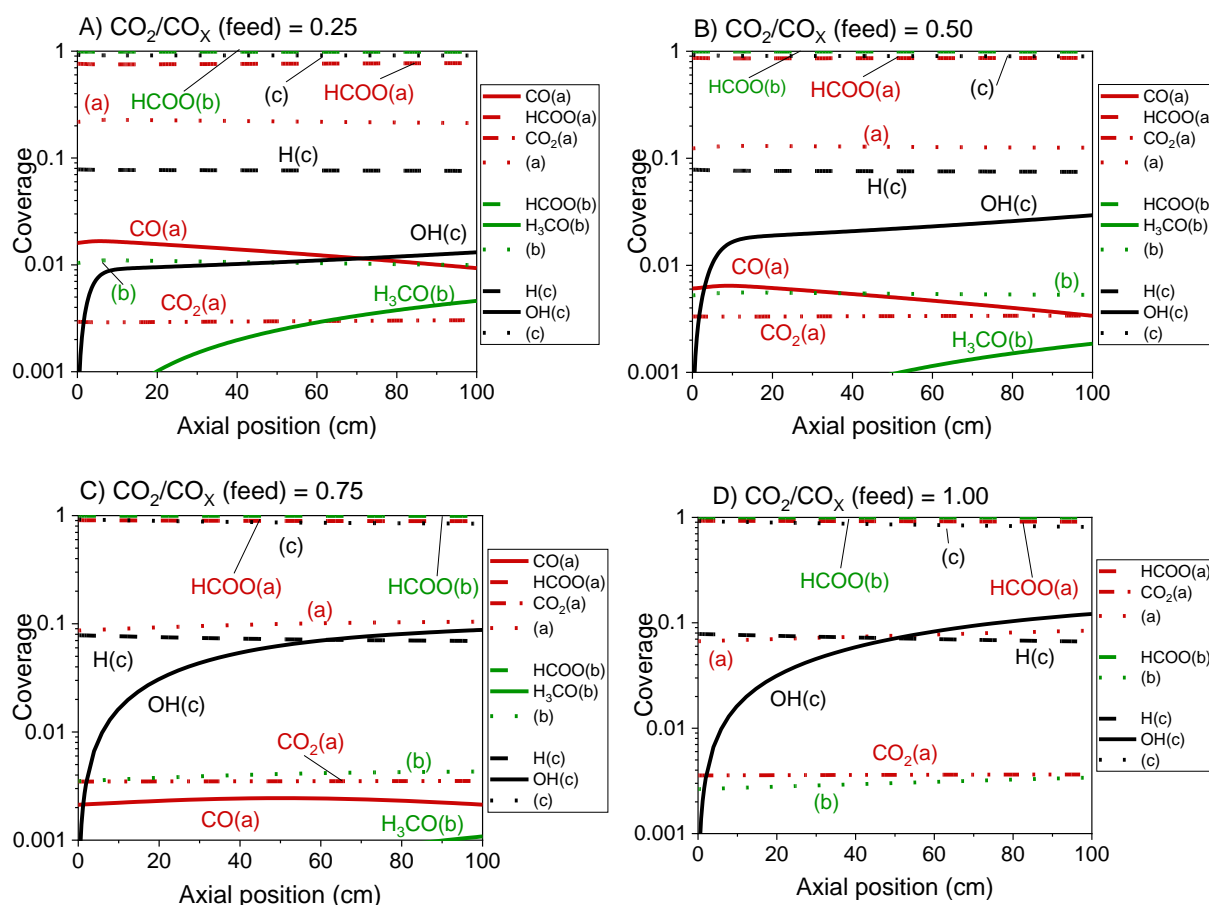


Fig. 2.9 Coverage of the surface species along the reactor with a length of 100 cm. Operating conditions: 220 °C, 60 bar, GHSV = 4.8 L_s·h⁻¹·g_{cat}⁻¹, feed concentration: H₂/CO_x = 80/20% v/v. A) CO₂/CO_x = 0.25. B) CO₂/CO_x = 0.50. C) CO₂/CO_x = 0.75. D) CO₂/CO_x = 1.00. Adapted with permission from Campos et al.⁷⁰. Copyright 2021, Royal Society of Chemistry.

In a recent work,⁸⁶ a methanol-assisted autocatalytic mechanism was proposed, with water as the only effective inhibitor of the methanol synthesis. If appropriate DFT calculations were accessible, our model could be extended accordingly, and this possibility could be investigated further.

In Fig. 2.10, the positive effects of pressure and CO₂ concentration, and the negative effect of temperature on formate coverage on Cu and on Cu/Zn are shown. Formate requires lower temperature, higher pressure, and higher CO₂ concentration to block the majority of Cu sites (Fig. 2.10A and B), but it covers most of the Cu/Zn sites even at mild conditions (Fig. 2.10C and D). Therefore, moderate consumption of CO₂ changes the formate coverage on Cu/Zn only slightly, and therefore the reaction rate of CO₂ hydrogenation is not as much affected by CO₂ consumption as by the factors previously discussed. This was experimentally demonstrated by varying the feed concentration of CO₂ while maintaining the other conditions constant, as shown in Fig. 2.11.

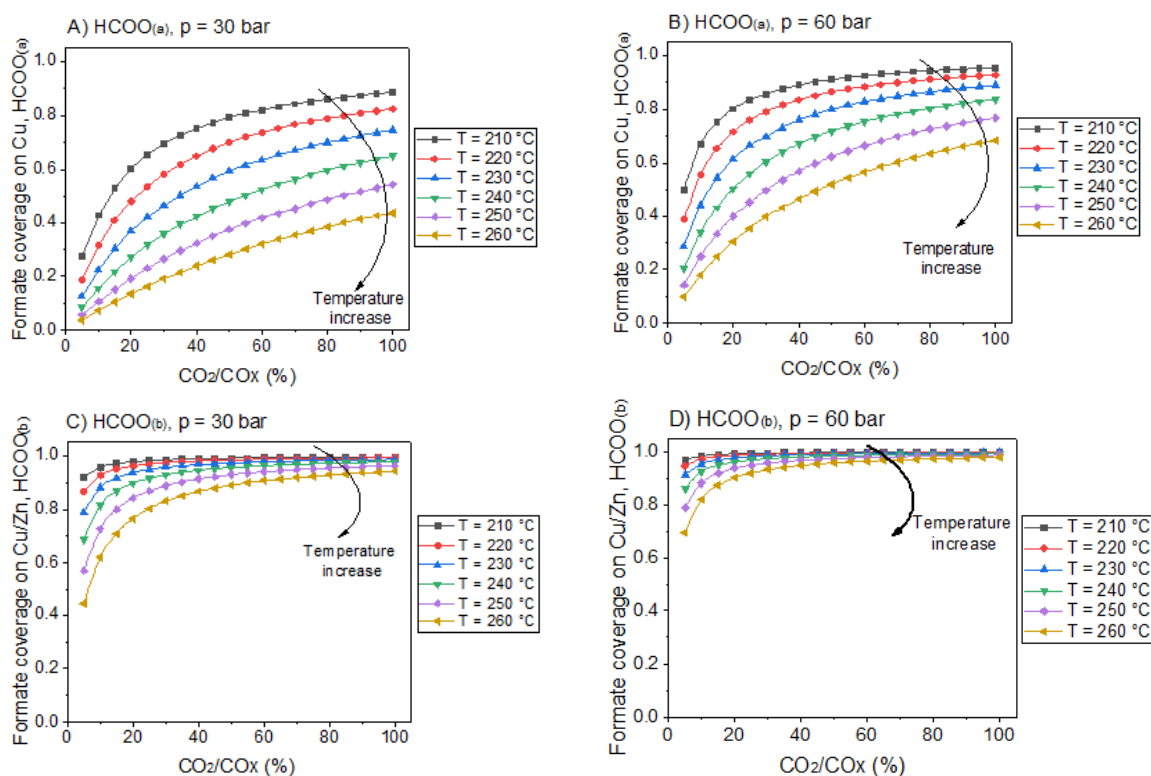


Fig. 2.10 Formate coverage on Cu and Cu/Zn active surfaces, as a function of CO₂/CO_x ratio in the gas phase. The gas phase concentration correspond to a typical low conversion condition: H₂/CO_x/CH₃OH/H₂O = 79.8/19.8/0.2/0.2 (% v/v). The curves correspond to different temperatures. A) HCOO_(a), 30 bar. B) HCOO_(a), 60 bar. C) HCOO_(b), 30 bar. D) HCOO_(b), 60 bar. Reproduced with permission from Campos et al.⁷⁰. Copyright 2021, Royal Society of Chemistry.

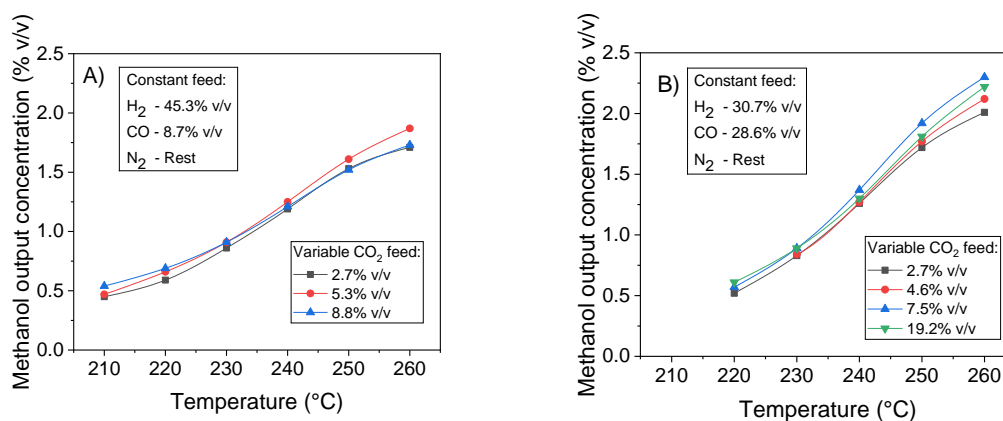


Fig. 2.11 Effect of CO₂ feed concentration on the methanol production at 41 bar, 220-260 °C and 32 L·h⁻¹·g_{cat}⁻¹. Reproduced with permission from Campos et al.⁷⁰. Copyright 2021, Royal Society of Chemistry.

The method of degree of rate control (DRC) is applied to investigate the sensitivity of the methanol production in relation to the free Gibbs energy of each surface intermediate and of each transition state of the reversible reactions. This analysis is shown at 60 bar (Fig. 2.12) and different temperatures considering a gas phase concentration at low conversion: H₂/CO_x/CH₃OH/H₂O = 79.8/19.8/0.2/0.2% v/v. A separate analysis is made for the case of little CO content in the gas (Fig. 2.13), which includes the sensitivity of both CO and methanol generation. The DRC was also applied to a pressure of 30 bar, and similar results to the ones at 60 bar were found (see Section S1.7 in the SM).

The most sensitive reaction according to our microkinetic model is the hydrogenation of formic acid (HCOOH_(b)) on Cu/Zn (R17, Table 2.2) for the entire operating region under study, which is in agreement with other DFT-derived models^{48, 87} and lumped kinetic models.^{31, 41} Xu et al.⁵¹ concluded that the hydrogenation of formic acid is the RDS for the CO₂ hydrogenation at lower formate coverages, and the H₂COOH* association (R19, Table 2) is the RDS for high formate coverages, the latter conclusion being a result of the one-site approach made by the authors (see section 2.3.1). Grabow et al.³¹ and Park et al.³³ found the hydrogenation of H₂CO* to be the RDS on Cu (111) without considering the zinc influence. Finally, the model presented here shows that the hydrogenation of formate (R15), a typically assumed RDS in formal kinetic models,^{34, 39} has a reasonable sensitivity in our model (0.20–0.35), but still far behind the sensitivity of R17 (0.50–0.70).

In the CO hydrogenation on Cu, the most sensible reaction of this microkinetic model is the hydrogenation of HCO_(a) (R11), which is in agreement with findings of Van Rensburg et al.⁴⁸ In formal kinetic modeling studies, Graaf et al.³¹ proposed the hydrogenation of H₂CO* (R20) to be the RDS, while Seidel et al.³⁴ assumed that the RDS is the hydrogenation of H₃CO* (R6).

From our DRC analysis of CO generation sensitivity at CO₂/CO_x = 0.987 (Fig. 2.13), COOH* formation on Cu (R24) is the RDS of the rWGS. Other reported models that include the WGS usually consider the redox mechanism^{34, 39} or the carboxyl mechanism without water

assistance⁴¹ to be the RDS, which have been tested here with DFT data and also evaluated elsewhere as not significant when compared to the water-assisted carboxyl mechanism.⁵⁴

Regarding the participating intermediates, our findings suggest that formate on Cu/Zn ($\text{HCOO}_{(b)}$) is the most sensitive species, as it is the most abundant species, and participates on the second most sensitive reaction (formate hydrogenation), which produces formic acid ($\text{HCOOH}_{(b)}$).

The rWGSr is mostly sensitive to formate adsorbed on Cu, although formate itself is a spectator of this reaction path, suggesting that formate may inhibit the rWGSr at a certain level. This hypothesis is further supported by the argument that the rWGSr is much slower on Cu/Zn, which has a formate coverage close to 1.

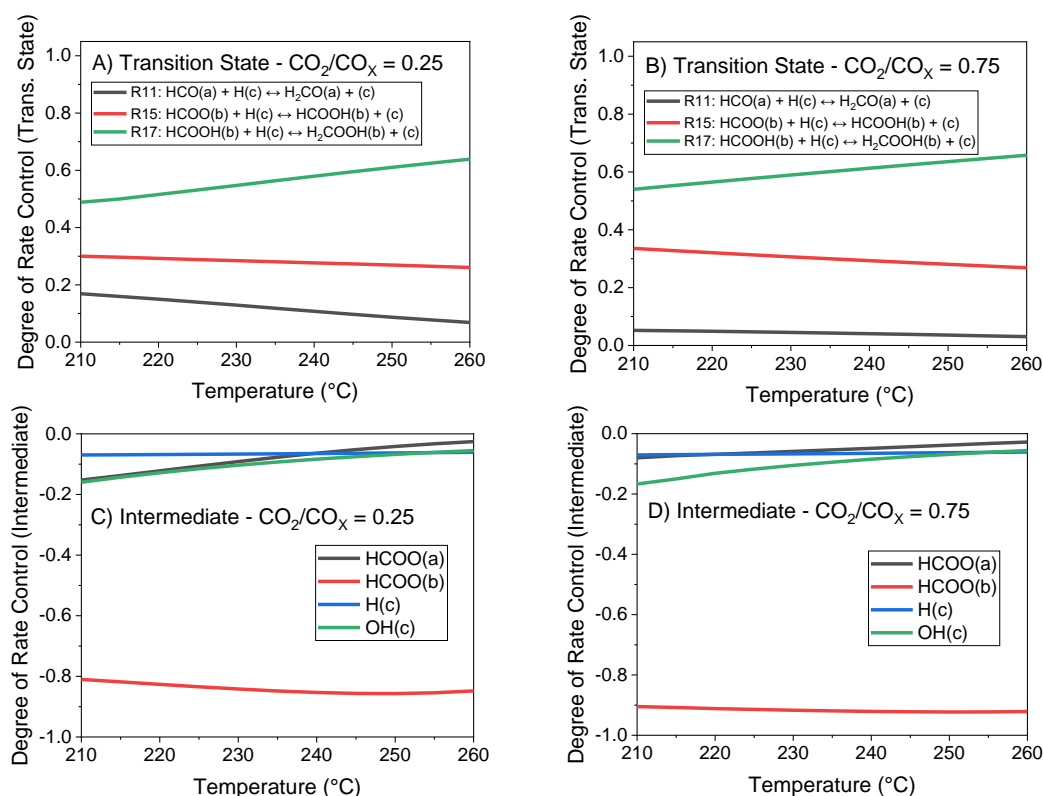


Fig. 2.12 Degree of Rate Control (DRC) analysis of the methanol production at 60 bar and 210-260 °C. Gas concentration: $\text{H}_2/\text{CO}_x/\text{CH}_3\text{OH}/\text{H}_2\text{O} = 79.8/19.8/0.2/0.2\%$ v/v. A) Trans. State - $\text{CO}_2/\text{CO}_x = 0.25$. B) Trans. State - $\text{CO}_2/\text{CO}_x = 0.75$. C) Intermediate - $\text{CO}_2/\text{CO}_x = 0.25$. D) Intermediate - $\text{CO}_2/\text{CO}_x = 0.75$. Reproduced with permission from Campos et al.⁷⁰. Copyright 2021, Royal Society of Chemistry.

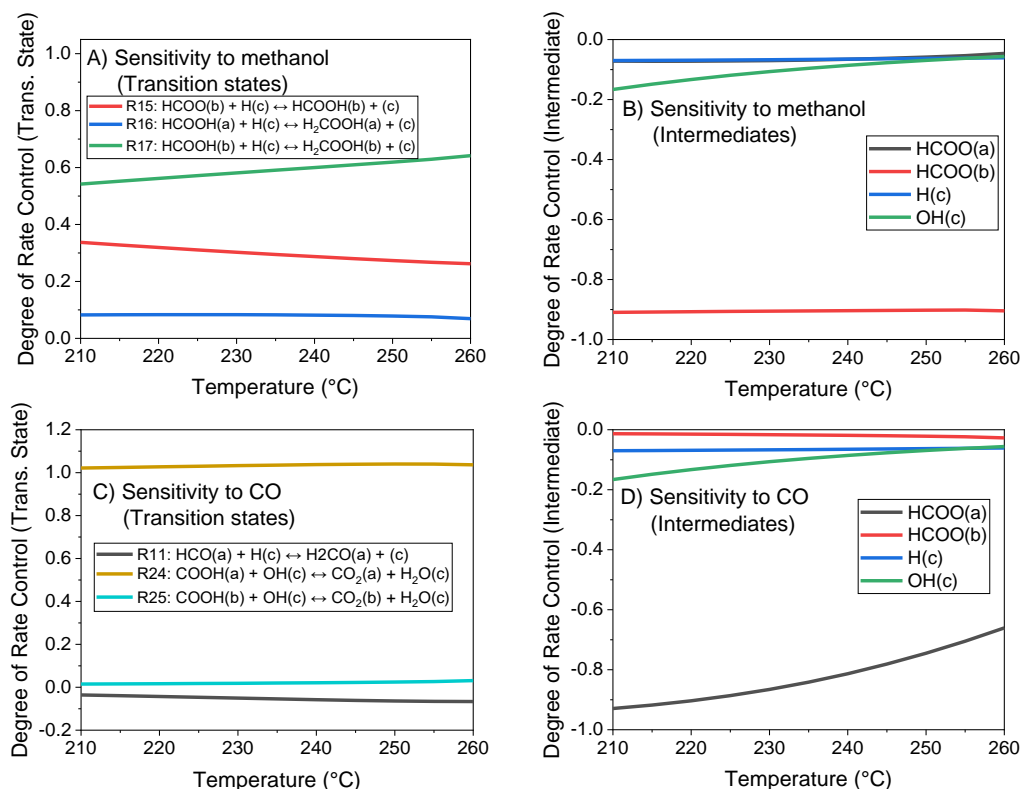


Fig. 2.13 Degree of Rate Control (DRC) analysis at 210-260 °C, 60 bar, and a gas concentration of $\text{H}_2/\text{CO}/\text{CO}_2/\text{CH}_3\text{OH}/\text{H}_2\text{O} = 79.8/0.2/19.6/0.2/0.2\%$ v/v. A) Sensitivity to methanol, transition states. B) Sensitivity to methanol, intermediates. C) Sensitivity to CO, transition states. D) Sensitivity to CO, intermediates. Reproduced with permission from Campos et al.⁷⁰. Copyright 2021, Royal Society of Chemistry.

2.5 Summary and conclusions

A thermodynamically consistent microkinetic model was successfully developed, based on first principles DFT derived kinetic data for the methanol synthesis and the WGS on Cu (211) and Cu/Zn (211). With an extensive validation consisting in 359 own experiments (available in the SI) and experiments from three different sources in literature (i.e. 139 data points from Seidel et al.,³⁴ 98 data points from Park et al.,³³ and 94 data points from Slotboom et al.⁴¹), the model reproduces the system quantitatively in a broad range of relevant conditions, showing discrepancies only for the combination of low temperature and high CO_2/CO_x concentration in feed. The proposed model is based on theoretical calculations, and we believe it has a high chance of accurately predicting the methanol synthesis outside the validation region.

The reaction flow analysis showed that methanol is mainly formed from CO_2 hydrogenation on site b (Cu/Zn), and that CO conversion is mostly due to the WGS on site a (Cu). At CO-rich conditions, direct CO hydrogenation is responsible for some of the methanol generation (e.g. 30% of the methanol production for $\text{CO}_2/\text{CO}_x = 0.25$). At higher CO_2 concentrations, this reaction pathway is strongly inhibited by formate accumulation on Cu surface.

The model suggests that formation of methanol and water leads to an accumulation of $\text{H}_3\text{CO}_{(b)}$ and $\text{OH}_{(c)}$, respectively, with both slowing down the overall reaction. This is particularly significant in the case of CO_2 -rich feeds, as high amounts of water are generated in the process. We assume that the productivity should be increased by using reactor designs that enable product extraction in situ, such as using membranes, or integrating reaction and product condensation steps. This is especially encouraged for the conversion of CO_2 to methanol.

The sensitivity analysis, using the method of the degree of rate control (DRC), pointed out that the formic acid hydrogenation on site b (Cu/Zn) ($\text{HCOOH}_{(b)}$) is the most sensitive step (DRC around 0.60). Formate ($\text{HCOO}_{(a)}$) was found to be the most sensitive intermediate in the rWGS, although it does not participate in this reaction, which suggests that the rWGS is slowed down due to formate blocking of free sites. With this finding and based on the premise that formate only reacts further to produce methanol, we formulate the following hypothesis: If a modification on the Cu/Zn-based catalysts is realized, in which formate binds stronger on the Cu site and achieves coverages closer to 1, the rWGS might be more effectively inhibited, and CO_2 conversion at CO_2 -rich systems should be enhanced.

The presented microkinetic model can be further extended with additional reaction paths if DFT calculations are available (e.g. methanol dehydration to DME or methanol-assisted autocatalytic reaction paths).

Chapter 3. Development of consistent kinetic models derived from a microkinetic model of the methanol synthesis

Declaration of contributions:

Bruno Lacerda de Oliveira Campos developed and validated the kinetic models, analyzed the results, and wrote the manuscript.

Karla Herrera Delgado conceptualized and supervised the work, contributed to the discussion, and reviewed the manuscript.

Stephan Pitter supervised the work, contributed to the discussion, and reviewed the manuscript.

Jörg Sauer supervised the work, contributed to the discussion, and reviewed the manuscript.

Chapter redrafted after:

Lacerda de Oliveira Campos, B.; Herrera Delgado, K.; Pitter, S.; Sauer, J. Development of consistent kinetic models derived from a microkinetic model of the methanol synthesis. *Ind. Eng. Chem. Res.*, 2021, **60**, 15074-15086. DOI: 10.1021/acs.iecr.1c02952

Abstract Chapter 3

The microkinetic model of the methanol synthesis and the water-gas shift reaction on Cu/Zn-based catalysts, which was described in chapter 2, is used to develop three particularly interesting formal kinetic models, drastically reducing model complexity. In the first model, kinetic parameters are taken from DFT data used in the microkinetic mechanism, and only a single parameter is fitted to experiments. Still, this model adequately simulates experiments with low to moderate CO₂ content in feed mixture. A second model, which has an increased number of estimated parameters (nine in total), performs well for the whole range of studied operating conditions. At last, a third model, which has six fitted parameters and neglects CO hydrogenation, adequately simulates conditions with CO₂-containing feed. Each developed kinetic model is either equally well or better suited for the simulation of the methanol synthesis than literature models with higher number of parameters.

3.1 Introduction

In general, it is believed that microkinetic models are more suitable to extrapolations than formal kinetic models, since in the latter approach different effects might be merged with kinetic parameters.⁴⁶ However, the implementation of microkinetic models is complex, and the simulations require higher computational costs comparing to formal kinetic models.

In order to get the advantages of both formal and microkinetic approaches, it is, therefore, of interest to extract the relevant theoretical information of a microkinetic model and implement a simpler and faster-computing model.⁸⁸ This theoretical information could contain: the reaction mechanism, the main reaction pathways, the rate-determining steps (RDS), the most abundant intermediates, and the kinetic parameters themselves. By performing sensitivity analyses with the microkinetic model, such as the degree of rate control (DRC),⁸⁴ rate-determining steps (RDS) can be identified, and global reaction rate equations can be derived.

In this chapter, three formal kinetic models are derived from the previously developed microkinetic model:

- Model-1p: the kinetic parameters of the microkinetic model are considered, and only a single parameter is fitted to the experimental data
- Model-9p: the kinetic parameters are lumped and refitted to the experimental data (totalizing nine parameters)
- Model-6p: the kinetic parameters are also lumped and refitted, but direct CO hydrogenation is not considering (totalizing six parameters)

All three proposed models are compared with state-of-the-art literature models.^{34, 41}

3.2 Development of the kinetic models

In this section, the derivation of the models and the parameter estimation are described.

3.2.1 Model-1p: direct reduction of the microkinetic model

In our recent work,⁷⁰ a microkinetic model for the methanol synthesis and the WGS was proposed based on first principles Density Functional Theory (DFT) calculations.^{18, 54} The model consists in a total of 25 reversible reactions and 23 surface species, and has a three-site approach: two for carbon-containing compounds (site a, pure Cu; site b, Cu/Zn) and one exclusively for hydrogen and water adsorption (site c). Five main reaction pathways were considered, which are described in Table S1.

In Model-1p, global reactions were derived from the elementary reactions listed in Table S1 by assuming rate-determining steps (RDS) for each reaction path. From the DRC analysis, our findings showed that $\text{HCO}_{(a)}$ formation (R_{11}) is the most sensitive step of CO

hydrogenation.⁷⁰ By considering R₁₁ as the RDS, and assuming the other elementary steps to be in equilibrium, the reaction rate for CO hydrogenation was derived:

$$\dot{r}_{CO} = n_{M,Cat} \cdot k_{11}^+ \cdot (1 - \phi_{Zn}) \cdot \theta_a \cdot \theta_c \cdot K_1 \cdot K_2 \cdot K_{10} \cdot f_{H_2} \cdot f_{CO} \cdot \left(1 - \frac{f_{CH_3OH}}{f_{H_2}^2 \cdot f_{CO} \cdot K_{P,CO\,hyd.}^0}\right) \quad (3.1)$$

Where $n_{M,Cat}$ is the quantity of active sites (mol·kg_{cat}⁻¹), k_{11}^+ is the kinetic constant of the forward reaction 11 (s⁻¹), ϕ_{Zn} is the zinc coverage on the catalyst surface, θ_a and θ_c are the surface coverage of free sites (a) and (c), respectively, K_k is the equilibrium constant of elementary reaction k, f_j is the fugacity of gas component j, and $K_{P,CO\,hyd.}^0$ is the equilibrium constant of the global CO hydrogenation. The fugacities of the gases are given in bars, so that the division by the reference pressure (1 bar) can be omitted.

CO₂ hydrogenation is only active on site (b),¹⁸ and formic acid (HCOOH_(b)) hydrogenation (R₁₇) is the most sensitive step of CO₂ hydrogenation, according to our DRC analysis.⁷⁰ Therefore, the reaction rate of the CO₂ hydrogenation is:

$$\dot{r}_{CO_2} = n_{M,Cat} \cdot k_{17}^+ \cdot \phi_{Zn} \cdot \theta_b \cdot \theta_c \cdot K_1^{1.5} \cdot K_5 \cdot K_{13} \cdot K_{15} \cdot f_{H_2}^{1.5} \cdot f_{CO} \cdot \left(1 - \frac{f_{CH_3OH} \cdot f_{H_2O}}{f_{H_2}^3 \cdot f_{CO_2} \cdot K_{P,CO_2\,hyd.}^0}\right) \quad (3.2)$$

Where θ_b is the surface coverage of free sites (b).

According to our DRC analysis, the carboxyl formation (COOH*) (R₂₄ and R₂₅) are the most sensitive steps for the reverse WGSR (rWGSR) on sites (a) and (b), respectively, and $k_{24}^- = k_{25}^-$.⁷⁰ The reaction rate of the rWGSR (sum of the reactions happening on both sites) is:

$$\dot{r}_{rWGSR} = n_{M,Cat} \cdot k_{24}^- \cdot \theta_c \cdot K_8 \cdot [(1 - \phi_{Zn}) \cdot \theta_a \cdot K_4 + \phi_{Zn} \cdot \theta_b \cdot K_5] \cdot f_{CO_2} \cdot f_{H_2O} \cdot \left(1 - \frac{f_{CO} \cdot f_{H_2O}}{f_{H_2} \cdot f_{CO_2} \cdot K_{P,rWGSR}^0}\right) \quad (3.3)$$

One might find strange that water is positively influencing the rWGSR. But this is because of considering the water-assisted carboxyl mechanism (see Table S2.1, Section S2.1 of the SM). Detailed mathematical derivation of the global kinetic equations from the elementary reactions is available in the SM (Section S2.1).

The fugacity coefficients were calculated through the Peng-Robinson Equation,⁶⁶ using binary interaction parameters and other necessary information from literature,^{67, 68} including an effective hydrogen acentric factor of -0.05.⁶⁹ The reaction rate and equilibrium constants were calculated as follows:

$$k_k^+ = \frac{k_b}{h} \cdot T^{(1+\beta_k^+)} \cdot \exp\left[\frac{\Delta S_k^{\ddagger,+}}{R} - \frac{E_{A,k}^+}{R \cdot T}\right] \quad (3.4)$$

$$K_k = \frac{k_k^+}{k_k^-} = T^{(\beta_k^+ - \beta_k^-)} \cdot \exp \left[\frac{(\Delta S_k^{\ddagger,+} - \Delta S_k^{\ddagger,-})}{R} - \frac{(E_{A,k}^+ - E_{A,k}^-)}{R \cdot T} \right] \quad (3.5)$$

$$K_{P,m}^0 = \exp \left(\frac{-\Delta G_{Reaction\ m}^0}{R \cdot T} \right) = \exp \left[-\frac{1}{R} \cdot \left(\frac{A_{1,m}}{T} + A_{2,m} + A_{3,m} \cdot \ln T \right) \right] \quad (3.6)$$

Here, k_b is the Boltzmann constant, h is the Planck constant, β is a constant used due to the thermodynamic consistency process,^{70, 73, 74} ΔS^\ddagger is the entropy barrier, E_A is the activation energy, $\Delta G_{Reaction\ m}^0$ is the free Gibbs energy variation of the global reaction, and $A_{1-3,m}$ are estimated parameters for the equilibrium constant.^{70, 75} The subscripts “+” and “-” refer to forward and reverse reaction k , respectively.

The free sites (a), (b) and (c) were calculated from the sites balance equations (Eqs. 3.7-3.9). The simulations with the microkinetic model showed that only $CO_{(a)}$, $HCOO_{(a)}$, $HCOO_{(b)}$, $H_3CO_{(b)}$, $H_{(c)}$, $OH_{(c)}$, (a), (b), and (c) have significant coverage values.⁷⁰ That is, 0.05 or more in at least one of the various conditions tested. Therefore, the other species were neglected in the sites balance.

$$\theta_a = (K_2 \cdot f_{CO} + K_1^{0.5} \cdot K_4 \cdot K_{12} \cdot f_{H_2}^{0.5} \cdot f_{CO_2} + 1)^{-1} \quad (3.7)$$

$$\theta_b = (K_1^{0.5} \cdot K_5 \cdot K_{13} \cdot f_{H_2}^{0.5} \cdot f_{CO_2} + K_1^{-0.5} \cdot K_7^{-1} \cdot f_{H_2}^{-0.5} \cdot f_{CH_3OH} + 1)^{-1} \quad (3.8)$$

$$\theta_c = (K_1^{0.5} \cdot f_{H_2}^{0.5} + K_1^{-0.5} \cdot K_8 \cdot K_9 \cdot f_{H_2}^{-0.5} \cdot f_{H_2O} + 1)^{-1} \quad (3.9)$$

It is also known that the surface of Cu/Zn-based catalysts changes depending on the operating conditions (i.e. gas composition and temperature), and the zinc coverage generally decreases with an increase in the CO_2 to CO_x ratio ($CO_x = CO + CO_2$).⁴³

Ovesen et al.⁷⁷ proposed a method to estimate the zinc coverage based on Wulff constructions, in which a parameter has to be fitted to the experiments. Kuld et al.⁴⁵ proposed a detailed method to describe the zinc coverage based on DFT calculations, which takes different effects into account (e.g. lower atom coordination in ZnO nanoparticles, Zn-Zn interaction energy reducing the segregation energies...). With this second method, the computational effort to solve the model is significantly increased, due to the need to numerically solve a highly non-linear equation at each integration step. In the microkinetic model,⁷⁰ the estimation of the zinc coverage (ϕ_{Zn}) was initially based on the method developed by Kuld et al.⁴⁵ but later on a third method was recommended instead, because it led to a more accurate simulation of the experiments.^{70, 78}

The third method consists in giving constant zinc coverage values depending on the CO_2 to CO_x ratio in feed mixture, named here $\bar{y}_{CO_2,0}$. The reference case is equal amounts of active copper and zinc on the surface ($\phi_{Zn} = 0.50$). For the case without CO_2 in feed ($\bar{y}_{CO_2,0} \leq 0.001$), an upper limit of $\phi_{Zn} = 0.95$ is settled.⁷⁰ Finally, for the case of very high CO_2 in feed ($\bar{y}_{CO_2,0} > 0.90$), a lower limit of $\phi_{Zn} = 0.10$ is given. The different methods were tested with the new formal kinetic models, and the experiments were more accurately

simulated with the third method. Since this method has the lowest computational costs and does not require extra fitting parameters, it was chosen for the kinetic models presented here.

The Model-1p is a reduced version of the microkinetic mechanism, being also based on data from DFT calculations. Therefore, only one parameter, the quantity of active sites ($n_{M,cat}$), was estimated with experimental data. All other parameters, summarized in Table S2.3, were directly transferred from the microkinetic model.⁷⁰

3.2.2 Model-9p: fitting the lumped parameters

In Model-9p, the same reaction network of Model-1p was considered, but the parameters were lumped and fitted to experiments instead of taken from DFT calculations. The objective of setting up this model was to correlate the simulations and experimental data with the smallest deviation possible. In order to reduce the number of parameters to be estimated, beta terms of Eqs. (3.4-3.5) were removed ($\beta_k^+, \beta_k^- = 0$), as they are not necessary here to ensure the thermodynamic consistency of the model. The derived reaction rate equations (Eqs. 3.10-3.12) are as follows:

$$\dot{r}_{CO} = \exp\left(A_1 - \frac{E_{A,1}}{R \cdot T}\right) \cdot (1 - \phi_{Zn}) \cdot \theta_a \cdot \theta_c \cdot f_{H_2} \cdot f_{CO} \cdot \left(1 - \frac{f_{CH_3OH}}{f_{H_2}^2 \cdot f_{CO} \cdot K_{P,CO}^0 \text{ hyd.}}\right) \quad (3.10)$$

$$\dot{r}_{CO_2} = \exp\left(A_2 - \frac{E_{A,2}}{R \cdot T}\right) \cdot \phi_{Zn} \cdot \theta_b \cdot \theta_c \cdot f_{H_2}^{1.5} \cdot f_{CO} \cdot \left(1 - \frac{f_{CH_3OH} \cdot f_{H_2O}}{f_{H_2}^3 \cdot f_{CO_2} \cdot K_{P,CO_2}^0 \text{ hyd.}}\right) \quad (3.11)$$

$$\dot{r}_{rWGSr} = \exp\left(A_3 - \frac{E_{A,3}}{R \cdot T}\right) \cdot \theta_c \cdot [(1 - \phi_{Zn}) \cdot \theta_a + \phi_{Zn} \cdot \theta_b] \cdot f_{CO_2} \cdot f_{H_2O} \cdot \left(1 - \frac{f_{CO} \cdot f_{H_2O}}{f_{H_2} \cdot f_{CO_2} \cdot K_{P,rWGSr}^0}\right) \quad (3.12)$$

Here, A_{1-3} are pre-exponential factors and $E_{A,1-3}$ are global activation energies, which are parameters to be fitted to the experiments and correspond to the lumping of the following terms (contained in Model-1p):

$$A_1 = \ln\left(n_{M,cat} \cdot \frac{k_b}{h}\right) + \frac{\Delta S_{11}^{\ddagger,+} + \Delta S_1^{\ddagger,+} - \Delta S_1^{\ddagger,-} + \Delta S_2^{\ddagger,+} - \Delta S_2^{\ddagger,-} + \Delta S_{10}^{\ddagger,+} - \Delta S_{10}^{\ddagger,-}}{R} \quad (3.13)$$

$$A_2 = \ln\left(n_{M,cat} \cdot \frac{k_b}{h}\right) + \frac{\Delta S_{17}^{\ddagger,+} + 1.5 \cdot (\Delta S_1^{\ddagger,+} - \Delta S_1^{\ddagger,-}) + \Delta S_5^{\ddagger,+} - \Delta S_5^{\ddagger,-}}{R} + \frac{\Delta S_{13}^{\ddagger,+} - \Delta S_{13}^{\ddagger,-} + \Delta S_{15}^{\ddagger,+} - \Delta S_{15}^{\ddagger,-}}{R} \quad (3.14)$$

$$A_3 = \ln\left(n_{M,cat} \cdot \frac{k_b}{h}\right) + \frac{\Delta S_{24}^{\ddagger,-} + \Delta S_8^{\ddagger,+} - \Delta S_8^{\ddagger,-} + \Delta S_4^{\ddagger,+} - \Delta S_4^{\ddagger,-}}{R} \quad (3.15)$$

$$E_{A,1} = \frac{E_{A,11}^+ + E_{A,1}^+ - E_{A,1}^- + E_{A,2}^+ - E_{A,2}^- + E_{A,10}^+ - E_{A,10}^-}{R} \quad (3.16)$$

$$E_{A,2} = \frac{E_{A,17}^{\pm,+} + 1.5 \cdot (E_{A,1}^+ - E_{A,1}^-) + E_{A,5}^+ - E_{A,5}^- + E_{A,13}^+ - E_{A,13}^- + E_{A,15}^+ - E_{A,15}^-}{R} \quad (3.17)$$

$$E_{A,3} = \frac{E_{A,24}^- + E_{A,8}^+ - E_{A,8}^- + E_{A,4}^+ - E_{A,4}^-}{R} \quad (3.18)$$

From the microkinetic model simulations,⁷⁰ it was seen that CO_(a), H₃CO_(b) and H_(c) rarely achieve coverages greater than 0.07, and therefore, have limited influence in the sites balance when compared to HCOO_(a), HCOO_(b), OH_(c). Therefore, in order to further reduce the number of parameters to be estimated, only HCOO_(a), HCOO_(b), OH_(c), (a), (b), and (c) were considered in the sites balance, described as follows.

$$\theta_a = (\bar{K}_1 \cdot f_{H_2}^{0.5} \cdot f_{CO_2} + 1)^{-1} \quad (3.19)$$

$$\theta_b = (\bar{K}_2 \cdot f_{H_2}^{0.5} \cdot f_{CO_2} + 1)^{-1} \quad (3.20)$$

$$\theta_c = (\bar{K}_3 \cdot f_{H_2}^{-0.5} \cdot f_{H_2O} + 1)^{-1} \quad (3.21)$$

Where \bar{K}_{1-3} are the lumped parameters related to the formation of HCOO_(a), HCOO_(b), and OH_(c), which need to be estimated. These parameters, often called adsorption constants, represent the following elementary equilibrium constants (contained in Model-1p):

$$\bar{K}_1 = K_1^{0.5} \cdot K_4 \cdot K_{12} \quad (3.22)$$

$$\bar{K}_2 = K_1^{0.5} \cdot K_5 \cdot K_{13} \quad (3.23)$$

$$\bar{K}_3 = K_1^{-0.5} \cdot K_8 \cdot K_9 \quad (3.24)$$

Elementary equilibrium constants are usually described by exponential Arrhenius type expressions ($e^{a+b/T}$), with a and b as constants. After testing this expression for \bar{K}_{1-3} and finding out that the b parameters were not significant, single constants ($A = e^a$) were used instead. Adsorption constants without temperature dependency have also been applied in recently published models.^{34, 41}

In Model-9p, nine parameters had to be fitted to the experiments: the pre-exponential factors A_{1-3} , the activation energies $E_{A,1-3}$, and the adsorption constants \bar{K}_{1-3} .

3.2.3 Model-6p: CO hydrogenation not considered

From simulations of the microkinetic model, it was concluded that the contribution of CO direct hydrogenation to the methanol synthesis is only significant at low CO₂ content in feed, because formate (an intermediate species derived from CO₂) binds strongly on the copper surface, almost completely inhibiting CO hydrogenation.^{18, 70} Therefore, we developed a simplified model (without considering CO hydrogenation) to simulate the methanol synthesis

with feeds containing CO₂, and compared with the model with all three reactions (Eqs. 1.1-1.3).

The alternative Model-6p is a reduced version of Model-9p for CO₂-containing feed ($\bar{y}_{CO_2,0} \geq 0.001$), considering only CO₂ hydrogenation and the rWGSr (Eqs. 1.2-1.3). It had initially seven parameters to be estimated (A_{2-3} , $E_{A,2-3}$, \bar{K}_{1-3}). In this re-parametrization, \bar{K}_1 tends to infinite, and, consequently, θ_a tends to zero. This is probably because CO hydrogenation is not considered, which happens on site a, contributing to the reduction in the statistical significance of \bar{K}_1 . Therefore, the model was further reduced to six parameters (\bar{K}_1 is removed), which were re-estimated. The final reaction rates are described as follows.

$$\dot{r}_{CO_2} = \exp\left(A_2 - \frac{E_{A,2}}{R \cdot T}\right) \cdot \phi_{Zn} \cdot \theta_b \cdot \theta_c \cdot f_{H_2}^{1.5} \cdot f_{CO} \cdot \left(1 - \frac{f_{CH_3OH} \cdot f_{H_2O}}{f_{H_2}^3 \cdot f_{CO_2} \cdot K_{P,CO_2}^{hyd.0}}\right) \quad (3.25)$$

$$\dot{r}_{rWGSr} = \exp\left(A_3 - \frac{E_{A,3}}{R \cdot T}\right) \cdot \theta_b \cdot \theta_c \cdot \phi_{Zn} \cdot f_{CO_2} \cdot f_{H_2O} \cdot \left(1 - \frac{f_{CO} \cdot f_{H_2O}}{f_{H_2} \cdot f_{CO_2} \cdot K_{P,rWGSr}^0}\right) \quad (3.26)$$

In Model-6p, six parameters were estimated: the pre-exponential factors A_{2-3} , the activation energies $E_{A,2-3}$, and the adsorption constants \bar{K}_{2-3} .

3.2.4 Reactor modeling and parameter estimation

An experimental database from three different sources was used,^{34, 41, 70} consisting of 557 data points. 80% of the data from each source was randomly selected as training experiments for parameter estimation, while the remaining 20% were used only for model validation. The operating conditions of the experiments are listed in Table 3.1, and it was reported that no significant amounts of side products were detected. Therefore, side reactions are neglected in the kinetic models.

Table 3.1. Operating conditions of the different setups considered. Reproduced with permission from Campos et al.⁸⁹. Copyright 2021, American Chemical Society.

Database	Pressure (bar)	Temperature (°C)	GHSV (L h ⁻¹ g _{cat.} ⁻¹)	Feed conc. (% v/v)			
				H ₂	CO	CO ₂	N ₂
Campos ⁷⁰	40 – 60	210 – 260	24 – 40	20 – 60	3 – 30	1.3 – 20	20 – 50
Seidel ³⁴	30 – 70	230 – 260	3.6	60 – 76	0 – 21	0 – 13	15 – 16
Slotboom ⁴¹	20 – 50	178 – 260	1.3 – 6.5	66 – 80	0	12 – 25	0 – 11

The experiments reported by Campos et al.⁷⁰ and Slotboom et al.⁴¹ were performed in a fixed-bed tube reactor. Since the reactors used are thin (12 and 6 mm respectively) and solid inert was used to dilute the catalyst, isothermal operation was considered (variations smaller

than 2 K are reported). As the catalyst particles are significantly small ($c_p \leq 500 \mu\text{m}$), mass transfer limitations were neglected. The influence of back-mixing is also neglected (assumption of plug flow reactor, PFR), and only variations along the reactor length were considered.

Derived from mass balances, ordinary differential equations describe the total mole flow (\dot{n}) and the mole fractions of each gas component i (y_i) along the reactor length (L):

$$\frac{d\dot{n}}{dz} = \frac{m_{cat}}{L} \cdot (-2 \cdot r_{CO} - 2 \cdot r_{CO_2}) \quad (3.27)$$

$$\frac{dy_i}{dz} = \frac{m_{cat}}{L \cdot \dot{n}} \cdot \sum_{k=1}^3 (v_{i,k} \cdot r_k) - y_i \cdot \frac{d\dot{n}}{dz} \quad (3.28)$$

Where m_{cat} is the total catalyst mass in the reactor, and $v_{i,k}$ is the stoichiometric gain of gas component i in reaction k . The integration of Eqs. (3.27-3.28) along the reactor length is made with Matlab function *ode45*, with absolute and relative tolerances of 10^{-8} .

The experiments reported by Seidel et al.³⁴ were performed in a modified CSTR (Micro-Berty reactor type). Perfect mixture was assumed, and heat and mass transfer limitations are neglected. Applying global and component mass balances, the following algebraic equations were obtained:

$$\dot{n}_{out} = \dot{n}_{in} + m_{cat} \cdot (-2 \cdot r_{CO} - 2 \cdot r_{CO_2}) \quad (3.29)$$

$$\dot{n}_{in} \cdot y_{i,in} - \dot{n}_{out} \cdot y_{i,out} + m_{cat} \cdot \sum_{k=1}^3 (v_{i,k} \cdot r_k) = 0 \quad (3.30)$$

Here, the subscript *in* and *out* refer to the flow entering and leaving the reactor, respectively. This non-linear algebraic system was solved with Matlab function *fsolve*, with a tolerance for both the function and the variables of 10^{-8} .

In order to estimate the kinetic parameters of each model, an optimization problem is created. Its objective function is the minimization of the normalized squared errors of the prediction of the carbon-containing compounds (CO, CO₂, and CH₃OH), the so-called chi-square (χ^2) regression method (Eq. 3.31). The normalization with the inverse of the squared experimental values gives a better weight distribution of the points.^{79, 80} For points without CO₂ in feed, only the error of CO and CH₃OH are considered.

$$\chi^2 = \sum_{i=1}^{N_p} \left[\frac{(y_{CO,out}^i - \hat{y}_{CO,out}^i)^2}{(y_{CO,out}^i)^2} + \frac{(y_{CH_3OH,out}^i - \hat{y}_{CH_3OH,out}^i)^2}{(y_{CH_3OH,out}^i)^2} \right] + \sum_{i=1}^{N_p^*} \left[\frac{(y_{CO_2,out}^i - \hat{y}_{CO_2,out}^i)^2}{(y_{CO_2,out}^i)^2} \right] \quad (3.31)$$

Here, N_p is the total number of points, N_p^* is the number of points with CO₂ in feed, $y_{j,out}^i$ is the experimental value of the output mole fraction of gas j in point i , and $\hat{y}_{j,out}^i$ is the simulated value of the output mole fraction of gas j in point i .

The optimization problem was solved with the Matlab function *fmincon* in order to constraint the variables to positive values, with a tolerance for both the function and the variables of 10^{-3} . For Model-1p, the first initial guess of $n_{M,Cat}$ is the value reported in the microkinetic model ($2 \text{ mol} \cdot \text{kg}_{cat}^{-1}$), while for Model-6p and Model-9p the initial guesses of the parameters are taken by deducing them from Model-1p (Eqs. 3.13-3.18 and Eqs. 3.22-3.24).

In an effort to find the global optimum and not only a local optimum solution, the optimization problem is solved many times, each time changing the initial guesses of multiple variables simultaneously.

The confidence interval of each parameter is obtained with the Matlab function *nlparci*, considering a valid t-distribution and 95% confidence. The mean squared error values for all points (*MSE*) are calculated as follows.

$$MSE = \frac{1}{2 \cdot N_p + N_p^*} \cdot \left\{ \sum_{i=1}^{N_p} \left[\frac{(y_{CO,out}^i - \hat{y}_{CO,out}^i)^2}{(y_{CO,out}^i)^2} + \frac{(y_{CH_3OH,out}^i - \hat{y}_{CH_3OH,out}^i)^2}{(y_{CH_3OH,out}^i)^2} \right] + \sum_{i=1}^{N_p^*} \left[\frac{(y_{CO_2,out}^i - \hat{y}_{CO_2,out}^i)^2}{(y_{CO_2,out}^i)^2} \right] \right\} \quad (3.32)$$

The new developed kinetic models are compared with the most accurate literature models (according to a recent model comparison⁴¹), which are the models of Seidel et al.³⁴ and Slotboom et al.⁴¹. The parameters of these literature models are re-estimated according to the procedure described above, in order to ensure a fair comparison. In the model of Seidel et al.,³⁴ some variables are allowed to be negative, due to the modified Arrhenius equation and the zinc coverage estimation. Kinetic parameters previously reported by the authors are used as initial guesses, and the procedure of solving the optimization many times by changing the initial guesses is repeated here.

Details of the parameter estimation of all models are summarized in Table 3.2. The parameters of the model of Slotboom et al.⁴¹ were re-estimated two times: once with all points (Slotboom A) (for comparison with Model-1p and 9p) and once with points in which $\bar{y}_{CO_2,0} \geq 0.001$ (Slotboom B) (for comparison with Model-6p).

3.3 Results and discussion

The new developed models and the literature models^{34, 41} were implemented, and the estimation of the parameters was successful. The discussion was divided between models considering the whole operating region (Model-1p Model-9p, Seidel, Slotboom A), and those models considering feeds containing CO₂ (Model-6p, Slotboom B).

Table 3.2. Estimated parameters and considered experimental data for each model. Reproduced with permission from Campos et al.⁸⁹. Copyright 2021, American Chemical Society.

Model	N° of Par.	Parameter description	N° of points		Considered database
			Train.	Valid.	
Model-1p	1	$n_{M,Cat}$	445	112	All points
Model-6p	6	$A_{2-3}, E_{A,2-3}, \bar{K}_{2-3}$	397	99	Only points with $\bar{y}_{CO_2,0} \geq 0.001$
Model-9p	9	$A_{1-3}, E_{A,1-3}, \bar{K}_{1-3}$	445	112	All points
Seidel	12	$k_{CO}(A, B), k_{CO_2}(A, B), k_{rWGSR}(A, B), K_{CO}, \frac{K_{H_2O}K_O}{K_{H_2}}, K_{CO_2}, K_{H_2O}, \sqrt{K_{H_2}}, \Delta G_3$	445	112	All points
Slotboom A	6	$k_{CO_2}(a, b), k_{rWGSR}(a, b), K_{H_2}, K_{H_2O/9}$	445	112	All points
Slotboom B	6	$k_{CO_2}(a, b), k_{rWGSR}(a, b), K_{H_2}, K_{H_2O/9}$	397	99	Only points with $\bar{y}_{CO_2,0} \geq 0.001$

3.3.1 Models considering the whole operating region

In Table 3.3, statistics of the kinetic model regressions considering the whole operating region ($0 \leq \bar{y}_{CO_2,0} \leq 1$) are summarized. Model-1p has expectedly the highest χ^2 (69.3), as it only has one fitted parameter. However, the greatest part of χ^2 is concentrated on specific operating conditions, such as H₂/CO in feed ($\chi^2 = 9.6$ for 61 points) and particularly H₂/CO₂ in feed ($\chi^2 = 45.5$ for 126 points), while for mixed feed conditions (H₂/CO/CO₂ in feed) the experiments are predicted adequately ($\chi^2 = 14.1$ for 370 points). In the latter conditions, the χ^2 of Model-1p is similar to the one of the microkinetic model (13.6), and less than one third of the χ^2 of Slotboom et al.⁴¹ (47.2), which has five more fitted parameters (six in total). The performance of Model-1p at mixed feed conditions is even comparable to the 12-parameter model of Seidel et al.³⁴ ($\chi^2 = 9.0$).

Model-9p simulates the whole range of conditions with low errors ($\chi^2 = 22.3$), similarly to that of Seidel et al.³⁴ ($\chi^2 = 24.7$), although the latter has three fitted parameters more (12 in total). Looking into the different conditions separately, Model-9p excels at mixed feed conditions ($MSE = 0.0066$), but also performs well at H₂/CO ($MSE = 0.0280$) and H₂/CO₂ feed conditions ($MSE = 0.0304$).

For all considered models, the MSE of the training set is relatively close to its respective MSE of the validation set, suggesting that interpolations inside the validated operating region are consistent.

In Fig. 3.1 and Fig. 3.2, parity plots of Model-1p and Model-9p are shown, respectively. From Fig. 3.1d and 3.1e, it can be seen that Model-1p shows discrepancies in the simulation of methanol output concentration at conditions with H₂/CO or H₂/CO₂ in feed. However,

Model-1p accurately simulates mixed feed experiments, with most of these points being inside the $\pm 20\%$ lines (99% of CO, 100% of CO₂, and 73% of CH₃OH points).

Table 3.3. Comparison of statistical values for the different kinetic models that consider the whole studied operating region ($0 \leq \bar{y}_{CO_2,0} \leq 1$). Reproduced with permission from Campos et al.⁸⁹. Copyright 2021, American Chemical Society.

	Model-1p	Model-9p	Microkinetic ^a	Slotboom A	Seidel
Number of fitted parameters	1	9	1	6	12
χ^2 – All Points (557 pts)	69.3	22.3	–	62.6	24.7
χ^2 – Feed: H ₂ /CO (61 pts)	9.6	3.4	9.3	5.1	4.1
χ^2 – Feed: H ₂ /CO/CO ₂ (370 pts)	14.1	7.4	13.6	47.2	9.0
χ^2 – Feed: H ₂ /CO ₂ (126 pts)	45.5	11.5	35.3	10.3	11.6
$\chi^2_{\text{Orig.Par.}}$ – All Points (557 pts)	–	–	58.2	270.9	144.2
MSE – All Points (557 pts)	0.0430	0.0138	0.0361	0.0387	0.0153
MSE – Feed: H ₂ /CO (61 pts)	0.0781	0.0280	0.0764	0.0414	0.0339
MSE – Feed: H ₂ /CO/CO ₂ (370 pts)	0.0127	0.0066	0.0123	0.0425	0.0081
MSE – Feed: H ₂ /CO ₂ (126 pts)	0.1200	0.0304	0.0934	0.0274	0.0306
MSE – Training (80% of the pts)	0.0398	0.0131	–	0.0395	0.0142
MSE – Validation (20% of the pts)	0.0557	0.0167	–	0.0363	0.0198

^a No parameter re-estimation is made for the microkinetic model.

In Fig. 3.2, it is shown that Model-9p simulations are in good agreement with the experiments in the whole range of conditions, with 93% of CO, 100% of CO₂, and 79% of CH₃OH points being inside the $\pm 20\%$ lines. Parity plots of the literature models considered in this work are available in the SM (Sections S2.2 and S2.3).

Experimental and simulated data of methanol output concentration at different operating conditions are shown in Fig. 3.3-3.5. Model-1p accurately predicts trends at low CO₂/CO_x feed concentration ($\bar{y}_{CO_2,0}$), either at low CO_x conversion (Fig. 3.3a and 3.3b) or at high CO_x conversion (Fig. 3.4a and 3.4b). By higher $\bar{y}_{CO_2,0}$, underestimations at low temperature and overestimations at high temperature are recognized, with small deviations at $\bar{y}_{CO_2,0} = 0.50$ (Fig. 3.3c), and higher deviations at $\bar{y}_{CO_2,0} \geq 0.70$ (Fig. 3.3d and 3.5a). Still, the model correctly

describes conditions of $\bar{y}_{CO_2,0} = 1$ at low temperature (220 °C, Fig. 3.5b). In general, the trends simulated by Model-1p look similar to those of the underlying microkinetic model. This confirms that the model reduction was successful, and most of the theoretical information was kept in the new model.

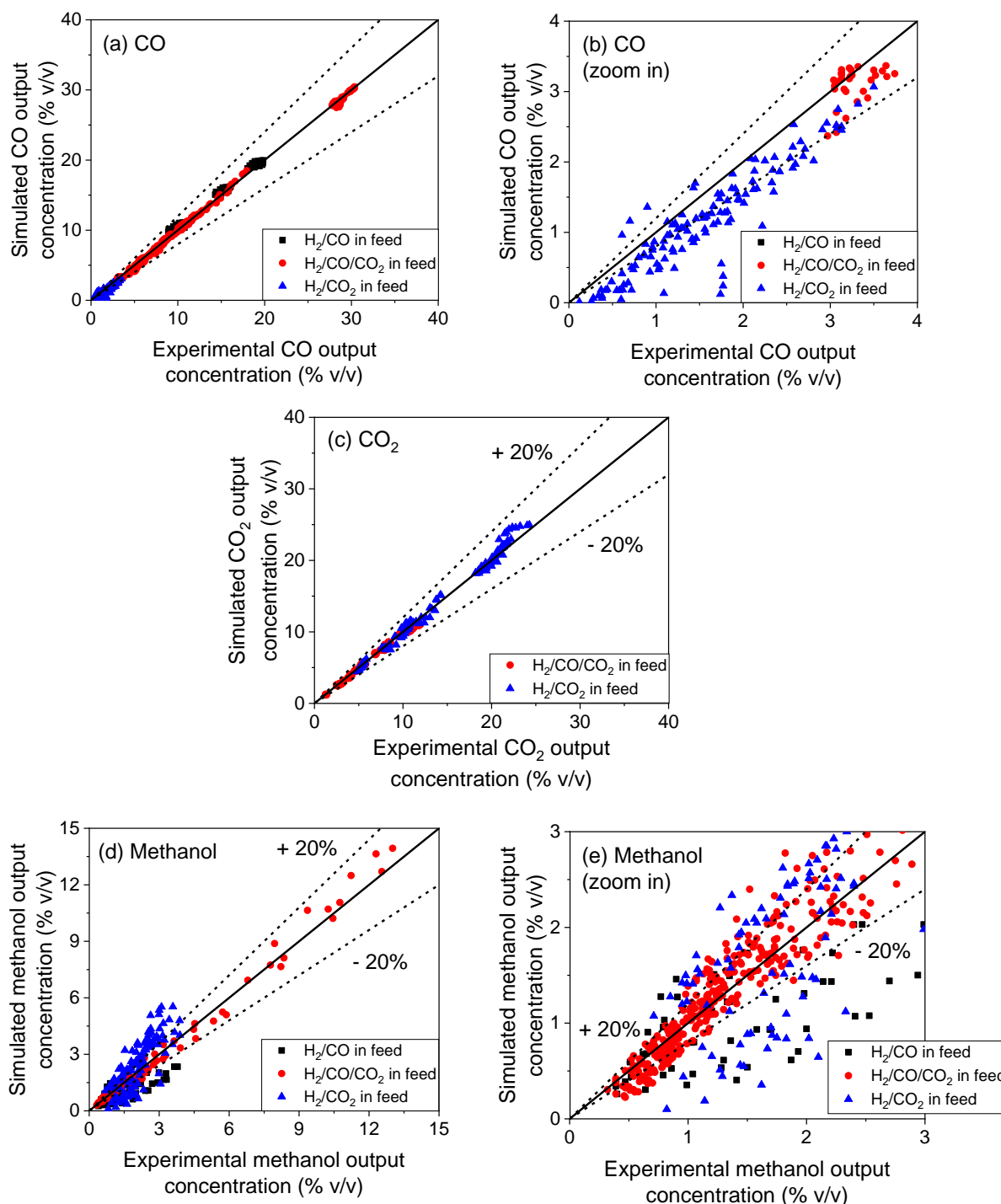


Fig. 3.1 Parity plots of Model-1p for measured and predicted CO (a-b), CO₂ (c) and methanol (d-e) concentrations in the product stream. Experimental conditions are reported in Table 3.1. Reproduced with permission from Campos et al.⁸⁹. Copyright 2021, American Chemical Society.

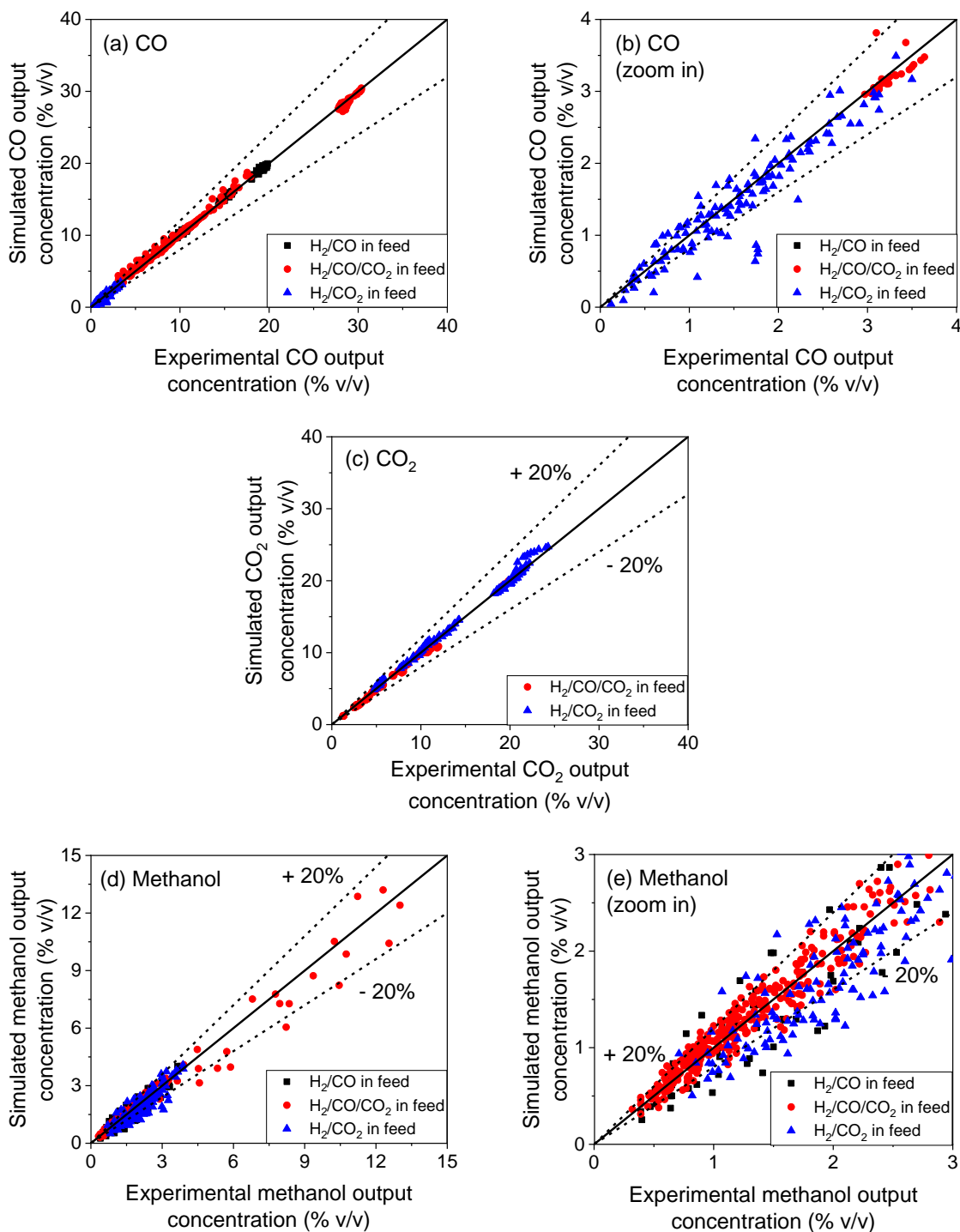


Fig. 3.2 Parity plots of Model-9p for measured and predicted CO (a-b), CO₂ (c) and methanol (d-e) concentrations in the product stream. Experimental conditions are reported in Table 3.1. Reproduced with permission from Campos et al.⁸⁹. Copyright 2021, American Chemical Society.

The reparametrized model of Slotboom et al.⁴¹ (Slotboom A) shows reasonable agreement to experimental data at low CO_x conversion (Fig. 3.3 and Fig. 3.5), with some underestimations, as in Fig. 3.3a and 3.3d, and some overestimations, like in Fig. 3.5b. At high CO_x conversion, however, there are high systematic deviations (see Fig. 3.4a-b).

Both Model-9p and model of Seidel et al.³⁴ show excellent agreement at low CO_x conversion (Fig. 3.3), and reasonable agreement at $\bar{y}_{CO_2,0} = 1$ (Fig. 3.5). At high CO_x conversion (Fig. 3.4), some underestimations are seen in both cases, with the simulations of the Model-9p being closer to the experimental data.

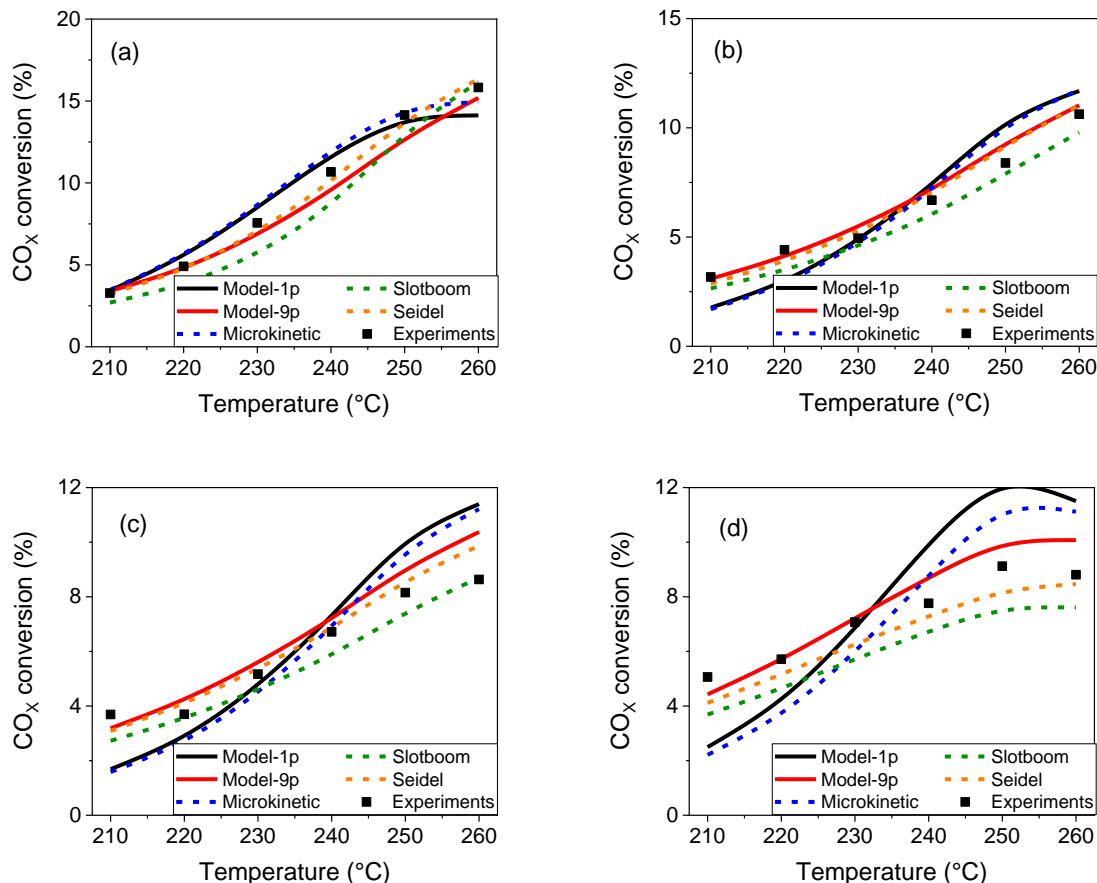


Fig. 3.3 CO_x conversion: simulation vs. experiments reported by Campos et al.⁷⁰. Conditions: All experiments were performed at 41 bar. (a) GHSV = 24 L·h⁻¹·g_{cat}⁻¹, H₂/CO/CO₂ (feed) = 45.3/11.7/2.7% v/v. (b) GHSV = 40 L·h⁻¹·g_{cat}⁻¹, H₂/CO/CO₂ (feed) = 45.3/8.9/5.6% v/v. (c) GHSV = 40 L·h⁻¹·g_{cat}⁻¹, H₂/CO/CO₂ (feed) = 45.2/8.9/8.8% v/v. (d) GHSV = 24 L·h⁻¹·g_{cat}⁻¹, H₂/CO/CO₂ (feed) = 45.2/4.3/10.4% v/v. Reproduced with permission from Campos et al.⁸⁹. Copyright 2021, American Chemical Society.

3.3.2 Models considering operation with CO₂ in feed

In Table 3.4, statistics for Model-6p and the Slotboom B model are summarized. Model-6p had a $\chi^2 = 16.9$ for the 496 data points, which is less than half the value of Slotboom B ($\chi^2 = 42.2$). While their performance is similar at H₂/CO₂ feed conditions ($\chi^2 = 12.3$ and $\chi^2 = 12.4$, respectively), significantly different simulation results are seen in the mixed feed conditions, with Model-6p showing a superior performance ($\chi^2 = 4.7$) in comparison with Slotboom B ($\chi^2 = 29.9$).

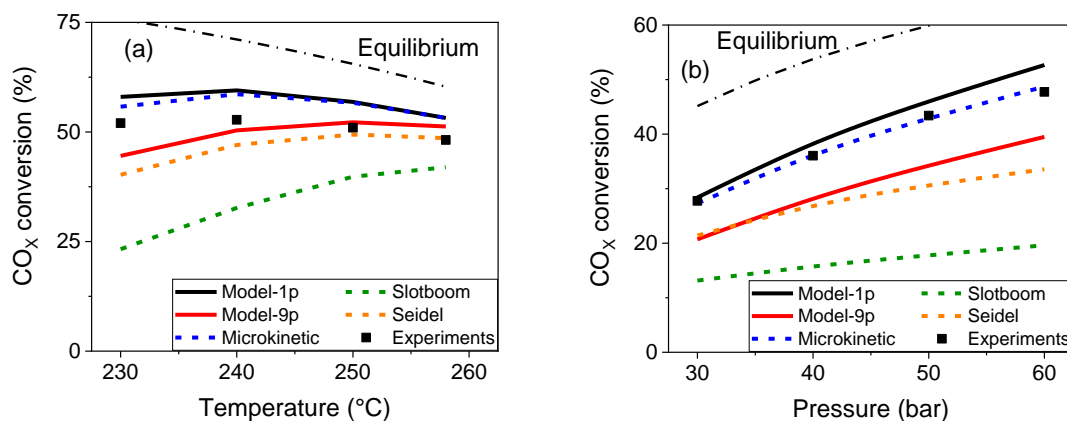


Fig. 3.4 CO_x conversion: simulation vs. experiments reported by Seidel et al.³⁴. All experiments are at GHSV = 3.6 L·h⁻¹·g_{cat}⁻¹. (a) 60 bar, H₂/CO/CO₂ (feed) = 69.5/11.6/3.2% v/v. (b) 230 °C, H₂/CO/CO₂ (feed) = 69.6/8.2/5.7% v/v. Reproduced with permission from Campos et al.⁸⁹. Copyright 2021, American Chemical Society.

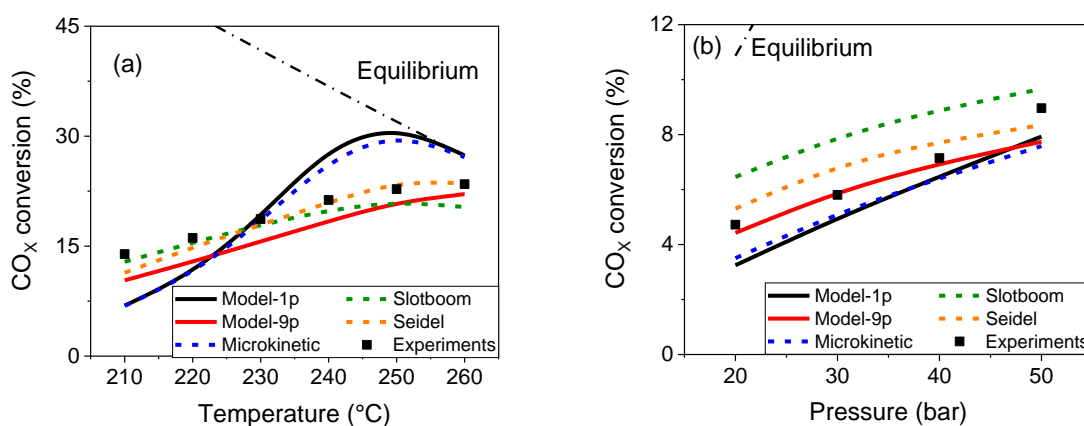


Fig. 3.5 CO_x conversion: simulation vs. experiments reported by Slotboom et al.⁴¹. All experiments are at H₂/CO₂ (feed) = 67.5/22.3%. (a) 50 bar, GHSV = 3.9 L·h⁻¹·g_{cat}⁻¹. (b) 220 °C, GHSV = 2.6 L·h⁻¹·g_{cat}⁻¹. Reproduced with permission from Campos et al.⁸⁹. Copyright 2021, American Chemical Society.

Model-6p had a similar performance to Model-9p and to Seidel's model for experiments with H₂/CO₂ in feed ($\chi_{6p}^2 = 12.3$, $\chi_{9p}^2 = 11.5$, and $\chi_{Seidel}^2 = 11.6$), and a significantly better performance at simulating mixed feed conditions ($\chi_{6p}^2 = 4.7$, $\chi_{9p}^2 = 7.4$, and $\chi_{Seidel}^2 = 9.0$). It is important to mention that Model-9p and Seidel's model are also simulating experiments with H₂/CO in feed, and, therefore, the comparison with Model-6p is not completely fair. Still, it is a remarkable performance for a model which has only six parameters, comparing with the nine parameters of Model-9p and the 12 parameters of Seidel's model.

Table 3.4. Comparison of statistical values for the models considering feeds containing CO₂ ($\bar{y}_{CO_2,0} \geq 0.001$). Reproduced with permission from Campos et al.⁸⁹. Copyright 2021, American Chemical Society.

	Model-6p	Slotboom B
Number of fitted parameters	6	6
χ^2 – All Points (496 pts)	16.9	42.2
χ^2 – Feed: H ₂ /CO/CO ₂ (370 pts)	4.7	29.9
χ^2 – Feed: H ₂ /CO ₂ (126 pts)	12.3	12.4
$\chi^2_{\text{Orig.Par.}}$ – All Points (496 pts)	-	255.3
MSE – All Points (496 pts)	0.0114	0.0284
MSE – Feed: H ₂ /CO/CO ₂ (370 pts)	0.0042	0.0269
MSE – Feed: H ₂ /CO ₂ (126 pts)	0.0325	0.0327
MSE – Training (80% of the pts)	0.0105	0.0272
MSE – Validation (20% of the pts)	0.0150	0.0332

In Fig. 3.6, parity plots of the Model-6p are shown. Deviations follow a narrow distribution, with the majority of the simulations having an error lower than $\pm 20\%$ (94% of CO, 100% of CO₂, and 86% of CH₃OH points). Parity plots of the Slotboom B model are provided in the SM (Section S2.2).

Experimental and simulated values of methanol output concentration for different operating conditions are shown in Fig. 3.7 and Fig. 3.8. Model-6p adequately predicts the trends for all operating conditions, while the Slotboom B model has significant deviations at high CO_x conversion (Fig. 3.8a).

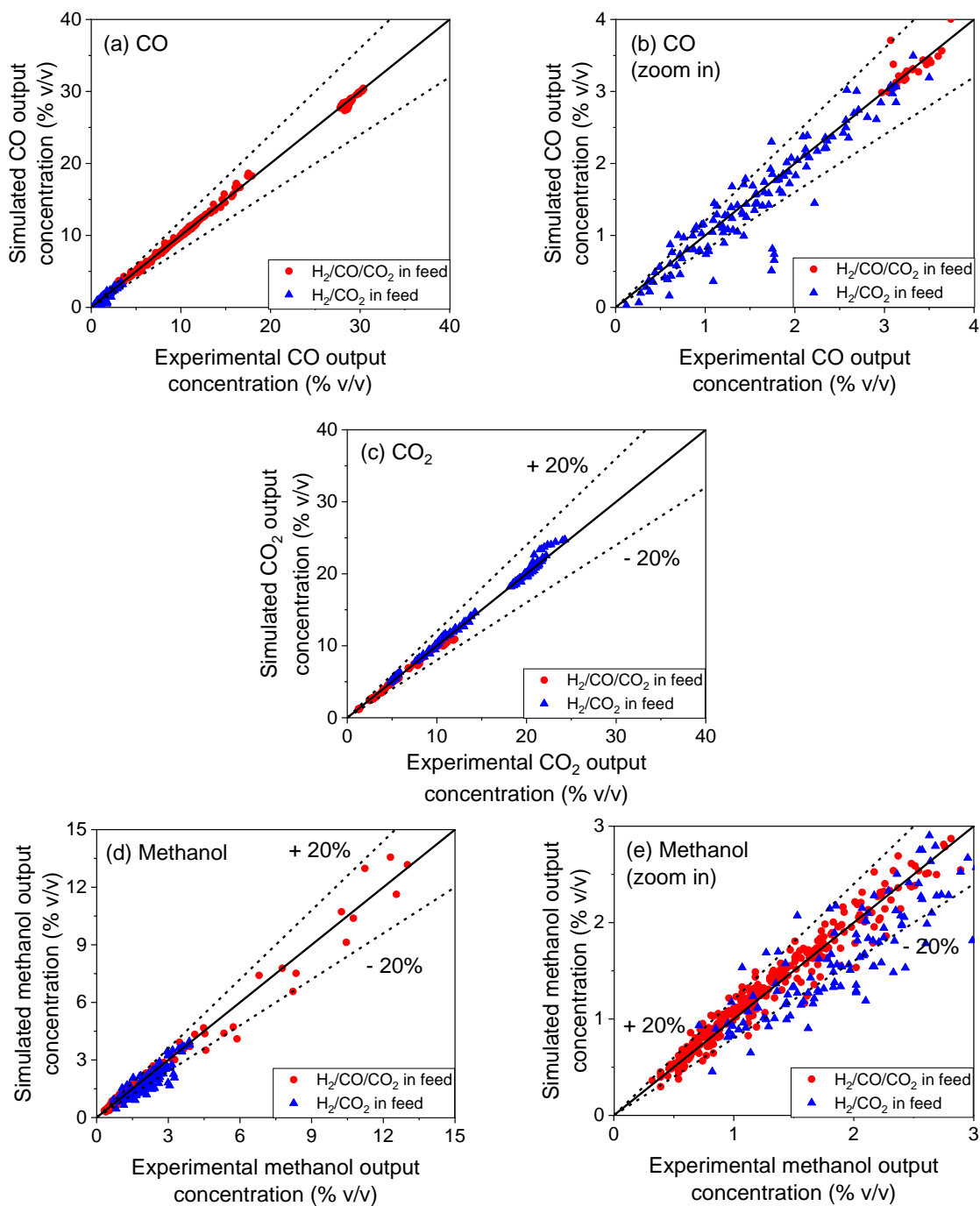


Fig. 3.6 Parity plots of Model-6p for measured and predicted CO (a-b), CO₂ (c) and methanol (d-e) concentrations in the product stream. Experimental conditions: points of Table 3.1 containing CO₂. Reproduced with permission from Campos et al.⁸⁹. Copyright 2021, American Chemical Society.

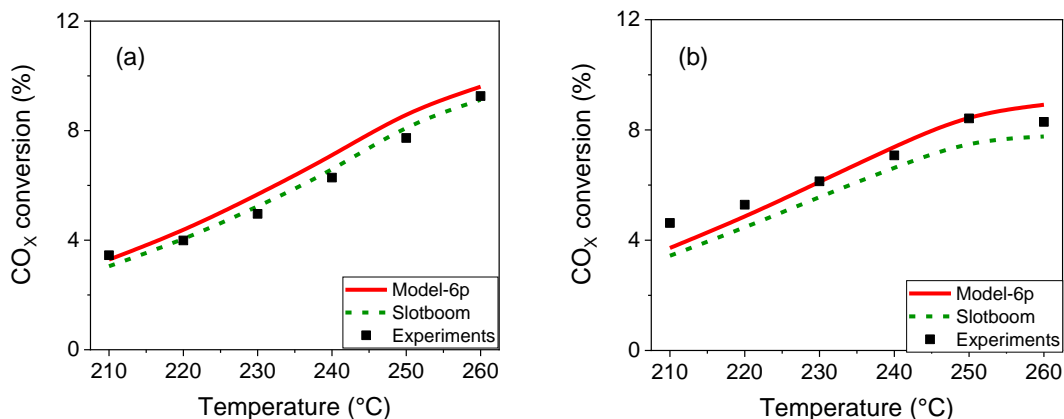


Fig. 3.7 CO_x conversion: simulation vs. experiments reported by Campos et al.⁷⁰ All experiments are performed at 41 bar. (a) GHSV = 40 L·h⁻¹·g_{cat}⁻¹, H₂/CO/CO₂ (feed) = 45.3/5.9/8.5% v/v. (b) GHSV = 32 L·h⁻¹·g_{cat}⁻¹, H₂/CO/CO₂ (feed) = 45.1/4.4/10.4% v/v. Reproduced with permission from Campos et al.⁸⁹. Copyright 2021, American Chemical Society.

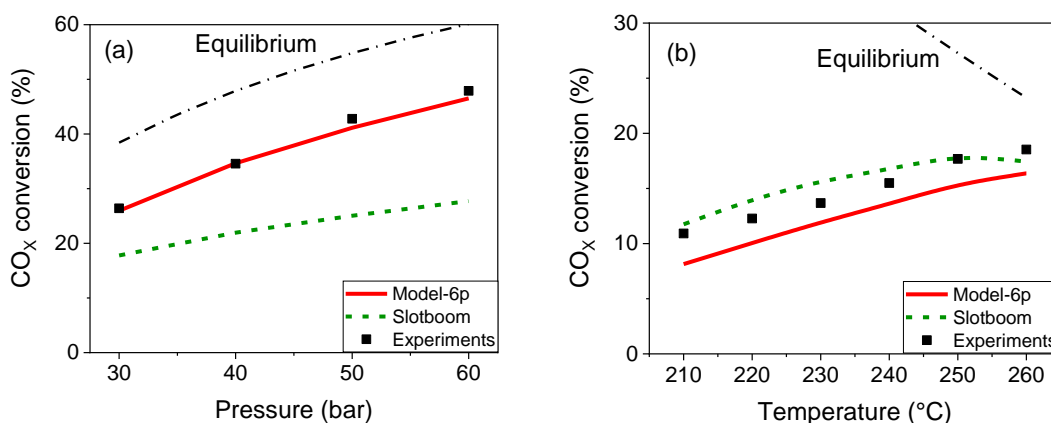


Fig. 3.8 CO_x conversion: simulation vs. experiments. (a) 240 °C, GHSV = 3.6 L·h⁻¹·g_{cat}⁻¹, H₂/CO/CO₂ (feed) = 69.6/8.2/5.7% v/v (experiments reported by Seidel et al.³⁴). (b) 50 bar, GHSV = 3.9 L·h⁻¹·g_{cat}⁻¹, H₂/CO₂ (feed) = 78.1/16.0% v/v (experiments reported by Slotboom et al.⁴¹). Reproduced with permission from Campos et al.⁸⁹. Copyright 2021, American Chemical Society.

3.3.3 Summary of the models

All necessary equations and optimized parameters for the implementation of the three developed models (Model-1p, Model-6p, Model-9p) are summarized in Tables 3.5-3.7. The optimized parameters of the literature models are provided in the SM (Sections S2.2 and S2.3).

Table 3.5. Equations summary of the new developed Model-1p. Reproduced with permission from Campos et al.⁸⁹. Copyright 2021, American Chemical Society.

Model-1p	
Recommended operating range: $0.001 \leq \bar{y}_{CO_2,0} \leq 0.65$	
$\dot{r}_{CO} = k_{CO} \cdot n_{M,cat} \cdot \theta_a \cdot \theta_c \cdot f_{H_2} \cdot f_{CO} \cdot \left(1 - \frac{f_{CH_3OH}}{f_{H_2}^2 \cdot f_{CO} \cdot K_{P,CO}^0}_{hyd.}\right)$	(3.33)
$\dot{r}_{CO_2} = k_{CO_2} \cdot n_{M,cat} \cdot \theta_b \cdot \theta_c \cdot f_{H_2}^{1.5} \cdot f_{CO_2} \cdot \left(1 - \frac{f_{CH_3OH} \cdot f_{H_2O}}{f_{H_2}^3 \cdot f_{CO_2} \cdot K_{P,CO_2}^0}_{hyd.}\right)$	(3.34)
$\dot{r}_{rWGSR} = k_{rWGSR} \cdot n_{M,cat} \cdot \theta_c \cdot [\theta_a \cdot K_A + \theta_b \cdot K_B] \cdot f_{CO_2} \cdot f_{H_2O} \cdot \left(1 - \frac{f_{H_2} \cdot f_{CO_2}}{f_{CO} \cdot f_{H_2O} \cdot K_{P,WGSR}^0}\right)$	(3.35)
$\theta_a = (K_C \cdot f_{CO} + K_D \cdot f_{H_2}^{0.5} \cdot f_{CO_2} + 1)^{-1}$	(3.36)
$\theta_b = (K_E \cdot f_{H_2}^{0.5} \cdot f_{CO_2} + K_F \cdot f_{H_2}^{-0.5} \cdot f_{CH_3OH} + 1)^{-1}$	(3.37)
$\theta_c = (K_G \cdot f_{H_2}^{0.5} + K_H \cdot f_{H_2}^{-0.5} \cdot f_{H_2O} + 1)^{-1}$	(3.38)
$k_{CO} = (1 - \phi_{Zn}) \cdot k_{11}^+ \cdot K_1 \cdot K_2 \cdot K_{10} = T^{0.103} \cdot \exp(-4632.9 \cdot T^{-1} - 2.934)$	(3.39)
$k_{CO_2} = \phi_{Zn} \cdot k_{17}^+ \cdot K_1^{1.5} \cdot K_5 \cdot K_{13} \cdot K_{15} = T^{-0.234} \cdot \exp(191.2 \cdot T^{-1} - 7.122)$	(3.40)
$k_{rWGSR} = k_{24}^- \cdot K_8 = T^{1.875} \cdot \exp(-3561.3 \cdot T^{-1} - 2.776)$	(3.41)
$K_A = (1 - \phi_{Zn}) \cdot K_4 = T^{-0.258} \cdot \exp[-17.233 + 6289.0 \cdot T^{-1}]$	(3.42)
$K_B = \phi_{Zn} \cdot K_5 = T^{-0.498} \cdot \exp[-15.637 + 6204.9 \cdot T^{-1}]$	(3.43)
$K_C = K_2 = \exp[-19.031 + 7020.3 \cdot T^{-1}]$	(3.44)
$K_D = K_1^{0.5} \cdot K_4 \cdot K_{12} = T^{-0.756} \cdot \exp[-20.480 + 11535.3 \cdot T^{-1}]$	(3.45)
$K_E = K_1^{0.5} \cdot K_5 \cdot K_{13} = T^{-1.234} \cdot \exp[-17.288 + 13049.6 \cdot T^{-1}]$	(3.46)
$K_F = K_1^{-0.5} \cdot K_7^{-1} = T^{0.736} \cdot \exp[-33.533 + 9702.4 \cdot T^{-1}]$	(3.47)
$K_G = K_1^{0.5} = \exp[-7.274 + 1409.6 \cdot T^{-1}]$	(3.48)
$K_H = K_1^{-0.5} \cdot K_8 \cdot K_9 = T^{1.036} \cdot \exp[-18.450 + 5390.6 \cdot T^{-1}]$	(3.49)
$K_{P,CO}^0_{hyd.} = T^{-3.384} \cdot \exp(10092.4 \cdot T^{-1} - 4.200)$	(3.50)
$K_{P,CO_2}^0_{hyd.} = T^{-4.481} \cdot \exp(4755.7 \cdot T^{-1} + 8.369)$	(3.51)
$K_{P,rWGSR}^0 = T^{-1.097} \cdot \exp(-5337.4 \cdot T^{-1} + 12.569)$	(3.52)
$n_{M,cat} = (1.559 \pm 0.107) \text{ mol} \cdot \text{kg}_{cat}^{-1}$	(Fitted parameter)

Table 3.6. Equations summary of the new developed Model-6p. Reproduced with permission from Campos et al.⁸⁹. Copyright 2021, American Chemical Society.

Model-6p	
Recommended operating range:	$\bar{y}_{CO_2,0} \geq 0.001$
$\dot{r}_{CO_2} = \exp\left(A_2 - \frac{E_{A,2}}{R \cdot T}\right) \cdot \phi_{Zn} \cdot \theta_b \cdot \theta_c \cdot f_{H_2}^{1.5} \cdot f_{CO_2} \cdot \left(1 - \frac{f_{CH_3OH} \cdot f_{H_2O}}{f_{H_2}^3 \cdot f_{CO_2} \cdot K_{P,CO_2,hyd}^0}\right)$	(3.53)
$\dot{r}_{rWGSR} = \exp\left(A_3 - \frac{E_{A,3}}{R \cdot T}\right) \cdot \theta_b \cdot \theta_c \cdot \phi_{Zn} \cdot f_{CO_2} \cdot f_{H_2O} \cdot \left(1 - \frac{f_{CO} \cdot f_{H_2O}}{f_{H_2} \cdot f_{CO_2} \cdot K_{P,rWGSR}^0}\right)$	(3.54)
$\theta_b = (\bar{K}_2 \cdot f_{H_2}^{0.5} \cdot f_{CO_2} + 1)^{-1}$	(3.55)
$\theta_c = (\bar{K}_3 \cdot f_{H_2}^{-0.5} \cdot f_{H_2O} + 1)^{-1}$	(3.56)
if $\bar{y}_{CO_2,0} \leq 0.90$	$\phi_{Zn} = 0.50$
if $\bar{y}_{CO_2,0} > 0.90$	$\phi_{Zn} = 0.10$
<i>Fitted parameters</i>	
$A_2 = 14.41 \pm 0.99$	$A_3 = 29.13 \pm 1.74$
$E_{A,2} = (94.73 \pm 4.18) \text{ kJ} \cdot \text{mol}^{-1}$ $E_{A,3} = (132.79 \pm 7.46) \text{ kJ} \cdot \text{mol}^{-1}$	
$\bar{K}_2 = (0.1441 \pm 0.0289) \text{ bar}^{-1.5}$ $\bar{K}_3 = (49.44 \pm 11.08) \text{ bar}^{-0.5}$	

3.4 Conclusions

Three kinetic models (Model-1p, Model-6p, and Model-9p) were developed, validated, and compared with other models from the literature.

If the operating region of interest involves feeds with and without CO₂ ($0 \leq \bar{y}_{CO_2,0} \leq 1$), then Model-9p is the most suitable, since it exhibited a small χ^2 , a moderate amount of estimated parameters (9), and exhibits adequate trends for different conditions.

If the operating region contains low to moderate CO₂ content in feed ($0.05 \leq \bar{y}_{CO_2,0} \leq 0.65$), then Model-1p is recommended, since its χ^2 is low, trends are adequately represented, and there is only one fitted parameter. In the whole range of studied conditions, the simulations performed with Model-1p are similar to those using the more complex microkinetic model, hence, confirming that the model reduction was successful, and most of the theoretical information was kept in the reduced model.

Finally, if the operating range considers CO₂-containing feeds ($\bar{y}_{CO_2,0} \geq 0.001$), then Model-6p offers the best fit. This model has the lowest χ^2 of the analyzed models, has a low amount of fitted parameters (6) and two global reactions.

The new models should efficiently simulate the methanol synthesis at various operating conditions, while also being suitable for reactor optimization and process scale-up.

An additional contribution of this work is the re-estimation of the parameters of literature models using a larger experimental database, increasing the validated operating window of

these kinetic models. These re-estimated parameters are provided in the Supporting Information.

Table 3.7. Equations summary of the new developed Model-9p. Reproduced with permission from Campos et al.⁸⁹. Copyright 2021, American Chemical Society.

Model-9p		
Recommended operating range:	$0 \leq \bar{y}_{CO_2,0} \leq 1$	
$\dot{r}_{CO} = \exp\left(A_1 - \frac{E_{A,1}}{R \cdot T}\right) \cdot (1 - \phi_{Zn}) \cdot \theta_a \cdot \theta_c \cdot f_{H_2} \cdot f_{CO_2} \cdot \left(1 - \frac{f_{CH_3OH}}{f_{H_2}^2 \cdot f_{CO} \cdot K_{P,CO}^0 \text{ hyd.}}\right)$	(3.58)	
$\dot{r}_{CO_2} = \exp\left(A_2 - \frac{E_{A,2}}{R \cdot T}\right) \cdot \phi_{Zn} \cdot \theta_b \cdot \theta_c \cdot f_{H_2}^{1.5} \cdot f_{CO} \cdot \left(1 - \frac{f_{CH_3OH} \cdot f_{H_2O}}{f_{H_2}^3 \cdot f_{CO_2} \cdot K_{P,CO_2}^0 \text{ hyd.}}\right)$	(3.59)	
$\dot{r}_{rWGSR} = \exp\left(A_3 - \frac{E_{A,3}}{R \cdot T}\right) \cdot \theta_c \cdot [(1 - \phi_{Zn}) \cdot \theta_a + \phi_{Zn} \cdot \theta_b] \cdot f_{CO_2} \cdot f_{H_2O} \cdot \left(1 - \frac{f_{CO} \cdot f_{H_2O}}{f_{H_2} \cdot f_{CO_2} \cdot K_{P,rWGSR}^0}\right)$	(3.60)	
$\theta_a = (\bar{K}_1 \cdot f_{H_2}^{0.5} \cdot f_{CO_2} + 1)^{-1}$	(3.61)	
$\theta_b = (\bar{K}_2 \cdot f_{H_2}^{0.5} \cdot f_{CO_2} + 1)^{-1}$	(3.62)	
$\theta_c = (\bar{K}_3 \cdot f_{H_2}^{-0.5} \cdot f_{H_2O} + 1)^{-1}$	(3.63)	
$\text{if } \bar{y}_{CO_2,0} \leq 0.001$	$\phi_{Zn} = 0.95$	
$\text{if } 0.001 \leq \bar{y}_{CO_2,0} \leq 0.90$	$\phi_{Zn} = 0.50$	
$\text{if } \bar{y}_{CO_2,0} > 0.90$	$\phi_{Zn} = 0.10$	
<i>Fitted parameters</i>		
$A_1 = 11.459 \pm 3.661$	$A_2 = 20.974 \pm 2.012$	$A_3 = 32.083 \pm 2.163$
$E_{A,1} = (90.65 \pm 16.57) \text{ kJ} \cdot \text{mol}^{-1}$	$E_{A,2} = (112.09 \pm 5.81) \text{ kJ} \cdot \text{mol}^{-1}$	
$E_{A,3} = (137.33 \pm 7.46) \text{ kJ} \cdot \text{mol}^{-1}$	$\bar{K}_1 = (0.968 \pm 0.393) \text{ bar}^{-1.5}$	
$\bar{K}_2 = (0.0489 \pm 0.0091) \text{ bar}^{-1.5}$	$\bar{K}_3 = (1420 \pm 2049) \text{ bar}^{-0.5}$	

Chapter 4. A detailed process and techno-economic analysis of the methanol synthesis from H₂ and CO₂ with intermediate condensation steps

Declaration of contributions:

Bruno Lacerda de Oliveira Campos conceptualized the work, implemented the model in Matlab, designed and implemented the detailed plants with heat integration in Aspen Plus, further developed the cost model, analyzed the results and wrote the manuscript.

Kelechi John gave support to the detailed plant simulation in Aspen Plus, implemented the first version of the cost model, wrote the methodology of the cost estimation, contributed to the discussion, and reviewed the manuscript.

Philipp Beeskow implemented the heat transfer model in Matlab, calculated the required size of the equipment, wrote the methodology of the heat transfer model, contributed to the discussion, and reviewed the manuscript.

Karla Herrera Delgado supervised the work, contributed to the discussion, and reviewed the manuscript.

Stephan Pitter contributed to the discussion and reviewed the manuscript.

Nicolaus Dahmen contributed to the discussion and reviewed the manuscript.

Jörg Sauer conceptualized and supervised the work, contributed to the discussion, and reviewed the manuscript.

Chapter redrafted after:

Lacerda de Oliveira Campos, B.; John, K.; Beeskow, P.; Herrera Delgado, K.; Pitter, S.; Dahmen, N.; Sauer, J. A detailed process and techno-economic analysis of the methanol synthesis from H₂ and CO₂ with intermediate condensation steps. *Processes*, 2022, **10**, 1535. DOI: 10.3390/pr10081535

Abstract Chapter 4

In order to increase the typically low equilibrium CO₂ conversion to methanol using commercially proven technology, the addition of two intermediate condensation units between reaction steps was evaluated in this work. Detailed process simulations with heat integration and techno-economic analyses of methanol synthesis from green H₂ and captured CO₂ are presented here, comparing the proposed process with condensation steps with the conventional approach. In the new process, a CO₂ single-pass conversion of 53.9% was achieved, which is significantly higher than the conversion of the conventional process (28.5%) and its equilibrium conversion (30.4%). Consequently, the total recycle stream flow was halved, which reduced reactant losses in the purge stream and the compression work of the recycle streams, lowering operating costs by 4.8% (61.2 M€·a⁻¹). In spite of the additional number of heat exchangers and flash drums related to the intermediate condensation units, the fixed investment costs of the improved process decreased by 22.7% (94.5 M€). This was a consequence of the increased reaction rates and lower recycle flows, reducing the required size of the main equipment. Therefore, intermediate condensation steps are beneficial for methanol synthesis from H₂/CO₂, significantly boosting CO₂ single-pass conversion, which consequently reduces both the investment and operating costs.

4.1 Introduction

As written in chapter 1, the product removal is an interesting approach to boost the methanol synthesis from H_2/CO_2 . In this chapter, one of the developed kinetic models presented in chapter 3 (Model-6p),⁸⁹ was applied to evaluate the economic feasibility of an alternative approach including two condensation steps (named here the ‘three-step process’), which was compared to the conventional approach (named here the ‘one-step process’). Both processes were implemented in Matlab in order to critically analyze and select key process parameters (i.e., cooling fluid temperature, number of reactor modules, and purge fraction). With the optimized parameters, detailed methanol synthesis plants with heat integration were implemented in Aspen Plus, and techno-economic analyses were performed.

4.2 Methodology

4.2.1 Process overview

In the present work, a methanol synthesis plant from H_2/CO_2 with a production of $145 \text{ ton}\cdot\text{h}^{-1}$ was considered. This value is based on an ongoing power-to-gasoline project via H_2/CO_2 conversion to methanol,¹⁶ whose final goal is a gasoline production of $5.5\cdot 10^8 \text{ L}\cdot\text{a}^{-1}$, which corresponds to a methanol production of $1.16 \text{ Mton}\cdot\text{a}^{-1}$ or $145 \text{ ton}\cdot\text{h}^{-1}$ (assuming a yield of 80% in the methanol-to-gasoline process and plant operating hours of $8000 \text{ h}\cdot\text{a}^{-1}$).

In our simulations, feed carbon dioxide comes from the cleaned flue gas of nearby industries (e.g., a cement industry) at $25 \text{ }^\circ\text{C}$ and 1 bar, with a purity of 99.5% mol/mol (the rest was water). Feed hydrogen comes from water electrolysis at $25 \text{ }^\circ\text{C}$ and 30 bar, with a purity of 99.5% mol/mol (the rest was nitrogen). Although it is possible to obtain these feedstocks in an extremely high purity (e.g., 99.99% mol/mol),^{90, 91} we chose a more conservative scenario, which also allows a proper simulation of inert material accumulation in the plant.

As pressure has a significant influence on the thermodynamic equilibrium of methanol synthesis (see Fig. 1.2), the reactor operating pressure was set to 70 bar. Although higher pressures are reported to have potential in methanol synthesis,^{92, 93} they were out of the scope of this work, since considerable extrapolations in the kinetic model would be necessary, and condensation inside the reactor might have to be taken into account. Besides, higher pressures increase compression costs and might also require more expensive materials to build the equipment.

The dimensions of the reactor modules were chosen to be close to the upper size limits that are currently commercially available. That is, each reactor module consisted of a shell containing 33,000 tubes with 12.5 m length and an inner diameter of 3.75 cm. Since the heat generation in CO_2 hydrogenation (Eq. 1.2) is lower than in CO hydrogenation (Eq. 1.1), less heat transfer area is necessary. Because of that, the tube inner diameter chosen in this work (3.75 cm) was larger than the size typically used for CO conversion to methanol (2.5 cm). Considering $1050 \text{ kg}\cdot\text{m}^{-3}$ as the apparent catalyst bed density,⁹⁴ the total CZA catalyst loading

of each reactor module was 478.13 ton. A total pressure loss of 0.75 bar was considered for each reactor module.⁹⁵

4.2.1.1 One-step approach — Process description

In Fig. 4.1, a detailed flowsheet of the one-step process is presented. This is an adapted version from a concept reported in the literature.⁹⁶⁻⁹⁸ Feed CO_2 is mixed with a low-pressure recycle stream, and then compressed from 1 to 70 bar in a three-stage process, including intermediate cooling (reducing compression work) and intermediate phase separation (to remove condensed methanol and water from the recycle stream). The resulting compressed stream is mixed with feed H_2 (compressed from 30 to 70 bar in one stage) and with a high pressure recycle stream. The mixed stream is preheated with the product gas and enters the inner tubes of parallel reactor modules, with the temperature being controlled by boiling water on the shell side.

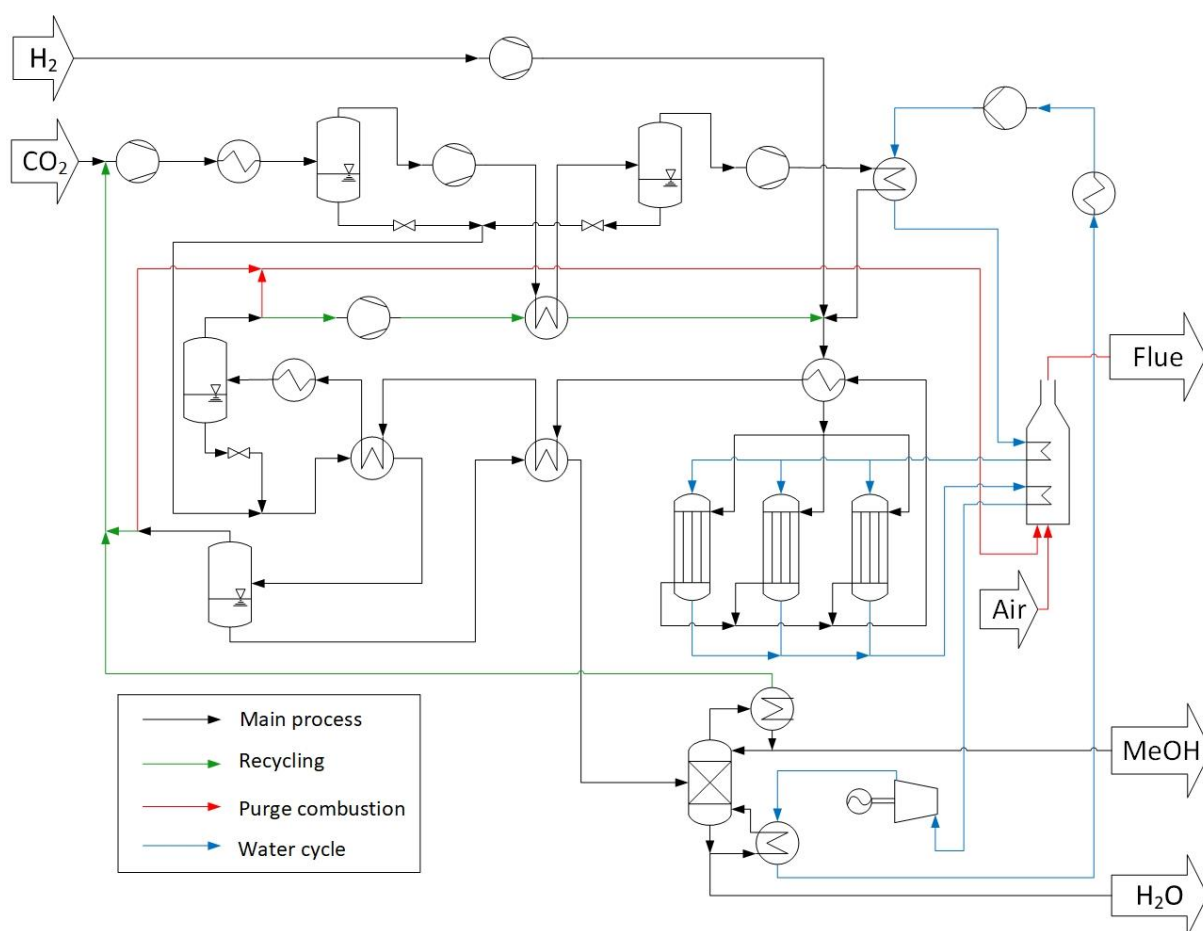


Fig. 4.1 One-step process — Detailed flowsheet with a total of three reactor modules. Cooling water streams are omitted. Reproduced with permission from Campos et al.¹¹. Copyright 2022, MDPI.

The product stream is cooled down to 30 °C in four heat exchangers, condensing water, methanol, and some CO_2 , which are separated from the light gases in a flash drum. A fraction

of the gas stream is purged, and the remaining stream is recompressed to 70 bar and recycled. The liquid stream from the flash drum is depressurized to 1 bar and heated to 30 °C, vaporizing most remaining CO₂. A liquid–gas separation is performed in another flash drum. A fraction of the gas stream from the low-pressure flash drum is purged, and the rest is recycled by mixing with feed CO₂. The liquid stream from the low-pressure flash drum is preheated and fed to a packed column, where methanol in high purity (>99.5% m/m) is recovered in the liquid distillate, water is recovered in the bottom, and most of the remaining CO₂ is recovered in the gas distillate.

The purge streams are burned with 15% air excess in a fired heater.⁹⁹ The heat of reaction of both the purge combustion and the methanol synthesis are used in a water Rankine cycle to produce electricity. The cycle starts with liquid water at 1 bar and 99.6 °C being pumped to a certain pressure, whose boiling temperature corresponds to the desired reactor temperature. Pressurized water reaches its boiling temperature in two steps (heat exchanger and fired heater) and vaporizes inside the reactor modules. The produced saturated steam is further heated in the fired heater and then performs work in a turbine, with a discharge pressure of 1.43 bar ($T_{boiling} = 110$ °C). The resulting low-pressure steam condenses partially in the column reboiler, and total condensation is completed in a heat exchanger, closing the water cycle.

4.2.1.2 Three-step approach — Process description

In Fig. 4.2, a detailed flowsheet of the three-step process is presented. In this approach, the feed compression and recycling of non-converted reactants occurs similarly to the one-step process. The mixed feed stream is preheated and enters the first reactor module. The product gas is cooled down to 45 °C in three steps, and the condensed stream (mostly water, methanol, and some CO₂) is separated from the light gases in a flash drum. The gas stream is preheated and enters the second reactor module. The second product gas is cooled down to 30 °C in three steps, and the condensed stream (mostly water, methanol, and some CO₂) is separated from the gas stream in another flash drum.

The gas phase is preheated and enters the third reactor module. The third product gas is cooled down, mixed with the condensed streams from the first and second reaction stages, and further cooled down to 30 °C.

Similar to the one-step process, component separation of the product stream is performed with one flash drum at high pressure, one flash drum at ambient pressure, and one distillation column.

The purge stream is burned in a fired heater with preheated air. In the water cycle, pressurized water is preheated and distributed to the reactor modules. A fraction of the produced saturated steam is split and used to preheat the water while the remaining steam is further heated in the fired heater. Supersaturated steam performs work in a turbine, with a discharge pressure of 1.43 bar ($T_{boiling} = 110$ °C). The resulting low-pressure steam is partially

condensed in the column reboiler, and total condensation is completed in a heat exchanger, closing the water cycle.

4.2.2 Process simulation in Matlab

Before implementing the final version of each plant in Aspen Plus, different scenarios were investigated in Matlab. Therefore, optimal key parameters were selected, such as the total number of reactor modules, the purge fraction, and the temperature of the cooling fluid in the reactor.

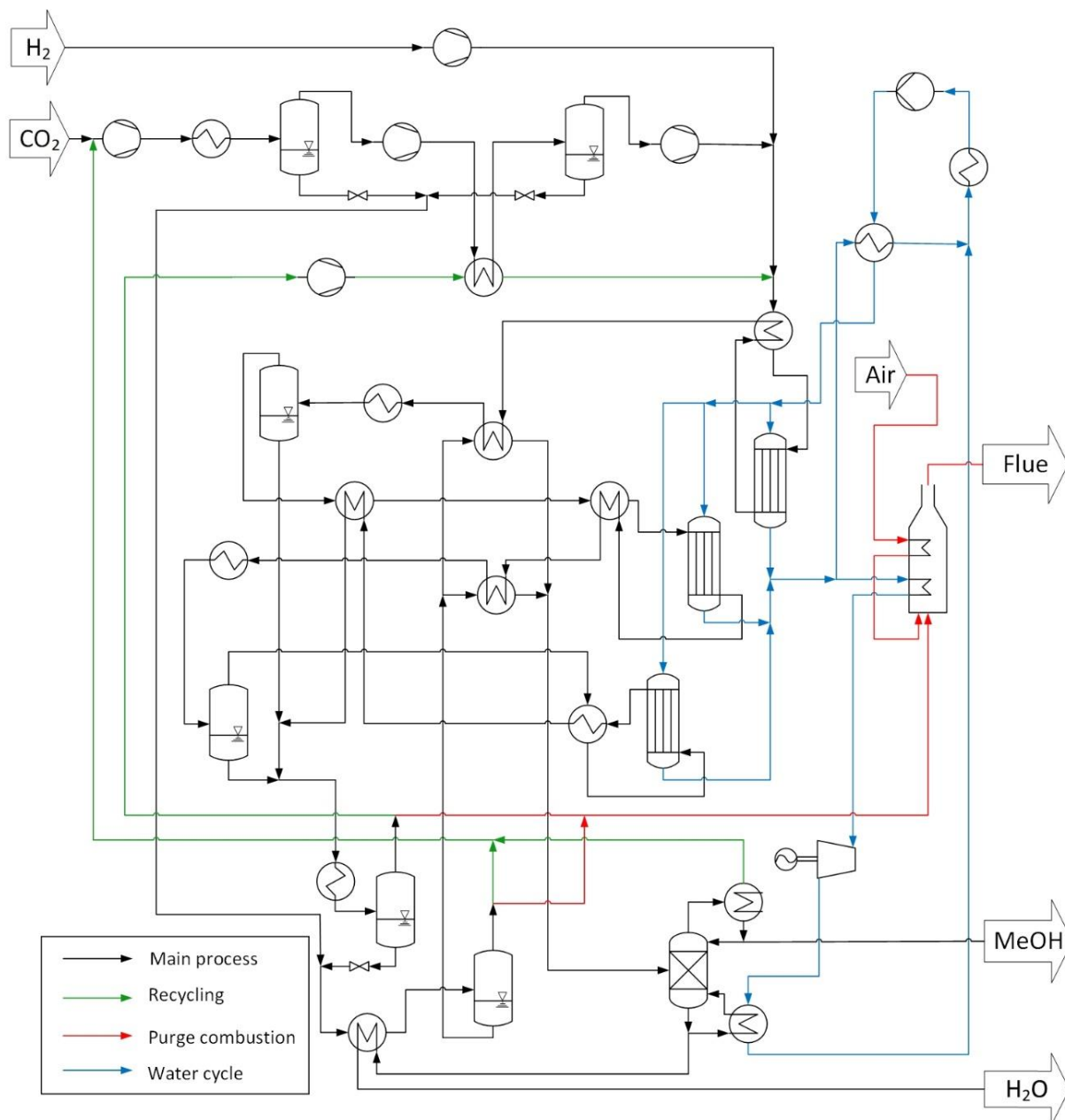


Fig. 4.2 Three-step process — Detailed flowsheet with a total of three reactor modules. Cooling water streams are omitted. Reproduced with permission from Campos et al.¹¹. Copyright 2022, MDPI.

In order to simulate the reactor, the following considerations were made: there are only variations along the length of the reactor (1D assumption), the influence of back-mixing is neglected (plug flow assumption), and the cooling fluid temperature (T_w , in K) is constant. Starting from mass and energy balances, the differential equations of the total mole flow of a single tube (\dot{n} , in mol·s⁻¹), the mole fraction of each component j (y_j), and the temperature (T , in K) in the axial direction z are shown as follows:

$$\frac{d\dot{n}}{dz} = \frac{m_{Cat}}{L} \cdot \sum_{j=1}^6 \sum_{k=1}^2 (v_{jk} \cdot \dot{r}_k) \quad (4.1)$$

$$\frac{dy_j}{dz} = \frac{1}{\dot{n}} \cdot \left\{ \frac{m_{Cat}}{L} \cdot \sum_{k=1}^2 (v_{jk} \cdot \dot{r}_k) - y_j \cdot \frac{d\dot{n}}{dz} \right\} \quad (4.2)$$

$$\frac{dT}{dz} = \frac{1}{(\dot{n} \cdot C_{p,f})} \cdot \left[-\frac{d\dot{n}}{dz} \cdot h_f - \dot{n} \cdot \sum_{j=1}^6 \left(h_j \cdot \frac{dy_j}{dz} \right) + U \cdot \pi \cdot D_i \cdot (T_w - T) \right] \quad (4.3)$$

Where m_{Cat} is the catalyst mass (kg), L is the reactor length (m), v_{jk} is the stoichiometric coefficient of component j in reaction k , \dot{r}_k is the rate of reaction k (mol·kg_{cat}⁻¹·s⁻¹), $C_{p,f}$ is the heat capacity of the fluid (J·mol⁻¹·K⁻¹), h_f is the specific enthalpy of the fluid (J·mol⁻¹), h_j is the specific enthalpy of component j (J·mol⁻¹·K⁻¹), U is the global heat transfer coefficient (W·m⁻²·K⁻¹), and D_i is the inner diameter of a single tube (m).

The temperature-dependent parameters ($C_{p,f}$, h_f , h_j , U) were updated in each integration point in the axial direction. Heat capacity and enthalpy were calculated with the thermodynamic functions provided by Goos et al.,⁷⁵ which are detailed in the Supplementary Material (SM) along with the derivation of the differential equations (see Section S3.1). The global heat transfer coefficient (U) was estimated by summing the heat transfer resistances in the axial direction, according to a methodology described in the literature^{100, 101} (see Section S3.2 of the SM).

The methodology to calculate the reaction rates (\dot{r}_k) is described in chapter 3 (Table 3.6). The system of differential equations was solved with the Matlab function *ode45*, with absolute and relative tolerances set to 10⁻¹⁰.

The side products of methanol synthesis on Cu/Zn-based catalysts (e.g., hydrocarbons or dimethyl ether) are typically at low concentrations.^{12, 45} Several studies reported that syngas conversion to hydrocarbons or dimethyl ether on commercial CZA at moderate temperatures ($T \leq 260$ °C) is significantly low or even below detection range,^{34, 41, 70} while Condero-Lanzac et al.²⁹ reported low methane production from H₂/CO₂ on CZA at high temperatures ($T \geq 275$ °C). Saito et al.¹⁰² observed that side product formation is further reduced by increasing CO₂/CO_x feed concentration. Therefore, the generation of side products is not considered in this work.

In order to simplify the simulation of the separation steps in Matlab, the following procedure was applied. Both processes were implemented in Aspen Plus, considering a total

of six reactor modules, a purge fraction of 2%, and $T_w = 235$ °C. The values of the split ratio of each component in the liquid and gas phase of each flash drum and the distillation column were extracted. For example, in the column of the one-step process, the methanol distribution in the outlet streams was: 3.80% in the gas distillate, 96.13% in the liquid distillate, and 0.06% in the bottom. The split ratio of all the components were taken from Aspen Plus and were considered constant for the different scenarios investigated in Matlab (i.e., variations in the number of reactor modules, purge fraction, and T_w). These split ratios are provided in the SM (see Section S3.3).

Flowsheet convergence was achieved in Matlab by an iterative method, as there were two cycles of streams due to recycling unconverted reactants. First, educated initial guesses of the composition and total mole flow of each recycle stream were given. In each iteration, the recycle stream mole flow and its composition were calculated and used in the next iteration until the tolerance criterion was fulfilled:

$$\frac{(\dot{n}_{rec,k+1} - \dot{n}_{rec,k})^2}{(\dot{n}_{rec,k+1})^2} \leq Tolerance \quad (4.4)$$

where $\dot{n}_{rec,k}$ is the total mole flow of the recycle stream at iteration k . The tolerance of the inner cycle and the outer cycle were set to 10^{-9} and 10^{-8} , respectively.

4.2.3 Process analysis and optimization

Considering the fixed methanol production of $145 \text{ ton}\cdot\text{h}^{-1}$ or $4525.6 \text{ kmol}\cdot\text{h}^{-1}$ and the 99.5% mol/mol purity of the reactants, the minimum required feed is $4548.2 \text{ kmol}\cdot\text{h}^{-1}$ of CO_2 and $13,645.1 \text{ kmol}\cdot\text{h}^{-1}$ of H_2 , totalizing $\dot{n}_{feed,min} = 18,193.3 \text{ kmol}\cdot\text{h}^{-1}$. Since there are reactant losses in the purge and product streams, an excess of feed is required. With a fix feed ratio $\text{H}_2:\text{CO}_2$ of 3:1, the excess of feed (Exc) is defined here as:

$$Exc = \frac{(\dot{n}_{feed} - \dot{n}_{feed,min})}{\dot{n}_{feed,min}} \cdot 100\% \quad (4.5)$$

It is, of course, of interest to minimize feed consumption, due to its high costs. Feed consumption is affected by key variables, such as reactor temperature and pressure, the number of reactor modules (which defines the total catalyst mass), and purge fraction. Avoiding large recycle streams is also important, as compressor work is required to get the pressure back to 70 bar, and larger equipment (i.e., heat exchangers, flash drums, compressors) are required to process higher flows.

Simulations were performed for a different number of reactor modules (from 3 to 12) and different purge fractions (from 0.5 to 5%). For each case, an initial guess for the feed excess was given ($Exc = 5\%$), and a fix feed ratio $\text{H}_2:\text{CO}_2$ of 3:1 (a stoichiometric ratio) was applied. Then, an optimization problem was solved in Matlab with the function `fminsearch` (function tolerance = $0.36 \text{ kmol}\cdot\text{h}^{-1}$, step tolerance = 0.1 °C), whose objective was to maximize methanol production by varying the reactor coolant temperature (T_w).

With the optimum T_w , the required excess of feed was calculated to meet the methanol demand (4525.6 kmol·h⁻¹) with Newton's method (function tolerance: 0.36 kmol·h⁻¹). The steps of the temperature optimization and Exc calculations were repeated until the temperature update was lower than 0.25 °C.

4.2.4 Detailed plant simulation in Aspen Plus

After analyzing the results of the Matlab simulations, optimum parameters were selected for each approach (i.e., the number of reactor modules, purge fraction, cooling fluid temperature) and a detailed plant simulation including heat integration was implemented in Aspen Plus V10.

The Peng–Robinson property method was selected for the reactor modules. All other equipment were simulated with the Non-Random Two-Liquid Model with a second set of binary parameters (NRTL2) as the property method.

The methanol synthesis reactor was simulated with the rigorous plug flow reactor model (RPLUG unit) and the kinetics described in Table 3.6 were implemented as a Langmuir–Hinshelwood–Hougen–Watson (LHHW) reaction model. The rearrangement of the model parameters to follow the software's specific input format is detailed in the Supplementary Material (see Section S3.4). Since the reactor cooling fluid is at a constant temperature due to water evaporation, both co-current and counter-current operations give the same results. Therefore, the co-current operation was selected in order to simplify the mathematical calculations.

The combustion of the purge streams in a fired heater was simulated with the RGIBBS unit, which considers that chemical equilibrium is achieved when the free Gibbs energy of the system is minimized.

The heat exchangers were simulated in counter-current flow with the HeatX unit, with a minimum temperature approach of 25 °C for the heat exchangers located inside the fired heater and a minimum temperature approach of 10 °C for all the other heat exchangers.

The compressors were modeled using the ASME method, assuming a mechanical efficiency of 0.95 and an isentropic efficiency of 0.80.²⁹ The pump was simulated assuming an efficiency of 0.70. The turbine was simulated with the ASME method, assuming a mechanical efficiency of 0.95 and an isentropic efficiency of 0.90.¹⁰³

The distillation column was simulated with the rigorous RadFrac model, considering a kettle reboiler and a partial condenser at 53 °C with liquid and vapor distillate. A Murphree efficiency of 0.75 was set to all intermediate stages.^{104, 105} In both processes, the column had 30 stages and a reflux ratio of 2, with the feed entering above the 24th stage.

The relative tolerance of all equipment calculations was set to 10⁻⁵. Flowsheet convergence was achieved using the Broyden method, with a relative tolerance of 10⁻⁴, which corresponds to a mass balance closure of 99.99%.

4.2.5 Efficiency evaluation

The chemical conversion efficiency (η_{CCE}) accounts for how much fuel energy remains in the final product in relation to the reactants. For methanol synthesis from H_2/CO_2 , it is calculated as follows:¹⁰⁶

$$\eta_{CCE} = \frac{\dot{m}_{MeOH} \cdot LHV_{MeOH}}{\dot{m}_{H_2} \cdot LHV_{H_2}} \quad (4.6)$$

Where \dot{m}_{MeOH} is the methanol mass production, \dot{m}_{H_2} is the hydrogen feed demand, and LHV is the low heating value. The maximum possible efficiency ($\eta_{CCE,max}$) occurs at 100% overall H_2 conversion to methanol (stoichiometric conversion):

$$\eta_{CCE,max} = \frac{M_{MeOH} \cdot LHV_{MeOH}}{3 \cdot M_{H_2} \cdot LHV_{H_2}} = 0.876 \quad (4.7)$$

Here, M_j is the molar mass of component j . In order to also account for heat and the work input, the exergy efficiency (η_{Ex}) is calculated:⁹⁸

$$\eta_{Ex} = \frac{\dot{m}_{MeOH} \cdot e_{MeOH}}{\dot{m}_{H_2} \cdot e_{H_2} + \dot{m}_{CO_2} \cdot e_{CO_2} + P_{el} + E_Q} \quad (4.8)$$

Where e_j is the specific exergy of component j , P_{el} is the total required electric power, and E_Q is the total exergy input associated with heat demand.

The specific exergy of a component (e_j) is divided between thermal and chemical exergy:⁹⁸

$$e_j(T, p) = [e_{j,therm}] + e_{j,chem} = [H_j - S_j \cdot T_0 - H_j^0 + S_j^0 \cdot T_0] + HHV_j \quad (4.9)$$

Here, $e_{j,therm}$ and $e_{j,chem}$ are the thermal and chemical exergies, H_j is enthalpy, S_j is entropy, H_j^0 and S_j^0 are the enthalpy and entropy at reference conditions (298.15 K and 1 bar), T_0 is the reference temperature, and HHV_j is the high heating value. In the exergy efficiency calculation, the HHV is used instead of the LHV , as water is liquid at reference conditions.

4.2.6 Techno-economic evaluation

In order to calculate the production costs, the standardized methodology from Albrecht et al.¹⁰⁷ was considered, which is a further development based on the work of Peters et al.¹⁰⁸

The main equipment costs (EC) were estimated based on reference equipment costs.^{108, 109} The scale up to the required capacity was performed with specific equipment scaling factors, and price inflation was corrected to 2020 with the Chemical Engineering Plant Cost Indexes ($CEPCI$). In Eq. (4.10), the costs of equipment j (EC_j) is described:

$$EC_j = EC_{j,ref} \cdot \left(\frac{C_j}{C_{j,ref}} \right)^M \cdot \left(\frac{CEPCI_{2020}}{CEPCI_{ref}} \right) \quad (4.10)$$

Here, the subscription ref relates to the reference equipment, C is the characteristic capacity, and M is the equipment scaling factor. The equipment is constructed with carbon steel. When

the reference price is in US dollars (USD), a conversion to euros (EUR) of 1.13 USD·EUR⁻¹ is applied (February 2022).¹¹⁰

The dimensions of the flash drums and the packed distillation column were calculated with the methodology reported by Towler and Sinnott.¹¹¹ The required heat transfer area of the heat exchangers, column condenser, and reboiler were estimated by assuming the typical global heat transfer coefficients reported by the VDI Atlas,¹⁰¹ according to each specific situation. Equipment dimensioning is detailed in the SM (see Section S3.7).

The fixed capital investment (*FCI*) was estimated by multiplying the total *EC* with the Lang Factor (*LF*), which accounts for all direct and indirect costs related to the plant construction. In this work, *LF* was assumed to be 4.86 (details are provided in the SM, Section S3.8).^{108, 109} A working capital (*WC*) of 10% of the total capital expenses (*CAPEX*) was considered.¹⁰⁷ Summarizing the equations:

$$FCI = LF \cdot \sum EC_j \quad (4.11)$$

$$CAPEX = FCI + WC \quad (4.12)$$

$$WC = 0.10 \cdot CAPEX \quad (4.13)$$

The equivalent annual capital costs (*ACC*) were estimated by applying the annuity method on the *FCI*, assuming an annual interest rate (*IR*) of 10%, a plant operating life (*t_p*) of 20 years, and no salvage value.¹¹² The working capital does not depreciate in value, and only its interest has to be taken into account.¹⁰⁷

$$ACC_{FCI} = \frac{FCI \cdot IR \cdot (1 + IR)^{t_p}}{[(1 + IR)^{t_p} - 1]} \quad (4.14)$$

$$ACC_{WC} = WC \cdot IR \quad (4.15)$$

$$ACC = ACC_{FCI} + ACC_{WC} = \frac{FCI \cdot IR \cdot (1 + IR)^{t_p}}{[(1 + IR)^{t_p} - 1]} + WC \cdot IR \quad (4.16)$$

The operating expenses (*OPEX*) were divided between direct and indirect costs. The costs related to the direct *OPEX* (*OPEX_{dir}*) are presented in Table 4.1, which include raw materials, catalysts, process water treating, and electricity. A catalyst lifetime of three years was considered. In the Rankine water cycle, a clean water replacement of 1% of the total flow was considered.¹¹³

The indirect *OPEX* consisted of operating labor (*OL*), operating supervision, maintenance, operating supplies, laboratory charges, taxes on property, insurance, plant overhead, administration, distribution, marketing, research, and development. The estimation of each of these items was based on typical values, which are dependent on *OL*, *FCI*, and the net production costs (*NPC*) (see the Supplementary Material, Section S3.8).^{107, 108} The total indirect *OPEX* (*OPEX_{ind}*) is calculated in Eq. (4.17).

Table 4.1 Costs of feedstock, catalyst, water treating, and electricity. Reproduced with permission from Campos et al.¹¹. Copyright 2022, MDPI.

Item	Costs	Ref.
Hydrogen	3097.4 €·ton ⁻¹	29
Carbon dioxide	44.3 €·ton ⁻¹	29
Cooling water	0.00125 €·ton ⁻¹	107
Clean water	2 €·ton ⁻¹	107
Total organic carbon (TOC) abatement of process water	1938 €·(ton C) ⁻¹	114
Electricity	90 €·MWh ⁻¹	104
Catalyst (Cu/ZnO/Al ₂ O ₃)	18,100 €·ton ⁻¹	115

$$OPEX_{ind} = 2.2125 \cdot OL + 0.081 \cdot FCI + 0.10 \cdot NPC \quad (4.17)$$

The required number of operators in a shift (n_{OP}) was estimated with the following equation:^{116, 117}

$$n_{OP} = (6.29 + 0.23 \cdot N_{np})^{0.5} \quad (4.18)$$

Where N_{np} is the number of non-particulate main processing units.

Considering daily working shifts, resting periods and vacations, the number of operators to fulfill each position in a continuous operation is approximately $F_{OP} = 4.5$. Therefore, the total number of operators (N_{OP}) is:^{116, 117}

$$N_{OP} = F_{OP} \cdot n_{OP} \quad (4.19)$$

The total costs of operating labor (OL) is then calculated as follows:

$$OL = W_{OP} \cdot N_{OP} \quad (4.20)$$

Where W_{OP} is the wage rate of each operator ($W_{OP} = 72,000 \text{ €} \cdot \text{a}^{-1}$).¹⁰⁴

The net production costs (NPC) are calculated in terms of average annual costs and in terms of average costs per kg of methanol:

$$NPC \left[\frac{\text{€}}{\text{a}} \right] = ACC + OPEX_{dir} + OPEX_{ind} \quad (4.21)$$

$$NPC \left[\frac{\text{€}}{\text{kg}} \right] = \frac{(ACC + OPEX_{dir} + OPEX_{ind})}{\dot{m}_{MEOH}} \quad (4.22)$$

4.3 Results and discussion

In this section, process simulation and analysis are presented separately for the one-step and the three-step approaches. Finally, the techno-economic analysis of both approaches is presented and discussed jointly.

4.3.1 One-step process

4.3.1.1 Selecting key parameters

The one-step process was successfully implemented in Matlab. Different scenarios were simulated by varying the number of reactor modules and the purge fraction, with the optimal temperature for a fixed methanol production ($145 \text{ ton}\cdot\text{h}^{-1}$) being estimated in each case. In Fig. 4.3, several contour plots are shown, where CO_2 single-pass conversion ($X_{\text{CO}_2,SP}$) (Fig. 4.3a), the required feed excess (Fig. 4.3b), the optimal temperature (Fig. 4.3c), and the total recycle stream (Fig. 4.3d) are plotted against the number of reactor modules and the purge fraction.

CO_2 single-pass conversion (Fig. 4.3a) was considerably enhanced by increasing the number of reactor modules. This was not only because the gas hourly space velocity (GHSV) decreased, but also because the optimal temperature had lower values (Fig. 4.3c), shifting the thermodynamic equilibrium towards higher methanol concentrations. In contrast, reducing the purge fraction had little effect on $X_{\text{CO}_2,SP}$. This should be the result of two competing effects: on one hand, a lower purge fraction means higher recycle streams (Fig. 4.3d), which increases the GHSV, reducing $X_{\text{CO}_2,SP}$. On the other hand, the recycle stream has a $\text{H}_2:\text{CO}_2$ ratio greater than three due to a limited rWGS extension. By increasing the recycle stream, the $\text{H}_2:\text{CO}_2$ ratio of the reactor feed stream is enhanced, positively contributing to $X_{\text{CO}_2,SP}$.

The required feed excess was significantly decreased both by increasing the number of reactor modules and by reducing the purge fraction. This occurred because the former procedure increased $X_{\text{CO}_2,SP}$ and the latter maintained $X_{\text{CO}_2,SP}$ roughly constant while increasing the gas flow inside the reactor modules.

Since the reactants (H_2 , CO_2) represent the highest costs of the plant, it is important to minimize the required feed excess, which according to Fig. 4.3b, occurred at 0.5% purge fraction. However, with such a low purge fraction, the total recycle stream was considerably high, demanding larger heat exchangers, flash drums, and compressors, as well as higher power consumption. Therefore, an intermediate value of 2% as the purge fraction was selected for the detailed simulation in Aspen Plus, agreeing with other studies and typical industrial values.^{29, 98, 111}

With the purge fraction fixed at 2%, six reactor modules were used in the detailed study, because further increasing the number of reactor modules only slightly reduced the required excess feed, not justifying further expenses in equipment and catalyst.

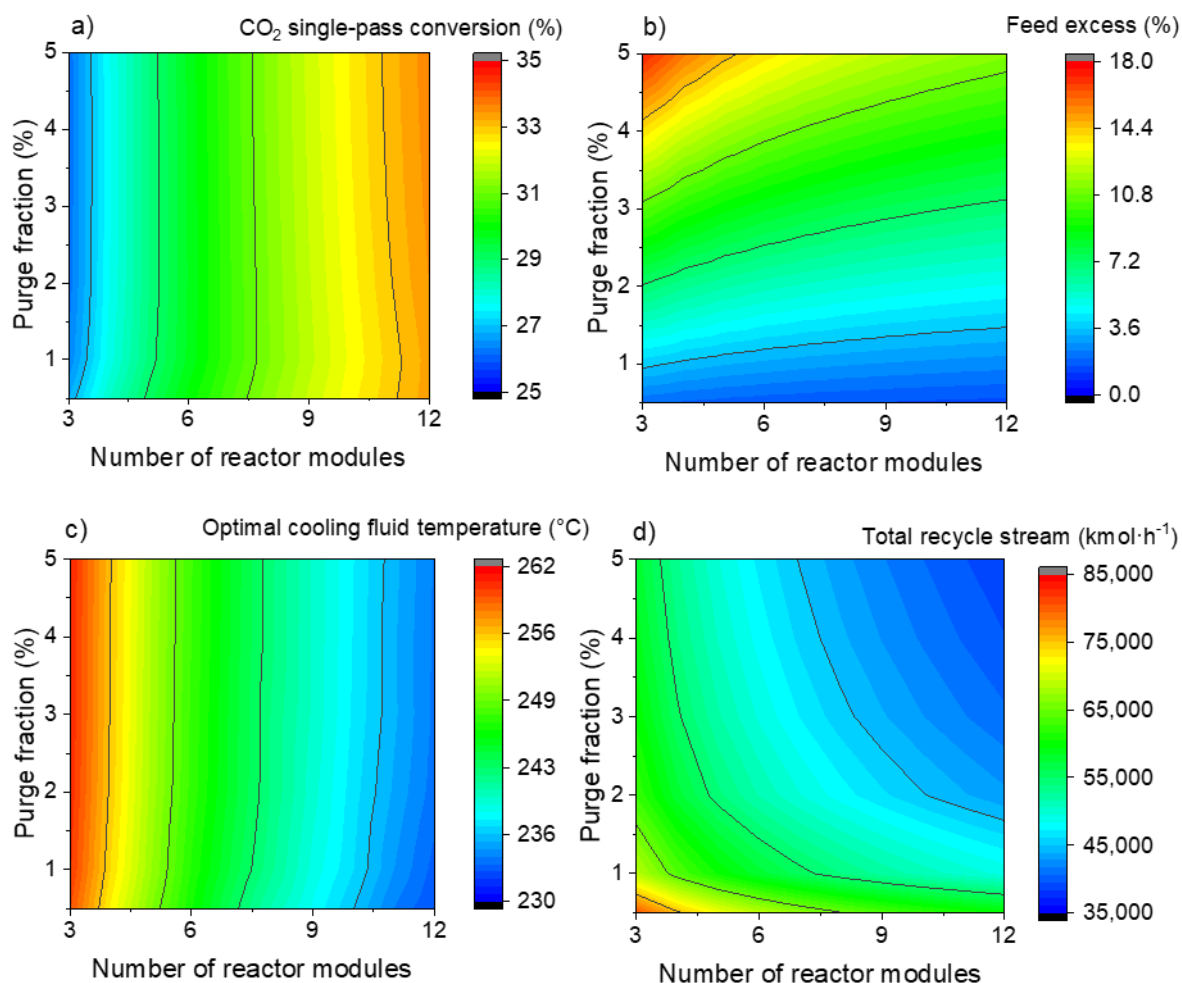


Fig. 4.3 One-step process — CO₂ single-pass conversion (a), required feed excess (b), optimal temperature (c), and total recycle stream (d) as a function of the number of reactor modules and the purge fraction. Reproduced with permission from Campos et al.¹¹. Copyright 2022, MDPI.

The value of the global heat transfer coefficient was updated point by point within mathematical integration along the reactor length. For the selected condition, $U_{z=0} = 160 \text{ W}\cdot\text{m}^{-2}\cdot\text{K}^{-1}$ and $U_{z=12.5 \text{ m}} = 150 \text{ W}\cdot\text{m}^{-2}\cdot\text{K}^{-1}$. Since Aspen Plus requires a constant value, the average value was used ($U_{avg} = 155 \text{ W}\cdot\text{m}^{-2}\cdot\text{K}^{-1}$).

4.3.1.2 Detailed plant simulation and process analysis

A detailed flowsheet of the one-step process presented in Figure 4.1 was implemented in Aspen Plus, considering 2% purge fraction, six reactor modules working in parallel, and the optimized temperature of the reactor cooling fluid ($T_w = 247.5 \text{ °C}$). A picture of the flowsheet in Aspen Plus, the properties of the streams, and a detailed plant description are provided in the Supplementary Material (see Section S3.5).

In Fig. 4.4, the concentration of the products along the reactor length is shown. The methanol and water feed concentrations were close to zero, and their outlet concentrations

were 7.4 and 7.2% mol/mol, respectively. The nitrogen concentration remained relatively low (inlet: 4.95% mol/mol, outlet: 5.65% mol/mol). Due to the recycle streams, CO entered the reactor modules at 1.50% mol/mol, although it was not a feedstock in the plant. CO was produced through the rWGSR until the length of 1.5 m, where its concentration reached 3.3% mol/mol. Then, due to high water concentration (4.30% mol/mol), the WGSR became faster than its reverse reaction and started to consume CO, which exited the reactor at 1.76% mol/mol and a marginal selectivity (0.5%). This virtually stabilized CO content in the plant led to a high methanol selectivity (99.5%).

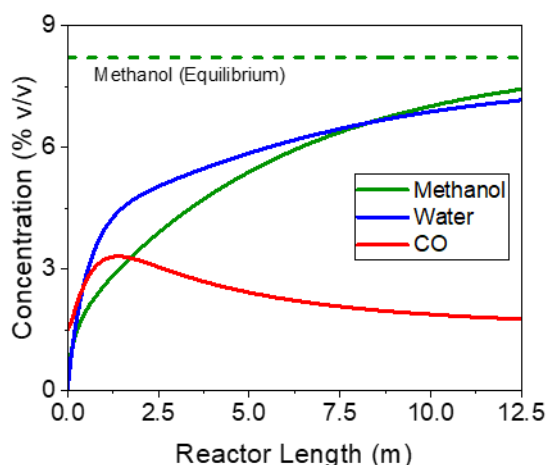


Fig. 4.4 One-step process — Product concentration along the reactor length. Reactor feed concentration: $\text{H}_2/\text{CO}/\text{CO}_2/\text{CH}_3\text{OH}/\text{H}_2\text{O}/\text{N}_2 = 71.3/1.5/21.9/0.3/0.0/5.0\%$ mol/mol. Reproduced with permission from Campos et al.¹¹. Copyright 2022, MDPI.

The CO_2 single-pass conversion was 28.5%, close to the equilibrium conversion (30.4%), while the feed excess was 6.05%, which corresponded to an overall CO_2 conversion to methanol of 94.3%. These values are in agreement with the Matlab simulations: $X_{\text{CO}_2,SP} = 29.7\%$, feed excess = 5.75%, overall CO_2 conversion to MeOH = 94.6%.

The chemical conversion efficiency (η_{CCE}) of the process was 82.6%, which was close to the maximum possible value ($\eta_{CCE,max} = 87.6\%$). With the heat integration, the one-step process was not only self-sufficient, but had a heat excess that could be supplied to other processes, in agreement with the literature.^{98, 118} In our case, as is commonly performed in industrial methanol synthesis plants, the heat excess was used to generate electricity via a water Rankine cycle, reducing the electricity consumption from 47.4 to 17.6 MW.

In Fig. 4.5, a global exergy balance and an exergy loss distribution are provided. No distinction was made between exergy destruction and exergy losses via side output streams (i.e., cooling water, process water, and flue gas). The exergy efficiency (η_{Ex}) of the process was 76.4%, with a total exergy loss of 281.9 MW. The main losses occurred due to the exothermic chemical reactions with heat recovery at low temperatures (reactor modules: 58.1%, fired heater: 14.8%). Additionally, exergy losses in the heat exchangers (11.1%) and in the column (9.0%) were also significant, mainly due to heat transfer to cooling water.

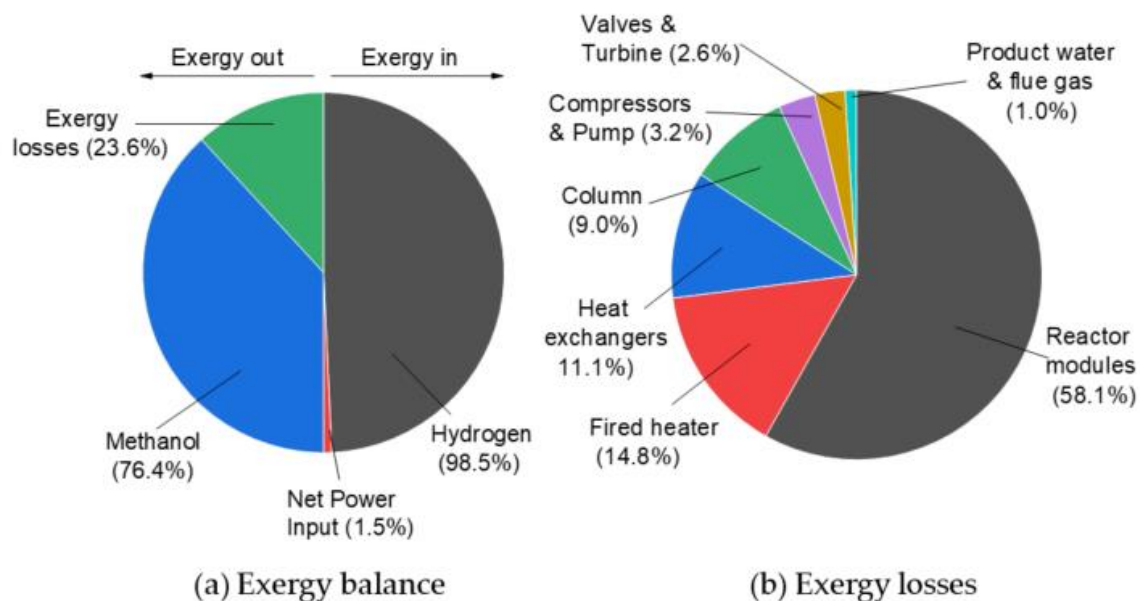


Fig. 4.5 One-step process — Exergy analysis. (a) Global exergy balance. Total exergy input: 1194.5 MW. (b) Distribution of exergy losses (total = 281.9 MW). Reproduced with permission from Campos et al.¹¹. Copyright 2022, MDPI.

4.3.2 Three-step process

4.3.2.1 Selecting key parameters

The three-step process was successfully implemented in Matlab. In Fig. 4.6, CO_2 single-pass conversion ($X_{\text{CO}_2,SP}$) (Fig. 4.6a), the required feed excess (Fig. 4.6b), the optimal temperature (Fig. 4.6c), and the total recycle stream (Fig. 4.6d) are described as a function of the number of reactor modules and the purge fraction. Since this process considers three reaction steps with intermediate cooling, the simulations were limited to multiples of three as the total number of reactor modules.

A significant improvement was seen in the three-step process in relation to the one-step approach. For similar conditions (i.e., the same total number of reactor modules and purge stream fraction), CO_2 single-pass conversion had approximately doubled, the required feed excess decreased by 60–70%, and the total recycle stream decreased by 50–70%. The optimal values for the reactor cooling fluid remained close to the ones of the first approach (between 230 and 260 °C).

Similarly to the one-step process, a purge fraction equal to 2% was chosen here, having a good compromise between minimizing the feed requirements and minimizing the total recycle stream. With this fixed purge fraction, a number of reactor modules equal to three was selected, as further increasing this amount gave limited improvement in the required feed excess and the total recycle stream, while considerably increasing equipment and catalyst costs.

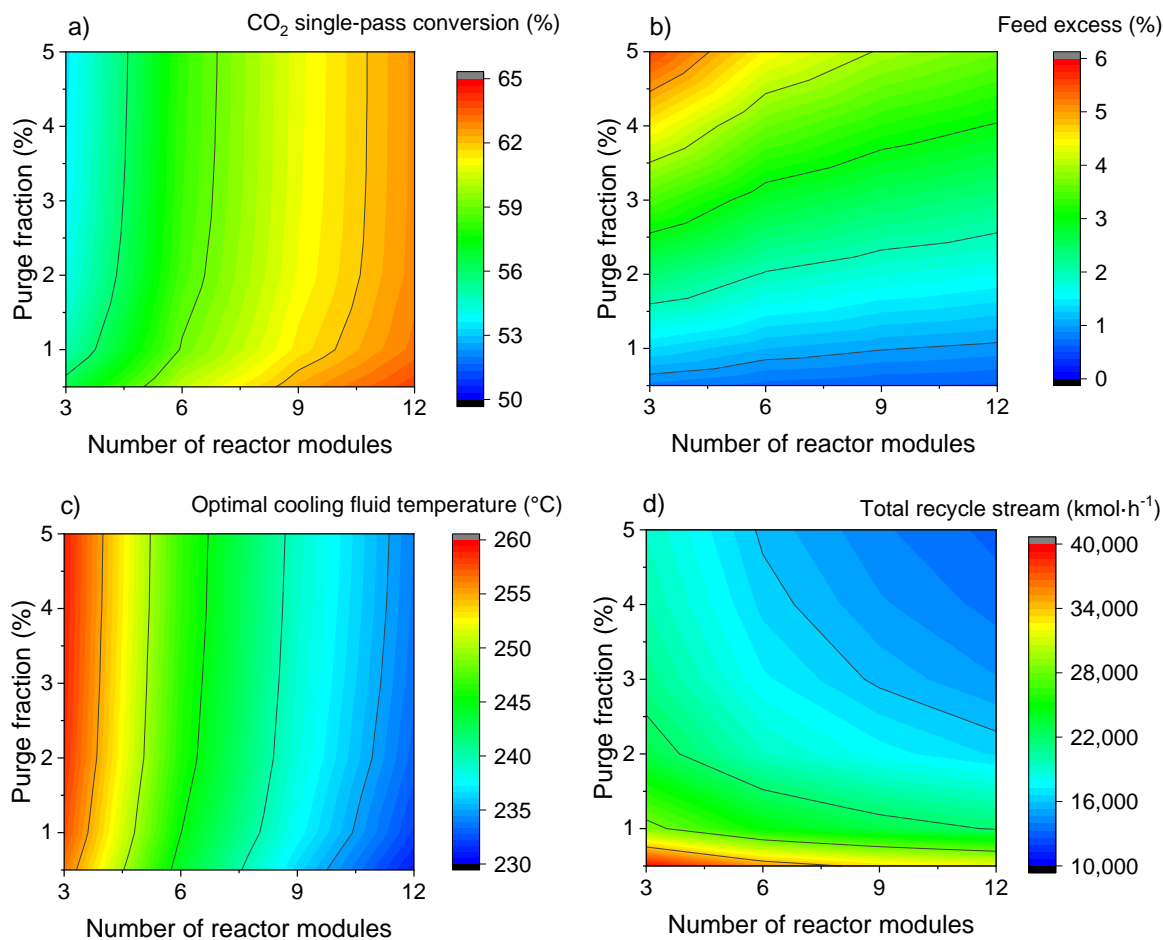


Fig. 4.6 Three-step process — CO₂ single-pass conversion (a), required feed excess (b), optimal temperature (c), and total recycle stream (d) as a function of the number of reactor modules and the purge fraction. Reproduced with permission from Campos et al.¹¹. Copyright 2022, MDPI.

When analyzing different scenarios in Matlab, the same cooling fluid temperature (T_w) was considered for all reactors. A further optimization was possible by allowing this temperature to be independently operated in each reactor. This possibility was checked for the chosen condition (2% purge fraction, three reactor modules), but only a marginal improvement was obtained (see Table 4.2), probably not justifying the increase in plant complexity. Therefore, in the detailed analysis, the cooling fluid temperature of all the reactors was set to 258.5 °C.

Similarly to the one-step process, the average heat transfer coefficients were obtained for each reactor and given to Aspen Plus: $U_1 = 327 \text{ W}\cdot\text{m}^{-2}\cdot\text{K}^{-1}$, $U_2 = 285 \text{ W}\cdot\text{m}^{-2}\cdot\text{K}^{-1}$, $U_3 = 246 \text{ W}\cdot\text{m}^{-2}\cdot\text{K}^{-1}$. The decrease in the coefficient values is associated with a decrease in the total flow, due to intermediate product removal. Still, the heat transfer coefficients were higher than in the one-step process ($155 \text{ W}\cdot\text{m}^{-2}\cdot\text{K}^{-1}$), which had lower flows for each reactor module because of parallel operation.

Table 4.2 Three-step synthesis — Performance indicators for two process approaches: same cooling fluid temperature in all reactors, and independent optimization of the cooling fluid temperature in each reactor. Reproduced with permission from Campos et al.¹¹. Copyright 2022, MDPI.

Approach	T_{w,R_1} (°C)	T_{w,R_2} (°C)	T_{w,R_3} (°C)	$X_{CO_2,SP}$ (%)	Feed Excess (%)	Total recycle stream (kmol·h ⁻¹)
Same T_w	258.5	258.5	258.5	54.1	2.42	23,038
Varying T_w	264.6	259.9	249.4	54.6	2.35	22,464

4.3.2.2 Detailed plant simulation and process analysis

A detailed flowsheet of the three-step process presented in Figure 4.2 was implemented in Aspen Plus, considering a 2% purge fraction, three reactor modules working in series with intermediate product condensation, and the previously optimized temperature of the reactor cooling fluid ($T_w = 258.5$ °C). A detailed plant description, stream properties, and a picture of the flowsheet in Aspen Plus are provided in the Supplementary Material (see Section S3.6).

In Fig. 4.7, the concentration of the products along the length of the three reactors is shown, as well as the product removal through the intermediate condensation steps. In Reactor 1, CO entered at a low concentration (1.3% mol/mol), peaked at $z = 2.5$ m, and left the reactor with a higher concentration (2.7% mol/mol). This CO production through the rWGSR increased the water concentration ($y_{H_2O}^{R_1,out} = 5.6\%$ mol/mol) and slowed down methanol production ($y_{MeOH}^{R_1,out} = 4.7\%$ mol/mol).

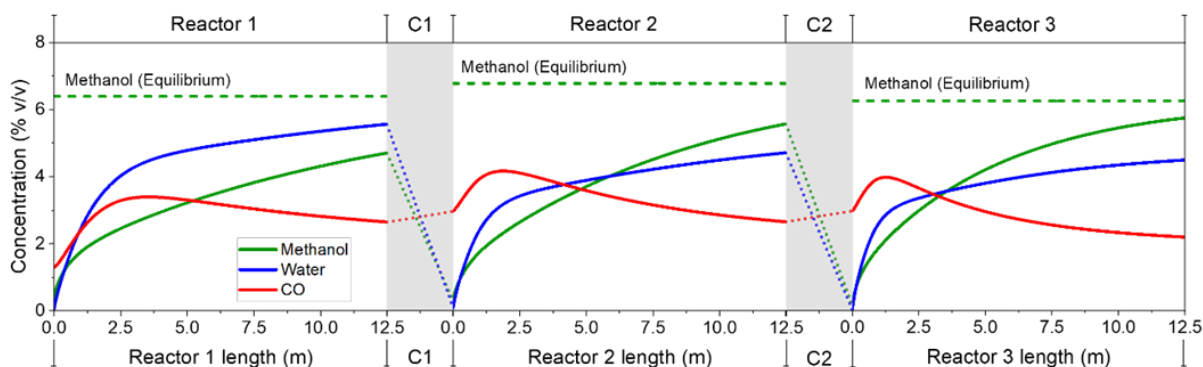


Fig. 4.7 Three-step process—methanol, water, and CO concentration along the length of each reactor, as well as in the intermediate condensation steps (C1 and C2). Reproduced with permission from Campos et al.¹¹. Copyright 2022, MDPI.

In Reactors 2 and 3, the CO inlet concentration was significantly higher (3.0% mol/mol for both cases), causing its concentration peak to come much sooner (at 1.8 m and 1.25 m, respectively). After that, the WGSR was faster than its reverse reaction and the CO concentration decreased, leaving both reactors with an overall positive CO consumption. Therefore, the water concentration in Reactors 2 and 3 was maintained at lower levels

($y_{H_2O}^{R_2,out} = 4.7\%$ mol/mol, $y_{H_2O}^{R_3,out} = 4.5\%$ mol/mol), enhancing the final methanol concentration ($y_{MeOH}^{R_2,out} = 5.6\%$ mol/mol, $y_{MeOH}^{R_3,out} = 5.8\%$ mol/mol).

Water is known to accelerate the deactivation of Cu-based catalysts.¹¹⁹ Therefore, the lower water concentration of the three-step process in relation to the one-step process ($y_{H_2O}^{1s,out} = 7.2\%$) should not only benefit the reaction rates, but also the catalyst lifetime.

In Table 4.3, the operating conditions and split ratios of the intermediate condensation steps are provided, while the reactor information is summarized in Table 4.4. Methanol and water were almost fully removed from the gas phase, but at the cost of ca. 9–13% CO₂ condensation. The split ratios of CO₂ and methanol were strongly dependent on temperature, with the chosen values ($T_1 = 45$ °C, $T_2 = 30$ °C) being derived from a sensitivity analysis.

Table 4.3 Three-step process — Operating conditions and split ratios of the intermediate condensation steps. Reproduced with permission from Campos et al.¹¹. Copyright 2022, MDPI.

Cond. Step	Temp. (°C)	Pres. (bar)	Phase	Split Ratio		
				CO ₂ (%)	MeOH (%)	H ₂ O (%)
#1	45	69.25	Gas	90.66	5.31	1.17
			Liquid	9.34	94.69	98.83
#2	30	68.50	Gas	87.36	2.46	0.52
			Liquid	12.64	97.54	99.48

Table 4.4 Three-step process — Heat transfer, inlet mole flow, mole fractions, and methanol production in the reactor modules. Reproduced with permission from Campos et al.¹¹. Copyright 2022, MDPI.

Item	Reactor 1	Reactor 2	Reactor 3
\dot{Q} (MW)	-18.5	-25.7	-22.7
\dot{n}_{in} (kmol·h ⁻¹)	40,833	33,209	26,366
$y_{H_2,in}$ (% mol/mol)	69.1	69.0	69.5
$y_{CO,in}$ (% mol/mol)	1.3	3.0	3.0
$y_{CO_2,in}$ (% mol/mol)	20.6	17.3	14.4
$y_{MeOH,out}$ (% mol/mol)	4.7	5.6	5.8
$y_{H_2O,out}$ (% mol/mol)	5.6	4.7	4.5
$\Delta\dot{n}_{MeOH}$ (kmol·h ⁻¹)	1616	1589	1325

The methanol production was similar in Reactors 1 and 2 (1616 and 1589 kmol·h⁻¹, respectively), while it was 18% lower in Reactor 3 (1325 kmol·h⁻¹). This shows the positive

effect of a higher CO concentration in the reactor feed, despite the lower total feed flow and CO₂ inlet concentration of Reactors 2 and 3 in relation to Reactor 1.

The CO₂ single-pass conversion ($X_{CO_2,SP}$) was 53.9%, with a selectivity to methanol of 99.8% and a selectivity to CO of 0.2%. The feed excess was 2.35%, leading to an overall conversion of CO₂ to methanol of 97.7%. These values are in agreement with the Matlab simulations ($X_{CO_2,SP}$) = 54.1%, Exc = 2.42%, overall CO₂ conversion to MeOH = 97.6%).

The three-step approach was significantly superior to the one-step process, even using only half the number of reactor modules (three vs. six). This superiority is clear when looking at the CO₂ single-pass conversion (53.9% vs. 28.5%), leading to a considerably higher overall conversion to methanol (97.7% vs. 94.3%).

With the heat integration, the three-step process was also self-sufficient in heat, while electricity was produced through a water Rankine cycle, reducing the total power consumption from 42.7 to 21.8 MW. The chemical conversion efficiency was $\eta_{CCE}^{3s} = 85.6\%$, which was higher than the value of the one-step process ($\eta_{CCE}^{1s} = 82.3\%$) and, therefore, even closer to the maximum possible value ($\eta_{CCE,max} = 87.6\%$).

In Fig. 4.8, an exergy analysis of the process is presented. The exergy efficiency was $\eta_{Ex}^{3s} = 78.8\%$, an improvement from the previous approach ($\eta_{Ex}^{1s} = 76.4\%$), with the total exergy losses decreasing in 13% (245.3 vs. 281.9 MW). Although the total power consumption decreased (42.7 vs. 47.4 MW), the net power consumption increased slightly (21.8 vs. 17.6 MW). This occurred because power generation was significantly lower in the three-step approach (20.8 vs. 29.8 MW) due to the much lower heat duty of the fired heater, as less reactant was lost in the purge streams.

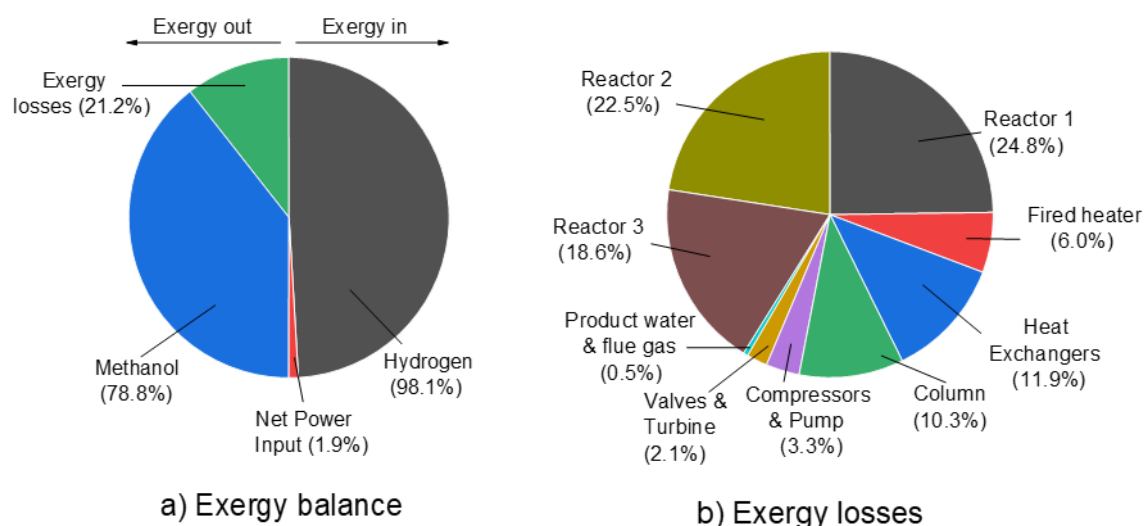


Fig. 4.8 Three-step process — Exergy analysis. (a) Global exergy balance (total exergy input = 1157.5 MW). (b) Distribution of exergy losses (total = 245.3 MW). Reproduced with permission from Campos et al.¹¹. Copyright 2022, MDPI.

Chemical reactions with heat recovery at low temperatures was also the main cause of exergy losses in the three-step approach (reactor modules: 66.0%, fired heater: 6.0%). Both

processes lost approximately the same exergy in the reactor modules and the distillation column. The main improvement in relation to the one-step process was a much lower exergy loss in the fired heater (14.7 vs. 41.4 MW), as the total purge stream flow decreased by 59% (455 against 1100 kmol·h⁻¹). Despite the higher number of cooling and warming operations and the higher total heat transfer duty in the three-step process (357.1 vs. 310.2 MW), the exergy losses in the heat exchangers were slightly lower for the three-step process (29.4 vs. 31.4 MW). Finally, moderate improvements were also seen in the compressors and pump (8.2 vs. 9.1 MW) and in the valves and turbine (5.0 vs. 7.4 MW).

In Table 4.5, the data comparing both processes is summarized, once again emphasizing the superior performance of the three-step approach.

4.3.3 Techno-economic analysis

In Figure 4.9, the distribution of the equipment costs (*EC*) is presented, with the reactor modules and the compressors representing the majority of the costs (>75%). The total *EC* was 85.5 and 66.1 M€ for the one-step and the three-step approach, respectively. This significant improvement of the three-step process was a consequence of the intermediate condensation steps, requiring a lower total reactor volume (due to an enhanced reaction velocity), lower compressor size (due to a lower recycle flow), and lower furnace, turbine, and generator size (due to a lower purge flow). The cost reduction in the aforementioned equipment was significantly higher than the additional costs of the heat exchangers and flash drums from the intermediate condensation units. The total fixed capital investment (*FCI*) was 415.9 and 321.4 M€ for the one-step and three-step approach, respectively. The detailed estimated capacity and price of each equipment is presented in the Supplementary Material (S3.8).

Table 4.5 Data comparison between the one-step and the three-step approach. Reproduced with permission from Campos et al.¹¹. Copyright 2022, MDPI.

Item	One-Step	Three-Step
Total methanol production (kmol·h ⁻¹)	4527	4525
CO ₂ single-pass conversion (%)	28.5	53.9
Overall CO ₂ conversion to methanol (%)	94.3	97.7
Feed excess (%)	6.05	2.35
Methanol selectivity (%)	99.5	99.8
Total recycle stream flow (kmol·h ⁻¹)	54,290	22,581
Maximum water concentration (% mol/mol)	7.2	5.6
Total exergy loss (MW)	281.9	245.3
Exergy efficiency (%)	76.4	78.8

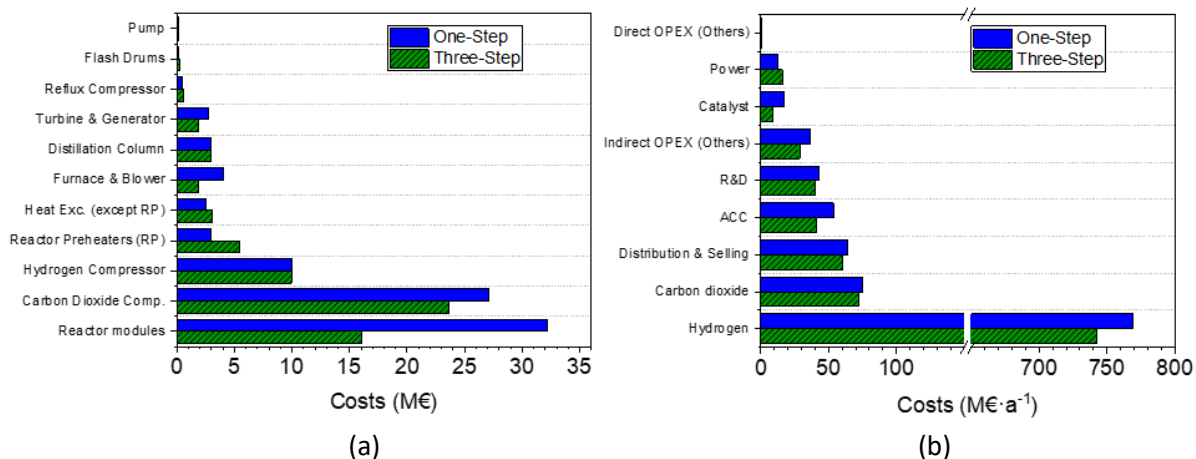


Fig. 4.9 Distribution of the costs. (a) Equipment Costs (*EC*). (b) Net Production Costs (*NPC*). Reproduced with permission from Campos et al.¹¹. Copyright 2022, MDPI.

In Figure 4.9b, the distribution of the net production costs (*NPC*) is detailed. The main operating costs were the reactant expenses (78–80% of *NPC*), with *ACC* contributing with only 4–5%, while the catalysts and electricity consisted of less than 3% of the *NPC*. Due to the higher overall CO₂ conversion to methanol, the *NPC* of the three-step process was 5.7% lower than the one-step approach. The detailed *OPEX* costs are presented in the Supplementary Material (S3.8).

In Table 4.6, a summary of the overall costs is presented. The *NPC* was 920 and 868 €·ton⁻¹ for the one-step and the three-step process, respectively, corresponding to an improvement of 5.7% for the new process. Besides the hydrogen and carbon dioxide costs, the fixed capital investment (*FCI*) and the discount rate were the most sensitive parameters to the methanol selling price, as shown in the tornado analysis (see Fig. 4.10).

In Figure 4.11, the net production costs are plotted against the hydrogen price. Although the methanol market price in Europe was still significantly below the values (495 €·ton⁻¹ in February 2022),^{120, 121} the green methanol produced from the proposed process would become economically competitive if the green hydrogen price reached 1468 €·ton⁻¹.

4.4 Conclusions

A detailed study of a methanol synthesis plant from H₂ and CO₂ with intermediate condensation units (the three-step process) is presented and compared with the conventional approach (the one-step process). The total production was fixed at 1.16 Mton MeOH·a⁻¹. The processes were first implemented in Matlab in order to critically analyze the number of reactor modules, the purge fraction, and the reactor operating temperature. Using the most suitable process parameters, detailed plants of both approaches were implemented in Aspen Plus, including heat integration and a water Rankine cycle to make use of the reaction enthalpy. Finally, techno-economic analyses were applied. Both processes offered an excess

of heat, which was used to generate electricity in our work, but could alternatively supply other plants (e.g., CCU, OME synthesis) in a larger process integration.

It was demonstrated that CO₂ single-pass conversion almost doubled when including intermediate condensation steps (53.9 vs. 28.5%), resulting in a significantly higher overall conversion to methanol (97.7 vs. 94.3%) and in a higher exergy efficiency (78.8 vs. 76.4%). Because of the enhanced conversion, the new process required lower recycle and feed streams, decreasing net production costs by 61.2 M€·a⁻¹ (5.7%). Although additional equipment (i.e., heat exchangers and gas–liquid separators) is necessary, the improved process was significantly more efficient than the conventional approach, requiring lower sizes of the main equipment (e.g., compressors, reactors, fired heater). Consequently, according to our analysis, the total investment costs were 94.5 M€ (22.7%) lower than for the conventional process.

Table 4.6 Summary of the costs of the one-step and the three-step process. Reproduced with permission from Campos et al.¹¹. Copyright 2022, MDPI.

Item	Costs		Decrease (%)
	One-step	Three-step	
Equipment Costs (<i>EC</i>)	85.5 M€	66.1 M€	22.7
Fixed capital investment (<i>FCI</i>)	415.9 M€	321.4 M€	22.7
Working capital (<i>WC</i>)	46.2 M€	35.7 M€	22.7
Total <i>CAPEX</i>	462.1 M€	357.1 M€	22.7
Annual Capital Costs (<i>ACC</i>)	53.5 M€·a ⁻¹	41.3 M€·a ⁻¹	22.7
Direct <i>OPEX</i> (<i>OPEX_{dir}</i>)	874.9 M€·a ⁻¹	839.6 M€·a ⁻¹	4.0
Indirect <i>OPEX</i> (<i>OPEX_{ind}</i>)	143.4 M€·a ⁻¹	129.6 M€·a ⁻¹	9.6
Total <i>OPEX</i>	1018.3 M€·a ⁻¹	969.3 M€·a ⁻¹	4.8
Net Production Costs (<i>NPC</i>)	1071.8 M€·a ⁻¹	1010.6 M€·a ⁻¹	5.7

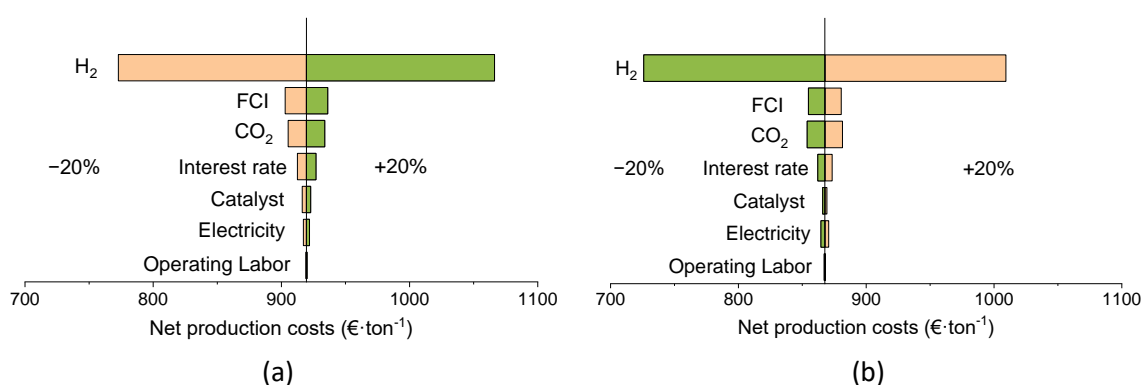


Fig. 4.10 Sensitivity analysis of the main cost factors in relation to the net production costs (NPC). Variation of $\pm 20\%$ in each factor. (a) One-step process. (b) Three-step process. Reproduced with permission from Campos et al.¹¹. Copyright 2022, MDPI.

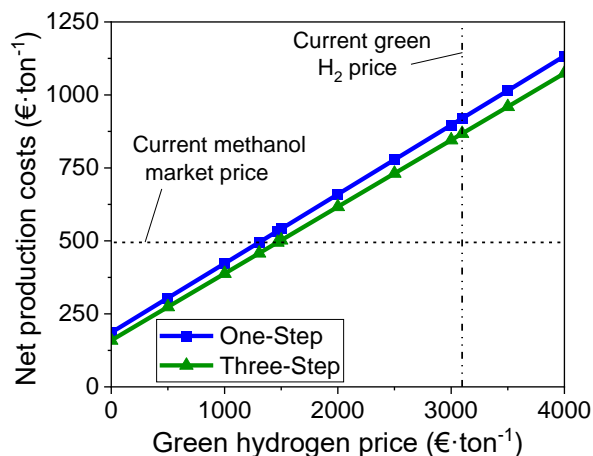


Fig. 4.11 Net production costs of methanol as a function of green hydrogen price. Reproduced with permission from Campos et al.¹¹. Copyright 2022, MDPI.

Intermediate condensation steps are therefore highly recommended for methanol production from H_2/CO_2 , reducing costs by improving CO_2 equilibrium conversion to methanol while using commercially proven technology. Besides, since water contributes to the deactivation of Cu-based catalysts, product intermediate removal should increase catalyst lifetime, as the average water concentration in the reactor is significantly lower than in the conventional process.

With our proposed process, the methanol net production costs amounted to $868 \text{ €}\cdot\text{ton}^{-1}$, which are still significantly higher than the current market price ($495 \text{ €}\cdot\text{ton}^{-1}$) but is believed to become economically viable with an effective reduction in the price of green hydrogen.

Chapter 5. Summary, Conclusions and Outlook

5.1 Summary and conclusions

The main goal of this thesis was to improve the mechanistic understanding and the kinetic modeling of the methanol synthesis at industrially relevant operating conditions. In order to address this objective, a microkinetic model of the methanol synthesis on Cu/Zn-based catalysts was developed, which was based on *ab initio* density functional theory calculations from Studt et al.^{18, 54} The reaction network of this model contemplates five possible reaction paths:

- CO hydrogenation on Cu active sites
- CO₂ hydrogenation on Cu active sites
- CO₂ hydrogenation on Cu/Zn active sites
- WGSR on Cu active sites via the water-assisted carboxyl path
- WGSR on Cu/Zn active sites via the water-assisted carboxyl path

Besides, since it is known from experimental and theoretical studies that dynamic changes on the surface of Cu/Zn-based catalysts (i.e., variation of the zinc coverage) may occur depending on the operating conditions, two different approaches were considered in the model:

- The DFT-based approach developed by Kuld et al.⁴⁵
- A simplified approach with constant zinc coverages based on the CO₂/CO_x initial ratio

Steady-state experiments at a variety of operating conditions were performed in a lab scale plug flow reactor. The microkinetic model adequately simulated both own experimental data and literature data. With the simplified approach for the zinc coverage estimation, better results were obtained than with the theoretical approach. Using the simplified approach, the average deviation of the model in relation to the experiments was 8%, 3%, and 21% for CO, CO₂ and methanol, respectively. While the model has some limitations to predict certain conditions at high CO₂-rich feed, accurate results were obtained at CO-rich feed.

With the validated microkinetic model, insights into the reaction mechanism were obtained. The main reaction pathway of the methanol synthesis proceeds via CO₂ hydrogenation on the active Cu/Zn site. If sufficient CO is available, the produced water reacts with CO via the WGSR, so that CO₂ is once again formed, and only CO is formally converted. Direct CO hydrogenation occurs at moderate rates if CO₂ concentration is low, but is mainly inhibited by formate strong adsorption (HCOO*) when CO₂ concentration is enhanced. At CO₂-rich conditions, CO and H₂O are produced via the rWGSR, whose reaction rate is highly sensitive to the operating temperature.

With the degree of rate control (DRC) method, it was found that formic acid (HCOOH*) hydrogenation followed by formate (HCOO*) hydrogenation are both rate controlling steps for methanol formation. In the rWGSR, the carboxyl (COOH*) formation was found to be the slowest step. Since formate covers most of the catalyst surface, it also contributes to the rWGSR inhibition. Therefore, catalyst design could address a stronger formate bonding, with which the rWGSR inhibition would be higher. Still, it cannot be excluded that the catalyst

activity towards CO₂ hydrogenation to methanol might also be negatively affected by stronger formate bonding.

An additional objective of this thesis was to deliver adequate kinetic models to be used in practical applications. To address this target, the developed microkinetic model was reduced to a formal kinetic model, due to its simplified implementation, and lower computational power requirements, making this type of model convenient for practical applications. Three different models were developed, with the most successful approach being Model-6p. In this model, concepts learned from the microkinetic model were extracted, i.e., the main reaction pathways, the rate-determining steps, and the most abundant surface species. The kinetic parameters were lumped and fitted to a large experimental database. Model-6p adequately simulated both own experimental data and literature data for the full studied operating region, with 86% of the 496 methanol points being inside the $\pm 20\%$ lines. With only six fitted parameters (typical amount of literature models: 10-12), it is unlikely that Model-6p is overfitting the data, which is supported by the adequate reproduction of the validation points (20% of the total database). The high accuracy of this model probably comes from the combination of fundamental theory and high quality experimental data.

The last objective of this thesis was to evaluate and optimize the production of methanol from H₂/CO₂. The developed Model-6p was used in a detailed plant simulation and a techno-economic analysis of the methanol synthesis from green H₂ and captured CO₂, in which the economic viability of intermediate condensation steps between reaction steps was evaluated. It was found out that the introduction of two condensation steps is significantly beneficial, as the CO₂ single-pass conversion increased from 28.5% (conventional process) to 53.9%, and the recycle stream reduced by 58%. Consequently, the required size of many equipment decreased significantly, so that the capital costs lowered by 94.5 M€ (-22.7%), in spite of extra equipment necessary for the condensation units. Besides, with lower recycle streams, less reactant is lost in the purge streams, enhancing the overall CO₂ conversion to methanol (from 94.3 to 97.7%), and being the main cause of a 49 M€·a⁻¹ reduction (-4.8%) of the operating costs. Thereby, it was shown that intermediate product removal via condensation steps is advantageous for a methanol synthesis plant with H₂/CO₂ as feed.

Additionally, plant simulations showed that CO concentration is maintained at low levels in the plant (between 1 and 4% v/v). In all reactor modules, there is an initial CO production via the rWGS, followed by CO consumption via the WGS, as the equilibrium direction is changed with an increase in water concentration. From a mass balance in each reactor, the conclusion is that CO is generated in the first reactor and consumed in the other two. While CO generation also produces water and slows down methanol production in the first reactor, it is beneficial to the operation of the other two reactors. This happens because water is removed in the intermediate condensation, but the extra CO remains, boosting the methanol synthesis. As a consequence, the optimized overall CO₂ selectivity to methanol is close to

100%. Therefore, in plant configurations with intermediate or in situ product removal, it is of little relevance to design a catalyst with lower selectivity for the rWGS than conventional Cu/Zn-based catalysts. First because the generated CO will boost methanol synthesis after water is removed, and second because the WGS equilibrium is shifted at an early stage (at low CO concentration).

5.2 Outlook

This contribution could be a basis for following advancements. Here, some suggestions for future works are given.

1. Extension of the microkinetic model to the methanol dehydration to DME

Direct DME synthesis from syngas, in which the Cu/Zn-based catalyst is mixed with an acid catalyst in a single reactor, is believed to gain increasing attractiveness, as the chemical equilibrium is pushed towards higher product formation (methanol and DME). As a further investigation, I suggest the straightforward development of a microkinetic model for the methanol dehydration to DME, which is then to be coupled with the methanol synthesis model. Due to the higher water amount from conversion of CO₂-rich feeds, zeolites are more suitable catalysts than γ -Al₂O₃, as it has been shown that the activity of the later drops significantly with an increase in water concentration.

2. Comparison of Power-to-methanol processes: With H₂O-electrolysis vs. with co-electrolysis of CO₂/H₂O

As concepts based on Power-to-X are needed in the transformation towards the future energy system, there are several options to combine related process steps. Two possibilities of syngas production from electricity and captured CO₂ are:

1. H₂O-electrolysis, producing O₂ and H₂, the latter can be combined with captured CO₂ to obtain a H₂/CO₂ synthesis gas;
2. Co-electrolysis of CO₂/H₂O, producing O₂, H₂ and CO. The resulting synthesis gas is a H₂/CO/CO₂ mixture.

In further investigations, the second option (co-electrolysis) could be simulated in combination with the methanol synthesis, evaluated economically, and compared with the first option (H₂O-electrolysis), which was presented in chapter 4 of this work. The comparison of both strategies is of interest, as the H₂O-electrolysis is less expensive but produces a less reactive gas (H₂/CO₂), while the more expensive co-electrolysis produces a more reactive mixture (H₂/CO/CO₂).

3. Comparison of power-to-DME processes: direct vs. indirect DME synthesis

Using the proposed model for the methanol synthesis (Model-6p), a formal kinetic model for the direct DME synthesis was developed in a parallel work.¹²² Using this new DME kinetic

model, the indirect and the direct route could be compared in a detailed process and economic analysis. While the advantage of the direct route is the improved chemical equilibrium in the reaction step, its disadvantage is the more complicated product separation process.

4. Using statistic models as an approximation method of DFT-derived data

DFT calculations and the resulting microkinetic model often succeed in predicting the trends and the influence of process parameters in the reaction rates, but may deviate from the absolute experimental values. In the present work, the microkinetic model adequately predicted the experiments for CO-rich feed, and more elevated deviations were seen for high CO₂ content in feed. With the development of the reduced Model-6p and the fitting of lumped parameters to the experimental data, it was possible to accurately simulate the whole studied operating region.

Statistic (or black-box) models could be an alternative approximation method to the formal kinetic model (gray-box). With a proper methodology, they could be trained by using both experimental data and simulated data from the microkinetic model, and might perform better than gray-box models in interpolations and extrapolations.

References

1. British Petroleum (BP) - bp Statistical review of world energy 2022 (71th ed.). Available at: <https://www.bp.com/content/dam/bp/business-sites/en/global/corporate/pdfs/energy-economics/statistical-review/bp-stats-review-2022-full-report.pdf> . (accessed June 2022).
2. M. Meinshausen, J. Lewis, C. McGlade, J. Gütschow, Z. Nicholls, R. Burdon, L. Cozzi and B. Hackmann, *Nature*, 2022, **604**, 304-309.
3. M. van der Spek, C. Banet, C. Bauer, P. Gabrielli, W. Goldthorpe, M. Mazzotti, S. T. Munkejord, N. A. Røkke, N. Shah, N. Sunny, D. Sutter, J. M. Trusler and M. Gazzani, *Energy & Environmental Science*, 2022, **15**, 1034-1077.
4. J. Artz, T. E. Müller, K. Thenert, J. Kleinekorte, R. Meys, A. Sternberg, A. Bardow and W. Leitner, *Chemical Reviews*, 2018, **118**, 434-504.
5. A. Sonthalia, N. Kumar, M. Tomar, V. Edwin Geo, S. Thiyagarajan and A. Pugazhendhi, *Clean Technologies and Environmental Policy*, 2021, DOI: 10.1007/s10098-021-02193-x.
6. Global Data - Methanol Market Capacity 2021. Available at: <https://www.globaldata.com/store/report/methanol-market-analysis/> . (accessed June 2022).
7. Methanol Institute - Methanol Fuel in China 2020. Available at: <https://www.methanol.org/methanol-fuel-in-china-full-report/> . (accessed July 2022).
8. X. Zhen and Y. Wang, *Renewable and Sustainable Energy Reviews*, 2015, **52**, 477-493.
9. Methanol Institute - Methanol safe handling manual. 2017, 4th Ed. Available at: <https://www.methanol.org/wp-content/uploads/2017/03/Safe-Handling-Manual.pdf> . (accessed July 2022).
10. Freepik., Flaticon Icons, <https://www.flaticon.com/authors/freepik>, (accessed June/2022).
11. B. Lacerda de Oliveira Campos, K. John, P. Beeskow, K. Herrera Delgado, S. Pitter, N. Dahmen and J. Sauer, *Processes*, 2022, **10**, 1535.
12. J. Ott, V. Gronemann, F. Pontzen, E. Fiedler, G. Grossmann, D. B. Kersebohm, G. Weiss and C. Witte, in *Ullmann's Encyclopedia of Industrial Chemistry*, 2012, DOI: 10.1002/14356007.a16_465.pub3.
13. G. Bozzano and F. Manenti, *Progress in Energy and Combustion Science*, 2016, **56**, 71-105.
14. D. Sheldon, *Johnson Matthey Technology Review*, 2017, **61**, 172-182.
15. Carbon Recycling International, *Renewable methanol from carbon dioxide*. Available at: <https://www.carbonrecycling.is/> . (accessed April 2022).
16. Siemens Energy, *The Haru Oni Hydrogen Plant*. Available at: <https://www.siemens-energy.com/global/en/news/magazine/2021/haru-oni.html> . (accessed February 2022).
17. M. Behrens, F. Studt, I. Kasatkin, S. Köhl, M. Hävecker, F. Abild-Pedersen, S. Zander, F. Girgsdies, P. Kurr, B.-L. Knief, M. Tovar, R. W. Fischer, J. K. Nørskov and R. Schlögl, *Science*, 2012, **336**, 893-897.
18. F. Studt, M. Behrens, E. L. Kunkes, N. Thomas, S. Zander, A. Tarasov, J. Schumann, E. Frei, J. B. Varley, F. Abild-Pedersen, J. K. Nørskov and R. Schlögl, *ChemCatChem*, 2015, **7**, 1105-1111.
19. R. M. Palomino, P. J. Ramírez, Z. Liu, R. Hamlyn, I. Waluyo, M. Mahapatra, I. Orozco, A. Hunt, J. P. Simonovis, S. D. Senanayake and J. A. Rodriguez, *The Journal of Physical Chemistry B*, 2018, **122**, 794-800.
20. T. Kamsuwan, C. Krutpijit, S. Praserttham, S. Phatanasri, B. Jongsomjit and P. Praserttham, *Heliyon*, 2021, **7**, e07682.
21. M. Behrens, *Catalysis Today*, 2015, **246**, 46-54.
22. N. Mota, R. Guil-Lopez, B. G. Pawelec, J. L. G. Fierro and R. M. Navarro, *RSC Advances*, 2018, **8**, 20619-20629.
23. U. Mondal and G. D. Yadav, *Green Chemistry*, 2021, **23**, 8361-8405.
24. S. Wild, S. Polierer, T. A. Zevaco, D. Guse, M. Kind, S. Pitter, K. Herrera Delgado and J. Sauer, *RSC Advances*, 2021, **11**, 2556-2564.

25. J. L. Snider, V. Streibel, M. A. Hubert, T. S. Choksi, E. Valle, D. C. Upham, J. Schumann, M. S. Duyar, A. Gallo, F. Abild-Pedersen and T. F. Jaramillo, *ACS Catalysis*, 2019, **9**, 3399-3412.
26. N. Lawes, I. Gow, L. R. Smith, K. Aggett, J. Hayward, L. Kabalan, A. J. Logsdail, T. Slater, M. Dearg, D. J. Morgan, N. F. Dummer, S. H. Taylor, R. Catlow, M. Bowker and G. Hutchings, *Faraday Discussions*, 2022, DOI: 10.1039/D2FD00119E.
27. Z. Han, C. Tang, J. Wang, L. Li and C. Li, *Journal of Catalysis*, 2021, **394**, 236-244.
28. S. Dang, B. Qin, Y. Yang, H. Wang, J. Cai, Y. Han, S. Li, P. Gao and Y. Sun, *Science Advances*, 2020, **6**, eaaz2060.
29. T. Cordero-Lanzac, A. Ramirez, A. Navajas, L. Gevers, S. Brunialti, L. M. Gandía, A. T. Aguayo, S. Mani Sarathy and J. Gascon, *Journal of Energy Chemistry*, 2022, **68**, 255-266.
30. B. An, J. Zhang, K. Cheng, P. Ji, C. Wang and W. Lin, *Journal of the American Chemical Society*, 2017, **139**, 3834-3840.
31. G. H. Graaf, E. J. Stamhuis and A. A. C. M. Beenackers, *Chemical Engineering Science*, 1988, **43**, 3185-3195.
32. H.-W. Lim, M.-J. Park, S.-H. Kang, H.-J. Chae, J. W. Bae and K.-W. Jun, *Industrial & Engineering Chemistry Research*, 2009, **48**, 10448-10455.
33. N. Park, M.-J. Park, Y.-J. Lee, K.-S. Ha and K.-W. Jun, *Fuel Processing Technology*, 2014, **125**, 139-147.
34. C. Seidel, A. Jörke, B. Vollbrecht, A. Seidel-Morgenstern and A. Kienle, *Chemical Engineering Science*, 2018, **175**, 130-138.
35. K. Klier, V. Chatikavanij, R. G. Herman and G. W. Simmons, *Journal of Catalysis*, 1982, **74**, 343-360.
36. H.-f. Ma, W.-y. Ying and D.-y. Fang, *Journal of Coal Science and Engineering (China)*, 2009, **15**, 98-103.
37. P. Villa, P. Forzatti, G. Buzzi-Ferraris, G. Garone and I. Pasquon, *Industrial & Engineering Chemistry Process Design and Development*, 1985, **24**, 12-19.
38. J. Skrzypek, M. Lachowska and H. Moroz, *Chemical Engineering Science*, 1991, **46**, 2809-2813.
39. K. M. V. Bussche and G. F. Froment, *Journal of Catalysis*, 1996, **161**, 1-10.
40. T. Kubota, I. Hayakawa, H. Mabuse, K. Mori, K. Ushikoshi, T. Watanabe and M. Saito, *Applied Organometallic Chemistry*, 2001, **15**, 121-126.
41. Y. Slotboom, M. J. Bos, J. Pieper, V. Vrieswijk, B. Likozar, S. R. A. Kersten and D. W. F. Brilman, *Chemical Engineering Journal*, 2020, **389**, 124181.
42. Y. Morikawa, K. Iwata, J. Nakamura, T. Fujitani and K. Terakura, *Chemical Physics Letters*, 1999, **304**, 91-97.
43. J. D. Grunwaldt, A. M. Molenbroek, N. Y. Topsøe, H. Topsøe and B. S. Clausen, *Journal of Catalysis*, 2000, **194**, 452-460.
44. R. van den Berg, G. Prieto, G. Korpershoek, L. I. van der Wal, A. J. van Bunningen, S. Lægsgaard-Jørgensen, P. E. de Jongh and K. P. de Jong, *Nature Communications*, 2016, **7**, 13057.
45. S. Kuld, M. Thorhauge, H. Falsig, C. F. Elkjær, S. Helveg, I. Chorkendorff and J. Sehested, *Science*, 2016, **352**, 969-974.
46. L. P. de Oliveira, D. Hudebine, D. Guillaume and J. J. Verstraete, *Oil Gas Sci. Technol. – Rev. IFP Energies nouvelles*, 2016, **71**, 45.
47. L. C. Grabow and M. Mavrikakis, *ACS Catalysis*, 2011, **1**, 365-384.
48. W. Janse van Rensburg, M. A. Petersen, M. S. Datt, J.-A. van den Berg and P. van Helden, *Catalysis Letters*, 2015, **145**, 559-568.
49. Y.-M. Liu, J.-T. Liu, S.-Z. Liu, J. Li, Z.-H. Gao, Z.-J. Zuo and W. Huang, *Journal of CO2 Utilization*, 2017, **20**, 59-65.
50. J. Park, J. Cho, Y. Lee, M.-J. Park and W. B. Lee, *Industrial & Engineering Chemistry Research*, 2019, **58**, 8663-8673.
51. D. Xu, P. Wu and B. Yang, *The Journal of Physical Chemistry C*, 2019, **123**, 8959-8966.
52. M. Huš, D. Kopač, N. S. Štefančič, D. L. Jurković, V. D. B. C. Dasireddy and B. Likozar, *Catalysis Science & Technology*, 2017, **7**, 5900-5913.
53. F. Studt, F. Abild-Pedersen, J. B. Varley and J. K. Nørskov, *Catalysis Letters*, 2013, **143**, 71-73.

54. F. Studt, M. Behrens and F. Abild-Pedersen, *Catalysis Letters*, 2014, **144**, 1973-1977.
55. Toyo Engineering, *G-Methanol*. Available at: <https://www.toyo-eng.com/jp/en/solution/g-methanol/>. (accessed May 2022).
56. Linde Engineering, *Isothermal reactor*. Available at: https://www.linde-engineering.com/en/process-plants/hydrogen_and_synthesis_gas_plants/gas_generation/isothermal_reactor/index.html. (accessed May 2022).
57. L. Perret, B. Lacerda de Oliveira Campos, K. Herrera Delgado, T. A. Zevaco, A. Neumann and J. Sauer, *Chemie Ingenieur Technik*, 2022, **94**, 1-22.
58. J. G. van Bennekom, R. H. Venderbosch, J. G. M. Winkelman, E. Wilbers, D. Assink, K. P. J. Lemmens and H. J. Heeres, *Chemical Engineering Science*, 2013, **87**, 204-208.
59. M. J. Bos and D. W. F. Brilman, *Chemical Engineering Journal*, 2015, **278**, 527-532.
60. M. Seshimo, B. Liu, H. R. Lee, K. Yogo, Y. Yamaguchi, N. Shigaki, Y. Mogi, H. Kita and S.-i. Nakao, *Membranes*, 2021, **11**, 505.
61. Johnson Matthey, *Methanol synthesis technology*. Available at: <https://matthey.com/en/products-and-services/chemical-processes/core-technologies/synthesis>. (accessed May 2022).
62. S. Polierer, J. Jelic, S. Pitter and F. Studt, *The Journal of Physical Chemistry C*, 2019, **123**, 26904-26911.
63. B. Hammer, *Physical Review B*, 2001, **63**, 205423.
64. A. B. Mhadeshwar, J. R. Kitchin, M. A. Barteau and D. G. Vlachos, *Catalysis Letters*, 2004, **96**, 13-22.
65. J. B. Hansen and P. E. H. Nielsen, in *Handbook of Heterogeneous Catalysis*, ed. E. H. G., Knözinger; F., Schüth; J., Weitkamp, 2nd edn., 2008, DOI: 10.1002/9783527610044.hetcat0148, 2920-2949.
66. D.-Y. Peng and D. B. Robinson, *Industrial & Engineering Chemistry Fundamentals*, 1976, **15**, 59-64.
67. L. Meng and Y.-Y. Duan, *Fluid Phase Equilibria*, 2005, **238**, 229-238.
68. L. Meng, Y.-Y. Duan and X.-D. Wang, *Fluid Phase Equilibria*, 2007, **260**, 354-358.
69. U. K. Deiters, *Fluid Phase Equilibria*, 2013, **352**, 93-96.
70. B. Lacerda de Oliveira Campos, K. Herrera Delgado, S. Wild, F. Studt, S. Pitter and J. Sauer, *Reaction Chemistry & Engineering*, 2021, **6**, 868-887.
71. H. Eyring, *The Journal of Chemical Physics*, 1935, **3**, 107-115.
72. M. G. Evans and M. Polanyi, *Transactions of the Faraday Society*, 1935, **31**, 875-894.
73. K. Herrera Delgado, L. Maier, S. Tischer, A. Zellner, H. Stotz and O. Deutschmann, *Catalysis*, 2015, **5**, 871-904.
74. H. Stotz, L. Maier, A. Boubnov, A. T. Gremminger, J. D. Grunwaldt and O. Deutschmann, *Journal of Catalysis*, 2019, **370**, 152-175.
75. E. Goos, A. Burcat and B. Ruscic, New NASA thermodynamic polynomials database. Available at: <http://garfield.chem.elte.hu/Burcat/THERM.DAT> (Access in Mar. 2022).
76. R. Schlögl, *Angewandte Chemie International Edition*, 2015, **54**, 3465-3520.
77. C. V. Ovesen, B. S. Clausen, J. Schiøtz, P. Stoltze, H. Topsøe and J. K. Nørskov, *Journal of Catalysis*, 1997, **168**, 133-142.
78. B. Lacerda de Oliveira Campos, K. Herrera Delgado, S. Wild, F. Studt, S. Pitter and J. Sauer, *Reaction Chemistry & Engineering*, 2021, **6**, 1483-1486.
79. B. Lacerda de Oliveira Campos, A. Oliveira Souza da Costa and E. Ferreira da Costa Junior, *Solar Energy*, 2017, **157**, 321-327.
80. B. Lacerda de Oliveira Campos, A. Oliveira Souza da Costa, K. Cecília de Souza Figueiredo and E. Ferreira da Costa Junior, *Desalination*, 2018, **437**, 184-194.
81. R. C. Kohberger, *Analytical Biochemistry*, 1980, **101**, 1-6.
82. B. Leite, T. Croguennec, A. Halabi and E. F. d. Costa Junior, *Journal of Food Engineering*, 2021, **292**, 110272.

83. C. Stegelmann, A. Andreasen and C. T. Campbell, *Journal of the American Chemical Society*, 2009, **131**, 8077-8082.
84. C. T. Campbell, *ACS Catalysis*, 2017, **7**, 2770-2779.
85. H. Ruland, H. Song, D. Laudenschleger, S. Stürmer, S. Schmidt, J. He, K. Kähler, M. Muhler and R. Schlögl, *ChemCatChem*, 2020, **12**, 3216-3222.
86. J. Thrane, S. Kuld, N. D. Nielsen, A. D. Jensen, J. Sehested and J. M. Christensen, *Angewandte Chemie International Edition*, 2020, **59**, 18189-18193.
87. M. S. Tameh, A. K. Dearden and C. Huang, *The Journal of Physical Chemistry C*, 2018, **122**, 17942-17953.
88. J. Park, H. S. Kim, W. B. Lee and M.-J. Park, *Catalysts*, 2020, **10**, 655.
89. B. Lacerda de Oliveira Campos, K. Herrera Delgado, S. Pitter and J. Sauer, *Industrial & Engineering Chemistry Research*, 2021, DOI: 10.1021/acs.iecr.1c02952.
90. Y. Guo, G. Li, J. Zhou and Y. Liu, *IOP Conference Series: Earth and Environmental Science*, 2019, **371**, 042022.
91. R. T. J. Porter, M. Fairweather, C. Kolster, N. Mac Dowell, N. Shah and R. M. Woolley, *International Journal of Greenhouse Gas Control*, 2017, **57**, 185-195.
92. J. G. v. Bennekom, J. G. M. Winkelman, R. H. Venderbosch, S. D. G. B. Nieland and H. J. Heeres, *Industrial & Engineering Chemistry Research*, 2012, **51**, 12233-12243.
93. R. Gaikwad, A. Bansode and A. Urakawa, *Journal of Catalysis*, 2016, **343**, 127-132.
94. Süd-Chemie AG. Safety Data Sheet - MegaMax 700. (2006).
95. J. Zhu, S. S. Araya, X. Cui, S. L. Sahlin and S. K. Kær, *Energies*, 2020, **13**, 610.
96. É. S. Van-Dal and C. Bouallou, *Journal of Cleaner Production*, 2013, **57**, 38-45.
97. F. Pontzen, W. Liebner, V. Gronemann, M. Rothaemel and B. Ahlers, *Catalysis Today*, 2011, **171**, 242-250.
98. D. Bongartz, J. Burre and A. Mitsos, *Industrial & Engineering Chemistry Research*, 2019, **58**, 4881-4889.
99. in *Reference Practice (RP) 535*, American Petroleum Institute (API), 3rd edn., 2014.
100. M. Gruber, *PhD Thesis, 275 p. Faculty of Chemical and Process Engineering, Karlsruhe Institute of Technology (KIT), Germany*, 2019.
101. *VDI Heat Atlas*, Springer, Berlin-Heidelberg, 2nd edn., 2010.
102. M. Saito and K. Murata, *Catalysis Surveys from Asia*, 2004, **8**, 285-294.
103. M. M. Campos Fraga, B. Lacerda de Oliveira Campos, M. S. Lisboa, T. B. Almeida, A. O. S. Costa and V. F. C. Lins, *Brazilian Journal of Chemical Engineering*, 2018, **35**, 1395-1403.
104. R. Nitzsche, M. Budzinski and A. Gröngröft, *Bioresource Technology*, 2016, **200**, 928-939.
105. D. W. Green and M. Z. Southard, *Perry's Chemical Engineers' Handbook*, McGraw Hill, 9th edn., 2018.
106. D. H. König, N. Baucks, R.-U. Dietrich and A. Wörner, *Energy*, 2015, **91**, 833-841.
107. F. G. Albrecht, D. H. König, N. Baucks and R.-U. Dietrich, *Fuel*, 2017, **194**, 511-526.
108. M. S. Peters, K. D. Timmerhaus and R. E. West, *Plant Design and Economics for Chemical Engineers*, McGraw-Hill Education Ltd, Boston, 5th edn., 2002.
109. M. Hennig and M. Haase, *Fuel Processing Technology*, 2021, **216**, 106776.
110. Travelex, *Worldwide money*. Available at: <https://www.travelex.com/currency/currency-pairs/usd-to-eur>. (accessed April 2022).
111. G. Towler and R. Sinnott, *Chemical Engineering Design - Principles, Practice and Economics of Plant and Process Design*, Elsevier, 2nd edn., 2013.
112. A. Aden, M. Ruth, K. Ibsen, J. Jechura, K. Neeves, J. Sheehan, B. Wallace, L. Montague, A. Slayton and J. Lukas, *Lignocellulosic Biomass to Ethanol Process Design and Economics Utilizing Co-Current Dilute Acid Prehydrolysis and Enzymatic Hydrolysis for Corn Stover*, United States, 2002.
113. N. P. Cheremisinoff, *Clean Electricity Through Advanced Coal Technologies*, Elsevier, 2012.
114. C. F. Bustillo-Lecompte, M. Mehrvar and E. Quiñones-Bolaños, *Journal of Environmental Management*, 2014, **134**, 145-152.

115. E. C. Tan, M. Talmadge, A. Dutta, J. Hensley, L. J. Snowden-Swan, D. Humbird, J. Schaidle and M. Bidy, *Biofuels, Bioproducts and Biorefining*, 2016, **10**, 17-35.
116. M. T. Ashraf and J. E. Schmidt, *Bioresource Technology*, 2018, **249**, 835-843.
117. J. F. O. Granjo and N. M. C. Oliveira, *Industrial & Engineering Chemistry Research*, 2016, **55**, 156-167.
118. S. Szima and C.-C. Cormos, *Journal of CO2 Utilization*, 2018, **24**, 555-563.
119. A. Prašnikar, A. Pavlišič, F. Ruiz-Zepeda, J. Kovač and B. Likozar, *Industrial & Engineering Chemistry Research*, 2019, **58**, 13021-13029.
120. Argus Media, *European Methanol Spot and Contract Prices*. Available at: <https://www.argusmedia.com/en/blog/2022/february/4/european-methanol-spot-and-contract-prices> . (accessed April 2022).
121. Methanol Institute - Methanol Prices, Supply and Demand. Available at: <https://www.methanol.org/methanol-price-supply-demand/> . (accessed April 2022).
122. S. Wild, B. Lacerda de Oliveira Campos, T. A. Zevaco, D. Guse, M. Kind, S. Pitter, K. Herrera Delgado and J. Sauer, *Reaction Chemistry & Engineering*, 2022, **7**, 943-956.

Supplementary Material (SM)

S1. Supplementary Material – Chapter 2

S1.1 Experimental setup

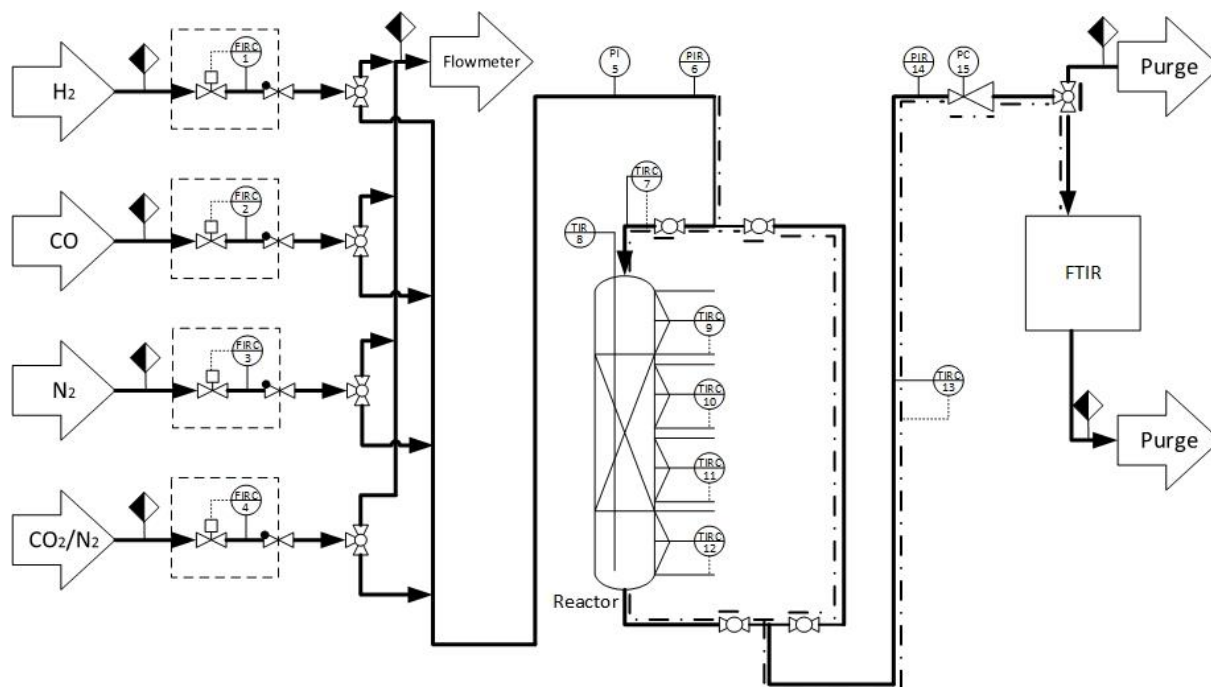


Fig. S1.1 Flow diagram of the single fixed-bed plug flow reactor (PFR). Reproduced with permission from Campos et al.⁷⁰. Copyright 2021, Royal Society of Chemistry.

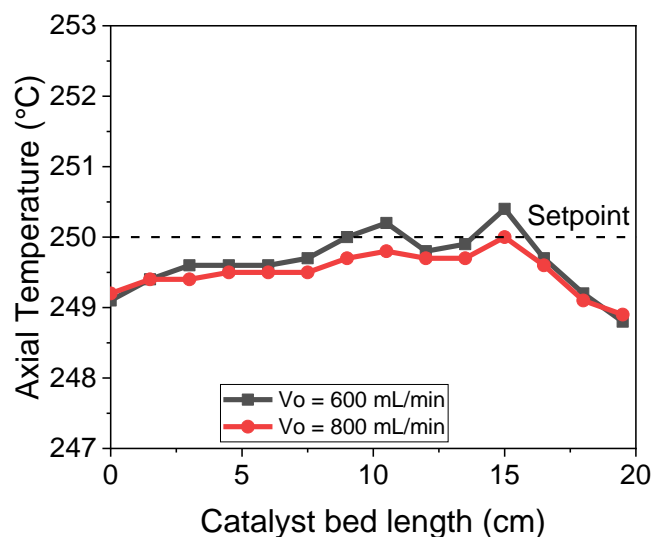


Fig. S1.2 Temperature axial profile of the reactor at 61 bar (abs.), 250 °C, $H_2/CO/CO_2/N_2 = 55/12/3/30\%$ v/v. Reproduced with permission from Campos et al.⁷⁰. Copyright 2021, Royal Society of Chemistry.

Table S1.1 Experimental data performed in the PFR. *Standard conditions: 298.15 K and 1 bar. Reproduced with permission from Campos et al.⁷⁰. Copyright 2021, Royal Society of Chemistry.

N°	Abs. Pres. (bar)	Vol. Flow* ($\frac{mL_s}{min}$)	Temp. (°C)	Inlet Flow (% v/v)				Outlet Flow (% v/v)		
				H ₂	CO	CO ₂	N ₂	CO	CO ₂	CH ₃ OH
1	41	600	220	35.33	11.51	2.68	50.48	10.9	2.58	0.77
2	41	600	235	35.33	11.51	2.68	50.48	10.82	2.61	1.13
3	41	600	250	35.33	11.51	2.68	50.48	10.47	2.66	1.65
4	41	800	220	35.32	11.55	2.68	50.45	11.11	2.58	0.58
5	41	800	235	35.32	11.55	2.68	50.45	11.02	2.6	0.87
6	41	800	250	35.32	11.55	2.68	50.45	10.69	2.64	1.34
7	41	600	220	35.37	8.61	5.50	50.52	8.23	5.28	0.8
8	41	600	235	35.37	8.61	5.50	50.52	8.11	5.32	1.11
9	41	600	250	35.37	8.61	5.50	50.52	7.83	5.41	1.52
10	41	800	220	35.36	8.63	5.50	50.51	8.43	5.26	0.62
11	41	800	235	35.36	8.63	5.50	50.51	8.31	5.29	0.86
12	41	800	250	35.36	8.63	5.50	50.51	8.12	5.37	1.24
13	41	600	220	35.34	5.80	8.37	50.49	5.55	7.98	0.78
14	41	600	235	35.34	5.80	8.37	50.49	5.49	7.98	1.02
15	41	600	250	35.34	5.80	8.37	50.49	5.34	7.99	1.23
16	41	800	220	35.36	5.75	8.37	50.52	5.65	7.97	0.63
17	41	800	235	35.36	5.75	8.37	50.52	5.68	7.94	0.83
18	41	800	250	35.36	5.75	8.37	50.52	5.55	7.98	1.03
19	41	600	210	45.38	12.94	1.34	40.34	12.71	1.25	0.54
20	41	600	220	45.38	12.94	1.34	40.34	12.65	1.28	0.74
21	41	600	230	45.38	12.94	1.34	40.34	12.45	1.3	1.12
22	41	600	240	45.38	12.94	1.34	40.34	12.13	1.32	1.59
23	41	600	250	45.38	12.94	1.34	40.34	11.78	1.34	2.02
24	41	600	260	45.38	12.94	1.34	40.34	11.59	1.36	2.27
25	41	800	210	45.34	13.01	1.35	40.30	12.83	1.26	0.39
26	41	800	220	45.34	13.01	1.35	40.30	12.73	1.28	0.54
27	41	800	230	45.34	13.01	1.35	40.30	12.64	1.29	0.83
28	41	800	240	45.34	13.01	1.35	40.30	12.36	1.31	1.19
29	41	800	250	45.34	13.01	1.35	40.30	12.09	1.33	1.61
30	41	800	260	45.34	13.01	1.35	40.30	11.87	1.35	1.89
31	41	600	210	45.32	11.71	2.69	40.28	11.48	2.59	0.51
32	41	600	220	45.32	11.71	2.69	40.28	11.35	2.56	0.79
33	41	600	230	45.32	11.71	2.69	40.28	11.03	2.59	1.16
34	41	600	240	45.32	11.71	2.69	40.28	10.68	2.62	1.7
35	41	600	250	45.32	11.71	2.69	40.28	10.26	2.65	2.21
36	41	600	260	45.32	11.71	2.69	40.28	10.05	2.68	2.51
37	41	800	210	45.29	11.76	2.70	40.25	11.62	2.56	0.39
38	41	800	220	45.29	11.76	2.70	40.25	11.49	2.55	0.59
39	41	800	230	45.29	11.76	2.70	40.25	11.32	2.57	0.88
40	41	800	240	45.29	11.76	2.70	40.25	11	2.6	1.27
41	41	800	250	45.29	11.76	2.70	40.25	10.63	2.62	1.74
42	41	800	260	45.29	11.76	2.70	40.25	10.34	2.65	2.09
43	41	1000	210	45.26	11.79	2.71	40.24	11.72	2.56	0.32
44	41	1000	220	45.26	11.79	2.71	40.24	11.56	2.55	0.47
45	41	1000	230	45.26	11.79	2.71	40.24	11.43	2.56	0.7
46	41	1000	240	45.26	11.79	2.71	40.24	11.18	2.58	1.02
47	41	1000	250	45.26	11.79	2.71	40.24	10.9	2.62	1.43
48	41	1000	260	45.26	11.79	2.71	40.24	10.61	2.64	1.79
49	41	600	210	45.33	11.72	5.68	37.27	11.65	5.44	0.64
50	41	600	220	45.33	11.72	5.68	37.27	11.55	5.51	0.86

Table S1.1 (continuation)

N°	Abs. Pres. (bar)	Vol. Flow* ($\frac{mL_s}{min}$)	Temp. (°C)	Inlet Flow (% v/v)				Outlet Flow (% v/v)		
				H ₂	CO	CO ₂	N ₂	CO	CO ₂	CH ₃ OH
51	41	600	230	45.33	11.72	5.68	37.27	11.23	5.57	1.22
52	41	600	240	45.33	11.72	5.68	37.27	10.88	5.64	1.73
53	41	600	250	45.33	11.72	5.68	37.27	10.49	5.73	2.23
54	41	600	260	45.33	11.72	5.68	37.27	10.33	5.79	2.48
55	41	800	210	45.34	11.72	5.66	37.28	11.74	5.45	0.5
56	41	800	220	45.34	11.72	5.66	37.28	11.69	5.48	0.66
57	41	800	230	45.34	11.72	5.66	37.28	11.53	5.53	0.92
58	41	800	240	45.34	11.72	5.66	37.28	11.21	5.56	1.3
59	41	800	250	45.34	11.72	5.66	37.28	10.87	5.64	1.75
60	41	800	260	45.34	11.72	5.66	37.28	10.68	5.72	2.06
61	41	600	210	45.37	10.10	4.20	40.33	9.93	3.99	0.61
62	41	600	220	45.37	10.10	4.20	40.33	9.93	4.06	0.82
63	41	600	230	45.37	10.10	4.20	40.33	9.63	4.09	1.18
64	41	600	240	45.37	10.10	4.20	40.33	9.22	4.14	1.66
65	41	600	250	45.37	10.10	4.20	40.33	8.9	4.2	2.09
66	41	600	260	45.37	10.10	4.20	40.33	8.74	4.23	2.25
67	41	800	210	45.36	10.12	4.20	40.32	10.09	4	0.48
68	41	800	220	45.36	10.12	4.20	40.32	10.08	4.03	0.63
69	41	800	230	45.36	10.12	4.20	40.32	9.87	4.05	0.89
70	41	800	240	45.36	10.12	4.20	40.32	9.62	4.11	1.26
71	41	800	250	45.36	10.12	4.20	40.32	9.24	4.14	1.66
72	41	800	260	45.36	10.12	4.20	40.32	9.06	4.18	1.9
73	41	600	210	45.36	8.54	2.76	43.34	8.41	2.55	0.59
74	41	600	220	45.36	8.54	2.76	43.34	8.38	2.59	0.78
75	41	600	230	45.36	8.54	2.76	43.34	8.09	2.62	1.13
76	41	600	240	45.36	8.54	2.76	43.34	7.75	2.66	1.56
77	41	600	250	45.36	8.54	2.76	43.34	7.42	2.69	1.89
78	41	600	260	45.36	8.54	2.76	43.34	7.31	2.7	1.98
79	41	800	210	45.33	8.63	2.73	43.31	8.52	2.55	0.45
80	41	800	220	45.33	8.63	2.73	43.31	8.46	2.59	0.59
81	41	800	230	45.33	8.63	2.73	43.31	8.37	2.6	0.86
82	41	800	240	45.33	8.63	2.73	43.31	8.05	2.63	1.19
83	41	800	250	45.33	8.63	2.73	43.31	7.79	2.66	1.53
84	41	800	260	45.33	8.63	2.73	43.31	7.6	2.68	1.71
85	41	600	210	45.35	8.76	5.58	40.31	8.63	5.28	0.6
86	41	600	220	45.35	8.76	5.58	40.31	8.53	5.28	0.86
87	41	600	230	45.35	8.76	5.58	40.31	8.36	5.31	1.19
88	41	600	240	45.35	8.76	5.58	40.31	7.98	5.35	1.63
89	41	600	250	45.35	8.76	5.58	40.31	7.61	5.39	2.05
90	41	600	260	45.35	8.76	5.58	40.31	7.5	5.4	2.2
91	41	800	210	45.30	8.84	5.59	40.27	8.72	5.29	0.47
92	41	800	220	45.30	8.84	5.59	40.27	8.69	5.29	0.66
93	41	800	230	45.30	8.84	5.59	40.27	8.54	5.27	0.91
94	41	800	240	45.30	8.84	5.59	40.27	8.37	5.31	1.25
95	41	800	250	45.30	8.84	5.59	40.27	8.08	5.31	1.61
96	41	800	260	45.30	8.84	5.59	40.27	7.82	5.35	1.87
97	41	1000	210	45.27	8.88	5.61	40.24	8.81	5.33	0.39
98	41	1000	220	45.27	8.88	5.61	40.24	8.72	5.28	0.54
99	41	1000	230	45.27	8.88	5.61	40.24	8.7	5.28	0.75
100	41	1000	240	45.27	8.88	5.61	40.24	8.5	5.3	1.03

Table S1.1 (continuation)

N°	Abs. Pres. (bar)	Vol. Flow* ($\frac{mL_s}{min}$)	Temp. (°C)	Inlet Flow (% v/v)				Outlet Flow (% v/v)		
				H ₂	CO	CO ₂	N ₂	CO	CO ₂	CH ₃ OH
101	41	1000	250	45.27	8.88	5.61	40.24	8.33	5.3	1.34
102	41	1000	260	45.27	8.88	5.61	40.24	8.04	5.33	1.62
103	41	600	210	45.19	8.82	8.84	37.15	8.84	8.37	0.67
104	41	600	220	45.19	8.82	8.84	37.15	8.72	8.38	0.87
105	41	600	230	45.19	8.82	8.84	37.15	8.52	8.41	1.16
106	41	600	240	45.19	8.82	8.84	37.15	8.26	8.47	1.51
107	41	600	250	45.19	8.82	8.84	37.15	8.06	8.54	1.83
108	41	600	260	45.19	8.82	8.84	37.15	8	8.59	2.01
109	41	800	210	45.15	8.89	8.83	37.13	8.86	8.39	0.54
110	41	800	220	45.15	8.89	8.83	37.13	8.89	8.41	0.69
111	41	800	230	45.15	8.89	8.83	37.13	8.74	8.37	0.91
112	41	800	240	45.15	8.89	8.83	37.13	8.54	8.39	1.21
113	41	800	250	45.15	8.89	8.83	37.13	8.36	8.41	1.52
114	41	800	260	45.15	8.89	8.83	37.13	8.28	8.47	1.73
115	41	600	210	45.19	7.32	7.33	40.16	7.28	6.82	0.66
116	41	600	220	45.19	7.32	7.33	40.16	7.21	6.86	0.85
117	41	600	230	45.19	7.32	7.33	40.16	6.99	6.86	1.12
118	41	600	240	45.19	7.32	7.33	40.16	6.74	6.9	1.44
119	41	600	250	45.19	7.32	7.33	40.16	6.48	6.92	1.72
120	41	600	260	45.19	7.32	7.33	40.16	6.49	6.97	1.76
121	41	800	210	45.17	7.35	7.32	40.16	7.39	6.86	0.53
122	41	800	220	45.17	7.35	7.32	40.16	7.36	6.87	0.67
123	41	800	230	45.17	7.35	7.32	40.16	7.19	6.82	0.89
124	41	800	240	45.17	7.35	7.32	40.16	7.03	6.84	1.16
125	41	800	250	45.17	7.35	7.32	40.16	6.79	6.87	1.43
126	41	800	260	45.17	7.35	7.32	40.16	6.69	6.88	1.58
127	41	600	210	45.19	5.82	5.81	43.18	5.74	5.3	0.64
128	41	600	220	45.19	5.82	5.81	43.18	5.65	5.3	0.82
129	41	600	230	45.19	5.82	5.81	43.18	5.45	5.3	1.08
130	41	600	240	45.19	5.82	5.81	43.18	5.2	5.32	1.36
131	41	600	250	45.19	5.82	5.81	43.18	5.03	5.36	1.56
132	41	600	260	45.19	5.82	5.81	43.18	5.05	5.35	1.55
133	41	800	210	45.18	5.84	5.80	43.18	5.79	5.3	0.51
134	41	800	220	45.18	5.84	5.80	43.18	5.78	5.32	0.65
135	41	800	230	45.18	5.84	5.80	43.18	5.64	5.28	0.86
136	41	800	240	45.18	5.84	5.80	43.18	5.45	5.27	1.1
137	41	800	250	45.18	5.84	5.80	43.18	5.31	5.31	1.32
138	41	800	260	45.18	5.84	5.80	43.18	5.24	5.3	1.39
139	41	600	210	45.31	5.87	8.54	40.28	5.85	8.08	0.67
140	41	600	220	45.31	5.87	8.54	40.28	5.79	8.04	0.88
141	41	600	230	45.31	5.87	8.54	40.28	5.65	7.98	1.15
142	41	600	240	45.31	5.87	8.54	40.28	5.43	7.98	1.45
143	41	600	250	45.31	5.87	8.54	40.28	5.28	7.98	1.67
144	41	600	260	45.31	5.87	8.54	40.28	5.29	7.97	1.7
145	41	800	210	45.31	5.89	8.52	40.28	5.92	8.14	0.54
146	41	800	220	45.31	5.89	8.52	40.28	5.9	8.06	0.71
147	41	800	230	45.31	5.89	8.52	40.28	5.83	7.98	0.92
148	41	800	240	45.31	5.89	8.52	40.28	5.7	7.94	1.16
149	41	800	250	45.31	5.89	8.52	40.28	5.56	7.94	1.39
150	41	800	260	45.31	5.89	8.52	40.28	5.48	7.9	1.51

Table S1.1 (continuation)

N°	Abs. Pres. (bar)	Vol. Flow* ($\frac{mL_s}{min}$)	Temp. (°C)	Inlet Flow (% v/v)				Outlet Flow (% v/v)		
				H ₂	CO	CO ₂	N ₂	CO	CO ₂	CH ₃ OH
151	41	1000	210	45.29	5.92	8.53	40.26	5.91	8.17	0.46
152	41	1000	220	45.29	5.92	8.53	40.26	5.96	8.08	0.6
153	41	1000	230	45.29	5.92	8.53	40.26	5.94	8.01	0.79
154	41	1000	240	45.29	5.92	8.53	40.26	5.87	7.94	0.99
155	41	1000	250	45.29	5.92	8.53	40.26	5.75	7.9	1.19
156	41	1000	260	45.29	5.92	8.53	40.26	5.62	7.84	1.33
157	41	600	210	45.14	4.34	10.39	40.13	4.44	9.74	0.7
158	41	600	220	45.14	4.34	10.39	40.13	4.45	9.68	0.87
159	41	600	230	45.14	4.34	10.39	40.13	4.39	9.58	1.03
160	41	600	240	45.14	4.34	10.39	40.13	4.34	9.57	1.19
161	41	600	250	45.14	4.34	10.39	40.13	4.29	9.45	1.32
162	41	600	260	45.14	4.34	10.39	40.13	4.4	9.39	1.33
163	41	800	210	45.12	4.37	10.41	40.10	4.47	9.79	0.58
164	41	800	220	45.12	4.37	10.41	40.10	4.5	9.7	0.72
165	41	800	230	45.12	4.37	10.41	40.10	4.51	9.61	0.89
166	41	800	240	45.12	4.37	10.41	40.10	4.5	9.52	1.04
167	41	800	250	45.12	4.37	10.41	40.10	4.45	9.4	1.16
168	41	800	260	45.12	4.37	10.41	40.10	4.54	9.34	1.2
169	41	600	210	45.34	2.86	11.49	40.31	3.04	11.18	0.66
170	41	600	220	45.34	2.86	11.49	40.31	3.13	11.24	0.82
171	41	600	230	45.34	2.86	11.49	40.31	3.22	11.09	0.96
172	41	600	240	45.34	2.86	11.49	40.31	3.16	10.94	1.07
173	41	600	250	45.34	2.86	11.49	40.31	3.38	10.86	1.17
174	41	600	260	45.34	2.86	11.49	40.31	3.52	10.74	1.13
175	41	800	210	45.35	2.87	11.46	40.32	3.05	11.3	0.55
176	41	800	220	45.35	2.87	11.46	40.32	3.13	11.31	0.68
177	41	800	230	45.35	2.87	11.46	40.32	3.24	11.16	0.84
178	41	800	240	45.35	2.87	11.46	40.32	3.25	10.94	0.95
179	41	800	250	45.35	2.87	11.46	40.32	3.47	10.84	1.07
180	41	800	260	45.35	2.87	11.46	40.32	3.6	10.7	1.06
181	41	1000	210	45.33	2.89	11.48	40.30	3.05	11.35	0.47
182	41	1000	220	45.33	2.89	11.48	40.30	3.13	11.42	0.59
183	41	1000	230	45.33	2.89	11.48	40.30	3.22	11.19	0.74
184	41	1000	240	45.33	2.89	11.48	40.30	3.32	11.01	0.87
185	41	1000	250	45.33	2.89	11.48	40.30	3.5	10.81	0.98
186	41	1000	260	45.33	2.89	11.48	40.30	3.64	10.67	1
187	41	600	220	55.22	11.94	2.72	30.12	11.62	2.53	0.88
188	41	600	235	55.22	11.94	2.72	30.12	11	2.59	1.73
189	41	600	250	55.22	11.94	2.72	30.12	10.18	2.66	2.89
190	41	800	220	55.15	12.03	2.74	30.08	11.72	2.53	0.66
191	41	800	235	55.15	12.03	2.74	30.08	11.34	2.56	1.28
192	41	800	250	55.15	12.03	2.74	30.08	10.59	2.62	2.22
193	41	600	220	55.23	8.99	5.66	30.12	8.74	5.26	0.96
194	41	600	235	55.23	8.99	5.66	30.12	8.25	5.29	1.73
195	41	600	250	55.23	8.99	5.66	30.12	7.56	5.41	2.62
196	41	800	220	55.20	9.02	5.67	30.11	8.91	5.27	0.76
197	41	800	235	55.20	9.02	5.67	30.11	8.54	5.25	1.31
198	41	800	250	55.20	9.02	5.67	30.11	8.06	5.33	2.04
199	41	600	220	55.17	6.01	8.72	30.10	5.98	8.06	1.04
200	41	600	235	55.17	6.01	8.72	30.10	5.68	8	1.6

Table S1.1 (continuation)

N°	Abs. Pres. (bar)	Vol. Flow* ($\frac{mL_s}{min}$)	Temp. (°C)	Inlet Flow (% v/v)				Outlet Flow (% v/v)		
				H ₂	CO	CO ₂	N ₂	CO	CO ₂	CH ₃ OH
201	41	600	250	55.17	6.01	8.72	30.10	5.31	8.01	2.15
202	41	800	220	55.16	6.03	8.72	30.09	6.08	8.09	0.85
203	41	800	235	55.16	6.03	8.72	30.09	5.93	7.95	1.29
204	41	800	250	55.16	6.03	8.72	30.09	5.65	7.93	1.75
205	41	600	220	60.31	15.84	3.75	20.10	15.68	3.79	0.96
206	41	600	250	60.31	15.84	3.75	20.10	14.44	4.02	3.18
207	41	800	220	60.19	16.01	3.74	20.06	15.85	3.76	0.74
208	41	800	250	60.19	16.01	3.74	20.06	14.93	3.91	2.37
209	41	600	220	60.10	12.12	7.75	20.03	11.84	7.85	1.07
210	41	600	250	60.10	12.12	7.75	20.03	10.61	8.05	2.8
211	41	800	220	60.07	12.16	7.75	20.02	11.98	7.88	0.83
212	41	800	250	60.07	12.16	7.75	20.02	11.25	7.9	2.17
213	41	600	220	60.27	8.01	11.63	20.09	8.07	11.95	1.13
214	41	600	250	60.27	8.01	11.63	20.09	7.45	11.94	2.33
215	41	800	220	60.31	8.00	11.59	20.10	8.23	11.98	0.92
216	41	800	250	60.31	8.00	11.59	20.10	7.91	11.82	1.92
217	61	600	220	35.37	11.47	2.64	50.52	11.02	2.56	0.96
218	61	800	220	35.33	11.52	2.67	50.48	11.25	2.57	0.72
219	61	600	220	45.38	11.66	2.63	40.33	11.01	2.52	1.07
220	61	800	220	45.31	11.75	2.67	40.27	11.3	2.51	0.81
221	61	1000	220	45.31	11.73	2.69	40.27	11.49	2.51	0.64
222	61	600	220	55.28	11.84	2.72	30.16	11.27	2.5	1.39
223	61	800	220	55.21	11.94	2.74	30.11	11.57	2.48	1.02
224	61	600	235	45.38	11.66	2.63	40.33	10.41	2.59	2.07
225	61	800	235	45.31	11.75	2.67	40.27	10.85	2.56	1.51
226	61	1000	235	45.31	11.73	2.69	40.27	11.17	2.55	1.18
227	61	600	250	45.38	11.66	2.63	40.33	9.33	2.69	3.64
228	61	800	250	45.31	11.75	2.67	40.27	9.93	2.64	2.81
229	61	1000	250	45.31	11.73	2.69	40.27	10.36	2.61	2.26
230	61	600	250	55.28	11.84	2.72	30.16	8.35	2.78	5.33
231	61	800	250	55.21	11.94	2.74	30.11	9.2	2.71	4.57
232	61	600	220	45.37	8.75	5.56	40.32	8.35	5.2	1.12
233	61	800	220	45.35	8.78	5.56	40.31	8.56	5.2	0.87
234	61	1000	220	45.36	8.77	5.55	40.32	8.7	5.22	0.72
235	61	600	235	45.37	8.75	5.56	40.32	7.73	5.29	1.91
236	61	800	235	45.35	8.78	5.56	40.31	8.18	5.23	1.47
237	61	1000	235	45.36	8.77	5.55	40.32	8.39	5.22	1.18
238	61	600	250	45.37	8.75	5.56	40.32	6.76	5.42	3.21
239	61	800	250	45.35	8.78	5.56	40.31	7.41	5.34	2.51
240	61	1000	250	45.36	8.77	5.55	40.32	7.82	5.29	2.03
241	61	600	220	35.37	5.75	8.36	50.52	5.54	7.94	0.99
242	61	800	220	35.36	5.75	8.37	50.52	5.72	7.95	0.79
243	61	600	220	45.33	5.86	8.52	40.29	5.68	7.94	1.1
244	61	800	220	45.35	5.85	8.48	40.32	5.84	7.94	0.93
245	61	1000	220	45.33	5.89	8.49	40.29	5.91	7.97	0.78
246	61	600	220	55.19	5.97	8.74	30.10	5.8	7.94	1.41
247	61	800	220	55.17	6.01	8.73	30.09	5.99	7.95	1.17
248	61	600	235	45.33	5.86	8.52	40.29	5.3	7.96	1.72
249	61	800	235	45.35	5.85	8.48	40.32	5.59	7.89	1.38
250	61	1000	235	45.33	5.89	8.49	40.29	5.75	7.84	1.17

Table S1.1 (continuation)

N°	Abs. Pres. (bar)	Vol. Flow* ($\frac{mL_s}{min}$)	Temp. (°C)	Inlet Flow (% v/v)				Outlet Flow (% v/v)		
				H ₂	CO	CO ₂	N ₂	CO	CO ₂	CH ₃ OH
251	61	600	250	35.37	5.75	8.36	50.52	4.62	8.08	2.17
252	61	800	250	35.36	5.75	8.37	50.52	5.04	8	1.78
253	61	600	250	45.33	5.86	8.52	40.29	4.67	7.97	2.6
254	61	800	250	45.35	5.85	8.48	40.32	5.14	7.9	2.05
255	61	1000	250	45.33	5.89	8.49	40.29	5.41	7.84	1.73
256	61	600	250	55.19	5.97	8.74	30.10	4.41	8.02	3.44
257	61	800	250	55.17	6.01	8.73	30.09	5.04	7.94	2.69
258	61	600	220	45.32	2.90	11.49	40.29	3.08	10.66	1.06
259	61	800	220	45.33	2.91	11.46	40.30	3.13	10.74	0.94
260	61	1000	220	45.31	2.94	11.48	40.27	3.13	10.78	0.83
261	61	600	235	45.32	2.90	11.49	40.29	3.07	10.4	1.42
262	61	800	235	45.33	2.91	11.46	40.30	3.18	10.42	1.24
263	61	1000	235	45.31	2.94	11.48	40.27	3.23	10.48	1.14
264	61	600	250	45.32	2.90	11.49	40.29	2.97	10.26	1.82
265	61	800	250	45.33	2.91	11.46	40.30	3.18	10.23	1.52
266	61	1000	250	45.31	2.94	11.48	40.27	3.31	10.23	1.41
267	41	600	220	20.67	28.30	4.53	46.50	28	4.53	0.53
268	41	600	230	20.67	28.30	4.53	46.50	27.92	4.54	0.82
269	41	600	240	20.67	28.30	4.53	46.50	27.95	4.59	1.16
270	41	600	250	20.67	28.30	4.53	46.50	27.88	4.64	1.4
271	41	600	260	20.67	28.30	4.53	46.50	27.77	4.66	1.42
272	41	800	220	20.62	28.51	4.49	46.38	28.1	4.52	0.39
273	41	800	230	20.62	28.51	4.49	46.38	28.21	4.53	0.61
274	41	800	240	20.62	28.51	4.49	46.38	28.03	4.55	0.89
275	41	800	250	20.62	28.51	4.49	46.38	28.11	4.62	1.15
276	41	800	260	20.62	28.51	4.49	46.38	27.88	4.63	1.23
277	41	600	220	30.78	28.56	2.70	37.96	28.4	2.68	0.71
278	41	600	230	30.78	28.56	2.70	37.96	28.38	2.7	1.12
279	41	600	240	30.78	28.56	2.70	37.96	28.21	2.74	1.67
280	41	600	250	30.78	28.56	2.70	37.96	27.98	2.79	2.16
281	41	600	260	30.78	28.56	2.70	37.96	27.83	2.84	2.39
282	41	800	220	30.74	28.64	2.71	37.91	28.39	2.67	0.52
283	41	800	230	30.74	28.64	2.71	37.91	28.35	2.68	0.83
284	41	800	240	30.74	28.64	2.71	37.91	28.47	2.72	1.26
285	41	800	250	30.74	28.64	2.71	37.91	28.19	2.76	1.72
286	41	800	260	30.74	28.64	2.71	37.91	27.92	2.8	2.01
287	41	600	230	30.78	28.72	4.58	35.92	28.51	4.62	1.12
288	41	600	240	30.78	28.72	4.58	35.92	28.53	4.7	1.7
289	41	600	250	30.78	28.72	4.58	35.92	28.22	4.77	2.26
290	41	600	260	30.78	28.72	4.58	35.92	28.16	4.83	2.54
291	41	800	230	31.07	28.16	4.53	36.24	28.72	4.59	0.84
292	41	800	240	31.07	28.16	4.53	36.24	28.59	4.64	1.27
293	41	800	250	31.07	28.16	4.53	36.24	28.59	4.73	1.77
294	41	800	260	31.07	28.16	4.53	36.24	28.27	4.76	2.12
295	41	600	220	30.72	29.02	7.49	32.77	28.93	7.46	0.77
296	41	600	230	30.72	29.02	7.49	32.77	28.96	7.58	1.2
297	41	600	240	30.72	29.02	7.49	32.77	28.78	7.68	1.84
298	41	600	250	30.72	29.02	7.49	32.77	28.59	7.82	2.48
299	41	600	260	30.72	29.02	7.49	32.77	28.19	7.86	2.76
300	41	800	220	30.72	29.03	7.49	32.76	28.9	7.42	0.57

Table S1.1 (continuation)

N°	Abs. Pres. (bar)	Vol. Flow* ($\frac{mL_s}{min}$)	Temp. (°C)	Inlet Flow (% v/v)				Outlet Flow (% v/v)		
				H ₂	CO	CO ₂	N ₂	CO	CO ₂	CH ₃ OH
301	41	800	230	30.72	29.03	7.49	32.76	28.89	7.47	0.89
302	41	800	240	30.72	29.03	7.49	32.76	28.95	7.58	1.37
303	41	800	250	30.72	29.03	7.49	32.76	28.83	7.69	1.92
304	41	800	260	30.72	29.03	7.49	32.76	28.42	7.75	2.3
305	41	600	220	30.31	30.32	19.17	20.20	30.36	19.33	0.79
306	41	600	230	30.31	30.32	19.17	20.20	30.13	19.39	1.18
307	41	600	240	30.31	30.32	19.17	20.20	29.95	19.61	1.74
308	41	600	250	30.31	30.32	19.17	20.20	29.89	19.97	2.37
309	41	600	260	30.31	30.32	19.17	20.20	29.57	20.11	2.75
310	41	800	220	30.17	30.42	19.29	20.12	30.37	19.15	0.61
311	41	800	230	30.17	30.42	19.29	20.12	30.32	19.26	0.89
312	41	800	240	30.17	30.42	19.29	20.12	30.34	19.46	1.3
313	41	800	250	30.17	30.42	19.29	20.12	30.18	19.72	1.81
314	41	800	260	30.17	30.42	19.29	20.12	29.78	19.86	2.22
315	41	600	220	40.66	29.25	4.68	25.41	28.96	4.62	0.91
316	41	600	230	40.66	29.25	4.68	25.41	29.09	4.69	1.47
317	41	600	240	40.66	29.25	4.68	25.41	28.85	4.78	2.31
318	41	600	250	40.66	29.25	4.68	25.41	28.71	4.92	3.27
319	41	600	260	40.66	29.25	4.68	25.41	28.46	5.01	3.91
320	41	800	220	40.65	29.27	4.68	25.40	29.16	4.6	0.68
321	41	800	230	40.65	29.27	4.68	25.40	28.89	4.61	1.06
322	41	800	240	40.65	29.27	4.68	25.40	29.06	4.71	1.69
323	41	800	250	40.65	29.27	4.68	25.40	28.9	4.81	2.47
324	41	800	260	40.65	29.27	4.68	25.40	28.59	4.91	3.16
325	41	600	210	35.42	13.98	0.00	50.60	13.84	0	0.07
326	41	600	250	35.42	13.98	0.00	50.60	13.64	0.01	0.3
327	41	800	210	35.42	13.97	0.00	50.61	13.91	0	0.05
328	41	800	250	35.42	13.97	0.00	50.61	13.75	0.01	0.21
329	41	600	210	45.40	14.24	0.00	40.36	14.14	0	0.09
330	41	600	220	45.40	14.24	0.00	40.36	14.03	0	0.12
331	41	600	230	45.40	14.24	0.00	40.36	14.02	0	0.17
332	41	600	240	45.40	14.24	0.00	40.36	14.01	0	0.25
333	41	600	250	45.40	14.24	0.00	40.36	13.87	0.01	0.4
334	41	600	260	45.40	14.24	0.00	40.36	13.77	0.02	0.51
335	41	800	210	45.28	14.47	0.00	40.25	14.16	0	0.06
336	41	800	220	45.28	14.47	0.00	40.25	14.15	0	0.09
337	41	800	230	45.28	14.47	0.00	40.25	14.12	0	0.12
338	41	800	240	45.28	14.47	0.00	40.25	14.1	0	0.17
339	41	800	250	45.28	14.47	0.00	40.25	14.06	0.01	0.28
340	41	800	260	45.28	14.47	0.00	40.25	13.96	0.01	0.34
341	41	600	210	55.34	14.46	0.00	30.20	14.32	0	0.1
342	41	600	250	55.34	14.46	0.00	30.20	14.05	0.01	0.46
343	41	800	210	55.69	13.93	0.00	30.38	14.42	0	0.08
344	41	800	250	55.69	13.93	0.00	30.38	14.27	0.01	0.31
345	61	600	220	45.35	14.26	0.00	40.39	14.19	0	0.21
346	61	800	220	45.33	14.35	0.00	40.32	14.27	0	0.15
347	61	1000	220	45.29	14.44	0.00	40.27	14.39	0	0.12
348	61	600	220	55.19	14.69	0.00	30.12	14.52	0	0.32
349	61	800	220	55.16	14.76	0.00	30.08	14.58	0	0.21
350	61	600	235	45.35	14.26	0.00	40.39	14.01	0	0.37

Table S1.1 (continuation)

N°	Abs. Pres. (bar)	Vol. Flow* ($\frac{mL_s}{min}$)	Temp. (°C)	Inlet Flow (% v/v)				Outlet Flow (% v/v)		
				H ₂	CO	CO ₂	N ₂	CO	CO ₂	CH ₃ OH
351	61	800	235	45.33	14.35	0.00	40.32	14.16	0	0.25
352	61	1000	235	45.29	14.44	0.00	40.27	14.28	0	0.19
353	61	600	250	35.35	14.16	0.00	50.49	13.76	0.02	0.54
354	61	800	250	35.31	14.24	0.00	50.45	13.94	0.01	0.39
355	61	600	250	45.35	14.26	0.00	40.39	13.89	0.02	0.64
356	61	800	250	45.33	14.35	0.00	40.32	14.14	0.01	0.44
357	61	1000	250	45.29	14.44	0.00	40.27	14.19	0	0.33
358	61	600	250	55.19	14.69	0.00	30.12	14.13	0.01	0.75
359	61	800	250	55.16	14.76	0.00	30.08	14.35	0.01	0.54

S1.2 Thermodynamic consistency

The estimated parameters for the 3-parameter equations to simulate the equilibrium of each global reaction are described in Table S1.2.

The constrained minimization problem of the thermodynamic consistency can be solved with the method of the Lagrangean multipliers. The Lagrangean function is:

$$\begin{aligned}
\mathcal{L}(E_{A,fk}^{TC}, E_{A,rk}^{TC}, \Delta S_{fk}^{\neq,TC}, \Delta S_{rk}^{\neq,TC}, \beta_{fk}^{TC}, \beta_{rk}^{TC}, \lambda_{1-3m}) = & \int_{T_1}^{T_2} \left\{ \sum_{k=1}^{Nr} w_k \cdot \left[E_{A,fk}^{TC} \right. \right. \\
& - T \cdot (\Delta S_{fk}^{\neq,TC} + \ln(T) \cdot \beta_{fk}^{TC}) - (E_{A,fk}^{Orig.} - T \cdot \Delta S_{fk}^{\neq,Orig.}) \left. \right]^2 + [E_{A,rk}^{TC} \\
& - T \cdot (\Delta S_{rk}^{\neq,TC} + \ln(T) \cdot \beta_{rk}^{TC}) - (E_{A,rk}^{Orig.} - T \cdot \Delta S_{rk}^{\neq,Orig.}) \left. \right]^2 \left. \right\} dT \\
& + \sum_{m=1}^{Nm} (\lambda_{1m} \cdot q_{1m} + \lambda_{2m} \cdot q_{2m} + \lambda_{3m} \cdot q_{3m})
\end{aligned} \tag{S1.1}$$

Where $\lambda_{1-3,m}$ are the Lagrangean multipliers. The solution of this problem (minimum) lies when all partial derivatives of the Lagrangean function are zero.

$$\frac{\partial \mathcal{L}}{\partial E_{A,fk}^{TC}} = \frac{\partial \mathcal{L}}{\partial E_{A,rk}^{TC}} = \frac{\partial \mathcal{L}}{\partial \Delta S_{fk}^{\neq,TC}} = \frac{\partial \mathcal{L}}{\partial \Delta S_{rk}^{\neq,TC}} = \frac{\partial \mathcal{L}}{\partial \beta_{fk}^{TC}} = \frac{\partial \mathcal{L}}{\partial \beta_{rk}^{TC}} = \frac{\partial \mathcal{L}}{\partial \lambda_{1-3m}} = 0 \tag{S1.2}$$

The calculation of the partial derivatives leads to a linear system, whose solution gives the corrected values of E_A , ΔS^{\neq} , and β .

Table S1.2 Estimated parameters of the free Gibbs energy change (Eq. 2.16) of the global reactions involved in the methanol synthesis. Reproduced with permission from Campos et al.⁷⁰. Copyright 2021, Royal Society of Chemistry.

	CO Hyd.	CO ₂ Hyd.	WGSR
m	1 (site a)	2 (site a) - 3 (site b)	4 (site a) - 5 (site b)
A ₁ [kJ·mol ⁻¹]	- 83.913	- 39.541	- 44.378
A ₂ ·10 ³ [kJ·mol ⁻¹ ·K ⁻¹]	34.924	- 69.587	104.505
A ₃ ·10 ³ [kJ·mol ⁻¹ ·K ⁻¹]	28.138	37.259	- 9.118
ΔH _{Tr} ⁰ [kJ·mol ⁻¹]	- 75.524	- 28.432	- 47.096
ΔS _{Tr} ⁰ ·10 ³ [kJ·mol ⁻¹ ·K ⁻¹]	- 223.384	- 179.957	- 43.438
Δc _p ·10 ³ [kJ·mol ⁻¹ ·K ⁻¹]	- 28.138	- 37.259	9.118

S1.3 Surface coverage – Initial guess

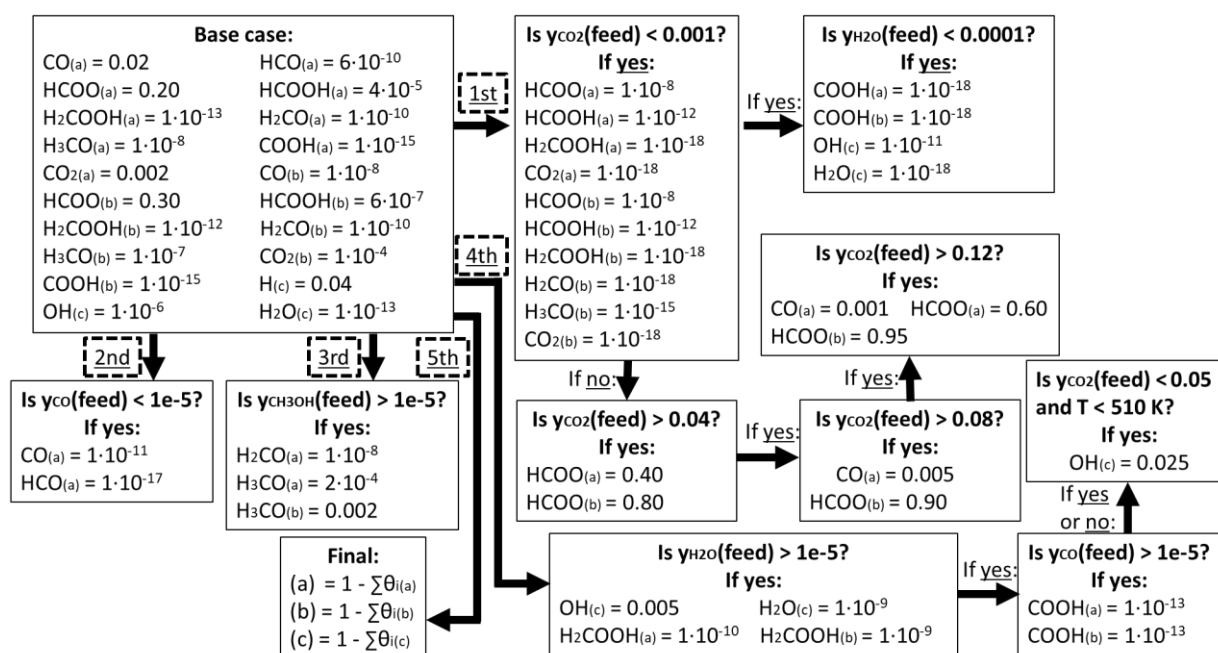


Fig. S1.3 Initial guess method: Finding a proper initial guess to calculate the coverages with the Newton-Raphson method instead of integrating the differential equations in time. Reproduced with permission from Campos et al.⁷⁰. Copyright 2021, Royal Society of Chemistry.

S1.4 Reactor simulation – Solving the differential equations of the PFR

The steady-state solution of the surface intermediate coverages (Eq. 2.41) can be found either by integrating the equations in time or by setting all time derivatives to zero and solving the non-linear algebraic system. The latter has much lower computational costs, but it requires a significantly close initial guess to converge to the correct answer. Therefore, in this work, a database of initial guesses was built for different temperatures, pressures and gas phase concentrations, both by integrating the equations in time, and by solving the non-linear algebraic system of equations with initial guesses chosen by trial and error. With this database, an initial guess method was created (Fig. S1.3), which gives sufficiently good initial guesses for the studied region of operating conditions. This algebraic system has to be solved for each axial position in the reactor, as the coverage of the species vary along the reactor length. A scheme of the procedure used to solve the PFR model is described in Fig. S1.4. The numerical simulations were performed using the commercial software Matlab 2018. By informing the analytical Jacobian matrix of the algebraic system (Eq. 2.41) to the mathematical solver, the computational time dropped significantly.

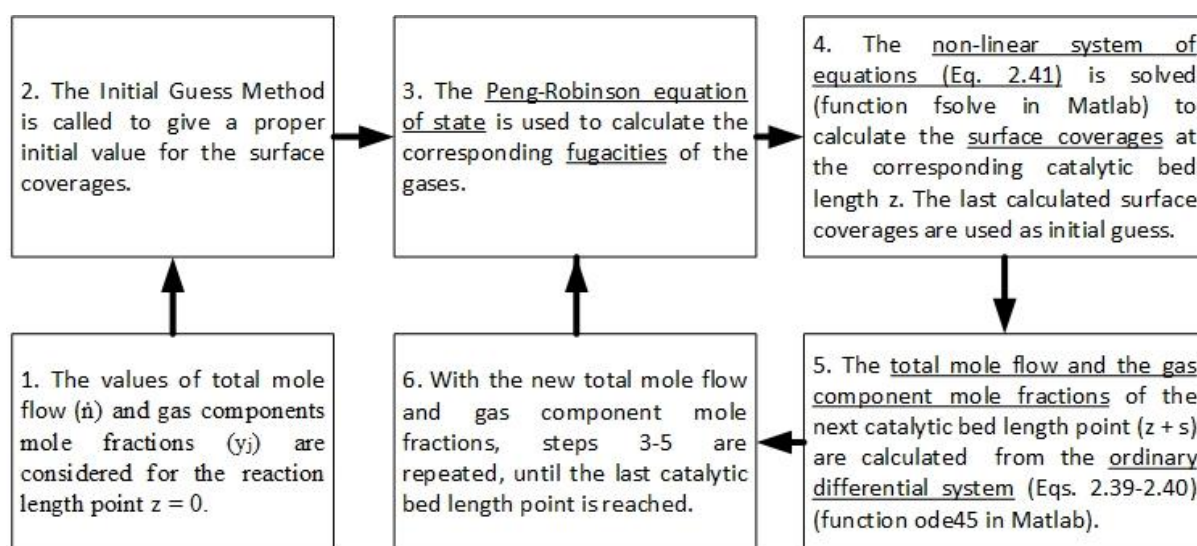


Fig. S1.4 Step-by-step method to solve the kinetic model of the PFR. Reproduced with permission from Campos et al.⁷⁰. Copyright 2021, Royal Society of Chemistry.

S1.5 Reactor simulation – Solving the differential equations of the CSTR

The ordinary set of differential equations of the CSTR requires a certain strategy to be solved. On one hand, the steady-state achievement by integrating the gas phase equations in time (Eq. 2.44 in the article) usually requires an integration period around 1 to 10^3 s (depending on the GHSV), while the steady-state achievement by integrating the surface coverages equations (Eq. 2.45 in the article) usually requires an integration period around 10^{-5} to 10^{-3} s. This large difference between integration periods creates numerical instability if attempting to integrate all equations together, unless a tiny time step is used, e.g. 10^{-7} s, which would take a longish computational time.

On the other hand, setting all the time derivatives to zero (steady-state definition) and solving the non-linear system of equations is also difficult, as it would only converge to the correct answer if a sufficiently good initial guess for all y_j and θ_i is given. The strategy chosen was somewhat similar to the approach of the PFR: the gas phase equations (Eq. 2.44) were integrated in time until steady-state was achieved. For each time step, the time derivatives of the surface species equations (Eq. 2.45) were set to zero and the non-linear algebraic system was solved. A schematic description of the procedure used to solve the CSTR model is described in Fig. S1.5.

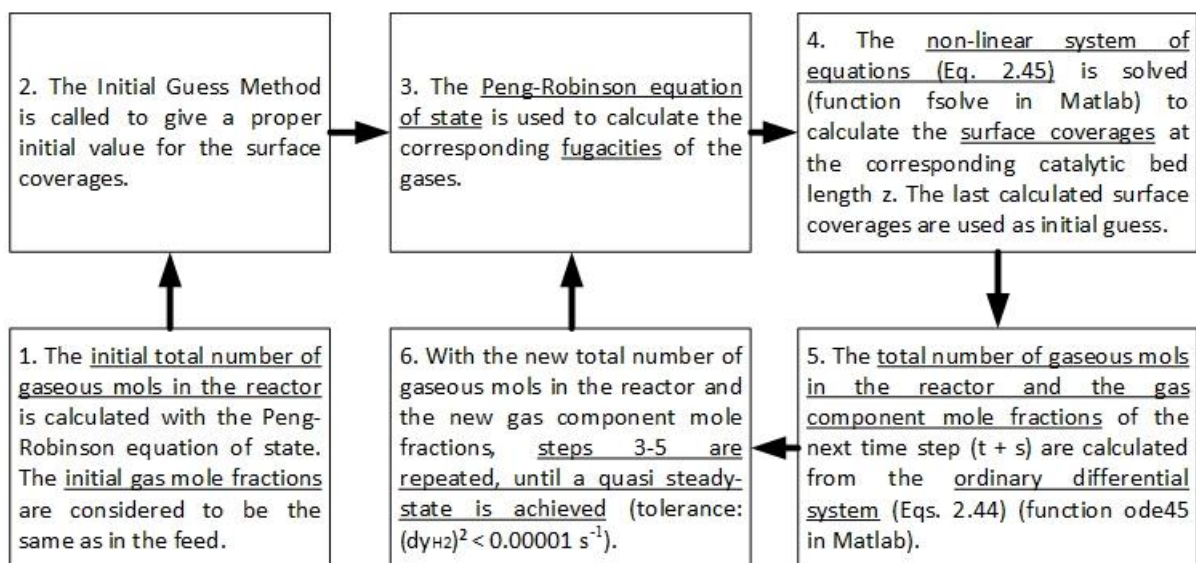


Fig. S1.5 Step-by-step method to solve the kinetic model of the CSTR. Reproduced with permission from Campos et al.⁷⁰. Copyright 2021, Royal Society of Chemistry.

S1.6 Reaction flow analysis

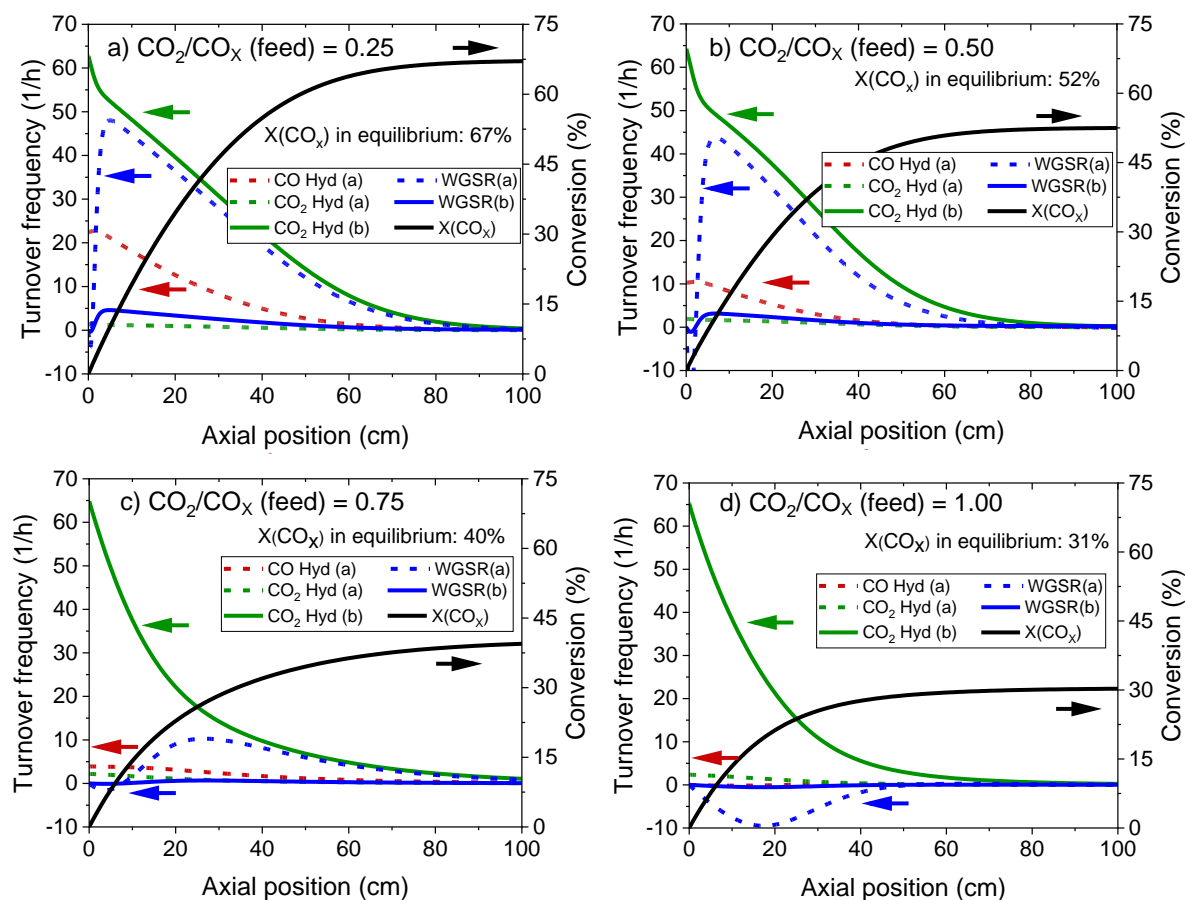


Fig. S1.6 Turnover frequency and conversion along a methanol synthesis reactor with a length of 100 cm. Operating conditions: 250 °C, 60 bar, GHSV = 4.8 L_S·h⁻¹·(g_{cat})⁻¹, feed concentration: H₂/CO_x = 80/20 % v/v. a) CO₂/CO_x = 25%. b) CO₂/CO_x = 50%. c) CO₂/CO_x = 75%. d) CO₂/CO_x = 100%. Adapted with permission from Campos et al.⁷⁰. Copyright 2021, Royal Society of Chemistry.

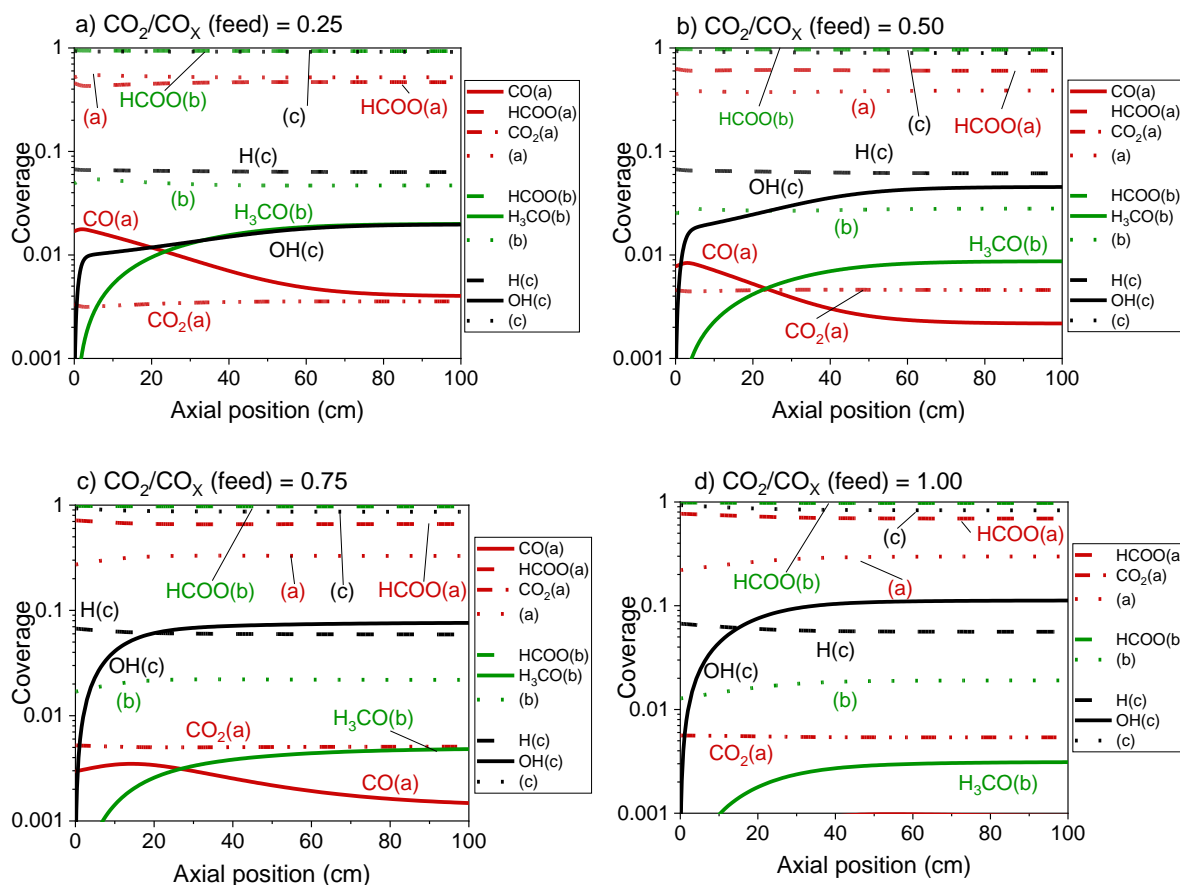


Fig. S1.7 Coverage of the surface species along the methanol synthesis reactor with a length of 100 cm. Operating conditions: 250 °C, 60 bar, GHSV = $4.8 \text{ L}_5 \cdot \text{h}^{-1} \cdot (\text{g}_{\text{cat}})^{-1}$, feed concentration: $\text{H}_2/\text{CO}_x = 80/20\%$ v/v. a) $\text{CO}_2/\text{CO}_x = 25\%$. b) $\text{CO}_2/\text{CO}_x = 50\%$. c) $\text{CO}_2/\text{CO}_x = 75\%$. d) $\text{CO}_2/\text{CO}_x = 100\%$. Adapted with permission from Campos et al.⁷⁰. Copyright 2021, Royal Society of Chemistry.

S1.7 Degree of rate control

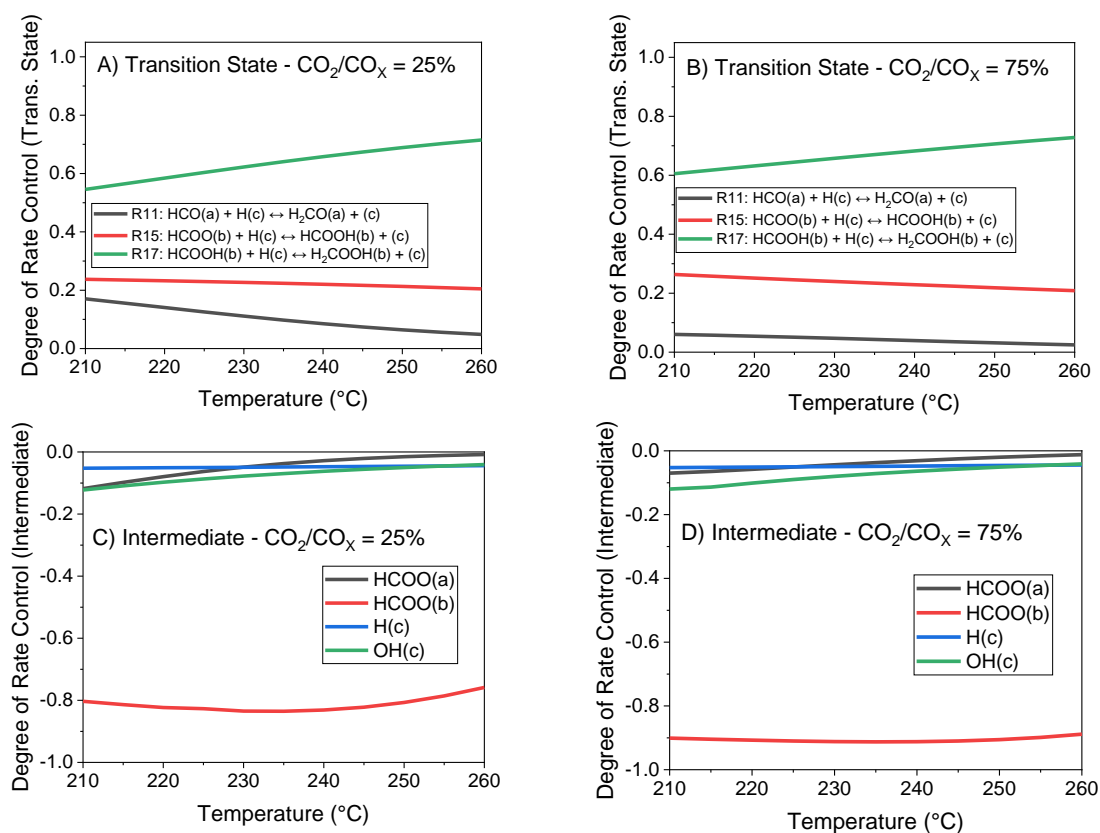


Fig. S1.8 Degree of Rate Control (DRC) analysis of the methanol production at 30 bar and 210-260 °C. Gas concentration: $H_2/CO_x/CH_3OH/H_2O = 79.8/19.8/0.2/0.2\%$ v/v. A) Trans. State - $CO_2/CO_x = 25\%$. B) Trans. State - $CO_2/CO_x = 75\%$. C) Intermediate - $CO_2/CO_x = 25\%$. D) Intermediate - $CO_2/CO_x = 75\%$. Reproduced with permission from Campos et al.⁷⁰. Copyright 2021, Royal Society of Chemistry.

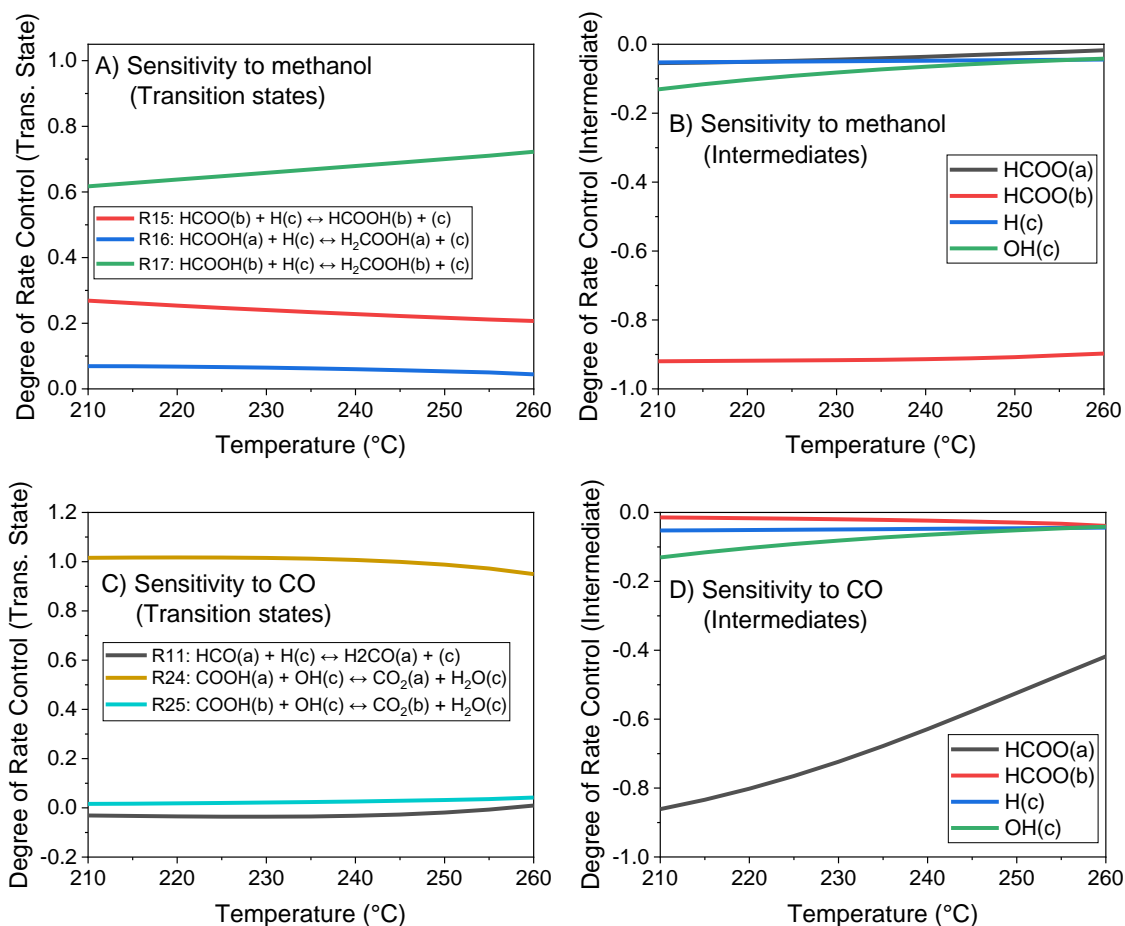


Fig. S1.9 Degree of Rate Control (DRC) analysis at 210–260 °C, 30 bar, and a gas concentration of $\text{H}_2/\text{CO}/\text{CO}_2/\text{CH}_3\text{OH}/\text{H}_2\text{O} = 79.8/0.2/19.6/0.2/0.2\%$ v/v. A) Sensitivity to methanol, transition states. B) Sensitivity to methanol, intermediates. C) Sensitivity to CO, transition states. D) Sensitivity to CO, intermediates. Reproduced with permission from Campos et al.⁷⁰. Copyright 2021, Royal Society of Chemistry.

S2. Supplementary Material – Chapter 3

S2.1 Mathematical derivation of the kinetic equations

The reaction pathways considered our previous work are described in Table S2.1. The reaction rate of an elementary reaction step k (r_k) is defined as:

$$r_k = n_{M,Cat} \cdot k_k^+ \cdot \prod_{j=1}^{N_g} [f_j^{v'_{j,k}}] \cdot \prod_{i=N_g+1}^{N_g+N_s} [\phi_i \cdot \theta_i^{v'_{i,k}}] - n_{M,Cat} \cdot k_k^- \cdot \prod_{j=1}^{N_g} [f_j^{v''_{j,k}}] \cdot \prod_{i=N_g+1}^{N_g+N_s} [\phi_i \cdot \theta_i^{v''_{i,k}}] \quad (S2.1)$$

Here, $n_{M,Cat}$ is the specific quantity of active sites ($\text{mol} \cdot \text{kg}_{cat}^{-1}$), k_k^+ and k_k^- are the reaction rate constant of the forward and the reverse reaction, respectively, N_g is the number of gases, N_s is the number of surface species, f_j is the fugacity of gas species j , θ_i is the coverage of surface species i , $v'_{j,k}$ is the stoichiometric coefficient of species j in the forward direction of reaction k , $v''_{j,k}$ is the stoichiometric coefficient of species j in the reverse direction of reaction k , ϕ_i is the coverage of site type of surface species i in relation to the total number of sites for carbon-containing compounds (sites a and b). ϕ_i is $(1 - \phi_{Zn})$ for site (a), ϕ_{Zn} for site (b), and 1 for site (c). For hydrogen adsorption (R_1), that is:

$$r_1 = n_{M,Cat} \cdot k_1^+ \cdot f_{H_2} \cdot \theta_c^2 - n_{M,Cat} \cdot k_1^- \cdot \theta_{H(c)}^2 \quad (S2.2)$$

The elementary equilibrium constant is defined as:

$$K_k = \frac{k_k^+}{k_k^-} \quad (S2.3)$$

Substituting Eq. (3) in Eq. (2) and grouping k_1^+ :

$$r_1 = n_{M,Cat} \cdot k_1^+ \cdot \left(f_{H_2} \cdot \theta_c^2 - \frac{\theta_{H(c)}^2}{K_1} \right) \quad (S2.4)$$

This step is assumed to be in equilibrium for all three global reactions. This means that:

$$k_1^+ \gg r_1 \quad \text{or} \quad \frac{r_1}{k_1^+} \approx 0 \quad (S2.5)$$

Substituting Eq. (5b) in Eq. (4) and making $\theta_{H(c)}$ explicit:

$$\theta_{H(c)} = \theta_c \cdot \sqrt{K_1 \cdot f_{H_2}} \quad (S2.6)$$

Analogous processes are done for all elementary steps that are considered to be in equilibrium. As a result, the coverage of all surface species can be described in terms of equilibrium constants, fugacities, free site coverages and zinc coverage, as shown in Table S2.

Table S2.1 Reaction network of the methanol synthesis and the WGSR.⁷⁰ Reproduced with permission from Campos et al.⁸⁹. Copyright 2021, American Chemical Society.

No.	Elementary reaction step
<i>Adsorption steps and water splitting</i>	
R ₁	$\text{H}_{2(\text{g})} + 2 \cdot (\text{c}) \rightleftharpoons 2 \cdot \text{H}_{(\text{c})}$
R ₂	$\text{CO}_{(\text{g})} + (\text{a}) \rightleftharpoons \text{CO}_{(\text{a})}$
R ₃	$\text{CO}_{(\text{g})} + (\text{b}) \rightleftharpoons \text{CO}_{(\text{b})}$
R ₄	$\text{CO}_{2(\text{g})} + (\text{a}) \rightleftharpoons \text{CO}_{2(\text{a})}$
R ₅	$\text{CO}_{2(\text{g})} + (\text{b}) \rightleftharpoons \text{CO}_{2(\text{b})}$
R ₈	$\text{H}_2\text{O}_{(\text{g})} + (\text{c}) \rightleftharpoons \text{H}_2\text{O}_{(\text{c})}$
R ₉	$\text{H}_2\text{O}_{(\text{c})} + (\text{c}) \rightleftharpoons \text{OH}_{(\text{c})} + \text{H}_{(\text{c})}$
<i>Reaction path 1 - CO hydrogenation on site (a)</i>	
R ₁₀	$\text{CO}_{(\text{a})} + \text{H}_{(\text{c})} \rightleftharpoons \text{HCO}_{(\text{a})} + (\text{c})$
R ₁₁	$\text{HCO}_{(\text{a})} + \text{H}_{(\text{c})} \rightleftharpoons \text{H}_2\text{CO}_{(\text{a})} + (\text{c})$
R ₂₀	$\text{H}_2\text{CO}_{(\text{a})} + \text{H}_{(\text{c})} \rightleftharpoons \text{H}_3\text{CO}_{(\text{a})} + (\text{c})$
R ₆	$\text{H}_3\text{CO}_{(\text{a})} + \text{H}_{(\text{c})} \rightleftharpoons \text{CH}_3\text{OH}_{(\text{g})} + (\text{a}) + (\text{c})$
<i>Reaction path 2 - CO₂ hydrogenation on site (a)</i>	
R ₁₂	$\text{CO}_{2(\text{a})} + \text{H}_{(\text{c})} \rightleftharpoons \text{HCOO}_{(\text{a})} + (\text{c})$
R ₁₄	$\text{HCOO}_{(\text{a})} + \text{H}_{(\text{c})} \rightleftharpoons \text{HCOOH}_{(\text{a})} + (\text{c})$
R ₁₆	$\text{HCOOH}_{(\text{a})} + \text{H}_{(\text{c})} \rightleftharpoons \text{H}_2\text{COOH}_{(\text{a})} + (\text{c})$
R ₁₈	$\text{H}_2\text{COOH}_{(\text{a})} + (\text{c}) \rightleftharpoons \text{H}_2\text{CO}_{(\text{a})} + \text{OH}_{(\text{c})}$
R ₂₀	$\text{H}_2\text{CO}_{(\text{a})} + \text{H}_{(\text{c})} \rightleftharpoons \text{H}_3\text{CO}_{(\text{a})} + (\text{c})$
R ₆	$\text{H}_3\text{CO}_{(\text{a})} + \text{H}_{(\text{c})} \rightleftharpoons \text{CH}_3\text{OH}_{(\text{g})} + (\text{a}) + (\text{c})$
<i>Reaction path 3 - CO₂ hydrogenation on site (b)</i>	
R ₁₃	$\text{CO}_{2(\text{b})} + \text{H}_{(\text{c})} \rightleftharpoons \text{HCOO}_{(\text{b})} + (\text{c})$
R ₁₅	$\text{HCOO}_{(\text{b})} + \text{H}_{(\text{c})} \rightleftharpoons \text{HCOOH}_{(\text{b})} + (\text{c})$
R ₁₇	$\text{HCOOH}_{(\text{b})} + \text{H}_{(\text{c})} \rightleftharpoons \text{H}_2\text{COOH}_{(\text{b})} + (\text{c})$
R ₁₉	$\text{H}_2\text{COOH}_{(\text{b})} + (\text{c}) \rightleftharpoons \text{H}_2\text{CO}_{(\text{b})} + \text{OH}_{(\text{c})}$
R ₂₁	$\text{H}_2\text{CO}_{(\text{b})} + \text{H}_{(\text{c})} \rightleftharpoons \text{H}_3\text{CO}_{(\text{b})} + (\text{c})$
R ₇	$\text{H}_3\text{CO}_{(\text{b})} + \text{H}_{(\text{c})} \rightleftharpoons \text{CH}_3\text{OH}_{(\text{g})} + (\text{b}) + (\text{c})$
<i>Reaction path 4 - Water-gas shift reaction on site (a)</i>	
R ₂₂	$\text{CO}_{(\text{a})} + \text{OH}_{(\text{c})} \rightleftharpoons \text{COOH}_{(\text{a})} + (\text{c})$
R ₂₄	$\text{COOH}_{(\text{a})} + \text{OH}_{(\text{c})} \rightleftharpoons \text{CO}_{2(\text{a})} + \text{H}_2\text{O}_{(\text{c})}$
<i>Reaction path 5 - Water-gas shift reaction on site (b)</i>	
R ₂₃	$\text{CO}_{(\text{b})} + \text{OH}_{(\text{c})} \rightleftharpoons \text{COOH}_{(\text{b})} + (\text{c})$
R ₂₅	$\text{COOH}_{(\text{b})} + \text{OH}_{(\text{c})} \rightleftharpoons \text{CO}_{2(\text{b})} + \text{H}_2\text{O}_{(\text{c})}$

Table S2.2 Coverage of the surface species as a function of elementary equilibrium constants, gas phase fugacities, free site coverages and zinc coverage. Reproduced with permission from Campos et al.⁸⁹. Copyright 2021, American Chemical Society.

Reaction	Equation	Eq. N°
R ₁	$\theta_{H(c)} = \sqrt{K_1 \cdot f_{H_2}} \cdot \theta_c$	(S2.7)
R ₂	$\theta_{CO(a)} = K_2 \cdot f_{CO} \cdot \theta_a \cdot (1 - \phi_{Zn})$	(S2.8)
R ₃	$\theta_{CO(b)} = K_3 \cdot f_{CO} \cdot \theta_b \cdot \phi_{Zn}$	(S2.9)
R ₄	$\theta_{CO_2(a)} = K_4 \cdot f_{CO_2} \cdot \theta_a \cdot (1 - \phi_{Zn})$	(S2.10)
R ₅	$\theta_{CO_2(b)} = K_5 \cdot f_{CO_2} \cdot \theta_b \cdot \phi_{Zn}$	(S2.11)
R ₆	$\theta_{H_3CO(a)} = \frac{f_{CH_3OH} \cdot \theta_a \cdot (1 - \phi_{Zn})}{\sqrt{K_1} \cdot K_6 \cdot \sqrt{f_{H_2}}}$	(S2.12)
R ₇	$\theta_{H_3CO(b)} = \frac{f_{CH_3OH} \cdot \theta_b \cdot \phi_{Zn}}{\sqrt{K_1} \cdot K_7 \cdot \sqrt{f_{H_2}}}$	(S2.13)
R ₈	$\theta_{H_2O(c)} = K_8 \cdot f_{H_2O} \cdot \theta_c$	(S2.14)
R ₉	$\theta_{OH(c)} = \frac{K_8 \cdot K_9 \cdot f_{H_2O} \cdot \theta_c}{\sqrt{K_1} \cdot f_{H_2}}$	(S2.15)
R ₁₀	$\theta_{HCO(a)} = \sqrt{K_1} \cdot K_2 \cdot K_{10} \cdot \sqrt{f_{H_2}} \cdot f_{CO} \cdot \theta_a \cdot (1 - \phi_{Zn})$	(S2.16)
R ₁₂	$\theta_{HCOO(a)} = \sqrt{K_1} \cdot K_4 \cdot K_{12} \cdot \sqrt{f_{H_2}} \cdot f_{CO_2} \cdot \theta_a \cdot (1 - \phi_{Zn})$	(S2.17)
R ₁₃	$\theta_{HCOO(b)} = \sqrt{K_1} \cdot K_5 \cdot K_{13} \cdot \sqrt{f_{H_2}} \cdot f_{CO_2} \cdot \theta_b \cdot \phi_{Zn}$	(S2.18)
R ₁₇	$\theta_{HCOOH(b)} = K_1 \cdot K_5 \cdot K_{13} \cdot K_{15} \cdot f_{H_2} \cdot f_{CO_2} \cdot \phi_{Zn}$	(S2.19)
R ₁₉	$\theta_{H_2COOH(b)} = \frac{f_{CH_3OH} \cdot f_{H_2O} \cdot K_8 \cdot K_9 \cdot \theta_b \cdot \phi_{Zn}}{K_1^{1.5} \cdot K_7 \cdot K_{19} \cdot K_{21} \cdot f_{H_2}^{1.5}}$	(S2.20)
R ₂₀	$\theta_{H_2CO(a)} = \frac{f_{CH_3OH} \cdot \theta_a \cdot (1 - \phi_{Zn})}{K_1 \cdot K_6 \cdot K_{20} \cdot f_{H_2}}$	(S2.21)
R ₂₁	$\theta_{H_2CO(b)} = \frac{f_{CH_3OH} \cdot \theta_b \cdot \phi_{Zn}}{K_1 \cdot K_7 \cdot K_{21} \cdot f_{H_2}}$	(S2.22)
R ₂₂	$\theta_{COOH(a)} = \frac{K_2 \cdot K_8 \cdot K_9 \cdot K_{22} \cdot f_{CO} \cdot f_{H_2O} \cdot \theta_a \cdot (1 - \phi_{Zn})}{\sqrt{K_1} \cdot f_{H_2}}$	(S2.23)
R ₂₃	$\theta_{COOH(b)} = \frac{K_3 \cdot K_8 \cdot K_9 \cdot K_{23} \cdot f_{CO} \cdot f_{H_2O} \cdot \theta_b \cdot \phi_{Zn}}{\sqrt{K_1} \cdot f_{H_2}}$	(S2.24)

The reaction rate of the rate-determining step (RDS) of CO hydrogenation (R₁₁) is then:

$$r_{11} = n_{M,Cat} \cdot k_{11}^+ \cdot \left(\theta_{HCO(a)} \cdot \theta_{H(c)} - \frac{\theta_{H_2CO(a)} \cdot \theta_c}{K_{11}} \right) \quad (S2.25)$$

Substituting Eqs. (7), (16), and (22) in Eq. (26):

$$r_{11} = n_{M,Cat} \cdot k_{11}^+ \cdot \left(\sqrt{K_1} \cdot K_2 \cdot K_{10} \cdot \sqrt{f_{H_2} \cdot f_{CO} \cdot \theta_a \cdot (1 - \phi_{Zn})} \cdot \sqrt{K_1 \cdot f_{H_2} \cdot \theta_c} \right. \\ \left. - \frac{f_{CH_3OH} \cdot \theta_a \cdot (1 - \phi_{Zn})}{K_1 \cdot K_6 \cdot K_{20} \cdot f_{H_2}} \cdot \frac{\theta_c}{K_{11}} \right) \quad (S2.26)$$

$$r_{11} = n_{M,Cat} \cdot k_{11}^+ \cdot (1 - \phi_{Zn}) \cdot K_1 \cdot K_2 \cdot K_{10} \cdot f_{H_2} \cdot f_{CO} \cdot \theta_a \cdot \theta_c \\ \left(1 - \frac{f_{CH_3OH}}{K_1^2 \cdot K_2 \cdot K_6 \cdot K_{10} \cdot K_{11} \cdot K_{20} \cdot f_{H_2}^2 \cdot f_{CO}} \right) \quad (S2.27)$$

The global equilibrium constant is built from the multiplication of the equilibrium constants of the elementary steps:

$$K_{P,CO\ hyd.}^0 = K_1^2 \cdot K_2 \cdot K_6 \cdot K_{10} \cdot K_{11} \cdot K_{20} \quad (S2.28)$$

Substituting Eq. (S2.28) in Eq. (S2.27), the final reaction rate equation appears.

$$r_{CO} = n_{M,Cat} \cdot k_{11}^+ \cdot (1 - \phi_{Zn}) \cdot \theta_a \cdot \theta_c \cdot K_1 \cdot K_2 \cdot K_{10} \cdot f_{H_2} \cdot f_{CO} \\ \cdot \left(1 - \frac{f_{CH_3OH}}{f_{H_2}^2 \cdot f_{CO} \cdot K_{P,CO\ hyd.}^0} \right) \quad (S2.29)$$

An analogous process is made to derive the reaction rate of CO₂ hydrogenation. In the case of the reverse water-gas shift reaction (rWGSR), it is active on both sites a and b, and R₂₄ and R₂₅ are the respective RDS. Therefore, the global rWGSR rate is the sum of these two pathways:

$$\dot{r}_{rWGSR} = -(\dot{r}_{24} + \dot{r}_{25}) \quad (S2.30)$$

$$\dot{r}_{WGSR} = n_{M,Cat} \cdot \left(-k_{24}^- \cdot K_{24} \cdot \theta_{COOH(a)} \cdot \theta_{OH(c)} + k_{24}^- \cdot \theta_{CO_2(a)} \cdot \theta_{H_2O(c)} \right. \\ \left. - k_{25}^- \cdot K_{25} \cdot \theta_{COOH(b)} \cdot \theta_{OH(c)} + k_{25}^- \cdot \theta_{CO_2(b)} \cdot \theta_{H_2O(c)} \right) \quad (S2.31)$$

Substituting Eqs. (10), (11), (14), (15), (23), and (24) in Eq. (31):

$$r_{rWGSR} = n_{M,Cat} \cdot k_{24}^- \cdot K_4 \cdot K_8 \cdot \theta_a \cdot \theta_c \cdot (1 - \phi_{Zn}) \cdot f_{CO_2} \cdot f_{H_2O} \\ \cdot \left(1 - \frac{f_{CO} \cdot f_{H_2O}}{f_{H_2} \cdot f_{CO_2}} \cdot \frac{K_2 \cdot K_8 \cdot K_9^2 \cdot K_{22} \cdot K_{24}}{K_1 \cdot K_4} \right) \\ + n_{M,Cat} \cdot k_{25}^- \cdot K_5 \cdot K_8 \cdot \theta_b \cdot \theta_c \cdot \phi_{Zn} \cdot f_{CO_2} \cdot f_{H_2O} \\ \cdot \left(1 - \frac{f_{CO} \cdot f_{H_2O}}{f_{H_2} \cdot f_{CO_2}} \cdot \frac{K_3 \cdot K_8 \cdot K_9^2 \cdot K_{23} \cdot K_{25}}{K_1 \cdot K_5} \right) \quad (S2.32)$$

The global rWGSR equilibrium constant can be built from the elementary steps of both reaction pathways.

$$K_{P,rWGSR}^0 = \frac{K_1 \cdot K_4}{K_2 \cdot K_8 \cdot K_9^2 \cdot K_{22} \cdot K_{24}} \quad (S2.33)$$

$$K_{P,rWGSR}^0 = \frac{K_1 \cdot K_5}{K_3 \cdot K_8 \cdot K_9^2 \cdot K_{23} \cdot K_{25}} \quad (S2.34)$$

According to the microkinetic model,⁷⁰ $k_{24}^- = k_{25}^-$. Therefore, substituting Eqs. (33) and (34) in Eq. (32):

$$\begin{aligned}
r_{rWGSR} = & n_{M,Cat} \cdot k_{24}^- \cdot \theta_a \cdot \theta_c \cdot K_4 \cdot K_8 \cdot (1 - \phi_{Zn}) \cdot f_{CO_2} \cdot f_{H_2O} \\
& \cdot \left(1 - \frac{f_{CO} \cdot f_{H_2O}}{f_{H_2} \cdot f_{CO_2}} \cdot \frac{1}{K_{P,rWGSR}^0} \right) \\
& + n_{M,Cat} \cdot k_{25}^- \cdot K_5 \cdot K_8 \cdot \theta_b \cdot \theta_c \cdot \phi_{Zn} \cdot f_{CO_2} \cdot f_{H_2O} \\
& \cdot \left(1 - \frac{f_{CO} \cdot f_{H_2O}}{f_{H_2} \cdot f_{CO_2}} \cdot \frac{1}{K_{P,rWGSR}^0} \right)
\end{aligned} \tag{S2.35}$$

$$\begin{aligned}
r_{rWGSR} = & n_{M,Cat} \cdot k_{24}^- \cdot \theta_c \cdot K_8 \cdot [(1 - \phi_{Zn}) \cdot \theta_a \cdot K_4 + \phi_{Zn} \cdot \theta_b \cdot K_5] \cdot f_{CO_2} \\
& \cdot f_{H_2O} \\
& \cdot \left(1 - \frac{f_{H_2} \cdot f_{CO_2}}{f_{CO} \cdot f_{H_2O}} \cdot \frac{1}{K_{P,WGSR}^0} \right)
\end{aligned} \tag{S2.36}$$

The kinetic and equilibrium constants needed for Model-1p are provided in Table S2.3.

Table S2.3 Kinetic constants, equilibrium constants, and zinc coverage.^{70, 78} Reproduced with permission from Campos et al.⁸⁹. Copyright 2021, American Chemical Society.

Parameter		Eq. N°
$k_{11}^+ = T^{0.701} \cdot \exp[25.652 - 6766.5 \cdot T^{-1}]$	$[s^{-1}]$	(S2.37)
$k_{17}^+ = T \cdot \exp[5.669 - 185.2 \cdot T^{-1}]$	$[s^{-1}]$	(S2.38)
$k_{24}^- = T^{1.119} \cdot \exp[21.071 - 7315.0 \cdot T^{-1}]$	$[s^{-1}]$	(S2.39)
$K_1 = \exp[-14.548 + 2819.2 \cdot T^{-1}]$		(S2.40)
$K_2 = \exp[-19.031 + 7020.3 \cdot T^{-1}]$		(S2.41)
$K_4 = T^{-0.258} \cdot \exp[-16.540 + 6289.0 \cdot T^{-1}]$		(S2.42)
$K_5 = T^{-0.498} \cdot \exp[-14.944 + 6204.9 \cdot T^{-1}]$		(S2.43)
$K_7 = T^{-0.736} \cdot \exp[26.259 - 8292.8 \cdot T^{-1}]$		(S2.44)
$K_8 = T^{0.756} \cdot \exp[-23.846 + 3753.7 \cdot T^{-1}]$		(S2.45)
$K_9 = T^{0.280} \cdot \exp[-1.878 + 3046.5 \cdot T^{-1}]$		(S2.46)
$K_{10} = T^{-0.598} \cdot \exp[5.686 - 7705.9 \cdot T^{-1}]$		(S2.47)
$K_{12} = T^{-0.498} \cdot \exp[3.334 + 3836.7 \cdot T^{-1}]$		(S2.48)
$K_{13} = T^{-0.736} \cdot \exp[4.930 + 5435.1 \cdot T^{-1}]$		(S2.49)
$K_{15} = \exp[19.739 - 15942.3 \cdot T^{-1}]$		(S2.50)
$K_{P,CO\ hyd.}^0 = T^{-3.384} \cdot \exp(10092.4 \cdot T^{-1} - 4.200)$		(S2.51)
$K_{P,CO_2\ hyd.}^0 = T^{-4.481} \cdot \exp(4755.7 \cdot T^{-1} + 8.369)$		(S2.52)
$K_{P,rWGSR}^0 = T^{-1.097} \cdot \exp(-5337.4 \cdot T^{-1} + 12.569)$		(S2.53)
$if \bar{y}_{CO_2,0} \leq 0.001$	$\phi_{Zn} = 0.95$	
$if 0.001 \leq \bar{y}_{CO_2,0} \leq 0.90$	$\phi_{Zn} = 0.50$	(S2.54)
$if \bar{y}_{CO_2,0} > 0.90$	$\phi_{Zn} = 0.10$	

S2.2 Parameter re-estimation of the model from Slotboom et al.

Since direct CO hydrogenation is neglected in the model of Slotboom et al.,⁴¹ the simulation of experiments without CO₂ in feed would not be possible. The authors overcame this problem by setting the feed concentration of CO₂/CH₃OH/H₂O to 50 ppm (this also avoids numerical errors which happen by setting concentrations to zero), allowing CO₂ hydrogenation and the WGSR to occur at slow rates in these conditions. This approach is also followed in this work.

Table S2.4 Original and optimized kinetic parameters from Slotboom et al.⁴¹ Reproduced with permission from Campos et al.⁸⁹. Copyright 2021, American Chemical Society.

Parameter		Original	Slotboom A ^a	Slotboom B ^b
k_{CO_2}	a	34.24 ± 0.71	29.93 ± 3.83	24.95 ± 5.57
	b	19960 ± 180	17706 ± 1932	18256 ± 2907
k_{RWGSR}	a	43.85 ± 1.2	39.44 ± 3.09	46.13 ± 7.97
	b	24500 ± 610	22687 ± 1601	27363 ± 4012
K_{H_2}		1.099 ± 0.66	1.03 ± 0.02	0.0937 ± 0.0548
$K_{H_2O/9}$		126.44 ± 66	212.84 ± 40.44	7.15 ± 1.90

^a All points were considered. ^b Only points with CO₂ in feed were considered.

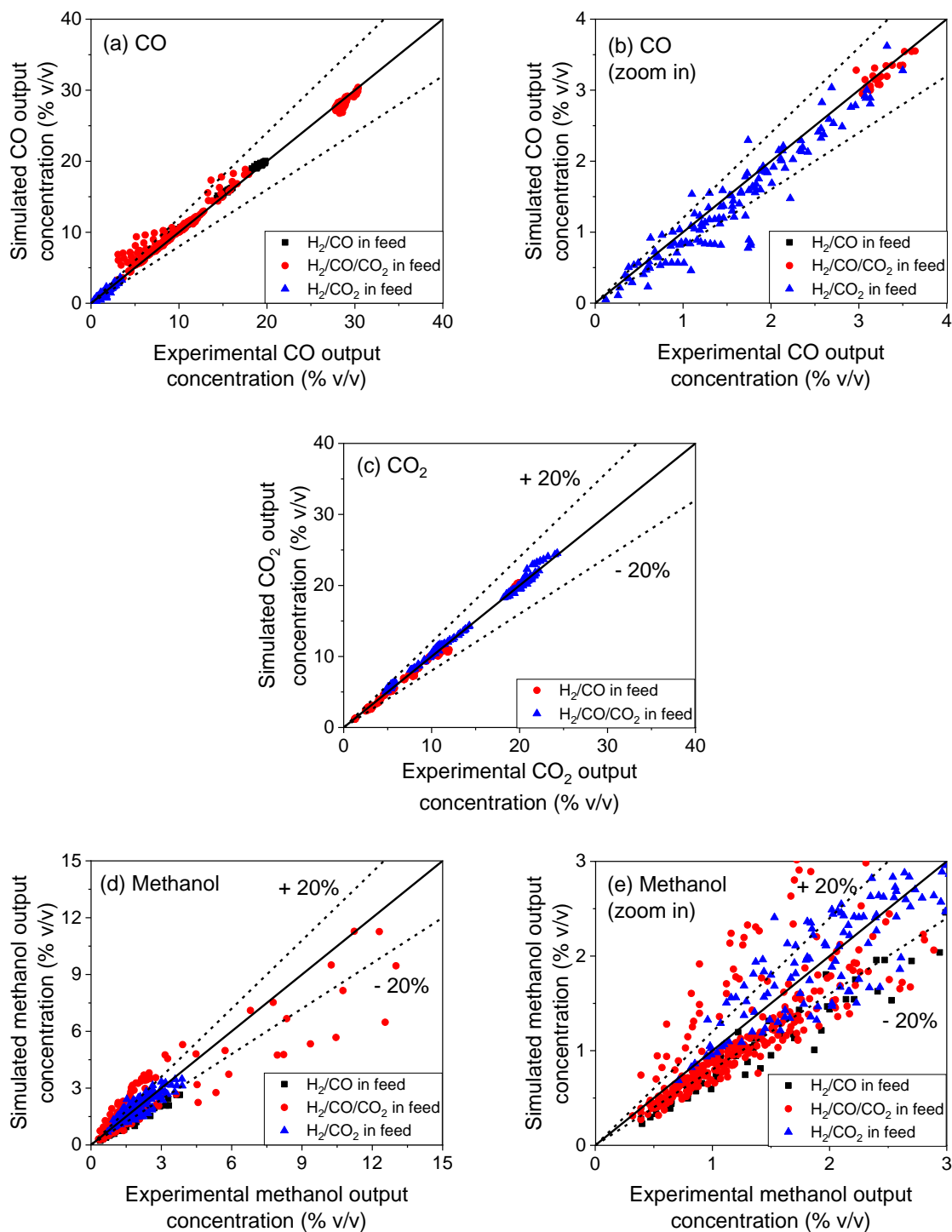


Fig. S2.1 Parity plots of model Slotboom A for measured and predicted CO (a-b), CO₂ (c) and methanol (d-e) concentrations in the product stream. Experimental conditions are reported in Table 3.3. Reproduced with permission from Campos et al.⁸⁹. Copyright 2021, American Chemical Society.

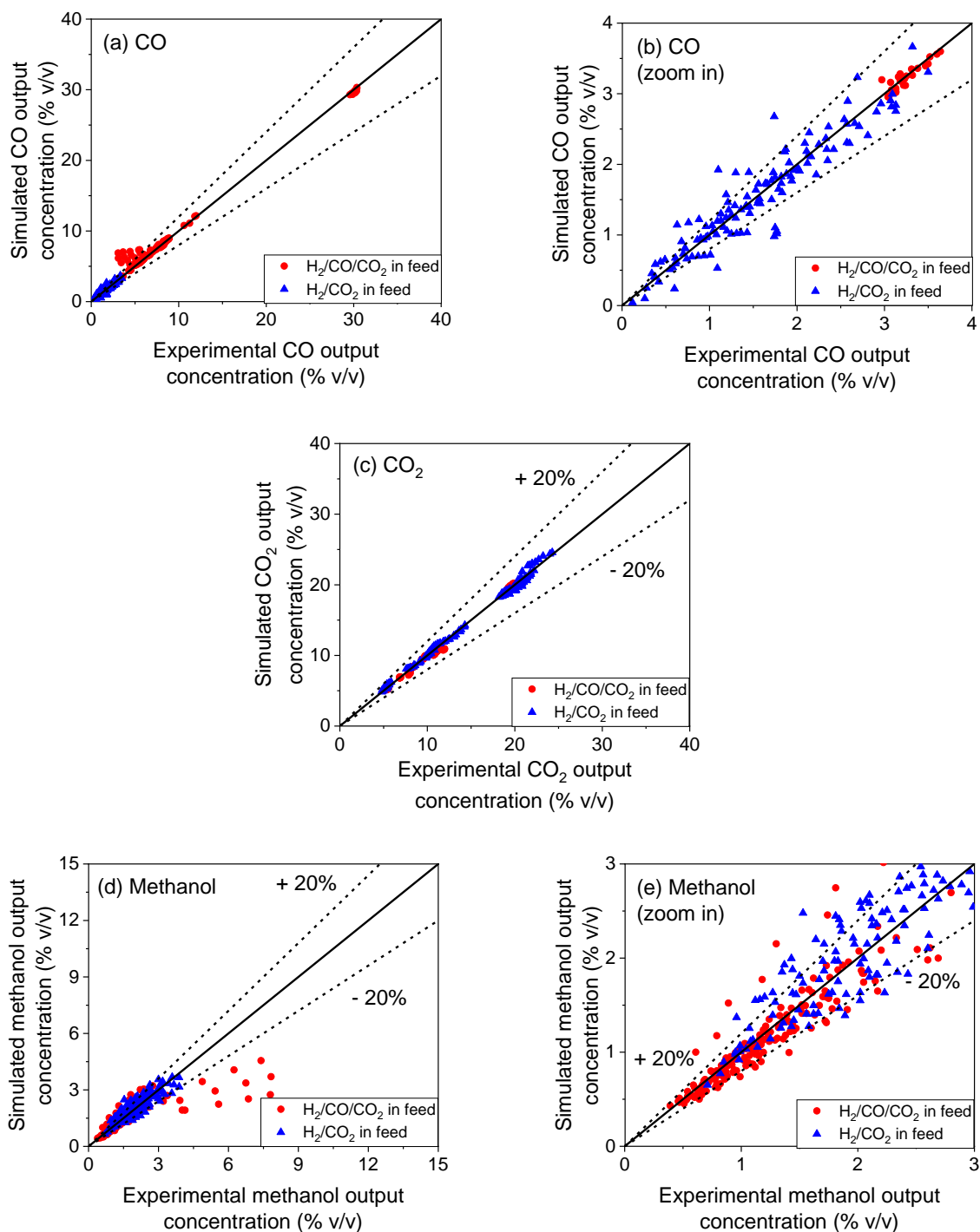


Fig. S2.2 Parity plots of model Slotboom B for measured and predicted CO (a-b), CO₂ (c) and methanol (d-e) concentrations in the product stream. Experimental conditions are all points reported in Table 3.3 that have a CO₂/CO_x feed ratio of at least 0.05. Reproduced with permission from Campos et al.⁸⁹. Copyright 2021, American Chemical Society.

S2.3 Parameter re-estimation of the model from Seidel et al.

The simplified version of the model of Seidel et al.³⁴ was considered here. All parameters were simultaneously fitted, instead of an alternative method used by the authors.

Table S2.5 Original and optimized kinetic parameters from Seidel et al.³⁴ Reproduced with permission from Campos et al.⁸⁹. Copyright 2021, American Chemical Society.

Parameter	Original (Re-estimation by Slotboom et al.)	Optimized
ΔG_3	-85.34 ± 120	-99.7 ± 1449.0
k_{CO}	A	-6.746 ± 0.53
	B	35.50 ± 1.3
k_{CO_2}	A	-4.613 ± 0.58
	B	22.26 ± 1.4
k_{RWGSR}	A	-5.277 ± 0.16
	B	37.02 ± 2.7
K_{CO}	0.2075 ± 0.054	0.28 ± 0.09
$\frac{K_{H_2O}K_O}{K_{H_2}}$	50.99 ± 12	55.97 ± 19.08
K_{CO_2}	0.00 ± 0.00	0.117 ± 0.037
K_{H_2O}	0.7283 ± 0.30	0.691 ± 0.328
$\sqrt{K_{H_2}}$	0.6433 ± 0.097	0.618 ± 0.118

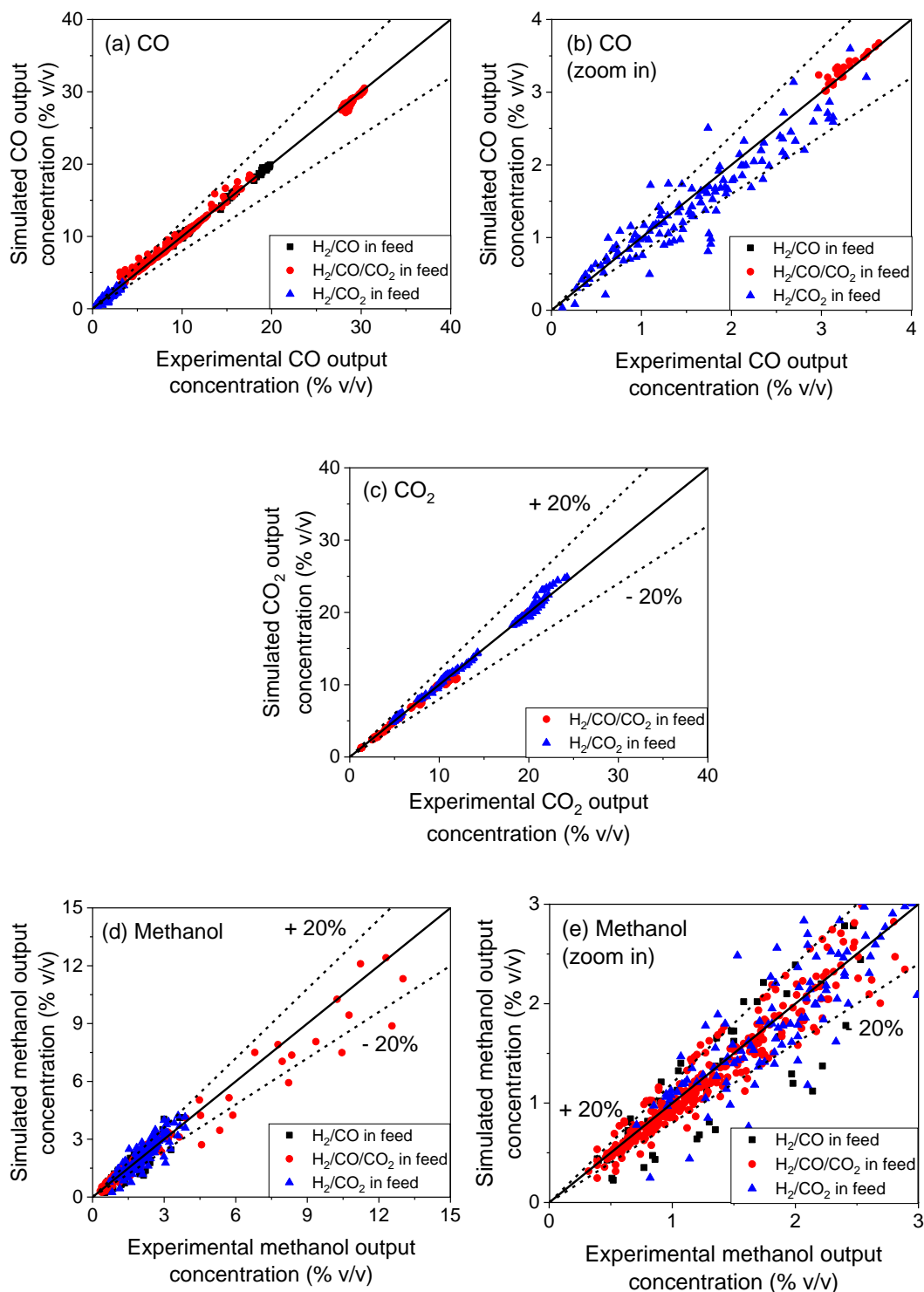


Fig. S2.3 Parity plots of the model from Seidel et al.³⁴ for measured and predicted CO (a-b), CO₂ (c) and methanol (d-e) concentrations in the product stream. Experimental conditions are reported in Table 3.3. Reproduced with permission from Campos et al.⁸⁹. Copyright 2021, American Chemical Society.

S3. Supplementary Material – Chapter 4

S3.1 Mathematical derivation of the reactor equations

A global mole balance in the reactor gives:

$$\frac{dn}{dt} = \dot{n}_{in} - \dot{n}_{out} + r \cdot m_{cat} \quad (\text{S3.1})$$

Where $\frac{dn}{dt}$ is the accumulation of material ($\text{mol} \cdot \text{s}^{-1}$), \dot{n}_{in} and \dot{n}_{out} are the mole flows entering and leaving the reactor respectively ($\text{mol} \cdot \text{s}^{-1}$), r is the total reaction rate ($\text{mol} \cdot \text{kg}_{cat} \cdot \text{s}^{-1}$) and m_{cat} is the total catalyst mass (kg) in the reactor.

There is no accumulation in steady-state operation: $\frac{dn}{dt} = 0$. With an infinitesimal control volume in the axial direction:

$$0 = \dot{n}_z - \dot{n}_{z+dz} + r \cdot dm_{cat} \quad (\text{S3.2})$$

Here, dm_{cat} is the catalyst mass (kg) between position z and $(z + dz)$. Developing each term:

$$d\dot{n} = \dot{n}_{z+dz} - \dot{n}_z \quad (\text{S3.3})$$

$$r = \sum_{j=1}^6 \sum_{k=1}^2 (v_{jk} \cdot r_k) \quad (\text{S3.4})$$

$$dm_{cat} = \frac{m_{cat}}{L} \cdot dz \quad (\text{S3.5})$$

Where L is the reactor length (m), v_{jk} is the stoichiometric coefficient of component j in reaction k , r_k is the rate of reaction k ($\text{mol} \cdot \text{kg}_{cat} \cdot \text{s}^{-1}$). Substituting Eqs. (S3.3-S3.5) in (S3.2) and isolating $\frac{d\dot{n}}{dz}$, the first differential equation is derived:

$$\frac{d\dot{n}}{dz} = \frac{m_{cat}}{L} \cdot \sum_{j=1}^6 \sum_{k=1}^2 (v_{jk} \cdot r_k) \quad (\text{S3.6})$$

From the total mole balance (S3.6), a mole balance from each component is derived:

$$\frac{d\dot{n}_j}{dz} = \frac{m_{cat}}{L} \cdot \sum_{k=1}^2 (v_{jk} \cdot r_k) \quad (\text{S3.7})$$

The mole flow of component j (\dot{n}_j) and its derivative is rewritten as:

$$\dot{n}_j = \dot{n} \cdot y_j \quad (\text{S3.8})$$

$$\frac{d\dot{n}_j}{dz} = \dot{n} \cdot \frac{dy_j}{dz} + y_j \cdot \frac{d\dot{n}}{dz} \quad (\text{S3.9})$$

Substituting Eq. (S3.9) in Eq. (S3.7) and isolating $\frac{dy_j}{dz}$, the second differential equation is derived:

$$\dot{n} \cdot \frac{dy_j}{dz} + y_j \cdot \frac{d\dot{n}_j}{dz} = \frac{m_{cat}}{L} \cdot \sum_{k=1}^2 (v_{jk} \cdot r_k) \quad (S3.10)$$

$$\frac{dy_j}{dz} = \frac{1}{\dot{n}} \cdot \left\{ \frac{m_{cat}}{L} \cdot \sum_{k=1}^2 (v_{jk} \cdot r_k) - y_j \cdot \frac{d\dot{n}}{dz} \right\} \quad (S3.11)$$

A global energy balance in the reactor is derived:

$$\frac{dU_{int}}{dt} = \dot{H}_{in} - \dot{H}_{out} + \dot{Q} \quad (S3.12)$$

Here, $\frac{dU_{int}}{dt}$ is the internal energy accumulation (W), \dot{H}_{in} and \dot{H}_{out} are the enthalpy flow entering and leaving the reactor respectively (W), and \dot{Q} is the heat transfer between the reaction medium and the cooling fluid (W). \dot{Q} is calculated as follows:

$$\dot{Q} = U \cdot A_i \cdot (T_w - T) \quad (S3.13)$$

Where U is the global heat transfer coefficient ($W \cdot m^{-2} \cdot K^{-1}$), A_i is the inner heat transfer area (m^2), T_w is the temperature of the cooling fluid (K), and T is the reactor temperature (K).

There is no accumulation in steady-state operation: $\frac{dU_{int}}{dt} = 0$. With an infinitesimal control volume in the axial direction:

$$0 = \dot{H}_z - \dot{H}_{z+dz} + U \cdot (T_w - T) \cdot dA_i \quad (S3.14)$$

$$0 = -d\dot{H} + U \cdot (T_w - T) \cdot \pi \cdot D_i \cdot dz \quad (S3.15)$$

The derivative of the enthalpy flow ($d\dot{H}$) is further developed:

$$d\dot{H} = d \left[\dot{n} \cdot \sum_{j=1}^6 (y_j \cdot h_j) \right] \quad (S3.16)$$

$$d\dot{H} = \sum_{j=1}^6 (\dot{n} \cdot y_j \cdot dh_j + \dot{n} \cdot h_j \cdot dy_j + y_j \cdot h_j \cdot d\dot{n}) \quad (S3.17)$$

Where h_j is the specific enthalpy of component j ($J \cdot mol^{-1}$). The derivative of the specific enthalpy is developed considering only temperature dependency:

$$dh_j = \frac{dh_j}{dT} \cdot dT = C_{p,j} \cdot dT \quad (S3.18)$$

Here, $C_{p,j}$ is the specific heat capacity of component j ($J \cdot mol^{-1} \cdot K^{-1}$). The fluid specific enthalpy (h_f) and the fluid heat capacity ($C_{p,f}$) are defined as:

$$C_{p,f} = \sum_{j=1}^6 C_{p,j} \cdot y_j \quad (\text{S3.19})$$

$$h_f = \sum_{j=1}^6 y_j \cdot h_j \quad (\text{S3.20})$$

Substituting Eqs. (S3.17-S3.20) in Eq. (S3.15) and isolating $\frac{dT}{dz}$, the third differential equation is derived:

$$\frac{dT}{dz} = \frac{1}{(\dot{n} \cdot C_{p,f})} \cdot \left[-\frac{d\dot{n}}{dz} \cdot h_f - \dot{n} \cdot \sum_{j=1}^6 \left(h_j \cdot \frac{dy_j}{dz} \right) + U \cdot \pi \cdot D_i \cdot (T_w - T) \right] \quad (\text{S3.21})$$

The specific heat capacity and the specific enthalpy were calculated by polynomial correlations. The parameters estimated by Goos et al.⁷⁵ are provided in Table S3.1.

$$C_{p,j}(T, 1 \text{ bar}) = R \cdot (a_{1,j} + a_{2,j} \cdot T + a_{3,j} \cdot T^2 + a_{4,j} \cdot T^3 + a_{5,j} \cdot T^4) \quad (\text{S3.22})$$

$$h_j(T, 1 \text{ bar}) = R \cdot \left(a_{1,j} \cdot T + \frac{a_{2,j}}{2} \cdot T^2 + \frac{a_{3,j}}{3} \cdot T^3 + \frac{a_{4,j}}{4} \cdot T^4 + \frac{a_{5,j}}{5} \cdot T^5 + a_{6,j} \right) \quad (\text{S3.23})$$

Table S3.1 Parameters for the estimation of the specific heat capacity and specific enthalpy of selected components in the gas phase.⁷⁵ Data reproduced with permission from Goos et al.⁷⁵. Table reproduced with permission from Campos et al.¹¹. Copyright 2022, MDPI.

Gas	a_1	$a_2 \cdot 10^3$	$a_3 \cdot 10^5$	$a_4 \cdot 10^8$	$a_5 \cdot 10^{11}$	$a_6 \cdot 10^{-4}$
H ₂	2.3443311	7.9805208	-1.9478151	2.0157209	-0.7376118	-0.0917935
CO	3.5795335	-0.6103537	0.1016814	0.0907006	-0.0904424	-1.4344086
CO ₂	2.3568130	8.9841299	-0.7122063	0.2457301	-0.0142885	-4.8371971
CH ₃ OH	5.6585105	-16.2983419	6.9193816	-7.5837293	2.8042755	-2.5611974
H ₂ O	4.1986352	-2.0364017	0.6520342	-0.5487927	0.1771968	-3.0293726
N ₂	3.5310053	-0.1236610	-0.0502999	0.2435306	-0.1408812	-0.1046976

S3.2. Calculation of the heat transfer coefficient in the reactor

In the methanol synthesis reactor, the global heat transfer coefficient between syngas and the cooling fluid (U) is calculated as a combination of four heat transfer resistances (R_{1-4}):

1. The heat transfer in the bulk of the two-phase system (catalyst and gas);
2. The heat transfer between the two-phase system and the tube inner wall;
3. The heat transfer through the reactor wall;
4. The heat transfer between the tube outer wall and the cooling fluid (boiling water).

This results from the use of a heat transfer coefficient model described in the VDI Heat Atlas (α_w – Model),¹⁰¹ where the radial thermal conductivity of the two-phase system is constant over the radius of the reactor tube. According to Gruber,¹⁰⁰ the global heat transfer coefficient (U) can be calculated as follows:

$$U \cdot A_i = R_1 + R_2 + R_3 + R_4 \quad (S3.24)$$

$$U \cdot A_i = \left(\frac{D_i}{8 \cdot \Lambda_r \cdot A_i} + \frac{1}{\alpha_{w,i} \cdot A_i} + \frac{s_t}{\lambda_t \cdot A_m} + \frac{1}{\alpha_{w,o} \cdot A_o} \right)^{-1} \quad (S3.25)$$

Where Λ_r is the effective radial thermal conductivity of the two-phase system, A_i is the inner surface area of the reactor tube, $\alpha_{w,i}$ is the heat transfer coefficient between the reactive system and the inner wall, s_t is the thickness of the reactor tube, λ_t is the thermal conductivity of the reactor tube, A_m is the averaged surface area of the reactor tube, $\alpha_{w,o}$ is the heat transfer coefficient between the outer wall and the cooling fluid, and A_o is the outer surface area of the reactor tube.

The effective radial thermal conductivity Λ_r is calculated as follows:

$$\frac{\Lambda_r}{\lambda_f} = \frac{\lambda_{bed}}{\lambda_f} + \frac{Pe_0}{K_r} \quad (S3.26)$$

Here, λ_f is the thermal conductivity of the fluid, Pe_0 is the Peclet number calculated with the superficial velocity, and K_r is the inverse of the inclination parameter.

The thermal conductivity of the two-phase system λ_{bed} is calculated from the ZBS-Model.¹⁰¹ In this work, only the primary parameters (λ_f), the thermal conductivity of the catalyst particles (λ_p) and the porosity of the bed ($\psi = 0.39$) were included. λ_{bed} can then be calculated as

$$\frac{\lambda_{bed}}{\lambda_f} = 1 - \sqrt{1 - \psi} + \sqrt{1 - \psi} \cdot k_c \quad (S3.27)$$

Where k_c is the thermal conductivity of the core of the unit cell. The estimation of $\alpha_{w,i}$ is made through the Nusselt number (Nu_w):

$$Nu_w = \frac{\alpha_{w,i} \cdot d_p}{\lambda_f} \quad (S3.28)$$

Here, d_p is the particle diameter ($d_p = 2$ mm). A correlation for Nu_w is used:¹⁰¹

$$Nu_w = \left(1.3 + 5 \cdot \frac{d_p}{D_i} \right) \cdot \frac{\lambda_{bed}}{\lambda_f} + 0.19 \cdot Re_0^{0.75} \cdot Pr^{1/3} \quad (S3.29)$$

Where d is the particle diameter, Re_0 is the Reynolds number, and Pr is the Prandtl number. This function is valid for a Peclet number (Pe_0) between 1 and 10^4 , and for D_i / d_p between 1.2 and 51.

Finally, a constant value of $\alpha_{w,o} = 1000 \text{ W} \cdot \text{m}^{-2} \cdot \text{K}^{-1}$ was considered for the heat transfer between the tube outer wall and boiling water.¹⁰¹

S3.3. Flash drums and distillation column – Assumptions for the Matlab simulations

Table S3.2 Liquid and gas fractions (% mol/mol) of the phase separation via flash drums and the separation via the distillation column in the one-step process. Values taken from Aspen Plus calculations and used for the Matlab simulations. Reproduced with permission from Campos et al.¹¹. Copyright 2022, MDPI.

Equipment	Phase	H ₂	CO	CO ₂	CH ₃ OH	H ₂ O	N ₂
Flash drums 1-2	Gas	100.00	99.92	99.12	28.32	6.41	99.93
	Liquid	0	0.08	0.88	71.68	93.59	0.07
Flash drum 3	Gas	99.87	97.93	77.16	1.09	0.21	98.08
	Liquid	0.13	2.07	22.84	98.91	99.79	1.92
Flash drum 4	Gas	99.97	99.58	94.69	6.42	1.37	99.61
	Liquid	0.03	0.42	5.32	93.59	98.63	0.39
Distillation Column	Gas Dist.	99.89	98.62	87.93	3.80	0.01	98.70
	Liquid Dist.	0.11	1.38	12.07	96.13	0.57	1.30
	Bottoms	0.00	0.00	0.00	0.06	99.42	0.00

Table S3.3 Liquid and gas fractions (% mol/mol) of the phase separation via flash drums and the separation via the distillation column in the three-step process. Values taken from Aspen Plus calculations and used for the Matlab simulations. Reproduced with permission from Campos et al.¹¹. Copyright 2022, MDPI.

Equipment	Phase	H ₂	CO	CO ₂	CH ₃ OH	H ₂ O	N ₂
Flash drums 1-2	Gas	100.00	99.94	99.32	34.02	8.29	99.94
	Liquid	0	0.06	0.68	65.98	91.71	0.06
Flash drum 3	Gas	99.91	98.86	88.92	4.39	0.98	98.93
	Liquid	0.09	1.14	11.08	95.61	99.02	1.07
Flash drum 4	Gas	99.92	98.77	86.22	2.37	0.50	98.86
	Liquid	0.08	1.23	13.78	97.63	99.50	1.14
Flash drum 5	Gas	99.69	95.56	61.86	0.60	0.12	95.85
	Liquid	0.31	4.44	38.14	99.40	99.88	4.15
Flash drum 6	Gas	99.95	99.29	91.34	3.90	0.82	99.34
	Liquid	0.05	0.71	8.66	96.10	99.18	0.66
Distillation Column	Gas Dist.	99.88	98.46	86.67	3.41	0.01	98.55
	Liquid Dist.	0.12	1.54	13.33	96.58	0.68	1.45
	Bottoms	0.00	0.00	0.00	0.01	99.31	0.00

S3.4 Kinetic model implementation in Aspen Plus

In order to implement a kinetic model in Aspen Plus, parameters must be rearranged to fulfill specific format requirements. The kinetic model type of Langmuir-Hinshelwood-Hougen-Watson (LHHW) was chosen, with a reacting phase containing only vapor, a rate basis in catalyst weight, and the concentration basis (C_i) in fugacity (Pa). As the fugacities of Model-6p⁸⁹ are with the unit 'bar', the reference pressure ($p_0 = 1$ bar) were omitted. However, since Aspen Plus require fugacity in 'Pa', the reference pressure ($p_0 = 10^5$ Pa) must appear, and therefore is seen in corresponding expressions between Aspen and Model-6p.

The reaction rates of the LHHW kinetic model type ($\text{kmol}\cdot\text{kg}^{-1}\cdot\text{s}^{-1}$) follow this expression:

$$r = \frac{[\textit{kinetic factor}] \cdot [\textit{Driving force expression}]}{[\textit{Adsorption expression}]} \quad (\text{S3.30})$$

The kinetic factor is described as:

$$[\textit{kinetic factor}] = k \cdot T^n \cdot \exp\left(\frac{-E_A}{R \cdot T}\right) \quad (\text{S3.31})$$

The corresponding expressions from Model-6p in relation to parameters k , n , E_A are detailed in Table S3.4.

The driving force expression has two terms, how are described as:

$$[\textit{Term 1}] = \exp\left[A + \frac{B}{T} + C \cdot \ln(T) + D \cdot T\right] \cdot \prod_{j=1}^{N_g} (f_j^{v_j}) \quad (\text{S3.32})$$

$$[\textit{Term 2}] = \exp\left[A + \frac{B}{T} + C \cdot \ln(T) + D \cdot T\right] \cdot \prod_{j=1}^{N_g} (f_j^{v_j}) \quad (\text{S3.33})$$

$$[\textit{Driving force expression}] = [\textit{Term 1}] - [\textit{Term 2}] \quad (\text{S3.34})$$

Table S3.4 Aspen kinetic factor and Model-6p corresponding expressions. Reproduced with permission from Campos et al.¹¹. Copyright 2022, MDPI.

Parameter in Aspen	Corresponding expression from Model-6p ⁸⁹	Value		Unit
		CO ₂ hyd.	rWGSr	
k	$\phi_{Zn} \cdot \exp(A_i) \cdot \frac{1 \text{ kmol}}{1000 \text{ mol}}$	181.211	$4.4771 \cdot 10^8$	$\frac{\text{kmol}}{\text{kg}_{\text{cat}} \cdot \text{s}}$
n	0	0	0	—
E	$E_{A,i}$	94.73	132.79	$\frac{\text{kJ}}{\text{mol}}$

In Table S3.5, the corresponding expressions from Model-6p in relation to the coefficients of the driving force constant (A , B , C , D) are detailed, while the concentration exponents v_j are described in Table S3.6.

Table S3.5 Coefficients of the driving force constant and the corresponding expressions from Model-6p. Reproduced with permission from Campos et al.¹¹. Copyright 2022, MDPI.

Term	Reaction	Parameter in Aspen	Corresponding expression in Model-6p	Value
1	CO ₂ hydrog.	A	$\ln(p_0^{-2.5})$	- 28.7823
		B	0	0
		C	0	0
		D	0	0
1	rWGSR	A	$\ln(p_0^{-2})$	- 23.0259
		B	0	0
		C	0	0
		D	0	0
2	CO ₂ hydrog.	A	$\ln(p_0^{-0.5}) - A_{eq.const.CO_2hyd.}$	- 14.1255
		B	$-B_{eq.const.CO_2hyd.}$	- 4755.7
		C	$-C_{eq.const.CO_2hyd.}$	4.481
		D	0	0
2	rWGSR	A	$\ln(p_0^{-2}) - A_{eq.const.rWGSR}$	- 35.5949
		B	$-B_{eq.const.rWGSR}$	5337.4
		C	$-C_{eq.const.rWGSR}$	1.097
		D	0	0

Table S3.6 Concentration exponents (v_j) of the driving force expression. Reproduced with permission from Campos et al.¹¹. Copyright 2022, MDPI.

Gas component	Methanol synthesis		rWGSR	
	Term 1	Term 2	Term 1	Term 2
H ₂	1.5	- 1.5	0	- 1
CO	–	–	0	1
CO ₂	1	0	1	0
CH ₃ OH	0	- 1	–	–
H ₂ O	0	- 1	1	2

The adsorption expression is:

$$[\text{Adsorption exp.}] = \sum_{k=1}^{N_t} \left\{ \exp \left[A_k + \frac{B_k}{T} + C_k \cdot \ln(T) + D_k \cdot T \right] \cdot \prod_{j=1}^{N_g} (f_j^{v_{j,k}}) \right\}^n \quad (\text{S3.35})$$

Where N_t is the number of terms. By looking at the expressions from Model-6p:

$$[\text{Adsorption exp. Model - 6p}] = (\theta_b \cdot \theta_c)^{-1} \quad (\text{S3.36})$$

$$[\text{Adsorption exp. Model - 6p}] = \left(\bar{K}_2 \cdot \frac{f_{H_2}^{0.5} \cdot f_{CO_2}}{p_0^{1.5}} + 1 \right) \cdot \left(\bar{K}_3 \cdot \frac{f_{H_2}^{-0.5} \cdot f_{H_2O}}{p_0^{0.5}} + 1 \right) \quad (\text{S3.37})$$

$$\begin{aligned} [\text{Adsorption exp. Model - 6p}] &= 1 + \bar{K}_2 \cdot \frac{f_{H_2}^{0.5} \cdot f_{CO_2}}{p_0^{1.5}} + \bar{K}_3 \cdot \frac{f_{H_2}^{-0.5} \cdot f_{H_2O}}{p_0^{0.5}} \\ &\quad + \bar{K}_2 \cdot \bar{K}_3 \cdot \frac{f_{CO_2} \cdot f_{H_2O}}{p_0^2} \end{aligned} \quad (\text{S3.38})$$

From Eq. (9), the adsorption expression exponent is $n = 1$. The correspondence with Model-6p is described in Table S3.7 (adsorption constants) and in Table S3.8 (concentration exponents).

Table S3.7 Adsorption constants and the corresponding expression of Model-6p. Reproduced with permission from Campos et al.¹¹. Copyright 2022, MDPI.

Adsorption constants	Corresponding expression in Model-6p	Value
A – Term 1	$\ln(1)$	0
A – Term 2	$\ln(\bar{K}_2 \cdot p_0^{-1.5})$	-18.237
A – Term 3	$\ln(\bar{K}_3 \cdot p_0^{-0.5})$	-3.64262
A – Term 4	$\ln(\bar{K}_2 \cdot \bar{K}_3 \cdot p_0^{-2})$	-21.8796

Table S3.8 Concentration exponents and the corresponding values of Model-6p. Reproduced with permission from Campos et al.¹¹. Copyright 2022, MDPI.

Gas components	Term 1	Term 2	Term 3	Term 4
CO ₂	0	1	0	1
H ₂	0	0.5	-0.5	0
H ₂ O	0	0	1	1

S3.5 One-step process – Simulation in Aspen Plus and stream properties

In Fig. S3.1, the Aspen flowsheet of the one-step process is presented. Feed CO₂ (1-CO₂, 4824 kmol·h⁻¹) is mixed with a recycle stream (39-REC, 2786 kmol·h⁻¹) (MIXER1), which mainly consists of CO₂, but also contains methanol, water, nitrogen, hydrogen, and traces of CO. The mixed gas is compressed from 1 to 70 bar in three stages with equal pressure ratio (CP1-CO₂, CP2-CO₂, CP3-CO₂). Intermediate cooling is performed with cooling water (HE1) and with a pressurized recycle stream (35) (HE2). Condensed methanol and water are separated in intermediate flash units (FLASH1 at 30 °C and FLASH2 at 45 °C), preventing liquid to enter the compressors. Finally, compressed CO₂ (9) is used to partially heat pressurized water (51W) (HE3), the latter serving as cooling fluid in the reactor modules later on.

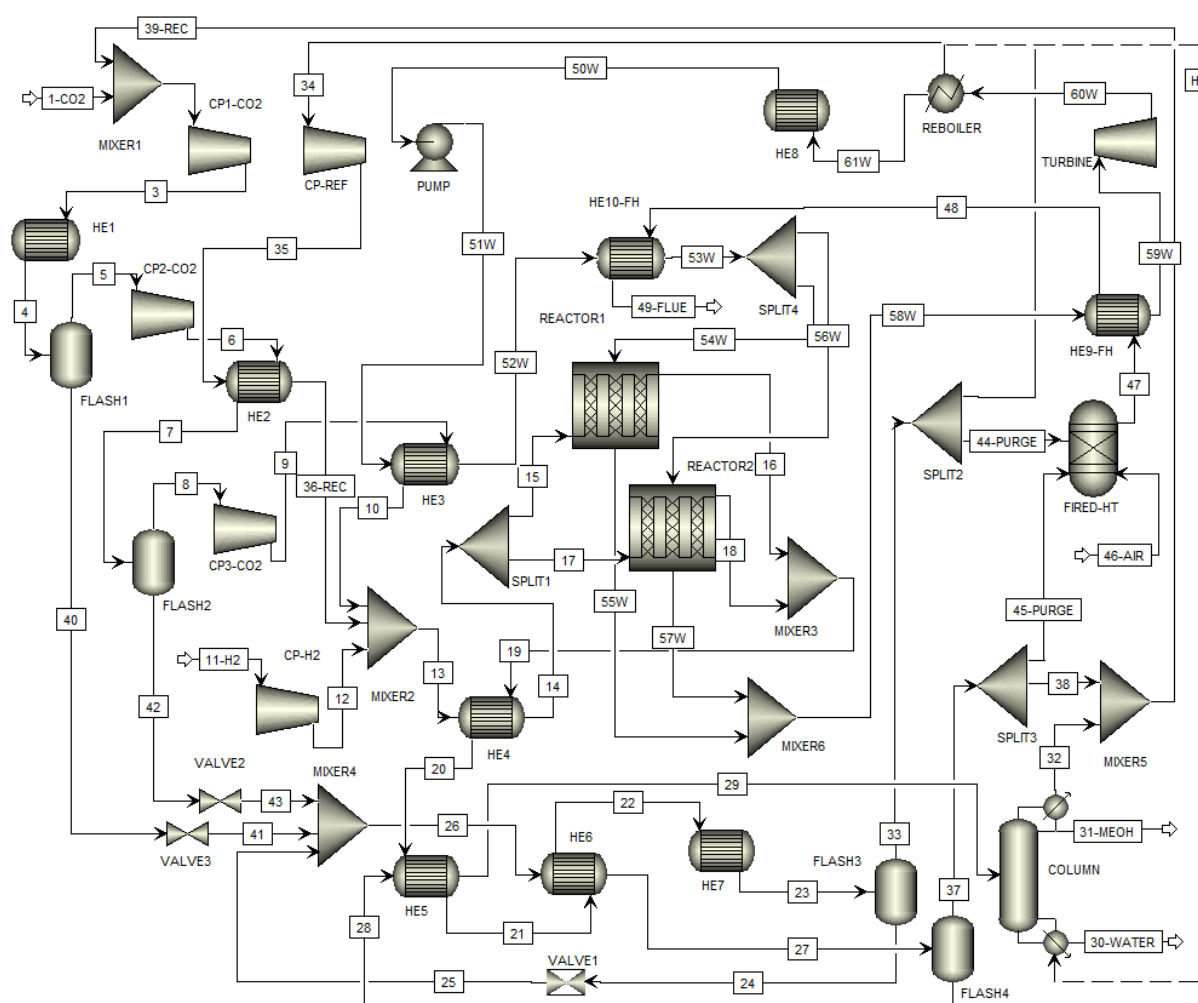


Fig. S3.1 One-step process – Aspen Plus flowsheet. Reproduced with permission from Campos et al.¹¹. Copyright 2022, MDPI.

Hydrogen (11-H₂, 14472 kmol·h⁻¹) is compressed in a single stage from 30 to 70 bar (CP-H₂). CO₂ (10) and H₂ (12) are combined with a pressurized recycle stream (36-REC, 51504 kmol·h⁻¹) (MIXER2), which is mainly composed of H₂ (73% mol/mol), CO₂

(18% mol/mol), and N_2 (7% mol/mol), but also contains low concentrations of CO, methanol and water.

The mixed gas (13) is pre-heated (HE4) with the product stream to 237.5 °C. The reactor feed stream (14) is split into the six reactor modules, which work in parallel and have boiling water at 247.5 °C as cooling fluid (54W and 56W). Here, the number of tubes of both RPLUG units (REACTOR1 and REACTOR2) was set to 99000 tubes, so that the parallel operation of six reactor modules with 33000 tubes each are simulated (tube quantity is limited to 99999 in Aspen). Reactor setpoint temperature (247.5 °C) is rapidly achieved ($z = 0.09$ m), after which isothermal conditions are maintained ($\Delta T_{max} < 3$ °C).

The reactor product streams (16 and 18) are combined (MIXER3) and cooled down to 30 °C in four stages: first by the reactor feed (13) (HE4), second by the column feed (28) (HE5), third by the feed of flash drum 4 (26) (HE6), and finally by cooling water (HE7). The first phase separation occurs in a flash drum (FLASH3 at 30 °C and 69.25 bar), with the gas phase (33) rich in H_2 , CO_2 and N_2 , and the liquid phase (24) rich in methanol and water, but still containing a considerable amount of CO_2 .

The gas stream (33) has a 2% purge (44-PURGE, $1051 \text{ kmol}\cdot\text{h}^{-1}$). The remaining recycle stream (34) is recompressed to 70 bar (CP-REC), partially heated (HE2), and mixed with the reactor feed (MIXER1).

The liquid stream (24) enters a choke valve (VALVE1), where its pressure is reduced to 1 bar, and afterwards is mixed (MIXER4) with the liquid fractions of FLASH1 and FLASH2 from the three-stage compression process. The mixed stream (26) is slightly heated to 30 °C (HE5), and enters another flash drum (FLASH4 at 30 °C and 1 bar), where more CO_2 is recovered in the gas phase (37). 2% of the gas stream (37) is purged from the system (45-PURGE, $51 \text{ kmol}\cdot\text{h}^{-1}$), and the remaining stream (38) is mixed with the gas distillate (32) (MIXER5) and with feed CO_2 (1-CO2) (MIXER1).

The liquid phase (28) from FLASH4, which mainly consists of methanol and water, is pre-heated (HE5) and then enters a distillation column with a partial vapor-liquid condenser at 53 °C and a kettle reboiler at 99.6 °C. The column has 30 stages, a reflux ratio of 2, and the feed enters above the 24th stage. Water as bottom stream (30-WATER, $4581 \text{ kmol}\cdot\text{h}^{-1}$) and methanol as liquid distillate (31-MEOH, $4542 \text{ kmol}\cdot\text{h}^{-1}$) are obtained in a purity of 99.99% and 99.67% mol/mol, respectively, while the gas distillate (32) consists of a mixture between methanol (62.97% mol/mol) and CO_2 (36.91% mol/mol).

The purge streams (44-PURGE and 45-PURGE) are fed into a fired heater and burned with air (46-AIR, $2232 \text{ kmol}\cdot\text{h}^{-1}$). Air excess is set to 15%, following the recommendation from the American Petroleum Institute.⁹⁹ The fired heater is composed of the burner (FIRED-HT) and two heat exchangers (HE9-FH and HE10-FH).

In order to make use of the energy generated in the methanol synthesis, the reactor cooling fluid (water) flows in a Rankine cycle. The cycle starts with liquid water at 1 bar and 99.6 °C (50W, $8120 \text{ kmol}\cdot\text{h}^{-1}$) being pumped to 38.07 bar, which is then heated until its boiling temperature (247.5 °C) in two steps: first by compressed CO_2 (9) (HE3), and then by the flue

gas (48) in the fired heater (HE10-FH). The boiling water stream (53W) is split into the reactor modules and evaporates with the heat released by the methanol synthesis. The resulting streams of saturated vapor (55W and 57W) are merged (MIXER6), and then further heated in the fired heater (HE9-FH) up to 542 °C. The resulting superheated steam (59W) is expanded until 1.43 bar in a turbine coupled with an electric generator, and 30.3 MW of electricity is gained. Low pressure steam (59W) at 155 °C and a boiling temperature of 110 °C exits the turbine and is the heat source of the column reboiler. The hot side is simulated in Aspen Plus with a heater block named REBOILER, and a heat stream is sent to the column (dashed line, H1). After being partially condensed in the reboiler, the remaining steam (61W) (vapor fraction: 0.47) is completely condensed with cooling water (HE13), completing the water cycle.

Table S3.9 Properties of the streams from the one-step process. Reproduced with permission from Campos et al.¹¹. Copyright 2022, MDPI.

Stream ID	Mole flow [kmol·h ⁻¹]	Mass flow [t·h ⁻¹]	Temp. [°C]	Pressure [bar]	Mole enthalpy [MJ·kmol ⁻¹]	Mole entropy [kJ·kmol ⁻¹ ·K ⁻¹]	Total Exergy [MJ·kmol ⁻¹]
1-CO2	4824	211.7	25.0	1.00	-392.75	3.02	0.0
2	7610	323.9	27.8	1.00	-373.65	-2.17	102.4
3	7610	323.9	155.3	4.12	-368.48	0.32	111.8
4	7610	323.9	30.0	4.12	-374.91	-17.99	109.7
5	7333	315.8	30.0	4.12	-379.32	-10.92	69.5
6	7333	315.8	158.6	16.98	-374.11	-8.44	78.6
7	7333	315.8	45.0	16.98	-379.57	-23.37	76.6
8	7138	309.3	45.0	16.98	-382.65	-18.86	47.1
9	7138	309.3	178.0	70.00	-377.20	-16.38	56.4
10	7138	309.3	111.0	70.00	-380.03	-23.16	54.8
11-H2	14472	31.1	25.0	30.00	0.00	-27.91	1176.9
12	14472	31.1	127.4	70.00	2.97	-26.38	1187.1
13	73113	948.6	81.4	70.00	-86.80	-22.14	4488.1
14	73113	948.6	237.5	70.00	-81.60	-10.00	4520.1
15	36557	474.3	237.5	70.00	-81.60	-10.00	2260.0
16	32021	474.3	247.9	69.25	-97.10	-17.44	2163.2
17	36557	474.3	237.5	70.00	-81.60	-10.00	2260.0
18	32021	474.3	247.9	69.25	-97.10	-17.44	2163.2
19	64042	948.5	247.9	69.25	-97.10	-17.44	4326.4
20	64042	948.5	133.2	69.25	-103.03	-30.71	4291.2
21	64042	948.5	62.0	69.25	-108.84	-46.20	4270.1
22	64042	948.5	56.9	69.25	-109.12	-47.04	4269.6
23	64042	948.5	30.0	69.25	-110.23	-50.19	4261.2
24	11488	328.0	30.0	69.25	-284.19	-162.33	950.1
25	11488	328.0	18.5	1.00	-284.19	-159.00	946.9
26	11960	342.6	18.9	1.00	-283.31	-160.44	1016.2
27	11960	342.6	30.0	1.00	-281.80	-155.45	1016.3
28	9412	238.8	30.0	1.00	-263.70	-195.62	949.2
29	9412	238.8	82.9	1.00	-224.18	-81.88	963.8
30-WATER	4581	82.5	99.6	1.00	-280.00	-145.98	1.0
31-MEOH	4542	145.7	53.0	1.00	-236.17	-231.08	912.6

Table S3.9 (Continuation)

Stream ID	Mole flow [kmol·h ⁻¹]	Mass flow [t·h ⁻¹]	Temp. [°C]	Pressure [bar]	Mole enthalpy [MJ·kmol ⁻¹]	Mole entropy [kJ·kmol ⁻¹ ·K ⁻¹]	Total Exergy [MJ·kmol ⁻¹]
32	289	10.5	53.0	1.00	-270.63	-71.02	36.8
33	52555	620.6	30.0	69.25	-72.20	-25.68	3311.1
34	51504	608.2	30.0	69.25	-72.20	-25.68	3244.9
35	51504	608.2	31.2	70.00	-72.16	-25.65	3245.3
36-REC	51504	608.2	56.7	70.00	-71.39	-23.19	3245.9
37	2548	103.8	30.0	1.00	-348.67	-7.11	67.2
38	2497	101.7	30.0	1.00	-348.67	-7.11	65.8
39-REC	2786	112.3	33.0	1.00	-340.58	-13.18	102.5
40	276	8.2	30.0	4.12	-258.07	-205.74	40.1
41	276	8.2	25.8	1.00	-258.07	-205.32	40.0
42	196	6.4	45.0	16.98	-267.32	-187.87	29.3
43	196	6.4	29.1	1.00	-267.32	-184.53	29.3
44-PURGE	1051	12.4	30.0	69.25	-72.20	-25.68	66.2
45-PURGE	51	2.1	30.0	1.00	-348.67	-7.11	1.3
46-AIR	2232	64.4	25.0	1.00	0.00	4.38	0.0
47	2944	78.9	1798.0	1.00	-31.81	65.74	38.9
48	2944	78.9	1095.9	1.00	-60.67	48.77	19.5
49-FLUE	2944	78.9	162.5	1.00	-94.18	8.51	1.9
50W	8120	146.3	99.6	1.00	-280.01	-145.97	1.5
51W	8120	146.3	100.9	38.07	-279.90	-145.70	1.6
52W	8120	146.3	130.3	38.07	-277.42	-139.47	3.0
53W	8120	146.3	247.5	38.07	-265.27	-115.18	14.1
54W	4060	73.1	247.5	38.07	-265.27	-115.18	7.0
55W	4060	73.1	247.5	38.07	-234.21	-55.53	22.0
56W	4060	73.1	247.5	38.07	-265.27	-115.18	7.0
57W	4060	73.1	247.5	38.07	-234.21	-55.53	22.0
58W	8120	146.3	247.5	38.07	-234.21	-55.53	44.0
59W	8120	146.3	528.8	38.07	-223.74	-39.50	56.8
60W	8120	146.3	147.5	1.43	-237.66	-35.61	22.8
61W	8120	146.3	110.0	1.43	-261.46	-97.58	10.8

Table S3.10 Molar composition (% mol/mol) of the streams from the one-step process.Reproduced with permission from Campos et al.¹¹. Copyright 2022, MDPI.

Stream ID	H ₂	CO	CO ₂	CH ₃ OH	H ₂ O	N ₂	O ₂
1-CO2	0.000	0.000	99.500	0.000	0.500	0.000	0.000
2	0.567	0.247	90.986	6.362	1.100	0.737	0.000
3	0.567	0.247	90.986	6.362	1.100	0.737	0.000
4	0.567	0.247	90.986	6.362	1.100	0.737	0.000
5	0.589	0.257	94.196	3.892	0.302	0.764	0.000
6	0.589	0.257	94.196	3.892	0.302	0.764	0.000
7	0.589	0.257	94.196	3.892	0.302	0.764	0.000
8	0.605	0.264	96.313	1.964	0.069	0.785	0.000
9	0.605	0.264	96.313	1.964	0.069	0.785	0.000
10	0.605	0.264	96.313	1.964	0.069	0.785	0.000
11-H2	99.500	0.000	0.000	0.000	0.000	0.500	0.000
12	99.500	0.000	0.000	0.000	0.000	0.500	0.000
13	71.346	1.515	21.874	0.292	0.026	4.946	0.000
14	71.346	1.515	21.874	0.292	0.026	4.946	0.000
15	71.346	1.515	21.874	0.292	0.026	4.946	0.000
16	60.170	1.765	17.855	7.415	7.147	5.647	0.000
17	71.346	1.515	21.874	0.292	0.026	4.946	0.000
18	60.170	1.765	17.855	7.415	7.147	5.647	0.000
19	60.170	1.765	17.855	7.415	7.147	5.647	0.000
20	60.170	1.765	17.855	7.415	7.147	5.647	0.000
21	60.170	1.765	17.855	7.415	7.147	5.647	0.000
22	60.170	1.765	17.855	7.415	7.147	5.647	0.000
23	60.170	1.765	17.855	7.415	7.147	5.647	0.000
24	0.383	0.167	18.545	40.688	39.718	0.498	0.000
25	0.383	0.167	18.545	40.688	39.718	0.498	0.000
26	0.368	0.161	18.226	41.958	38.809	0.478	0.000
27	0.368	0.161	18.226	41.958	38.809	0.478	0.000
28	0.000	0.001	1.285	50.041	48.671	0.002	0.000
29	0.000	0.001	1.285	50.041	48.671	0.002	0.000
30-WATER	0.000	0.000	0.000	0.015	99.985	0.000	0.000
31-MEOH	0.000	0.000	0.316	99.667	0.016	0.000	0.000
32	0.004	0.029	36.909	62.974	0.004	0.080	0.000
33	73.238	2.115	17.704	0.142	0.028	6.772	0.000
34	73.238	2.115	17.704	0.142	0.028	6.772	0.000
35	73.238	2.115	17.704	0.142	0.028	6.772	0.000
36-REC	73.238	2.115	17.704	0.142	0.028	6.772	0.000
37	1.728	0.751	80.793	12.107	2.386	2.235	0.000
38	1.728	0.751	80.793	12.107	2.386	2.235	0.000
39-REC	1.550	0.676	76.245	17.379	2.139	2.012	0.000
40	0.000	0.001	5.828	71.894	22.273	0.003	0.000
41	0.000	0.001	5.828	71.894	22.273	0.003	0.000

Table S3.10 (Continuation)

Stream ID	H ₂	CO	CO ₂	CH ₃ OH	H ₂ O	N ₂	O ₂
42	0.001	0.004	16.991	74.209	8.783	0.012	0.000
43	0.001	0.004	16.991	74.209	8.783	0.012	0.000
44-PURGE	73.238	2.115	17.704	0.142	0.028	6.772	0.000
45-PURGE	1.728	0.751	80.793	12.107	2.386	2.235	0.000
46-AIR	0.000	0.000	0.000	0.000	0.000	79.000	21.000
47	0.088	0.136	8.612	0.000	26.662	62.336	2.166
48	0.088	0.136	8.612	0.000	26.662	62.336	2.166
49-FLUE	0.088	0.136	8.612	0.000	26.662	62.336	2.166
50W	0.000	0.000	0.000	0.000	100.000	0.000	0.000
51W	0.000	0.000	0.000	0.000	100.000	0.000	0.000
52W	0.000	0.000	0.000	0.000	100.000	0.000	0.000
53W	0.000	0.000	0.000	0.000	100.000	0.000	0.000
54W	0.000	0.000	0.000	0.000	100.000	0.000	0.000
55W	0.000	0.000	0.000	0.000	100.000	0.000	0.000
56W	0.000	0.000	0.000	0.000	100.000	0.000	0.000
57W	0.000	0.000	0.000	0.000	100.000	0.000	0.000
58W	0.000	0.000	0.000	0.000	100.000	0.000	0.000
59W	0.000	0.000	0.000	0.000	100.000	0.000	0.000
60W	0.000	0.000	0.000	0.000	100.000	0.000	0.000
61W	0.000	0.000	0.000	0.000	100.000	0.000	0.000

S3.6 Three-step process – Simulation in Aspen Plus and stream properties

In Figure S3.2, a detailed flowsheet of the three-step methanol synthesis plant implemented in Aspen Plus is presented. Feed CO₂ (1-CO₂, 4655 kmol·h⁻¹) is mixed with a recycle stream (58-REC, 1927 kmol·h⁻¹) (MIXER1), which mainly consists of CO₂ (70% mol/mol), methanol (19% mol/mol), and nitrogen (6%), and has low amounts of other components. Similarly to the previous approach, CO₂ is compressed in a three-stage process from 1 to 70 bar (CP1-CO₂, CP2-CO₂, CP3-CO₂), with intermediate cooling (HE1 and HE2) and intermediate phase separation (FLASH 1 at 30 °C and 4.12 bar, FLASH2 at 45 °C and 16.98 bar).

Hydrogen (10-H₂, 13964 kmol·h⁻¹) is compressed in a single stage from 30 to 70 bar (CP-H₂). Hydrogen (11) and CO₂ (9) are mixed (MIXER2) with a pressurized recycle stream (51-REC, 20654 kmol·h⁻¹), which is rich in H₂ (69% mol/mol), N₂ (16% mol/mol), and CO₂ (12% mol/mol).

The mixed stream (12) is pre-heated with the first product stream (14) up to 248.5 °C (HE3), and enters Reactor 1. The reactor cooling is performed with water at 248.5 °C and 45.75 bar ($T_{\text{boiling}} = 258.5$ °C). Reactor setpoint temperature (258.5 °C) is rapidly achieved by both phases ($z = 0.75$ m), after which isothermal conditions are maintained ($\Delta T_{\text{max}} < 3$ °C). Similar temperature profiles occur in Reactors 2 and 3.

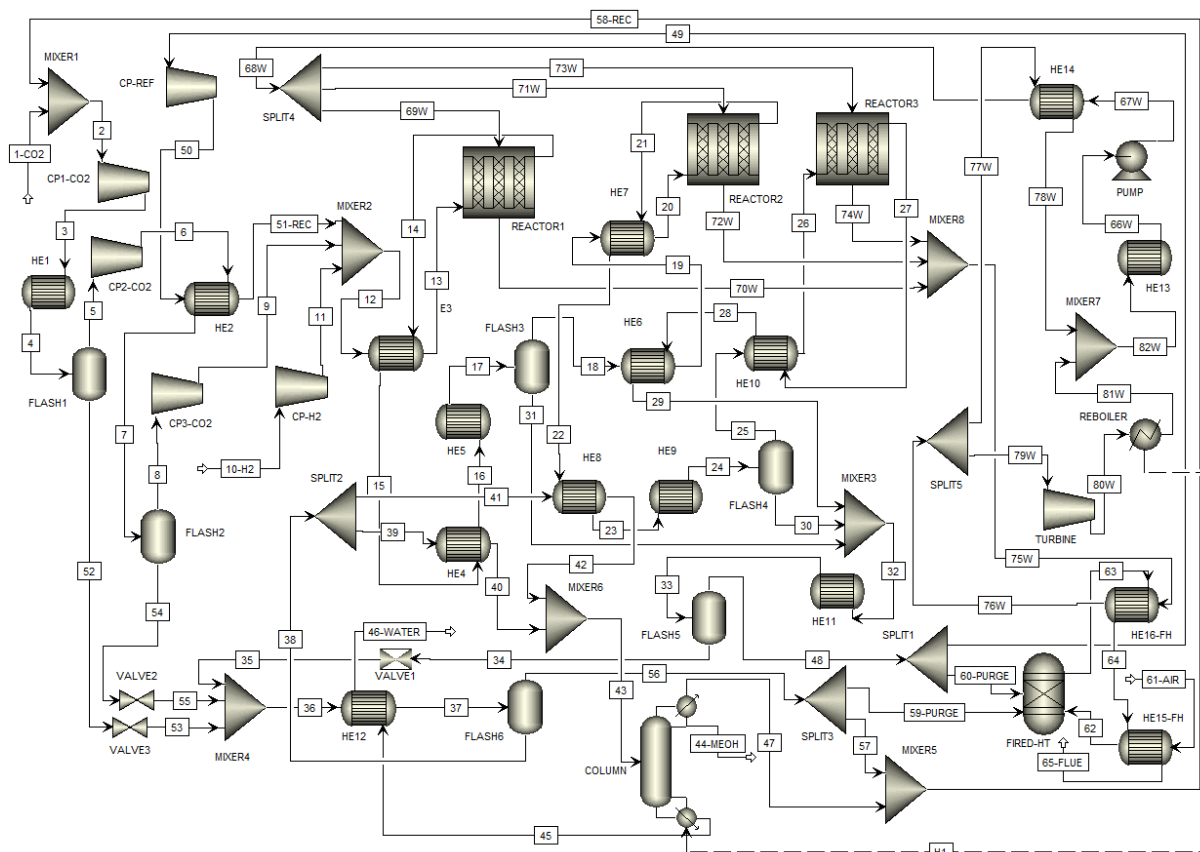


Fig. S3.2 Three-step process – Aspen Plus flowsheet. Reproduced with permission from Campos et al.¹¹. Copyright 2022, MDPI.

The first product stream (14) is cooled down to 45 °C in three stages: first by the first feed stream (12) (HE3), second by a fraction of the column feed (39) (HE4), and finally by cooling water (HE5). A phase separation of the cooled stream (17) occurs in flash drum (FLASH3, 45 °C and 69.25 bar), where most water (98.8%) and methanol (94.7%), as well as some CO₂ (9.3%) remain in the liquid stream (31).

The remaining gas stream (18) is warmed back to 248.5 °C in two stages: first by the third product stream (28) (HE6), and then by the second product stream (21) (HE7). The warmed stream (20) enters Reactor 2, where similar cooling to the first reactor is applied. The product stream (21) is cooled down to 30 °C in three stages: first by the second reactor feed (19) (HE7), second by a fraction of the column feed (41) (HE8), and finally by cooling water (HE9). Then, a phase separation occurs (FLASH4, 30 °C and 68.5 bar), where most water (99.5%), methanol (97.5%), as well as some CO₂ (12.6%) remain in the liquid stream (30).

The gas stream (25) is heated to 248.5 °C by the third product stream (27) (HE10). The warmed stream (26) enters Reactor 3, with similar cooling to the other ones. The product stream (27) is cooled by the third reactor feed (25) (HE10), and then by the gas stream of flash drum 3 (18) (HE6). After that, the third product stream (29) is mixed with the liquid streams from the intermediate condensation steps (30 and 31) (MIXER3), and the mixture is cooled down to 30 °C with cooling water (HE11). A phase separation occurs (FLASH5, 30 °C and

67.75 bar), where most water (99.9%), methanol (99.3%), and a significant amount of CO₂ (34.5%) remain in the liquid stream (34).

The gas stream (48) has a 2% purge (60-PURGE, 422 kmol·h⁻¹). The remaining recycle stream (49) is recompressed to 70 bar (CP-REC), and pre-heated by feed CO₂ (6) (HE2). Then, the recycle stream (51-REC, 20654 kmol·h⁻¹) is mixed with the compressed feed streams (MIXER2).

The liquid stream from flash drum 5 (34) has a pressure reduction to 1 bar in a choke valve (VALVE1), and is mixed with the liquid fraction from the flash drums 1-2 (53 and 55) (MIXER4). The mixed stream (36) is slightly heated to 30 °C with boiling water from the column (45) (HE12), and then a phase separation occurs (FLASH6, 30 °C and 1 bar). Most of the water (99.1%) and the methanol (95.8%) from the feed stream are recovered in the liquid phase, as well as some CO₂ (8.1%).

The gas stream (56) has a 2% purge (59-PURGE, 34 kmol·h⁻¹). The remaining recycle stream (57) is mixed with the gas distillate (47) (MIXER5), and the resulting stream (58-REC, 1927 kmol·h⁻¹) is mixed with feed CO₂ (1) (MIXER1).

The liquid stream from flash drum 6 (38) is split into two parts (stream 39 with 65%, stream 41 with 35%), and these resulting streams are heated in parallel (HE4, HE8) with the first and the second product streams (15 and 22, respectively). The warmed streams (40 and 42) are mixed (MIXER6) and fed to the distillation column, which has a partial vapor-liquid condenser at 53 °C and a kettle reboiler at 99.6 °C. The column has 30 stages, a reflux ratio of 2, and the feed enters above the 24th stage. Water as bottom stream (stream 45, 4563 kmol·h⁻¹) and methanol as liquid distillate (44-MEOH, 4540 kmol·h⁻¹) are obtained in a purity of 99.99% mol/mol and 99.67% mol/mol, respectively. The gas distillate is mainly composed of methanol (62.97% mol/mol) and CO₂ (36.68% mol/mol).

The purge streams (59-PURGE, 60-PURGE) are burned in a fired heater with air (61-AIR, 873 kmol·h⁻¹) at 15% excess, the latter being pre-heated with the flue gas (64) (HE15-FH).

Similarly to the one-step process, a water Rankine cycle is also present in this approach. Condensed water at 99.6 °C and 1 bar (66W, 7680 kmol·h⁻¹) is pumped to 45.75 bar. Compressed water (67W) is heated up to 248.5 °C with superheated vapor (77W) (HE14). The warmed water (68W, T_{boiling} = 258.5 °C) is split into three fractions, and each one is fed to a reactor as cooling fluid. The split fraction are chosen according to the heat duty from each respective reactor, that is: 27.7% for Reactor 1, 38.4% for Reactor 2, and 33.9% for Reactor 3. The saturated steams (70W, 72W, 74W), which were vaporized with the reaction enthalpy, are mixed (MIXER8) and further heated in the fired heater up to 513 °C (HE16-FH). The supersaturated steam (76W) is split into two fractions. The first one (77W, 2077 kmol·h⁻¹) is used to pre-heat the water that flows to the reactors (67W) (HE14), while the second one (79W, 5602 kmol·h⁻¹) generates 20.94 MW of work in a turbine. Low pressure steam (80W) leaves the turbine at 123 °C and 1.43 bar and enters the reboiler of the distillation column as the hot fluid. This is simulated in Aspen Plus with a Heat unit and a heat stream (H1). Finally, a water stream (81W) at 110 °C, 1.43 bar and a vapor fraction of 0.105 is mixed with the water

stream from heat exchanger 14 (78W) (MIXER7), and the mixed stream (82W) is fully condensed (HE13), completing the cycle.

Table S3.11 Properties of the streams from the three-step process. Reproduced with permission from Campos et al.¹¹. Copyright 2022, MDPI.

Stream ID	Mole flow [kmol·h ⁻¹]	Mass flow [t·h ⁻¹]	Temp. [°C]	Pressure [bar]	Mole enthalpy [MJ·kmol ⁻¹]	Mole entropy [kJ·kmol ⁻¹ ·K ⁻¹]	Total Exergy [MJ·kmol ⁻¹]
1-CO2	4655	204.3	25.0	1.00	-392.75	3.02	0.0
2	6582	279.8	27.5	1.00	-370.74	-0.89	78.7
3	6582	279.8	155.6	4.12	-365.58	1.59	86.8
4	6582	279.8	30.0	4.12	-371.65	-15.58	85.1
5	6406	274.6	30.0	4.12	-374.75	-10.38	60.0
6	6406	274.6	159.1	16.98	-369.54	-7.90	68.0
7	6406	274.6	45.0	16.98	-374.99	-22.79	66.2
8	6239	269.1	45.0	16.98	-377.87	-18.39	41.3
9	6239	269.1	178.5	70.00	-372.42	-15.90	49.4
10-H2	13964	30.0	25.0	30.00	0.00	-27.91	1135.6
11	13964	30.0	127.4	70.00	2.97	-26.38	1145.4
12	40857	545.2	122.3	70.00	-80.39	-18.34	2439.9
13	40857	545.2	248.5	70.00	-76.20	-9.14	2456.3
14	37619	545.2	259.4	69.25	-84.52	-12.09	2387.1
15	37619	545.2	138.1	69.25	-89.08	-21.88	2370.1
16	37619	545.2	60.0	69.25	-94.99	-37.62	2357.3
17	37619	545.2	45.0	69.25	-95.54	-39.05	2353.8
18	33222	427.0	45.0	69.25	-71.44	-22.73	2012.5
19	33222	427.0	90.5	69.25	-70.03	-18.61	2014.1
20	33222	427.0	248.5	69.25	-65.02	-7.17	2028.9
21	30048	426.9	259.4	68.50	-74.94	-12.82	1962.2
22	30048	426.9	125.1	68.50	-80.48	-25.08	1946.4
23	30048	426.9	65.0	68.50	-85.02	-37.32	1939.0
24	30049	426.9	30.0	68.50	-86.55	-41.76	1935.1
25	26387	323.5	30.0	68.50	-60.12	-24.05	1602.1
26	26387	323.5	248.5	68.50	-53.34	-7.23	1615.1
27	23738	323.5	259.0	67.75	-62.71	-13.64	1559.4
28	23738	323.5	100.5	67.75	-70.26	-31.14	1544.1
29	23738	323.5	72.0	67.75	-72.22	-36.59	1541.8
30	3661	103.4	30.0	68.50	-276.99	-169.43	333.0
31	4397	118.3	45.0	69.25	-277.64	-162.34	341.3
32	31796	545.2	59.6	67.75	-124.21	-69.10	2217.0
33	31796	545.2	30.0	67.75	-125.88	-74.13	2212.6
34	10721	294.1	30.0	67.75	-274.41	-171.56	944.0
35	10721	294.1	21.5	1.00	-274.41	-169.30	942.0
36	11064	304.7	21.7	1.00	-274.05	-170.03	991.6
37	11064	304.7	30.0	1.00	-273.01	-166.60	991.7
38	9368	237.5	30.0	1.00	-263.55	-195.79	945.6
39	6089	154.4	30.0	1.00	-263.55	-195.79	614.6
40	6089	154.4	81.8	1.00	-227.00	-90.43	623.3
41	3279	83.1	30.0	1.00	-263.55	-195.79	331.0

Table S3.11 (Continuation)

Stream ID	Mole flow [kmol·h ⁻¹]	Mass flow [t·h ⁻¹]	Temp. [°C]	Pressure [bar]	Mole enthalpy [MJ·kmol ⁻¹]	Mole entropy [kJ·kmol ⁻¹ ·K ⁻¹]	Total Exergy [MJ·kmol ⁻¹]
42	3279	83.1	83.7	1.00	-221.93	-76.18	336.4
43	9368	237.5	82.5	1.00	-225.22	-85.43	959.7
44-MEOH	4540	145.6	53.0	1.00	-236.17	-231.08	912.2
45	4563	82.2	99.6	1.00	-280.00	-145.98	0.9
46-WATER	4563	82.2	67.8	1.00	-282.55	-153.01	0.4
47	265	9.6	53.0	1.00	-269.76	-70.90	33.7
48	21075	251.2	30.0	67.75	-50.33	-24.57	1268.6
49	20654	246.1	30.0	67.75	-50.33	-24.57	1243.2
50	20654	246.1	33.5	70.00	-50.23	-24.50	1243.7
51-REC	20654	246.1	89.3	70.00	-48.54	-19.44	1244.8
52	176	5.2	30.0	4.12	-258.84	-204.42	24.9
53	176	5.2	25.9	1.00	-258.84	-204.01	24.9
54	167	5.5	45.0	16.98	-267.39	-187.51	24.8
55	167	5.5	29.3	1.00	-267.39	-184.22	24.7
56	1696	67.2	30.0	1.00	-325.19	-5.35	46.1
57	1662	65.9	30.0	1.00	-325.19	-5.35	45.2
58-REC	1927	75.5	34.0	1.00	-317.58	-13.64	78.8
59-PURGE	34	1.3	30.0	1.00	-325.19	-5.35	0.9
60-PURGE	422	5.0	30.0	67.75	-50.33	-24.57	25.4
61-AIR	873	25.2	25.0	1.00	0.00	4.38	0.0
62	873	25.2	258.5	1.00	6.90	21.44	0.4
63	1181	31.5	1879.5	1.00	-22.21	67.16	16.5
64	1181	31.5	283.5	1.00	-83.55	16.68	1.4
65-FLUE	1181	31.5	124.4	1.00	-88.65	5.91	0.7
66W	7680	138.4	99.6	1.00	-280.01	-145.97	1.4
67W	7680	138.4	101.2	45.75	-279.88	-145.65	1.5
68W	7680	138.4	248.5	45.75	-265.14	-114.97	13.4
69W	2129	38.4	248.5	45.75	-265.14	-114.97	3.7
70W	2129	38.4	258.5	45.75	-233.85	-56.37	11.9
71W	2951	53.2	248.5	45.75	-265.14	-114.97	5.2
72W	2951	53.2	258.5	45.75	-234.04	-56.73	16.4
73W	2600	46.8	248.5	45.75	-265.14	-114.97	4.6
74W	2600	46.8	258.5	45.75	-233.86	-56.40	14.5
75W	7680	138.4	258.5	45.75	-233.92	-56.52	42.8
76W	7680	138.4	509.3	45.75	-224.49	-41.98	53.7
77W	2077	37.4	509.3	45.75	-224.49	-41.98	14.5
78W	2077	37.4	111.8	45.75	-279.00	-143.37	0.5
79W	5602	100.9	509.3	45.75	-224.49	-41.98	39.2
80W	5602	100.9	120.4	1.43	-238.59	-37.90	15.4
81W	5602	100.9	110.0	1.43	-274.91	-132.69	2.8
82W	7680	138.4	110.0	1.43	-276.02	-135.58	3.3

Table S3.12 Molar composition (% mol/mol) of the streams from the three-step process. Reproduced with permission from Campos et al.¹¹. Copyright 2022, MDPI.

Stream ID	H ₂	CO	CO ₂	CH ₃ OH	H ₂ O	N ₂	O ₂
1-CO2	0.000	0.000	99.500	0.000	0.500	0.000	0.000
2	0.575	0.310	90.708	5.592	0.957	1.858	0.000
3	0.575	0.310	90.708	5.592	0.957	1.858	0.000
4	0.575	0.310	90.708	5.592	0.957	1.858	0.000
5	0.590	0.318	93.045	3.814	0.322	1.909	0.000
6	0.590	0.318	93.045	3.814	0.322	1.909	0.000
7	0.590	0.318	93.045	3.814	0.322	1.909	0.000
8	0.606	0.327	95.083	1.950	0.075	1.960	0.000
9	0.606	0.327	95.083	1.950	0.075	1.960	0.000
10-H2	99.500	0.000	0.000	0.000	0.000	0.500	0.000
11	99.500	0.000	0.000	0.000	0.000	0.500	0.000
12	69.148	1.301	20.603	0.376	0.027	8.545	0.000
13	69.148	1.301	20.603	0.376	0.027	8.545	0.000
14	60.953	2.651	16.835	4.711	5.570	9.279	0.000
15	60.953	2.651	16.835	4.711	5.570	9.279	0.000
16	60.953	2.651	16.835	4.711	5.570	9.279	0.000
17	60.953	2.651	16.835	4.711	5.570	9.279	0.000
18	68.971	2.974	17.283	0.283	0.074	10.415	0.000
19	68.971	2.974	17.283	0.283	0.074	10.415	0.000
20	68.971	2.974	17.283	0.283	0.074	10.415	0.000
21	61.037	2.664	14.451	5.594	4.739	11.515	0.000
22	61.037	2.664	14.451	5.594	4.739	11.515	0.000
23	61.037	2.664	14.451	5.594	4.739	11.515	0.000
24	61.037	2.664	14.451	5.594	4.739	11.515	0.000
25	69.456	3.001	14.377	0.157	0.028	12.982	0.000
26	69.456	3.001	14.377	0.157	0.028	12.982	0.000
27	61.594	2.209	11.528	5.754	4.484	14.431	0.000
28	61.594	2.209	11.528	5.754	4.484	14.431	0.000
29	61.594	2.209	11.528	5.754	4.484	14.431	0.000
30	0.362	0.236	14.984	44.780	38.689	0.949	0.000
31	0.370	0.213	13.448	38.169	47.100	0.699	0.000
32	46.077	1.706	12.192	14.731	14.316	10.979	0.000
33	46.077	1.706	12.192	14.731	14.316	10.979	0.000
34	0.360	0.194	12.500	43.384	42.399	1.164	0.000
35	0.360	0.194	12.500	43.384	42.399	1.164	0.000
36	0.349	0.188	12.458	44.266	41.612	1.128	0.000
37	0.349	0.188	12.458	44.266	41.612	1.128	0.000
38	0.000	0.001	1.188	50.087	48.715	0.008	0.000
39	0.000	0.001	1.188	50.087	48.715	0.008	0.000
40	0.000	0.001	1.188	50.087	48.715	0.008	0.000
41	0.000	0.001	1.188	50.087	48.715	0.008	0.000
42	0.000	0.001	1.188	50.087	48.715	0.008	0.000
43	0.000	0.001	1.188	50.087	48.715	0.008	0.000
44-MEOH	0.000	0.000	0.314	99.668	0.017	0.000	0.000

Table S3.12 (Continuation)

Stream ID	H ₂	CO	CO ₂	CH ₃ OH	H ₂ O	N ₂	O ₂
45	0.000	0.000	0.000	0.010	99.990	0.000	0.000
46-WATER	0.000	0.000	0.000	0.010	99.990	0.000	0.000
47	0.006	0.051	36.679	62.974	0.004	0.285	0.000
48	69.332	2.474	12.035	0.155	0.030	15.973	0.000
49	69.332	2.474	12.035	0.155	0.030	15.973	0.000
50	69.332	2.474	12.035	0.155	0.030	15.973	0.000
51-REC	69.332	2.474	12.035	0.155	0.030	15.973	0.000
52	0.000	0.001	5.785	70.187	24.018	0.008	0.000
53	0.000	0.001	5.785	70.187	24.018	0.008	0.000
54	0.001	0.005	16.820	73.579	9.565	0.030	0.000
55	0.001	0.005	16.820	73.579	9.565	0.030	0.000
56	2.274	1.218	74.689	12.118	2.388	7.313	0.000
57	2.274	1.218	74.689	12.118	2.388	7.313	0.000
58-REC	1.963	1.058	69.470	19.100	2.061	6.348	0.000
59-PURGE	2.274	1.218	74.689	12.118	2.388	7.313	0.000
60-PURGE	69.332	2.474	12.035	0.155	0.030	15.973	0.000
61-AIR	0.000	0.000	0.000	0.000	0.000	79.000	21.000
62	0.000	0.000	0.000	0.000	0.000	79.000	21.000
63	0.145	0.216	7.548	0.000	25.558	64.303	2.230
64	0.145	0.216	7.548	0.000	25.558	64.303	2.230
65-FLUE	0.145	0.216	7.548	0.000	25.558	64.303	2.230
66W	0.000	0.000	0.000	0.000	100.000	0.000	0.000
67W	0.000	0.000	0.000	0.000	100.000	0.000	0.000
68W	0.000	0.000	0.000	0.000	100.000	0.000	0.000
69W	0.000	0.000	0.000	0.000	100.000	0.000	0.000
70W	0.000	0.000	0.000	0.000	100.000	0.000	0.000
71W	0.000	0.000	0.000	0.000	100.000	0.000	0.000
72W	0.000	0.000	0.000	0.000	100.000	0.000	0.000
73W	0.000	0.000	0.000	0.000	100.000	0.000	0.000
74W	0.000	0.000	0.000	0.000	100.000	0.000	0.000
75W	0.000	0.000	0.000	0.000	100.000	0.000	0.000
76W	0.000	0.000	0.000	0.000	100.000	0.000	0.000
77W	0.000	0.000	0.000	0.000	100.000	0.000	0.000
78W	0.000	0.000	0.000	0.000	100.000	0.000	0.000
79W	0.000	0.000	0.000	0.000	100.000	0.000	0.000
80W	0.000	0.000	0.000	0.000	100.000	0.000	0.000
81W	0.000	0.000	0.000	0.000	100.000	0.000	0.000
82W	0.000	0.000	0.000	0.000	100.000	0.000	0.000

S3.7 Equipment dimensioning

S3.7.1 Flash drum

According to Towler & Sinnott,¹¹¹ the diameter (D) of a flash drum with a demister pad can be estimated by following equation:

$$D = \sqrt{\frac{4 \cdot \dot{V}_g}{\pi \cdot u_t}} \quad (\text{S3.39})$$

Where \dot{V}_g is the gas volumetric flow rate ($\text{m}^3 \cdot \text{s}^{-1}$) and u_t is the settling velocity of the liquid droplets, which is estimated as follows:

$$u_t = 0.07 \cdot \sqrt{\frac{\rho_L - \rho_g}{\rho_g}} \quad (\text{S3.40})$$

Here, ρ_L and ρ_g are the liquid the gas densities ($\text{kg} \cdot \text{m}^{-3}$).

According to Towler & Sinnott,¹¹¹ the adequate height (H , in m) of the flash drum is estimated as follows:

$$H = 1.5 \cdot D + 0.5 + \frac{\dot{V}_L}{A_c} \cdot t_h \quad (\text{S3.41})$$

Where \dot{V}_L is the liquid volumetric flow rate ($\text{m}^3 \cdot \text{s}^{-1}$), A_c is the cross section area (m^2), and t_h is the liquid hold up time (s), which is typically 10 minutes for low viscous fluids.

The estimated dimensions of the flash drums are summarized in Table S3.13.

Table S3.13 Dimension of the flash drums of the one-step and the three-step processes. Reproduced with permission from Campos et al.¹¹. Copyright 2022, MDPI.

Process	Equipment	Diameter (m)	Height (m)	Volume (m^3)
One-step	Flash 1	4.59	7.48	123.5
	Flash 2	3.25	5.54	46.0
	Flash 3	4.33	11.18	164.8
	Flash 4	3.77	10.37	115.6
Three-step	Flash 1	4.28	6.99	100.6
	Flash 2	3.04	5.21	37.7
	Flash 3	3.59	8.14	82.6
	Flash 4	3.13	7.77	59.8
	Flash 5	2.78	13.94	84.9
	Flash 6	3.05	11.47	84.0

S3.7.2 Distillation column

Since methanol production is fixed for both processes, and the inlet feed of the distillation column mainly consists in methanol and water at 50/50% mol/mol, the operating conditions of this equipment is similar in both processes, and, therefore, the same dimensions applies for both cases.

In a packed distillation column, the capacity is associated with the column cross-section area (i.e. its diameter), while the separation efficiency is associated with the column height (i.e. the number of theoretical stages). Towler and Sinnott¹¹¹ recommend a packing size between 50 and 76 mm if the column diameter is larger than 0.9 m. We chose then carbon steel pall rings with 76 mm packing size, which correspond to a packing factor (F_P) of 52 m⁻¹.

In order to estimate the required cross-section area, first a stress factor (F_{LV}) is calculated:

$$F_{LV} = \frac{\dot{m}_L}{\dot{m}_g} \cdot \sqrt{\frac{\rho_g}{\rho_L}} \quad (\text{S3.42})$$

Here, \dot{m}_L and \dot{m}_g are the liquid and gas mass flow rates (kg·s⁻¹), ρ_L and ρ_g are the liquid and gas densities (kg·m⁻³).

Towler and Sinnott¹¹¹ recommend a pressure drop in packed distillation columns to be between 40 and 80 (mm H₂O)·(m of packed height)⁻¹. Considering a pressure drop around 80 (mm H₂O)·(m of packed height)⁻¹, and a calculated stress factor of 0.059, a constant K_4 of 2.1 is obtained from a generalized pressure drop correlation.¹¹¹ The required cross-section area (A_c) of the column is 39.1 m², which is calculated with following equation:¹¹¹

$$A_c = \dot{m}_g \cdot \sqrt{\frac{13.1 \cdot F_P}{K_4 \cdot \rho_g \cdot (\rho_L - \rho_g)}} \cdot \left(\frac{\mu_L}{\rho_L}\right)^{0.1} \quad (\text{S3.43})$$

In order to provide the required cross-section area, two columns are proposed, each with a diameter of $D = 5$ m (combined $A_c = 39.27$ m²). The height the packed columns is estimated by multiplying the number of stages (30) to a height equivalent to a theoretical plate (HETP). A typical value for large packing size of HETP = 1 m is assumed,¹¹¹ corresponding to a total column height of 30 m.

S3.7.3 Heat exchanger

The estimation of the required surface area of a heat exchanger (A_S) is made considering a global heat transfer coefficient (U) and logarithmic mean temperature difference (ΔT_{LM}), as follows:

$$A_S = \frac{\dot{Q}}{U \cdot \Delta T_{LM}} \quad (\text{S3.44})$$

$$\Delta T_{LM} = \frac{(\Delta T_{hot} - \Delta T_{cold})}{\ln\left(\frac{\Delta T_{hot}}{\Delta T_{cold}}\right)} \quad (\text{S3.45})$$

Where ΔT_{hot} and ΔT_{cold} are the inlet/outlet temperature difference of the hot fluid and the cold fluid, respectively, and \dot{Q} is the heat transfer duty.

The heat transfer coefficient of each heat exchanger (U), including the condenser and reboiler of the distillation columns, is selected from the typical values presented in the VDI Atlas,¹⁰¹ which depend on the conditions of both fluids. In Table S3.14, the considered coefficients, the heat duties and the surface areas of the heat exchangers are summarized.

Table S3.14 Heat transfer duty, global heat transfer coefficients, and estimated surface area of the heat exchangers of the one-step and the three-step process. Reproduced with permission from Campos et al.¹¹. Copyright 2022, MDPI.

Process	Equipment	\dot{Q} (MW)	U (W·m ⁻² ·K ⁻¹)	A_S (m ²)
One-step	HE1	13.6	50	5800
	HE2	11.1	70	3610
	HE3	5.6	200	1160
	HE4	105.5	150	27,270
	HE5	103.3	300	8520
	HE6	5.0	600	240
	HE7	24.2	300	4280
	HE8	41.8	1500	340
	Col. Condenser	143.6	1000	2360
	Col. Reboiler	53.7	1000	2580
Three-step	HE1	11.1	50	4730
	HE2	9.7	70	4280
	HE3	47.6	150	24,060
	HE4	61.8	300	4940
	HE5	7.7	300	870
	HE6	13.0	150	5050
	HE7	46.3	150	15,050
	HE8	14.3	300	2210
	HE9	37.9	300	3320
	HE10	49.7	150	10,530
	HE11	14.8	300	2490
	HE12	3.2	300	190
	HE13	8.5	1500	70
	HE14	31.5	1000	410
	Col. Condenser	143.0	1000	2350
	Col. Reboiler	56.5	1000	2690

S3.8 Techno-economic analysis

Table S3.15 Calculation of the Capital Expenses (CAPEX) depending on the total equipment costs (EC). Reproduced with permission from Campos et al.¹¹. Copyright 2022, MDPI.

Item	Costs
Direct costs (D)	
Equipment costs (EC)	$\sum EC_j$
Installation	$0.47 \cdot \sum EC_j$
Instrumentation controls	$0.36 \cdot \sum EC_j$
Piping	$0.68 \cdot \sum EC_j$
Electrical systems	$0.11 \cdot \sum EC_j$
Buildings	$0.18 \cdot \sum EC_j$
Yard improvement	$0.10 \cdot \sum EC_j$
Service facilities	$0.55 \cdot \sum EC_j$
Indirect costs (I)	
Engineering & supervision	$0.33 \cdot \sum EC_j$
Construction expenses	$0.41 \cdot \sum EC_j$
Legal expenses	$0.4 \cdot \sum EC_j$
Contractors	$0.05 \cdot (D + I) = 0.2115 \cdot \sum EC_j$
Contingency	$0.10 \cdot (D + I) = 0.4230 \cdot \sum EC_j$
Fixed capital investment (FCI)	$4.8645 \cdot \sum EC_j$
Working capital (WC)	$0.10 \text{ of CAPEX} = 0.5405 \cdot \sum EC_j$
Capital expenses (CAPEX)	$FCI + WC = 5.4050 \cdot \sum EC_j$

Table S3.16 Estimation of indirect operating expenses ($OPEX_{ind}$). Reproduced with permission from Campos et al.¹¹. Copyright 2022, MDPI.

Item	Costs
Operating labor (OL)	OL
Operating supervision (OS)	$0.15 \cdot OL$
Maintenance labor (ML)	$0.02 \cdot FCI$
Maintenance material (MM)	$0.02 \cdot FCI$
Operating supplies	$0.15 \cdot (ML + MM) = 0.006 \cdot FCI$
Laboratory charges	$0.20 \cdot OL$
Insurance and taxes	$0.02 \cdot FCI$
Plant overhead (PO)	$0.60 \cdot (OL + OS + ML) = 0.69 \cdot OL + 0.012 \cdot FCI$
Administrative costs	$0.25 \cdot PO = 0.1725 \cdot OL + 0.003 \cdot FCI$
Distribution & Marketing costs	$0.06 \cdot NPC$
Research & Development	$0.04 \cdot NPC$
Total $OPEX_{ind}$	$2.2125 \cdot OL + 0.081 \cdot FCI + 0.10 \cdot NPC$

Table S3.17 Equipment characteristic dimensions and equipment costs (*EC*) of the one-step approach. All equipment is built with carbon steel. All equipment reference price is taken from Peters et al.,¹⁰⁸ except for the power generator, whose ref. price is taken from Hennig and Haase.¹⁰⁹ Reproduced with permission from Campos et al.¹¹. Copyright 2022, MDPI.

Equipment ID	Scaling factor	Characteristic capacity	Total cost in 2020 (M€)
<i>Centrifugal compressors and pumps</i>			
CP1-CO2	0.69	Power = 11.50 MW	9.15
CP2-CO2	0.69	Power = 11.16 MW	8.89
CP3-CO2	0.69	Power = 11.37 MW	9.06
CP-H2	0.69	Power = 12.58 MW	10.02
CP-REC	0.69	Power = 0.57 MW	0.52
Pump	0.33	Volumetric flow rate = 0.044 m ³ ·s ⁻¹ , Discharge pressure = 38.07 bar	0.11
<i>Flash drums</i>			
FLASH1	0.57	Volume = 124 m ³	0.05
FLASH2	0.57	Volume = 46 m ³	0.03
FLASH3	0.57	Volume = 165 m ³	0.05
FLASH4	0.57	Volume = 116 m ³	0.05
<i>Fixed-tubed heat exchangers and reactor modules</i>			
HE1	0.44	Heat transfer area = 5800 m ²	0.52
HE2	0.44	Heat transfer area = 3610 m ²	0.40
HE3	0.44	Heat transfer area = 1160 m ²	0.13
HE4	0.44	Heat transfer area = 27270 m ²	3.01
HE5	0.44	Heat transfer area = 8520 m ²	0.94
HE6	0.44	Heat transfer area = 240 m ²	0.04
HE7	0.44	Heat transfer area = 4280 m ²	0.48
HE8	0.44	Heat transfer area = 340 m ²	0.04
Reactor (6 units)	0.44	Heat transfer area = 48600 m ²	32.18
<i>Distillation column (2 units of each equipment)</i>			
Condenser	0.44	Heat transfer area = 2360 m ²	0.43
Reboiler	0.60	Heat transfer area = 2580 m ²	0.50
Packed Column	0.86	Diameter = 5 m, Height = 30 m	2.06
<i>Fired heater and air blower</i>			
Fired heater	0.60	Heat duty = 51.00 MW	3.54
Blower	0.616	Air flow = 15.36 m ³ ·s ⁻¹	0.56
<i>Steam turbine and power generator</i>			
Steam Turbine	0.44	Power = 29.82 MW	1.04
Generator	1	Power = 29.82 MW	1.71

Table S3.18 Equipment characteristic dimensions and equipment costs (EC) of the three-step approach. All equipment is built with carbon steel, and the costs include 10% delivery costs. All equipment reference price is taken from Peters et al.,¹⁰⁸ except for the power generator, whose ref. price is taken from Hennig and Haase.¹⁰⁹ Reproduced with permission from Campos et al.¹¹. Copyright 2022, MDPI.

Equipment ID	Scaling factor	Characteristic capacity	Total cost in 2020 (M€)
<i>Centrifugal compressors and pumps</i>			
CP1-CO2	0.69	Power = 9.94 MW	7.92
CP2-CO2	0.69	Power = 9.75 MW	7.77
CP3-CO2	0.69	Power = 9.95 MW	7.93
CP-H2	0.69	Power = 12.14 MW	9.97
CP-REC	0.69	Power = 0.63 MW	0.57
Pump	0.33	Volumetric flow rate = 0.042 m ³ ·s ⁻¹ , Discharge pressure = 45.76 bar	0.13
<i>Flash drums</i>			
FLASH1	0.57	Volume = 101 m ³	0.05
FLASH2	0.57	Volume = 38 m ³	0.03
FLASH3	0.57	Volume = 83 m ³	0.05
FLASH4	0.57	Volume = 60 m ³	0.04
FLASH5	0.57	Volume = 85 m ³	0.05
FLASH6	0.57	Volume = 84 m ³	0.05
<i>Fixed-tubed heat exchangers and reactor modules</i>			
HE1	0.44	Heat transfer area = 4730 m ²	0.42
HE2	0.44	Heat transfer area = 4280 m ²	0.48
HE3	0.44	Heat transfer area = 24060 m ²	2.66
HE4	0.44	Heat transfer area = 4940 m ²	0.55
HE5	0.44	Heat transfer area = 870 m ²	0.10
HE6	0.44	Heat transfer area = 5050 m ²	0.56
HE7	0.44	Heat transfer area = 15050 m ²	1.66
HE8	0.44	Heat transfer area = 2210 m ²	0.25
HE9	0.44	Heat transfer area = 3320 m ²	0.37
HE10	0.44	Heat transfer area = 10530 m ²	1.17
HE11	0.44	Heat transfer area = 2490 m ²	0.28
HE12	0.44	Heat transfer area = 190 m ²	0.03
HE13	0.44	Heat transfer area = 70 m ²	0.01
HE14	0.44	Heat transfer area = 410 m ²	0.05
Reactor (3 units)	0.44	Heat transfer area = 48600 m ²	16.09

Table S3.18 (continuation)

Equipment ID	Scaling factor	Characteristic capacity	Total cost in 2020 (M€)
<i>Distillation column (2 units of each equipment)</i>			
Fixed-tubed Condenser	0.44	Heat transfer area = 2350 m ²	0.43
U-tubed Reboiler	0.60	Heat transfer area = 2690 m ²	0.52
Packed Column	0.86	Diameter = 5 m, Height = 30 m	2.06
<i>Fired heater and air blower</i>			
Fired Heater	0.60	Heat duty = 21.80 MW	1.70
Blower	0.616	Air flow = 6.01 m ³ ·s ⁻¹	0.22
<i>Steam turbine and power generator</i>			
Steam Turbine	0.44	Power = 20.84 MW	0.74
Generator	1	Power = 20.84 MW	1.19

Table S3.19 Detailed operating expenditures (OPEX) of the one-step and the three-step approach. Reproduced with permission from Campos et al.¹¹. Copyright 2022, MDPI.

Item	Process Requirements		Costs (M€·a ⁻¹)	
	One-Step	Three-Step	One-Step	Three-Step
Direct OPEX			874.94	839.6
Hydrogen	31.1 ton·h ⁻¹	30.0 ton·h ⁻¹	769.50	742.51
Carbon dioxide	211.7 ton·h ⁻¹	204.3 ton·h ⁻¹	74.93	72.30
Cooling water	38490 ton·h ⁻¹	34645 ton·h ⁻¹	0.38	0.35
Clean water	1.46 ton·h ⁻¹	1.38 ton·h ⁻¹	0.02	0.02
Total organic carbon (TOC) abatement of process water	7.75 kg·h ⁻¹	5.72 kg·h ⁻¹	0.12	0.09
Electricity	17.6 MW	21.83 MW	12.66	15.72
Catalyst (Cu/ZnO/Al ₂ O ₃)	956.2 ton·a ⁻¹	478.1 ton·a ⁻¹	17.31	8.65
Indirect OPEX			142.08	128.6
Operating labor (OL)	16 operators	16 operators	1.15	1.15
Operating supervision (OS)			0.17	0.17
Maintenance labor (ML)			8.06	6.23
Maintenance material (MM)			8.06	6.23
Operating supplies			2.42	1.87
Laboratory charges			0.23	0.23
Insurances and taxes			8.06	6.23
Plant overhead (PO)			5.63	4.53
Administrative Costs			1.41	1.13
Distribution & Marketing Costs			64.13	60.50
Research & Development			42.75	40.33

Nomenclature

A	Surface area (m ²)
A_n	Parameter n of Model-6p and Model-9p
$A_{n,m}$	Coefficient n of the Gibbs function (or equil. constant) for reaction path m
$a_{n,j}$	Coefficient n of the Gibbs term of gas species j (Eq. 2.14)
a_j	Activity of gas component j
C_j	Characteristic capacity of equipment j
$C_{P,f}$	Heat capacity of the fluid (kJ·mol ⁻¹ ·K ⁻¹)
$C_{P,j}$	Heat capacity of component j (kJ·mol ⁻¹ ·K ⁻¹)
$\Delta c_{p,m}$	Heat capacity change of global reaction m (kJ·mol ⁻¹ ·K ⁻¹)
D_i	Inner diameter of a single tube (m)
d_i	Crystallite diameter of species i (m)
d_p	Particle diameter (m)
DRC_i	Degree of rate control of a transition state or surface intermediate i
$E_{A,k}$	Activation energy of reaction k (kJ·mol ⁻¹)
E_Q	Exergy input associated with heat demand (kJ)
Exc	Excess of feed (%)
e_j	Exergy of component j (kJ·mol ⁻¹)
F_{LV}	Stress factor (-)
F_{OP}	Number of operators to fulfill each position in a continuous operation (-)
f_j	Fugacity of gas component j (bar)
$G_j^0(T)$	Free Gibbs energy at 1 bar and temperature T (kJ·mol ⁻¹)
$\Delta G_R^0(T)$	Free Gibbs energy of reaction R at 1 bar and temperature T (kJ·mol ⁻¹)
H	Height (m)
\dot{H}	Enthalpy flow (kW)
h	Planck constant (6.62607·10 ⁻³⁴ J·s)
h_f	Specific enthalpy of the fluid (kJ·mol ⁻¹)
h_j	Specific enthalpy of component j (kJ·mol ⁻¹)
$\Delta H_{298.15 K}^0$	Standard reaction enthalpy (kJ·mol ⁻¹)
ΔH_{seg}^0	Segregation enthalpy at 1 bar (kJ·mol ⁻¹)
\bar{K}_j	Adsorption parameter j (Model-6p and Model-9p)
K_4	Constant of a generalized pressure correlation (column size estimation)
K_R	Equilibrium constant of elementary reversible reaction R
K_r	Inverse of the inclination parameter (-)
k_b	Boltzmann constant (1.38065·10 ⁻²³ J·K ⁻¹)
k_c	Thermal conductivity of the core of the unit cell (W·m ⁻² ·K ⁻¹)
k_k	Rate constant of reaction k
L	Catalyst bed length (m)

\mathcal{L}	Lagrangean function
M_i	Molar mass of species i ($\text{kg}\cdot\text{mol}^{-1}$)
m	Mass (kg)
\dot{m}	Mass flow rate ($\text{kg}\cdot\text{s}^{-1}$)
N_g	Number of gas components (-)
N_{np}	Number of non-particulate main processing units
N_{OP}	Total number of operators (-)
n_{OP}	Required number of operators in a shift (-)
N_p	Number of experimental points (-)
N_p^*	Number of experimental points containing CO_2 in feed
N_r	Number of surface reactions (-)
N_s	Number of surface intermediates (-)
$n_{M,Cat}$	Specific catalyst site quantity ($\text{mol}\cdot\text{kg}^{-1}$)
\dot{n}	Total mole flow ($\text{mol}\cdot\text{s}^{-1}$)
$\Delta\dot{n}_{MeOH}$	Methanol production in the reactor ($\text{kmol}\cdot\text{h}^{-1}$)
Nu_w	Nusselt number (-)
P_{el}	Total required electric power (kW)
p_j	Partial pressure of component j (bar)
p_0	Reference pressure (1 bar)
Pe_0	Peclet number
Pr	Prandtl number
\dot{Q}	Heat transfer duty (kW)
$q_{n,m}$	Thermodynamic constraint n of reaction pathway m
R	Universal gas constant ($8.31446\cdot 10^{-3} \text{ kJ}\cdot\text{mol}^{-1}\cdot\text{K}^{-1}$)
r_k	Turnover frequency of reversible reaction k (s^{-1})
\dot{r}_k	Rate of reaction k ($\text{mol}\cdot\text{kg}_{cat}^{-1}\cdot\text{s}^{-1}$)
Re_0	Reynolds number (-)
\dot{S}	Entropy rate (kW)
s_j	Specific entropy ($\text{kJ}\cdot\text{mol}^{-1}\cdot\text{K}^{-1}$)
\dot{s}_k	Rate of reaction k ($\text{mol}\cdot\text{m}^{-2}\cdot\text{s}^{-1}$)
s_t	Thickness of the reactor tube (m)
ΔS_k^\ddagger	Entropy barrier of reaction k ($\text{kJ}\cdot\text{mol}^{-1}\cdot\text{K}^{-1}$)
T	Temperature (K)
T_0	Reference temperature (298.15 K)
ΔT_{LM}	Logarithmic Mean Temperature Difference (K)
ΔT	Temperature difference (K)
t_p	Plant operating life (a)
t_h	Liquid hold-up time (s)
U	Global heat transfer coefficient ($\text{W}\cdot\text{m}^{-2}\cdot\text{K}^{-1}$)
U_{int}	Internal energy (kJ)

u_t	Settling velocity of the liquid droplets ($\text{m}\cdot\text{s}^{-1}$)
\dot{V}	Volumetric flow rate ($\text{m}^3\cdot\text{s}^{-1}$)
W_{OP}	Wage rate of each operator ($\text{€}\cdot\text{a}^{-1}$)
w_k	Selectable weight of reaction k (-)
y_j	Mole fraction of gas component j (mol/mol)
$y_{j,out}^n$	Experimental value (point n) of mole fraction of gas component j of point n in the reactor outlet (mol/mol)
$\hat{y}_{j,out}^n$	Simulated value (point n) of mole fraction of gas component j of point n in the reactor outlet (mol/mol)
X_{Zn}	Solubility of zinc in the copper bulk (mol/mol)

Greek

α	Proposed linear relation parameter between the zinc oxide activity and the zinc solubility in the Cu bulk (-)
$\alpha_{w,i}$	Heat transfer coefficient between the reactive system and the inner wall ($\text{W}\cdot\text{m}^{-2}\cdot\text{K}^{-1}$)
$\alpha_{w,o}$	Heat transfer coefficient between the outer wall and the cooling fluid ($\text{W}\cdot\text{m}^{-2}\cdot\text{K}^{-1}$)
β_k	Correction term of reaction k because of the thermodynamic consistency (-)
Γ	Surface site density ($\text{mol}\cdot\text{m}^{-2}$)
γ_{Zn}	Activity coefficient of metallic zinc (-)
$\bar{\gamma}_i$	Surface energy of species i ($\text{kJ}\cdot\text{m}^{-2}$)
δ	Step size of the finite differences method ($\text{kJ}\cdot\text{mol}^{-1}$)
$\zeta_{k,m}$	Stoichiometric coefficient of a reversible surface reaction k in the global reaction pathway m (-)
η	Efficiency (-)
θ_i	Surface coverage of species i (-)
Λ_r	Effective radial thermal conductivity of the two-phase system ($\text{W}\cdot\text{m}^{-1}\cdot\text{K}^{-1}$)
$\lambda_{i,m}$	Lagrange multiplier i
λ_{bed}	Thermal conductivity of the catalyst bed ($\text{W}\cdot\text{m}^{-1}\cdot\text{K}^{-1}$)
λ_f	Thermal conductivity of the fluid ($\text{W}\cdot\text{m}^{-1}\cdot\text{K}^{-1}$)
μ	Dynamic viscosity ($\text{Pa}\cdot\text{s}$)
ρ_i	Density of species i ($\text{kg}\cdot\text{m}^{-3}$)
σ_i	Number of surface sites occupied by species i (-)
ν'_{ik}	Stoichiometric coefficient of reactant i in reaction k (-)
ν''_{ik}	Stoichiometric coefficient of product i in reaction k (-)
ν_{ik}	Stoichiometric gain of species i in reaction k (-)
ϕ_i	Fraction of the site type of surface species i in relation to the total number of sites for carbon-containing compounds (sites a and b)
χ_i	Species i (-)

ψ Bed porosity (-)

Subscription

<i>3p</i>	Related to the three-parameter Gibbs function (Eq. 3.19)
<i>7p</i>	Related to the seven-parameter Gibbs function (Eq. 3.14)
<i>avg</i>	Average value
<i>bed</i>	Catalyst bed
<i>c</i>	Cross-section
<i>Cat</i>	Catalyst
<i>CCE</i>	Chemical Conversion Efficiency
<i>chem</i>	Related to the chemical exergy
<i>cold</i>	Cold fluid
<i>DFT</i>	Values from DFT calculations
<i>Ex</i>	Exergy
<i>f</i>	Fluid
<i>feed</i>	Feed stream
<i>g</i>	Gas
<i>hot</i>	Hot fluid
<i>i</i>	Inner tube side
<i>in</i>	Species entering the reactor
<i>L</i>	Liquid
<i>m</i>	Reaction path number (See Fig. 3.2)
<i>max</i>	Maximum
<i>min</i>	Minimum
<i>o</i>	Outer tube side
<i>out</i>	Species leaving the reactor
<i>R_i</i>	Related to reactor <i>i</i> (three-step process)
<i>rec</i>	Recycle stream
<i>ref</i>	Reference
<i>therm</i>	Related to the thermal exergy
<i>w</i>	Cooling fluid

Superscription

0	Related to the reference state (298.15 K and 1 bar)
+	Related to the forward reaction
-	Related to the reverse reaction
<i>Orig.</i>	Original DFT value
<i>TC</i>	Thermodynamically consistent value

List of Abbreviations

ACC	Annual Capital Costs
ASME	American Society of Mechanical Engineers
CAPEX	Capital Expenses
CCE	Chemical Conversion Efficiency
CCU	Carbon Capture Unit
CEPCI	Chemical Engineering Plant Cost Indexes
CSTR	Continuous Stirred Tank Reactor
CZA	Cu/ZnO/Al ₂ O ₃
DFT	Density Functional Theory
DME	Dimethyl Ether
DMFC	Direct Methanol Fuel Cell
DRC	Degree of Rate Control
EC	Equipment Costs
FCI	Fixed Capital Investment
FTIR	Fourier Transform Infrared Spectrometer
GHSV	Gas Hourly Space Velocity
GRP	Gas Reducing Power
HETP	Height Equivalent to a Theoretical Plate
LHHW	Langmuir–Hinshelwood–Hougen–Watson (Model)
LHV	Low Heating Value
LF	Lang Factor
ICI	Imperial Chemical Industries
IR	Interest Rate
ME	Mean Error
MFC	Mass Flow Controller
MOFs	Metal-Organic Frameworks
MSE	Mean Squared Error
MTBE	Methyl Tert-Butyl Ether
MTOE	Million Tons of Oil Equivalent
NPC	Net Production Costs
NRTL	Non-Random Two-Liquid (Model)
OL	Operating Labor
OME	Oxymethylene Ether
OPEX	Operating Expenses
PFR	Plug Flow Reactor
PID	Proportional-Integral-Derivative
RDS	Rate-Determining Step
rWGS	Reverse Water-Gas Shift Reaction

SM	Supplementary Material
TOC	Total Organic Carbon
WC	Working Capital
WGSR	Water-Gas Shift Reaction

List of Figures

Fig. 1.1 From syngas sources to higher added-value chemicals and fuels via methanol synthesis.	3
Fig. 1.2 CO _x equilibrium conversion to methanol at different temperatures and pressures, with stoichiometric feed gas composition.	10
Fig. 1.3 Basic types of methanol reactor.	11
Fig. 1.4 Outline of the PhD thesis.	13
Fig. 2.1 Reaction network of the carbon-containing species in the methanol synthesis and the WGSR.	19
Fig. 2.2 Methanol equilibrium concentration calculated with Aspen Plus and with the microkinetic model.	24
Fig. 2.3 Solubility of zinc in the Cu-bulk (a) and zinc coverage (b) as functions of the gas reducing power.	26
Fig. 2.4 Original model simulation (one-case): normalized residues of CO concentration in the simulation of the experiments from this work (1-359), from Seidel et al. ³⁴ (360-498), from Park et al. ³³ (499-596), and from Slotboom et al. ⁴¹ (597-690).	32
Fig. 2.5 Two-case model simulation: normalized residues of the simulation of the experiments from this work (1-359), from Seidel et al. ³⁴ (360-498), from Park et al. ³³ (499-596), and from Slotboom et al. ⁴¹ (597-690). A) Carbon monoxide. B) Carbon dioxide. C) Methanol.	33
Fig. 2.6 Experimental and simulated values of methanol output concentration at different conditions.	35
Fig. 2.7 Simulation error (color) as a function of CO ₂ /CO _x in feed and temperature.	35
Fig. 2.8 Turnover frequency and conversion of CO _x (<i>X</i>) along a methanol synthesis reactor with a length of 100 cm, simulated with the kinetic model.	36
Fig. 2.9 Coverage of the surface species along the reactor with a length of 100 cm.	37
Fig. 2.10 Formate coverage on Cu and Cu/Zn active surfaces, as a function of CO ₂ /CO _x ratio in the gas phase.	38
Fig. 2.11 Effect of CO ₂ feed concentration on the methanol production at 41 bar, 220-260 °C and 32 L·h ⁻¹ ·g _{cat} ⁻¹ .	39
Fig. 2.12 Degree of Rate Control (DRC) analysis of the methanol production at 60 bar and 210-260 °C.	40
Fig. 2.13 Degree of Rate Control (DRC) analysis at 210-260 °C, 60 bar, and a gas concentration of H ₂ /CO/CO ₂ /CH ₃ OH/H ₂ O = 79.8/0.2/19.6/0.2/0.2% v/v.	41

Fig. 3.1 Parity plots of Model-1p for measured and predicted CO (a-b), CO ₂ (c) and methanol (d-e) concentrations in the product stream.	55
Fig. 3.2 Parity plots of Model-9p for measured and predicted CO (a-b), CO ₂ (c) and methanol (d-e) concentrations in the product stream.	56
Fig. 3.3 CO _x conversion: simulation vs. experiments reported by Campos et al. ⁷⁰ .	57
Fig. 3.4 CO _x conversion: simulation vs. experiments reported by Seidel et.al ³⁴ .	58
Fig. 3.5 CO _x conversion: simulation vs. experiments reported by Slotboom et al. ⁴¹	58
Fig. 3.6 Parity plots of Model-6p for measured and predicted CO (a-b), CO ₂ (c) and methanol (d-e) concentrations in the product stream.	60
Fig. 3.7 CO _x conversion: simulation vs. experiments reported by Campos et al. ⁷⁰	61
Fig. 3.8 CO _x conversion: simulation vs. experiments.	61
Fig. 4.1 One-step process — Detailed flowsheet with a total of three reactor modules.	68
Fig. 4.2 Three-step process — Detailed flowsheet with a total of three reactor modules.	70
Fig. 4.3 One-step process — CO ₂ single-pass conversion (a), required feed excess (b), optimal temperature (c), and total recycle stream (d) as a function of the number of reactor modules and the purge fraction.	78
Fig. 4.4 One-step process — Product concentration along the reactor length.	79
Fig. 4.5 One-step process — Exergy analysis.	80
Fig. 4.6 Three-step process — CO ₂ single-pass conversion (a), required feed excess (b), optimal temperature (c), and total recycle stream (d) as a function of the number of reactor modules and the purge fraction.	81
Fig. 4.7 Three-step process—methanol, water, and CO concentration along the length of each reactor, as well as in the intermediate condensation steps (C1 and C2).	82
Fig. 4.8 Three-step process — Exergy analysis.	84
Fig. 4.9 Distribution of the costs.	86
Fig. 4.10 Sensitivity analysis of the main cost factors in relation to the net production costs (NPC).	87
Fig. 4.11 Net production costs of methanol as a function of green hydrogen price.	88
Fig. S1.1 Flow diagram of the single fixed-bed plug flow reactor (PFR).	100

Fig. S1.2 Temperature axial profile of the reactor at 61 bar (abs.), 250 °C, H ₂ /CO/CO ₂ /N ₂ = 55/12/3/30% v/v.	100
Fig. S1.3 Initial guess method: Finding a proper initial guess to calculate the coverages with the Newton-Raphson method instead of integrating the differential equations in time.	109
Fig. S1.4 Step-by-step method to solve the kinetic model of the PFR.	110
Fig. S1.5 Step-by-step method to solve the kinetic model of the CSTR.	111
Fig. S1.6 Turnover frequency and conversion along a methanol synthesis reactor with a length of 100 cm.	112
Fig. S1.7 Coverage of the surface species along the methanol synthesis reactor with a length of 100 cm.	113
Fig. S1.8 Degree of Rate Control (DRC) analysis of the methanol production at 30 bar and 210-260 °C.	114
Fig. S1.9 Degree of Rate Control (DRC) analysis at 210-260 °C, 30 bar, and a gas concentration of H ₂ /CO/CO ₂ /CH ₃ OH/H ₂ O = 79.8/0.2/19.6/0.2/0.2% v/v.	115
Fig. S2.1 Parity plots of model Slotboom A for measured and predicted CO (a-b), CO ₂ (c) and methanol (d-e) concentrations in the product stream.	122
Fig. S2.2 Parity plots of model Slotboom B for measured and predicted CO (a-b), CO ₂ (c) and methanol (d-e) concentrations in the product stream.	123
Fig. S2.3 Parity plots of the model from Seidel et al. ³⁴ for measured and predicted CO (a-b), CO ₂ (c) and methanol (d-e) concentrations in the product stream.	125
Fig. S3.1 One-step process – Aspen Plus flowsheet.	134
Fig S3.2 Three-step process – Aspen Plus flowsheet.	140

List of Tables

Table 1.1 Summary of different formal kinetic models reported in literature.	6
Table 2.1 Values of ϕ_i depending on the site type.	21
Table 2.2 Zinc coverage value depending on the CO ₂ to CO _x ratio in feed.	27
Table 2.3 Three-site field extended reaction mechanism for the methanol synthesis and the water-gas shift reaction over Cu (211) and Cu/Zn (211), thermodynamically consistent.	31
Table 2.4 Operating conditions of the considered database, which consists of different setups.	32
Table 2.5 Statistical indicators of the model performance in predicting the carbon-containing compounds. Considerations: two-case model, simplified method for zinc coverage estimation.	34
Table 3.1. Operating conditions of the different setups considered.	50
Table 3.2. Estimated parameters and considered experimental data for each model.	53
Table 3.3. Comparison of statistical values for the different kinetic models that consider the whole studied operating region ($0 \leq \bar{y}_{CO_2,0} \leq 1$).	54
Table 3.4. Comparison of statistical values for the models considering feeds containing CO ₂ ($\bar{y}_{CO_2,0} \geq 0.001$).	59
Table 3.5. Equations summary of the new developed Model-1p.	62
Table 3.6. Equations summary of the new developed Model-6p.	63
Table 3.7. Equations summary of the new developed Model-9p.	64
Table 4.1 Costs of feedstock, catalyst, water treating, and electricity.	76
Table 4.2 Three-step synthesis — Performance indicators for two process approaches: same cooling fluid temperature in all reactors, and independent optimization of the cooling fluid temperature in each reactor.	82
Table 4.3 Three-step process — Operating conditions and split ratios of the intermediate condensation steps.	83
Table 4.4 Three-step process — Heat transfer, inlet mole flow, mole fractions, and methanol production in the reactor modules.	83
Table 4.5 Data comparison between the one-step and the three-step approach.	85

Table 4.6 Summary of the costs of the one-step and the three-step process.	87
Table S1.1 Experimental data performed in the PFR.	101
Table S1.2 Estimated parameters of the free Gibbs energy change (Eq. 19 of the article) of the global reactions involved in the methanol synthesis.	109
Table S2.1 Reaction network of the methanol synthesis and the WGSR. ⁷⁰	117
Table S2.2 Coverage of the surface species as a function of elementary equilibrium constants, gas phase fugacities, free site coverages and zinc coverage.	118
Table S2.3 Kinetic constants, equilibrium constants, and zinc coverage. ^{70, 78}	120
Table S2.4 Original and optimized kinetic parameters from Slotboom et al. ⁴¹	121
Table S2.5 Original and optimized kinetic parameters from Seidel et al. ³⁴	124
Table S3.1 Parameters for the estimation of the specific heat capacity and specific enthalpy of selected components in the gas phase. ⁷⁵	128
Table S3.2 Liquid and gas fractions (% mol/mol) of the phase separation via flash drums and the separation via the distillation column in the one-step process.	130
Table S3.3 Liquid and gas fractions (% mol/mol) of the phase separation via flash drums and the separation via the distillation column in the three-step process.	130
Table S3.4 Aspen kinetic factor and Model-6p corresponding expressions.	131
Table S3.5 Coefficients of the driving force constant and the corresponding expressions from Model-6p.	132
Table S3.6 Concentration exponents (ν_j) of the driving force expression.	132
Table S3.7 Adsorption constants and the corresponding expression of Model-6p.	133
Table S3.8 Concentration exponents and the corresponding values of Model-6p.	133
Table S3.9 Properties of the streams from the one-step process.	136
Table S3.10 Molar composition (% mol/mol) of the streams from the one-step process.	138
Table S3.11 Properties of the streams from the three-step process.	142

Table S3.12 Molar composition (% mol/mol) of the streams from the three-step process.	144
Table S3.13 Dimension of the flash drums of the one-step and the three-step processes.	146
Table S3.14 Heat transfer duty, global heat transfer coefficients, and estimated surface area of the heat exchangers of the one-step and the three-step process.	148
Table S3.15 Calculation of the Capital Expenses (CAPEX) depending on the total equipment costs (EC).	149
Table S3.16 Estimation of indirect operating expenses ($OPEX_{ind}$).	150
Table S3.17 Equipment characteristic dimensions and equipment costs (EC) of the one-step approach.	151
Table S3.18 Equipment characteristic dimensions and equipment costs (EC) of the three-step approach.	152
Table S3.19 Detailed operating expenditures (OPEX) of the one-step and the three-step approach.	153

List of publications

This list was written in April 2023. For an updated list, see:

- Orcid (<https://orcid.org/0000-0002-1820-5173>)
- ResearchGate (<https://www.researchgate.net/profile/Bruno-Campos-3>)
- Lattes (<http://lattes.cnpq.br/0334287076094179>)
- Google Scholar (<https://scholar.google.com/citations?user=WQzAfg4AAAAJ&hl=en>)

Peer-reviewed manuscripts

[13] Lacerda de Oliveira Campos, B.; John, K.; Beeskow, P.; Herrera Delgado, K.; Pitter, S.; Dahmen, N.; Sauer, J. A detailed process and techno-economic analysis of the methanol synthesis from H₂ and CO₂ with intermediate condensation steps. *Processes*, 2022, 10, 1535. DOI: 10.3390/pr10081535

[12] Perret, L.; Lacerda de Oliveira Campos, B.; Herrera Delgado, K.; Zevaco, T. A.; Neumann, A.; Sauer, J. CO_x-fixation to elementary building blocks: anaerobic syngas fermentation vs. chemical catalysis. *Chemie Ingenieur Technik*, 2022, **94** (11), 1-22. DOI: 10.1002/cite.202200153

[11] Fraga, M. M. C.; Lacerda de Oliveira Campos, B.; Hendrawidjaja, H.; Schmitt, C. C.; Raffelt, K.; Dahmen, N. Fast Pyrolysis Oil Upgrading via HDO with Fe-Promoted Nb₂O₅-Supported Pd-Based Catalysts. *Energies*, 2022, **15**, 4762. DOI: 10.3390/en15134762

[10] Wild, S.; Lacerda de Oliveira Campos, B.; Zevaco, T. A.; Guse, D.; Kind, M.; Pitter, S.; Herrera Delgado, K.; Sauer, J. Experimental investigations and model-based optimization of CZZ/H-FER 20 bed compositions for the direct synthesis of DME from CO₂-rich syngas. *React. Chem. Eng.*, 2022, **7**, 943-956. DOI: 10.1039/d1re00470k

[9] Lacerda de Oliveira Campos, B.; Herrera Delgado, K.; Pitter, S.; Sauer, J. Development of consistent kinetic models derived from a microkinetic model of the methanol synthesis. *Ind. Eng. Chem. Res.*, 2021, 60 (42), 15074-15086. DOI: 10.1021/acs.iecr.1c02952

[8] Lacerda de Oliveira Campos, B.; Herrera Delgado, K.; Wild, S.; Studt, F.; Pitter, S.; Sauer, J. Surface reaction kinetics of the methanol synthesis and the water gas shift reaction on Cu/ZnO/Al₂O₃. *React. Chem. Eng.*, 2021, 6, 868-887. DOI: 10.1039/d1re00040c

[7] Lacerda de Oliveira Campos, B.; Fraga, M. M. C.; Costa, A. O. S.; Costa Jr., E. F. Analysis of the process of solar desalination with emphasis in the humidification and dehumidification method. *Engenharia Sanitária e Ambiental*, 2019, **24** (5), 861-873. DOI: 10.1590/S1413-41522019177407

[6] Moreira, J.; Lacerda de Oliveira Campos, B.; Costa Jr., E. F.; Costa, A. O. S. Exergy and sensibility analysis of each individual effect in a kraft multiple effect evaporator. *Tappi Journal*, 2019, **18** (10), 607-618. DOI: 10.32964/TJ18.10.605

[5] Fraga, M. M. C.; Lacerda de Oliveira Campos, B.; Lisboa, M. S.; Almeida, T. B.; Lins, V. F. C.; Costa, A. O. S. Analysis of a Brazilian thermal plant operation applying energetic and exergetic balances. *Brazilian*

Journal of Chemical Engineering, 2018, **35** (4), 1395-1403. DOI: 10.1590/0104-6632.20180354s20170425

[4] Lacerda de Oliveira Campos, B.; Costa, A. O. S.; Figueiredo, K. C. S.; Costa Jr., E. F. Performance comparison of different mathematical models in the simulation of a solar desalination by humidification-dehumidification. *Desalination*, 2018, **437**, 184-194. DOI: 10.1016/j.desal.2018.03.014

[3] Fraga, M. M.; Lacerda de Oliveira Campos, B.; Fonseca, J. M. F.; Almeida, T. B.; Lins, V. F. C. Analysis of the soiling effect on the performance of photovoltaic modules on a soccer stadium in Minas Gerais, Brazil. *Solar Energy*, 2018, **163**, 387-397. DOI: 10.1016/j.solener.2018.02.025

[2] Lacerda de Oliveira Campos, B.; Costa, A. O. S.; Costa Jr., E. F. Mathematical modeling and sensibility analysis of a solar humidification-dehumidification desalination system considering saturated air. *Solar Energy*, 2017, **157**, 321-327. DOI: 10.1016/j.solener.2017.08.029

[1] Lacerda de Oliveira Campos, B.; Fraga, M. M.; Costa Jr., E. F. Study of the vapor pressure of sodium chloride solutions. *Enciclopédia Biosfera*, 2016, **13** (24), 1670-1679. DOI: 10.18677/EnciBio_2016B_153

Conference Proceedings

[3] Herfet, M.; Lacerda de Oliveira Campos, B.; Herrera Delgado, K.; Guse, D.; Kind, M.; Dessel, I.; Warmuth, L.; Wild, S.; Zevaco, T.; Pitter, S.; Sauer, J. Experimental and Simulation Studies of Methanol and DME Synthesis from CO₂-rich Syngas on Cu/ZnO/ZrO₂ Catalysts. *DGMK/ÖGEW/SCI-Conference 'The Role of Catalysis for the Energy-Transition'*, Ludwigshafen, Germany, October 5-7, 2022.

[2] Nogueira, I. M.; Lacerda de Oliveira Campos, B.; Fraga, M. M. C.; Costa Jr., E. F.; Costa, A. O. S. Descrição da dinâmica de coletor solar para aquecimento de água salobra ou salgada. *CBTermo - X Congresso Brasileiro de Termodinâmica Aplicada*, Nova Friburgo (RJ), Brazil, November 3-8, 2019.

[1] Lacerda de Oliveira Campos, B.; Silva, M. E. S. R.; Freitas, R. F. S.; Sousa, R. G. Estudo da influência de diferentes iniciadores na síntese do hidrogel superabsorvente de acrilamida e ácido acrílico. *12º Congresso Brasileiro de Polímeros (12ºCBPol)*, Florianópolis (SC), Brazil, September 22-26, 2013.

Conference oral presentations

[3] Lacerda de Oliveira Campos, B.; Costa Jr., E. F. Herrera Delgado, K.; Costa, A. O. S.; Pitter, S.; Sauer J. Development of an artificial neural network to reproduce a microkinetic model for the methanol synthesis. *56. Jahrestreffen Deutscher Katalytiker*, Weimar, Germany, March 15-17, 2023.

[2] Lacerda de Oliveira Campos, B.; Herfet, M.; Rodrigues Niquini, G.; Wild, S.; Herrera Delgado, K.; Pitter, S.; Sauer J. Multi-scale modeling of methanol and direct dimethyl ether synthesis from CO₂-rich syngas. *19th Nordic Symposium on Catalysis*, Espoo, Finland, June 6-8, 2022.

[1] Lacerda de Oliveira Campos, B.; Herrera Delgado, K.; Wild, S.; Studt, F.; Pitter, S.; Sauer, J. Surface reaction kinetics of the methanol synthesis on Cu/Zn-based catalysts. *Annual Meeting On Reaction Engineering 2021*, Würzburg, Germany (online event), May 10-12, 2021.

Conference poster presentations

[3] Lacerda de Oliveira Campos, B.; Costa Jr., E. F.; Herrera Delgado, K.; Costa, A. O. S.; Sauer, J. Simulation of the methanol synthesis with artificial neural networks. *10th Brazil Germany Symposium for Sustainable Development*, Niterói (RJ), Brazil, September 18-20, 2022.

[2] Lacerda de Oliveira Campos, B.; Wild, S.; Herrera Delgado, K.; Pitter, S.; Sauer, J. Kinetic modeling and optimization of the methanol and dimethyl ether synthesis. *Annual Meeting On Reaction Engineering 2022*, Würzburg, Germany, July 16-18, 2022.

[1] Lacerda de Oliveira Campos, B.; Herrera Delgado, K.; Wild, S.; Studt, F.; Pitter, S.; Sauer, J. Microkinetic modeling of the methanol synthesis on Cu/Zn-based catalysts. *54. Jahrestreffen Deutscher Katalytiker*, Weimar, Germany (online event), March 16-19, 2021.